# Interaction of a Copper Surface with Light:

## Plasmons, Electrons & Molecular Vibrations

---

Natalia García Rey

Surface Science Research Centre
Department of Chemistry
University of Liverpool

Submitted for the degree of Doctor of Philosophy

September 2011

# Abstract

The interaction of light with a copper surface has been explored in this thesis in order to understand and enhance a photochemical process. The thesis is split into three main results sections: **Surface photochemistry**: from NO/Cu(110) photochemistry (chapter 3), towards the analysis of the nonlinear response of Cu(110) (chapter 4). **Vibrational dynamics at surfaces**, pyridine analyzed by SFG in combination with work function measurements (chapter 5) and, the ultrafast dynamics of pyridine/Cu(110) (chapter 6). **Surface enhanced photochemistry**, where we present our conclusions on plasmon-enhanced photochemistry combined with field enhancement modeling on copper surfaces (chapter 7).

In chapter 3 we investigate the photochemistry of NO dimers on a Cu(110) surface. Green light irradiation splits the dimer to generate a monomer on a thermally inaccessible atop site. The dimer dissociation is reversible. Wavelength-dependent measurements indicate that long-lived hot holes at the top of the copper d-band are responsible for the observed photochemistry.

In chapter 4 we investigate the electronic structure of clean and oxygen or pyridine covered Cu(110) using electronic sum frequency generation. We discover dynamically enhanced sum frequency related to long decoherence times of hot holes in the d-band.

Chapter 5 investigates the adsorption of pyridine on copper using vibrational sum frequency generation and work function measurements. A monolayer of pyridine/Cu(110) is revealed as an ultra-low work function surface (1.46 eV). The connection between the nonresonant sum frequency response and the surface work function is investigated for pyridine and some substituted pyridines.

Chapter 6 looks at the charge transfer between the Cu(110) surface and adsorbed pyridine in real time using femtosecond pump - broadband vibrational SFG probe spectroscopy. We investigate the ultrafast charge transfer for a range of coverages, pump wavelengths and pump polarisation and fluence. We detect a long-lived (400 fs) excited state of pyridine which is tentatively identified as an anion or a dipole-bound electron. Upon deexcitation this causes disorder in the highly ordered pyridine layer which relaxes on a 40 picosecond timescale.

Chapter 7 finally looks into the question how efficiently photochemical processes can be enhanced by plasmon excitation on copper. We use finite element modeling to calculate electric field enhancement and and look at how this is related to the absorption cross section. We summarise our calculations in a guide of how to successfully use plasmons to enhance photochemical reaction rates.

# Publications

1. *Hot hole-induced dissociation of NO dimers on a copper surface* Natalia Garcia Rey and Heike Arnolds, The Journal of Chemical Physics, 135 (22): 224708, 2011. link [1]
2. *The adsorption of pyridine on Cu(110) - a low work function interface* Natalia Garcia Rey, Heike Arnolds, *in preparation*
3. *Dynamically enhanced electronic sum frequency generation on copper surfaces* Natalia Garcia Rey, Heike Arnolds, *in preparation*
4. *The ultrafast vibrational dynamics of pyridine on copper - long-lived anions or dipole-bound electrons?* Natalia Garcia Rey, Heike Arnolds, *in preparation*

---

[1] Chapter 3 is the submitted version of the paper and based on my second year report.

# Acknowledgments

After four years of enjoying science, nothing of this would happen if Heike Arnolds had not offered me the opportunity to join her group. I immensely appreciate, *with sugar on top*, her knowledge transfer and her patience; for inspiriting and modulating this work. Having Heike as a supervisor is a present, she combines to be a boss, good colleague and post-doc together. Always a cheerful friend and a very good colleague. I will always keep in my memories these years, *her everyday smile, the nice birthday's chocolate cakes, her always availability and many, many good details everyday.* Thank you very much!

From the first day to the last, our group was composed by many undergraduate students, from whom I learnt and spent very good time in the lab, so I thank all of them: from the chatty and joyful Krit, I miss you around; to Dave, to Scott and Paul, who also took part in the experimental part of chapter 4. The last two lab colleagues I thank, but not the least important, are: Scott, who always replied my questions and, also for the good moments we spent together with communal friends. As well as, to the new phD student, Sergio Mauri, who always waited for me for lunch, listened, understood my stress, being helpful and kind. He is someone to, at last, discuss and learn about optics and lasers. Thanks Sergio, for all the discussions, understanding and of course, for all the Italian goods I had enjoyed.

I would also special thanks to Sam, who always takes care of all of us in the surface science. He is always very helpful and available for everything you ask, every time. Also, for giving me the opportunity of working with him, we did the experiments of chapter 2 in his UHV chamber. Thanks for letting me learn a lot of good skills as a scientist and UHV handling.

Many thanks to Ian, Dave and Vin, working in their lab make me feel very lucky. Special thanks to Ian, who manipulated their equipment, spending a lot of time to bring out the UPS measurements.

Special acknowledgments to Andrew, who lend us his Kelvin probe to do our last set of experiments, which were indeed fundamental for the completion and understanding of the results presented in chapter 5 and 6 of this thesis. I cannot forget Fiona, who explained us the Kelvin Probe use, many thanks for always kindly answer our questions.

Thanks to Giovanni, who offered us to reproduced the STM images of sputtered copper surface, apart from digging out his thesis, finally he provided with the information we asked, which is shown in chapter 7.

Thanks to all the colleges around everyday in the Surface Science: to Rene, my dear sweet closest friend always, to Lisa and Teresa, making more cheerful the work environment. To Chris B., who always encouraged me. To Paul, the good ambassador. To the best cake baker ever: Fiona. To Matthew F., the best mate for having a smile and a nice chat. To Chris, John, Piotr, Phil and the last incorporation, Alan, thanks for his good vibes. To my favourite Argentinian: Ivan, who took care of me, being the nicest thesis-physiologist ever. To my brilliant friend Gilberto, one of the best person and scientist I have ever met. To Andrew, who also greatly helped me as the *postdoc* we did not have.

Thanks to my great friends in Liverpool, *mis neninas*: Martilu and Angelina, for all their confidence, nice dances and moments. To Barbara, Gita and Laura, for their always supporting, listening and laughs. These are very strong women, an impressive example to follow. To my dear Ben and Minos, always with a good sense of humor. To Jonas always nice and a good friend. To Naser, Santi, Jesus, ”Adolfito hijo”, Kenneth, Marco, Kay and Israel for all the moments we spent together. To my dear Tony, the first scouser friend we had, always transferring liverpoolian knowledge.

To my far away friends, however very, very close to me, *mis nenitas*: always having good times with them, always supporting me, listening, being just always there, making me feel so happy and lucky: Amparo, Berta and Ana. To my old college friends: Elena, Yolanda, Rosa, Iris and Eva, who always have been there. To my dear confident friends Javi, Davide and Pablo, always an example to follow. To my sister friend Anita. To my crazy friend Isa. To Elena, Alvaro, Angi and "la gente de la mesa".

To my neighborhood, who always were a family for us: Violet, Sarah, Kia, Michelle and Tom.

A mis padres, Teresa y Vicente, muchas gracias por estar ahí cada día tras el telefono, escuchándome; por vuestros sabios consejos. Cuanto os echo de menos!Máma, pápa, sois de verdad un ejemplo a seguir, siempre luchando, siempre ayudando y siempre por vuestros hijos. A Paula, mi querida hermana, y Vicen, my hermano favorito; siempre estáis ahí cuidándome. No tengo palabras para expresar lo mucho que me habéis apoyado y cuidado toda mi vida, muchas gracias, sin vuestro apoyo hasta aquí no hubiera llegado. A mis queridos sobris Vicente y Julia, que a pesar de la distancia siempre me hacen sentir muy tía. A mis queridos cuñados, los que mejor podía tener, María y Antonio, siempre escuchando y teniendo buenos momentos con ellos. A mis queridos sobris gemelos, qué ganas tenía de conoceros. A mi nueva familia, qué puedo decir, sois muy importantes en mi vida, y sin vuestro apoyo y jovialidad todo es más llevadero. Gracias a Antonio, una de las mejores personas que he conocido nunca y con mejor sentido del humor. Te echo mucho de menos. A mi amiga Goyis, que me cuida mucho, nos trae comidita, me hace muchas rosquillas y vestidos (o vestidos como rosquillas) y siempre con amor. Siempre me acordaré de las dos mamis en liverpool, el mejor regalo. A María que siempre da buenos consejos y good vibes. A la pequeña Marina, esperando su respuesta: ”cómo te lo pasas?": -"Pipa!". A mi sambarina compañera y amiga Paloma, no dejes de estar ahí. A Manu siempre divertido y agradable.

Finalmente, si estoy escribiendo estos agradecimientos, sólo hay una persona que siempre esta ahí a mi lado: mi amor y mejor amigo Alejandro. Gracias por apoyarme todos los días, siempre con alegría y risas, siempre juntos para los buenos momentos y los malos. Durante estos últimos meses, gracias por prepararme comiditas y aguantar mis agobios. Cada hora siempre enamorándome de ti, como persona, como amigo, como mi acompañante. You sound!!! *Amor, eres lo mejor que me ha pasado nunca. Muchísimas gracias por estar SIEMPRE AHÍ. Sin ti esta tesis no se hubiera acabado.*

# Contents

Chapter 1

# The initial plan

## 1.1 Overview

One of the most exciting scientific challenges of science today is the optimization of materials to benefit the sunlight as a energy source. Photovoltaics devices, based on semiconductors, generate electrical power from the conversion of sun radiation. Further development has been done into this field in the recent years, by the introduction of $TiO_2$ nanoparticles into a low-cost device called Gräzel cell [1, 2]. Semiconductors and $TiO_2$ nanoparticles are also studied as a potencial *photocatalyst* in the large-scale $H_2$ production via solar water [3, 4] or carbon dioxide [5] splitting; and consequently, synthesizing organic fuels [6]. Nowadays, the development to pattern materials into a sub-molecular scale, has enabled to nanostructure semiconductors [7, 8], to create new materials [9] or cocatalysing (i.e. metal nanoparticles) [9–12] in order to optimise these photochemical reactions, which in turn make feasible a low cost fabrication devices and a increase of the photochemical yield.

However, this is one of the main weakness: the low quantum efficiency *overall* visible spectra. To overcome the lack of tuneability in the visible spectrum, a new perspective on the use of nanostructured noble metals has been introduced since the later 80's. As a first sight, this idea seems unsuitable, as the efficiency to absorb light for a noble metal in the visible region of the spectrum is less than 10%, however plasmon excitation on metals opens a new channel to harvest the sun energy thougout all the visible region. Plasmons are an intrinsic property of metals due to the high density of electrons in the conduction band. On nanopatterned or noble metal nanopaticles, due to the confinement of free electrons, the light can excited a surface plasmon wave which propagates throught the surface. This concentrate energy on the surface has been studied for many different applications [13] like light coupled-devices [14–17], photocatalalyst [18–24] or light-absorbers [25–27].

Surface science photochemistry on metal surfaces is interesting itself even if the metal substrate is not nanostructured (plasmon excitation is not allowed on a flat surface). The molecule-metal bonding offer a new reaction paths, since the surface shifts the energy levels [28] (see figure 7.3 on pag. 122). This new energy channel is commonly called *surface mediated photochemistry* [29].

The combination of these two ideas just presented are the pillars of this thesis; enhancing the heterogeneous photocatalysis by plasmon excitation. In fact, further studies has been observed this effect, which is addressed to the excitation of *plasmons* on the nanostructured metal [29–34]. From these discoveries, two exciting scientific questions arise:

- understand the role of plasmon in the process of enhancing the photochemistry, which has not been elucidated yet [30, 35];
- if the plasmon tuneability is feasible on different metals. Ag or Au has been fantastic either for plasmonic [1] applications or for surface enhanced Raman scattering [37]. However, the main principle behind these fields, is to achieve more efficient coupling of light into the plasmons due to the nanostructure of the material, where the surface plasmon wave propagates resulting in a *field o absorbance enhancement*. In terms of photochemistry this has not been further investigated yet [38, 39].

These two questions will be discussed in the chapter 7 of this thesis. Thereon, I will present the initial idea and how this work has been developed.

## 1.2 The beginning

The initial work done in this thesis is the calculation of the electromagnetic field enhancement as identification of plasmon excitation. This enhanced factor has been explored on copper nanostructured surfaces, in contrast with silver and gold, and modeled by the finite element method (COMSOL© Multiphysics 3.5a). The results are translated into the language of photochemistry, to finally give the insights into photochemical enhancement by plasmon excitation.

In our experiments, the nanostructure models are based on $Ar^+$ sputtering of single crystal surfaces. This technique has been used on metals or semiconductors as a way to tune nanopatterning producing pits, ripples, etc... whose size and orientation on the crystal surface; depend on experimental conditions;

---

[1] A newly developed are of condensed matter research which uses surface plasmon on nanostructured metals to enhance sensing or light transmission and propagating [36].

like substrate temperature, ion incidence angle and time [40–45]. These surfaces are prepared in ultra high vacuum (UHV) and are practical for the surface science community, as ion-sputtering is a crystal cleaning technique. In our case a Cu(110) single crystal surface is studied, on which a wide range of sputter-induced patterns have been produced [46–49]. Here we explore a Cu substrate as a potential photocatalyst, which shows a high photoactivity [50, 51] at the visible region. Furthermore much more abundant on earth crust than Ag and Au.

Two main experimental techniques are used in this thesis. Firstly UHV, as it is the most controlled environment to study the interaction of molecules adsorbed on surfaces. Secondly sum frequency generation (SFG), a powerful surface specific vibrational technique. SFG is a nonlinear response of the surface and adsorbate after a infrared (IR) and near-IR ultrafast laser pulses overlap in time and space on the surface [52]. One of its main advantages is that the vibrational mode of a molecule can be followed in the visible range by the upconversion of the IR spectrum by the near-visible. This enables one to use the powerful information the vibration of a molecule can provide [53] with the latest developments in visible photon detectors, like intensified charge coupled devices (ICCD).

SFG is a versatile technique which can be used in combination with another ultrashort pulse [54], to follow the response of the adsorbate and substrate to the laser pulse on a very short time scale. This is called pump-probe spectroscopy. It is used within this thesis to elucidate the energy flow between light in the visible region and the adsorbate molecule [55].

The initial plan was to study NO dimers on a Cu(110) surfaces, nanostructured $Ar^+$-sputtering, following-up the vibrational dynamics to obtain insights into enhancement of photochemical processes. The photochemistry of NO on Ag(111) versus roughened silver, has been previously and extensively studied [30, 56–58]; as well as on Ag nanoclusters [24, 59–61]. However, the high reactivity of NO on Cu(110) [62], together with a non detectable SFG signal from the $(NO)_2$, made the pump-probe experiments not being feasible. Furthermore, photochemistry of NO on Cu(110) was investigated by continuous light irradiation and is presented in chapter 3.

Figure 1.1 shows a diagrams of the photodesorption of NO, enhanced by plasmon excitation. On the left figure, the light irradiates the surface, exciting the plasmon which decays into the creation of more electron holes pares, enhancing the photodissociation of the dimer. On the right figure, the products of the reaction.

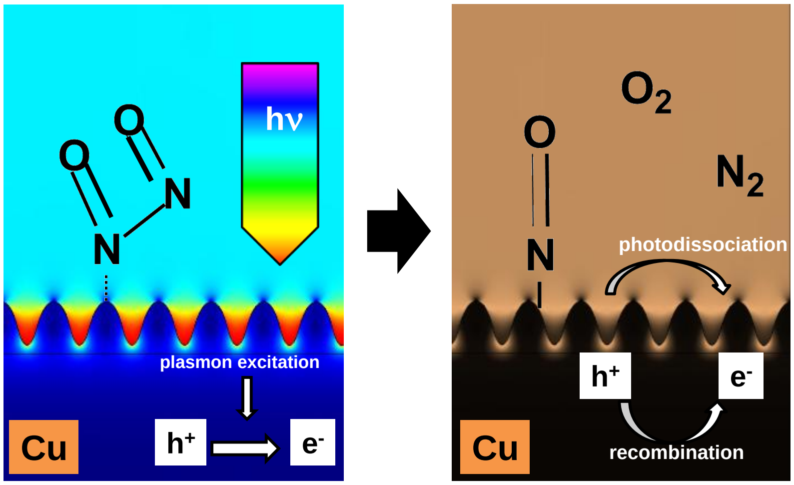

*Figure 1.1:* Diagram of an *ideally* photodissociation of NO adsorbed on nanostructured copper by substrate mediate mechanism, enhanced by the plasmon excitation.

## 1.3 The second plan

This "failure to upconvert"[2] led us to much more exciting experiments with pyridine, deeper insights into copper photochemistry and better understanding of the dynamics of the SFG process on metal surfaces, the latter presented in chapter 4. In particular, the pyridine/Cu(110) surface chemistry is presented in chapter 5 and the femtochemistry of pyridine/Cu(110) is analysed in chapter 6. This investigation provides new insights into the dynamics of bigger molecules, as most of the studies of femtosecond dynamics have been carried out on diatomic molecules [63–69].

Due to the many (partly-colourful) specialist techniques used in each part of this thesis, I will not present a preliminary introduction into any of the topics, as further details will be presented in each part. Just enjoy your reading during this photon journey through the Cu(110) surface to induce chemical reactions, divided into three main parts: **Surface photochemistry**: from NO/Cu(110) photochemistry (chapter 3), towards the analysis of the nonlinear response of Cu(110) (chapter 4). **Vibrational dynamics at surfaces**, pyridine analyzed by SFG in combination with work function measurements (chapter 5) and, the ultrafast dynamics of pyridine/Cu(110) (chapter 6). **Surface enhanced photochemistry**, where we present our conclusions on plasmon-enhanced photochemistry combined with field enhancement modeling on copper surfaces (chapter 7).

---

[2] Upconvert is referring to the use of this term in sfg, when the IR pulse excites the vibrational modes, this is upconvert by the visible beam, being, then, detected in the visible range. This sentence refers to the lack of SFG signal detected from the NO dimer and therefore "failure to upconvert".

# Surface Photochemistry

Chapter 2

# Experimental

The fundamental study of a reaction between a molecule and a surface requires ultra high vacuum (UHV) , meaning the vacuum regime below $10^{-9}$ mbar. To justify the use of UHV in surface science, let me present a typical simple calculation of how fast contamination of a surface occurs at atmospheric pressure. At 1 torr at room temperature $\sim 10^{20}$ molecules hit the surface per cm$^2$ per second; so with a typical $\sim 10^{15}$ adsorption sites per cm$^2$ and sticking probability of one, it only takes 10 $\mu$s to fill the surface. To ensure a clean surface over the experimental timescale of several hours, pressures below $10^{-9}$ torr are needed.

The dynamics of molecules on Cu(110) under light irradiation are the focus of this thesis. All the experiments are carried out in a UHV chamber, where the light impinges on the sample and produces the perturbation.

This chapter is composed of two main experimental parts. Firstly, the description of the UHV experimental techniques employed and secondly, an insight into the vibrational spectroscopy at surfaces and the main techniques used: reflection-absorption infrared spectroscopy (RAIRS) and sum frequency generation (SFG) . Both of them are based on the same principle: *excite and detect IR active modes of the molecule on the surface* and they are described in the following section 2.2.

## 2.1 Ultra high vacuum

The vacuum chamber (Vacuum Generators) is fully equipped with the usual UHV characterization techniques, having two experimental levels. The upper level has two quadrupole mass spectrometers[1], low-energy electron diffraction (LEED) optics and an Argon ion sputter gun for sample cleaning and

---

[1] One of the mass spectrometers allows to record different masses simultaneously. In both cases, the temperature reading is monitored at the same time by a computer.

roughening purposes. The lower level is mainly for laser experiments, with a $CaF_2$ input window (250 $\mu$m to 7 $\mu$m transmittance) and a quartz exit window. There is also an electron-gun in combination with a hemispherical analyser for Auger spectroscopy, a K/Cs getter source, as well as a Kelvin probe.

The UHV base pressure is typically $3{\cdot}10^{-10}$ mbar (measured by a Varian ion gauge). The chamber is continuously pumped by an oil diffusion pump, with a backing roughing pump. The UHV chamber is isolated by high precision dosing valves from the gas lines, which are pumped by a roughing pump or a small oil diffusion pump.

Some of the experimental results were in collaboration with other groups. RAIRS (Section 2.2.1) in combination with photo-induced experiments was carried out in Dr. Sam Haq's UHV chamber, where the crystal has different dimensions (see chapter 3), but similar dosing, cooling, cleaning and temperature monitoring procedures. UV photoelectron spectroscopy (UPS) , was carried out in Dr. Vin Dhanak's laboratory, with the help of Ian McLeod.

### 2.1.1 Single crystal surface: Cu(110)

The Cu(110) crystal is attached to an x-y-z-$\theta$ manipulator, differentially pumped by a roughing pump. For a detailed description of the sample holder see the previous theses [66, 70] of the group. The Cu(110) crystal is held by two tungsten wires (see figuere 2.1) for resistive heating, which are electrically isolated from the cooling reservoir. The crystal has dimensions of 10 mm diameter and 1 mm thickness (Surface Preparation Laboratory). Two type-K (NiCr-Ni) thermocouples monitor the temperature of the crystal; one is inserted into a hole in the crystal, the other one is spot-welded to the leg of the holder. A base temperature of 97 K is achieved by thermal contact to a liquid nitrogen reservoir.

The preparation of the sample consists of cleaning by repeated cycles of $Ar^+$ sputtering at 300 K and annealing up to 650 K. Afterwards, a sharp LEED (1x1) pattern is obtained. Once the background pressure is recovered, the cleaned sample is cooled down to 97 K. Sample cleanliness is confirmed by reproducible vibrational spectra. The desired molecules are dosed into the chamber, either by a background pressure or by a directional doser which maintains low background pressure during adsorption. The directional doser is made of a stainless steel tube of 2 mm of diameter, set up at 10 cm distance from the sample. Liquid molecules such as pyridine are degased by freeze-throw cycles and dosed from the vapour pressure over a room temperature liquid. The dose is calibrated by LEED (section 2.1.3),

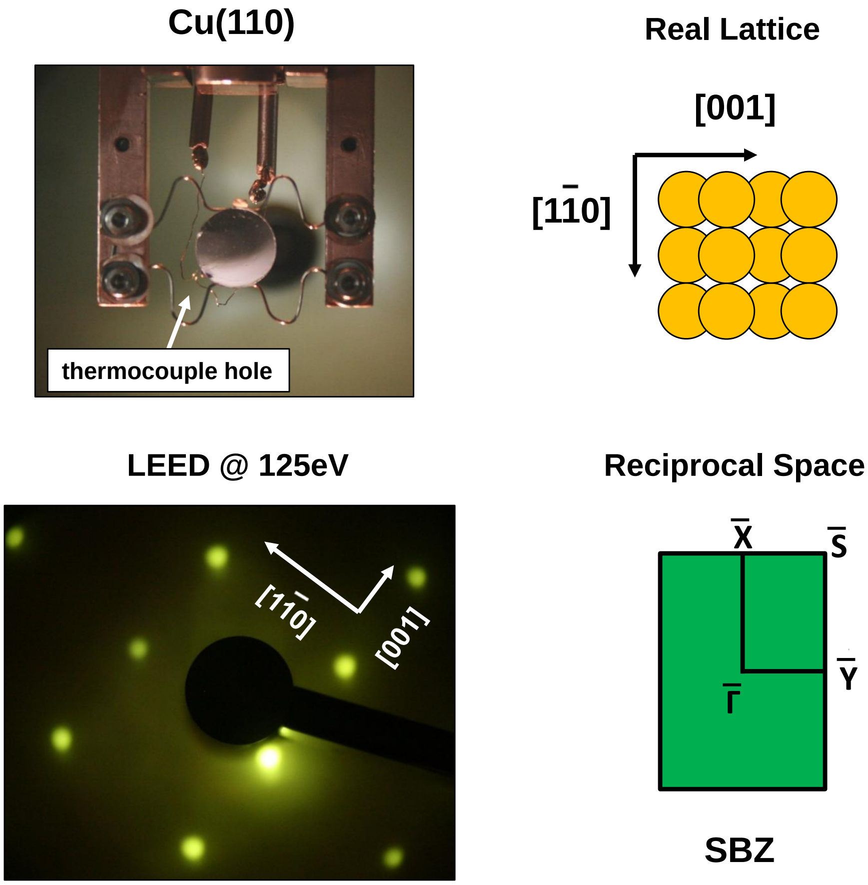

*Figure 2.1:* Top left: mounted Cu(110) crystal. Top right: atomic view of the crystal surface. Bottom left: LEED, notice the tilted unit cell of ∼60° off $[1\bar{1}0]$ direction with respect to lab vertical. Bottom right: the surface reciprocal space, also called the surface Brillouin zone (SBZ).

temperature programmed desorption (TPD) (section 2.1.2) and vibrational spectroscopy (section 2.2).

### 2.1.2 Temperature programmed desorption

This is a fundamental and simple technique in UHV, where the crystal surface is heated with a constant heating rate of 2 K $s^{-1}$ in our case; and the molecules desorbed from the surface are monitored by a mass spectrometer. From the temperature programmed desorption (TPD) curve, a wide range of information such as the strength of the interaction between the surface and adsorbed species, temperature and desorption order as well as adsorption site change as a function of coverage can be inferred. This technique was used daily, for example after finishing each experiment, to monitor the layer on the surface. The dosing was also calibrated from TPD measurements.

### 2.1.3 Low-energy electron diffraction

Low-energy electron difraction (LEED) is an excellent surface sensitive technique, where a beam of electrons of energy $E$ are backscattered towards a series of spherical grids to form a diffraction pattern of the surface structure. In other words, a LEED pattern is the image of the surface reciprocal net when the view is along the surface normal, at great distance from the surface [71]. The first and last meshes are earthed, and the grids in between serve as a cut-off filter, with negative potential, to ensure only the elastically backscattered electrons reach the detector. The latter is biased at high positive voltage to accelerate the electrons enough to produce phosphorescence on the screen. Our LEED is a 3-grid instrument and therefore has a relatively high background.

The physics involved in this technique: an electron beam of energy E $\sim$ 20-500 eV has a de Broglie wavelength of $\lambda$(Å)=$\sqrt{\frac{150.6}{E(eV)}} \approx 5 - 10$Å; comparable to the atomic plane spacing. Therefore diffraction is observed from the ordered atoms, providing the structure of the crystal surface as well as the adsorbate arrangement. LEED is surface sensitive because a typical electron kinetic energy of 150 eV corresponds to an electron mean free path of $\leq$ 10 Å according to the universal curve [71, 72]. The diffraction condition for a lattice constant of $a$ is: $\sin\theta = \frac{n\lambda}{a}$, where the angle $\theta$ is measured from the n$^{th}$-order diffracted spot to the electron beam gun and the normal of the surface in the reflected position.

This technique was used to ensure the cleanness of the surface, though a sharp LEED pattern does not ensure a completely clean surface, as small amounts of impurities such as C (emitted from the filaments) could still be adsorbed on the surface. Auger spectroscopy was used to check for impurities. Our LEED optics allow to calibrate adsorbate coverages for certain molecules (CO, $O_2$), while others (NO, pyridine) are either damaged by the high drain current, do not form ordered structures or do not produce a detectable superstructure due to the low grid resolution.

### 2.1.4 Photo-induced desorption

In a photo-induced desorption (PID) experiment, monochromatic continuous light illuminates the whole surface homogeneously and induces desorption. The photodesorbed molecules from the surface are detected by a mass spectrometer. The distance between the crystal and the mass detector is less than 10 cm. The photon source is a 500 W Hg(Xe) Arc lamp in combination with different bandpass filters (FWHM 10 nm) and a water filter, which absorbs the infrared radiation. A beam splitter creates a reference to monitor long-term stability of the arc lamp, monitored by a photodiode. The beam is focussed at $\sim$35° incidence angle with a spot size matching the crystal. A $MgF_2$ window transmits visible and ultraviolet light into the chamber. The temperature increase from illumination is monitored, and is typically less than 2 K.

### 2.1.5 Ultraviolet photoelectron spectroscopy

In our case, a photon beam of $E_\nu$ = 21.2 eV is emitted from a discharge He(I) lamp onto the sample, at 45° incidence angle. Then the metal surface ejects electrons with kinetic energy $E_K$ which are detected by a hemispherical electron analyser [2]. The relationship with the photon energy is $E_K = E_\nu - E_B - \phi$. $E_B$ is the binding energy of the surface electrons and $\phi$ is the work function. UPS probes the occupied density of states of the valence band and electronic states of the adsorbate. The analyser detects mainly electrons emitted along the surface normal, but the finite acceptance angle means the spectra are an average of the surface Brillouin zone (SBZ) around the $\bar{\Gamma}$ point. For example, the occupied surface at $\bar{Y}$ is still seen in the set-up used.

Since it was difficult to recreate the temperature and dosing conditions used in the SFG chamber, only clean Cu(110) and low coverage pyridine spectra will be presented.

### 2.1.6 Kelvin probe

The work function $\phi$ is a surface property related to the surface dipole moment, defined as the energy diference between the fermi energy and the vacuum level. That is created due to breaking the translational symmetry along the surface normal, where the electrons spill out beyond the ion cores. For example, from a closed-packed to an open surface due to the lower density of atoms, the electron overspill becomes smaller, inducing a smaller dipole and smaller $\phi$ [73].

A molecule adsorbed on the surface, depending on its electron affinity, will produce a change of the dipole layer. The simplest example is an electropositive adsorbate, eg. an alkali with tendency to donate electrons to the substrate [74], creating a dipole in opposite direction to the surface dipole, thus lowering the $\phi$ [75]. An electronegative adsorbate like $O_2$ will increase the adsorbate-surface dipole, increasing $\phi$ [76]. More complex adsorbates may deviate from this behaviour, as will be discussed in chapter 6.

---

[2] The UPS energy resolution is excellent because of the narrow natural linewidths of the He atoms.

The Kelvin probe (**Besocke** Delta PHI Gmbh) allows to measure the change, $\Delta\phi$, as a function of adsorbate coverage. The fundamental principle is to measure the change in contact potential difference (CPD) between two surfaces coming into proximity. When they are in electrical contact, the contact potential difference is equal to the energy difference between the metal work functions; $e^{-} \cdot CPD = |\phi_2 - \phi_1|$. The Kelvin probe consists of a thin Au grid, which is approached to the crystal to within 1 mm. Varying the distance of the Au plate by a frequency of 170 Hz produces a surface charge oscillation, inducing an AC current to keep the electric field between both surfaces constant. This AC current is Auto-mode converted into a voltage difference, corresponding to the absolute change in work function $\Delta\phi$ measured.

In our experiments $\Delta\phi$ is measured during background dosing or after stepwise heating. Since the difference potential applied to the crystal changes when TPD is carried out, a synchronized TPD-$\phi$ measurement was not possible.

## 2.2 Vibrational spectroscopy at surfaces

Measuring the vibrational spectra of a molecule chemisorbed on a metal substrate provides many more insights than one might expect [77, 78]. Frequencies can reveal adsorption sites [79–83] or the reaction mechanism [62, 84–89]. Linewidth and lineshapes give information on vibrational life [90], dephasing times [91], interaction between adsorbates and adsorbate order [92–94]. Vibrational spectroscopy has been applied to many surfaces, from metal crystal-single surfaces [95], stepped surfaces [88] to nanoparticles [96, 97], in UHV, at high pressures [98–101] or under liquids even [102–104]. Vibrational modes of molecules are excited by interaction with an electromagnetic field **E**. The type of interaction depends on the spectroscopy used. Three vibrational techniques are briefly presented: **IR absorption**, **Raman scattering** and **Sum Frequency generation** (SFG). The latter is the main experimental technique pursued in this thesis to analyse the dynamics of molecules on Cu(110).

In **RAIRS**, an IR electromagnetic field $\mathbf{E}_{IR}$ produces a change in the transition dipole moment $\mu$ along a vibrational coordinate Q. In a vibrational state picture, this corresponds to a transition from the fundamental vibrational state $\nu$=0 to the first excited state $\nu$=1. The **Raman scattering** transition, normally to a virtual electronic state, is excited by a visible electromagnetic field $\mathbf{E}_{VIS}$, where the light is absorbed and emitted instantaneously by scattering. The Raman intensity represents just how much

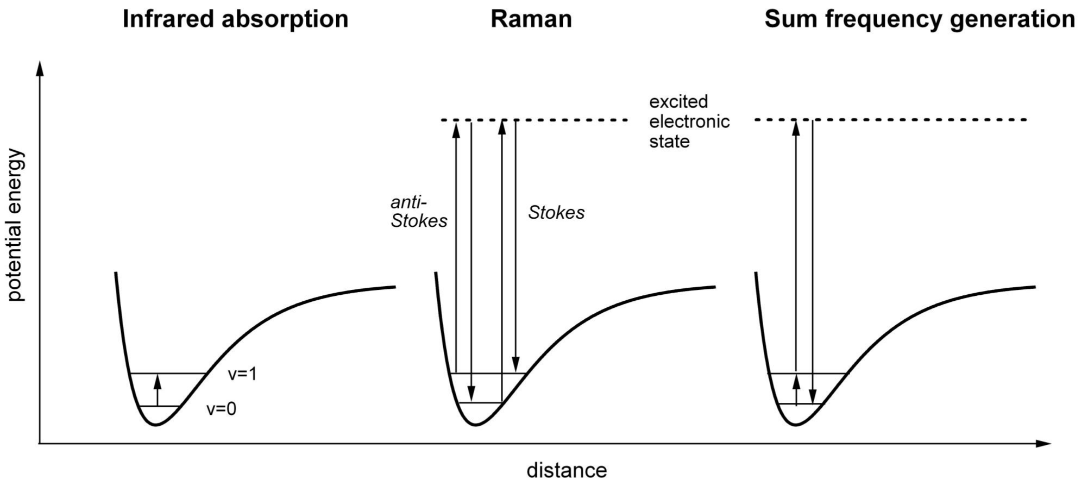

*Figure 2.2:* Comparison of vibrational spectroscopies from reference [53].

the molecule gets distorted by the incoming electric field. In other words, Raman detects the change in the molecular polarizability $\alpha$ with the vibrational coordinate Q. The intensity is proportional to the induced dipole moment and the emitted scattered light. Two types of molecular inelastic scattering are possible: *anti-Stokes* and *Stokes* transitions. In the former, the atom or molecule loses energy and the emitted photon has more energy than the absorbed photon. In the latter, the atom or molecule absorbs energy and the emitted photon has less energy than the absorbed photon. In both Stokes and anti-Stokes processes, the energy difference between the absorbed and emitted photons corresponds to the transition between vibrational levels of the molecule. Finally, a *coherent* combination of IR and Raman transitions results in the nonlinear optical technique **SFG**. For an adsorbate-metal system, SFG has contributions from both the molecule and the surface, as a result of an IR absorption and a Raman scattering process occurring in both, where the SFG intensity depends on both IR and Raman intensities:

$$I_{SFG} \propto I_{IR} \cdot I_{Raman} \propto \left(\frac{\partial \mu}{\partial Q}\right)^2 \left(\frac{\partial \alpha}{\partial Q}\right)^2 |\mathbf{E}_{IR}|^2 \, |\mathbf{E}_{Raman}|^2 \ . \tag{2.1}$$

A more detailed explanation of SFG is found in section 2.2.2.

On metal surfaces an additional selection rule comes into play. The surface electrons create an image dipole such that only normal components of IR-active vibrational modes can be seen. Another way of phrasing this is to say that only totally symmetric vibrations can be seen. For example, upright CO on a metal surface has IR-active C-O and M-CO stretching modes, while flat-lying CO is IR inactive (see left onset in figure 2.3). A tilted NO dimer has IR active symmetric and asymmetric stretches (see right onset in figure 2.3) while a U-shaped configuration would only have an IR active symmetric stretch. This is also shown in figure 3.2 and used in section 3.4.1 to identify the orientation of the dimer on the Cu(110) surface.

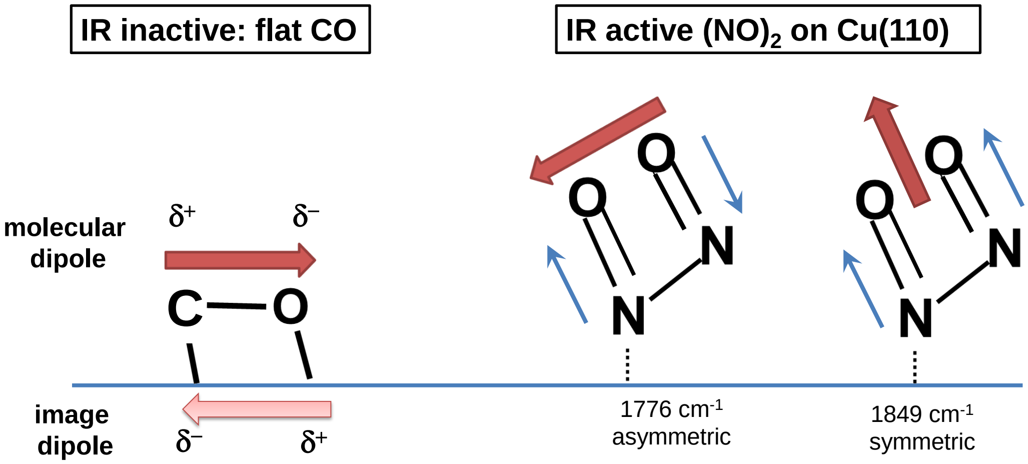

*Figure 2.3:* Schematic representation of allowed and forbidden molecular dipoles. A flat CO molecule is IR inactive. The $(NO)_2$ asymmetric and symmetric stretches are both IR active.

### 2.2.1 Reflection-absorption IR spectroscopy

Reflection-absorption IR spectroscopy (RAIRS) measures the absorption of IR light (typical sources cover the 600-4000 $cm^{-1}$ range) by adsorbates. It is typically carried out at grazing incidence ($\sim$85°), as only p-polarised light is efficiently absorbed by a metal surface, and s-polarised light is almost cancelled by reflection at grazing incident. Moreover, the adsorbed molecule might have a transition dipole moment large and perpendicular to the surface.

RAIR spectra (4 $cm^{-1}$ resolution) are being recorded using a Mattson Galaxy 6020 FTIR spectrometer and a narrow band MCT detector. Spectra are typically presented as ratioed to the background reflectance measured from the clean surface.

### 2.2.2 Ultrafast dynamics probed by sum frequency generation

Sum frequency generation (SFG) is a nonlinear optical process and requires the use of high-intensity, short-pulse lasers to generate detectable signals. Since temporally short laser pulses cover a broad spectral range, spectral resolution in SFG is more complex than in other spectroscopies and will be explained in the following.

The great distinction between linear and nonlinear optics (e.g. RAIRS vs SFG) is the dependence of the material response on the electric field strength in nonlinear optics. Linear optics is described by field strength independent parameters, e.g absorption coefficient, index of refraction. The development of short-pulse, high-intensity lasers since the 1960s has allowed the study of nonlinear effects. The polarisation **P** induced in the medium is a nonlinear function described by a polynomial expansion in the electric field **E**:

$$\begin{aligned}\frac{\mathbf{P}}{\varepsilon_o} &= \chi^{(1)}\mathbf{E} && (2.2)\\ &+ \chi^{(2)}\mathbf{E}^2 && (2.3)\\ &+ \chi^{(3)}\mathbf{E}^3 && (2.4)\\ &+ \ldots ,\end{aligned}$$

where the optical susceptibility $\chi^{(i)}$ describes the material-light interaction, $(i)$ stands for the susceptibility order and $\varepsilon_o$ is the electric permittivity in vacuum. The first term (2.2) describes linear optics through refractive index and absorption coefficient, while the higher-order terms (2.3,2.4) account for nonlinear optics, such as second-harmonic generation (SHG), sum frequency generation (SFG), difference frequency generation or third-harmonic generation and so on....

Nonlinear optical processes with an even number of incoming photons are only allowed in media without inversion symmetry, e.g. at interfaces. In a medium with inversion symmetry, axis reversal ($\mathbf{r} \longmapsto$ -$\mathbf{r}$) leads to a reversal of the directions of the polarisation and electric field vectors, such that:

$$\begin{aligned}\mathbf{P}^{(2)}(-\mathbf{r}) =& -\mathbf{P}^{(2)}(\mathbf{r}) && (2.5a)\\ =&\chi^{(2)}(\mathbf{E}(-\mathbf{r}))\cdot(\mathbf{E}(-\mathbf{r}))\\ =&\chi^{(2)}(-\mathbf{E}(\mathbf{r}))\cdot(-\mathbf{E}(\mathbf{r}))\\ =&\chi^{(2)}\mathbf{E}\cdot\mathbf{E} = \mathbf{P}^{(2)}(\mathbf{r})\\ \therefore \chi^{(2)} =&0 \; . && (2.5b)\end{aligned}$$

Therefore second-order NLO processes are not allowed in the bulk (in the electric dipole approximation) and are therefore inherently surface sensitive.

$\chi^{(2)}$ of a surface-adsorbate system is the coherent sum of contributions from the surface electrons (so-called nonresonant $\chi^{(2)}_{NR}$) and adsorbate vibrations $\chi^{(2)}_{R}$:

$$\chi^{(2)} = \chi^{(2)}_{R} + \chi^{(2)}_{NR} = A_0 \exp(i\phi) + \sum_n \frac{A_n}{\omega_{IR} - \omega_n + i\Gamma_n} \ . \tag{2.6}$$

Here, $A_0$ and $\phi$ are the magnitude and phase of the nonresonant surface contribution, respectively, and $A_n$, $\omega_n$ and $\Gamma_n$ are the amplitude, frequency and half-width of the n$^{th}$ resonance. In most cases of studying SFG on surfaces, the IR pulse will be resonant with a vibrational mode of an adsorbed molecule, giving a large signal. In addition, the VIS pulse can excite a real electronic state either from the molecule or the particular surface, leading to enhancement as will be seen in chapter 4.

Despite the high intensity pulses used, the SF signal is not visible to the *naked eye*. However, the outgoing SF beam is highly directional, since surface parallel momentum and energy need to be conserved:

$$\mathbf{k}_{SF} = \mathbf{k}_{VIS} + \mathbf{k}_{IR} \ , \tag{2.7a}$$

$$\frac{n\left(\omega_{SF}\right)\omega_{SF}}{c} = \frac{n\left(\omega_{VIS}\right)\omega_{VIS}}{c} + \frac{n\left(\omega_{IR}\right)\omega_{IR}}{c} \ , \tag{2.7b}$$

$$\omega_{SF} = \omega_{VIS} + \omega_{IR} \ . \tag{2.7c}$$

where k and $\omega$ are the propagating vector and the frequency of the IR, VIS or SFG beams. n($\omega_i$) is the index of refraction of the medium, dependent on the frequency. Since the IR wavevector is much smaller than the visible, the SFG beam is quite close to the reflected visible beam.

### Broadband SFG

SFG is a powerful surface sensitive technique, able to resolve *vibrational resonances* with a resolution of a few wavenumbers. The laser system (described in more detail later) generates broadband (ca. 150 cm$^{-1}$) VIS and IR pulses. In the SF process, the molecule will select IR photons of the right frequency out of the broadband pulse (figure 2.4). To conserve the vibrational linewidth, the visible upconversion pulse has to be spectrally narrowed as sketched, otherwise the vibrational resonance would be smeared out across the spectrum. In the spectrum shown, the broadband background is the nonresonant SFG from the surface electrons, reflecting the bandwidth of the IR pulse, and the narrow peak in this case is the C-H stretch of pyridine. The lineshape shows the effect of the phase in eq. 2.6. We used two methods to generate spectrally narrow visible pulses- a home-built pulse **shaper** and an **etalon**.

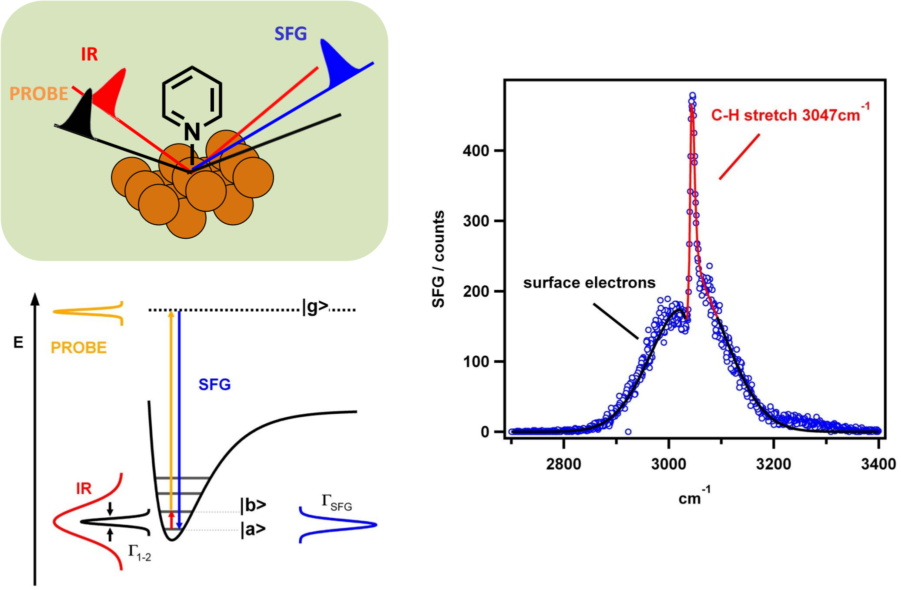

*Figure 2.4:* On top, the sketch of a conventional SFG experiment. Below, the energy level SFG diagram. On the right, SFG spectrum of pyridine adsorbed on Cu(110).

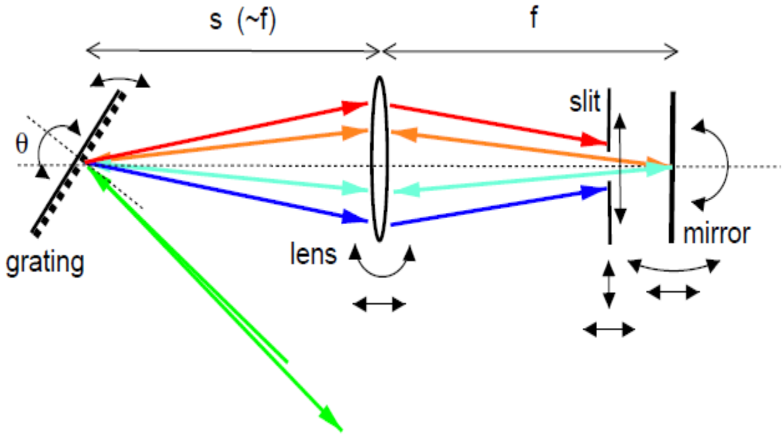

*Figure 2.5:* Pulse shaper from reference [70]

## Pulse shaper

The pulse shaper consists of a grating (1400 g/mm), a cylindrical lens (f=16 cm) and a mirror (see figure 2.5). The stretcher spreads the different frequency components of the pulse in space by diffraction. If the lens is at a focal distance *f* from the mirror, and a distance *s* away from the grating, then the pulse is stretched in time by:

$$\Delta\tau = \Delta\omega \times \frac{4\pi^2 c}{\omega^3 d^2 \cos^2\theta} (2f - 2s),$$

where $d$ is the groove distance and $\theta$ the incidence angle [105]. The shaper is aligned such that f=s and the effect on the pulse width is zero without slit. A slit in front of the mirror selects a frequency range. The spectral content of the pulse is spread spatially in form of a stripe on the mirror and a narrow bandwidth can be selected by inserting a slit. The spectrum of this pulse is square-cut in the frequency domain, which gives the temporal profile the characteristic $\sin(\sigma t)/t$ function with wings and maximum intensity at the origin [106]. *The size of the slit determines the spectral resolution of the VIS pulse, and consequently the SFG spectral resolution*. For a slit width of 200 $\mu$m, the spectral resolution is 5 cm$^{-1}$ with our setup.

While the spectral resolution can be adapted to the vibration of linewidth for optimum detection, the interference between nonresonant and resonant signals can complicate data fitting, so we employed an etalon as an alternative.

### Etalon

The etalon was introduced in our setup in order to separate the molecular and surface contributions of the pyridine/Cu(110) SFG spectra. This fact brought up a range of advantages with respect to the previous pulse shaper. Firstly, this pocket-size optical device makes the everyday alignment much easier. Secondly, the narrow band outgoing pulse has more energy, allowing SF alignment directly, rather than via the intermediate step of overlapping fs-IR and VIS pulses first on the molecule plus metal sample. The time asymmetric outgoing pulse from the Fabry-Perot interferometer can select by time delay the vibrational contribution of the molecule with or without SF from the surface electrons. This new method was first developed by Dlott's group [107, 108]. The induced polarisation of the molecule $P_{RES}(t)$ lasts a few picoseconds, whereas the nonresonant response $P_{NR}(t)$ is only present when IR and VIS are overlapped in time. Delaying the 800 nm pulse by 600 fs removes the nonresonant background, and the SFG is generated from the tail of the decaying molecular polarisation. A delay of 600 fs was necessary in our setup in order to completely suppress the nonresonant background.

The Fabry-Perot etalon consists of two parallel mirrors separated by a distance $d$: the VIS pulse reflects multiple times, generating a train of broadband pulses, interfering to result in a narrow band pulse. The train of broadband pulses is spaced in time by $\tau_{RT} = 2d/c$, which is the so-called free spectral range *FSR*. The phase difference $\delta$ between reflections depends on the incident wavelength $\lambda_0$, the index of refraction $n$ between mirrors, the incident angle $\theta$ and the thickness $d$ [109]:

$$\delta = \frac{4\pi}{\lambda_0} \cdot n \cdot d \cdot cos\left(\theta\right) \ .$$

For a fixed angle, the constructively transmitted beams are spectrally narrow, where the intensity is described by the Airy formula:

$$\frac{I^t}{I^i} = \frac{1}{1 + F\sin\left(\frac{\delta}{2}\right)} \ . \tag{2.8}$$

The parameter F depends on the reflectivity R of the mirror $F = \frac{4R}{(1+R)^2}$. The intensity distribution consists of very bright fringes on a dark background for high reflectivity (see figure 2.6 which shows time- and frequency-domain spectra). The ratio of the separation of adjacent fringes and the FWHM is the so-called finesse, $\mathcal{F} = \frac{\pi\sqrt{F}}{2}$.

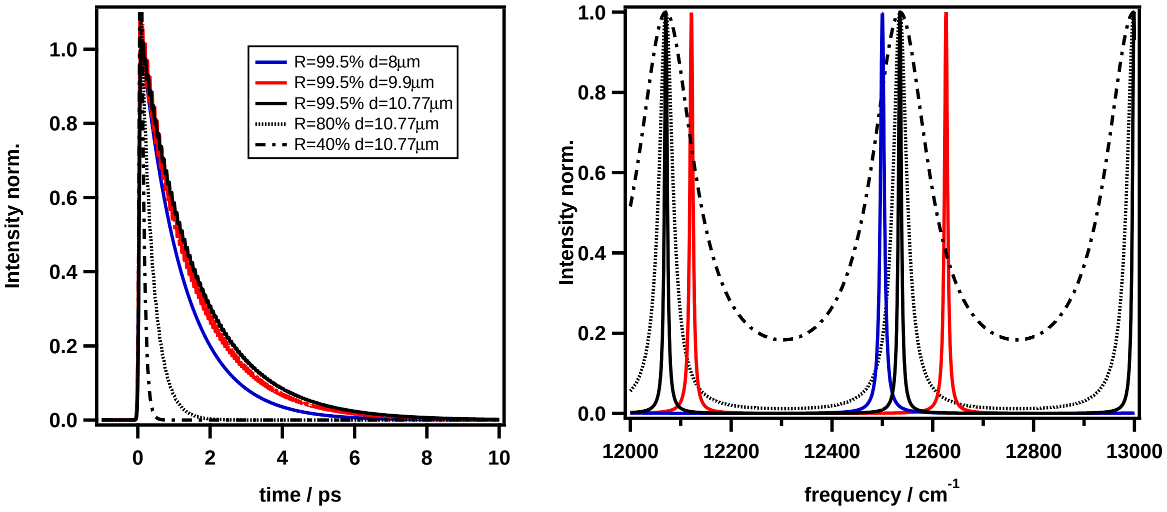

*Figure 2.6:* Temporal and spectral profile of the etalon shaped outgoing beams. The black traces different R values. The solid lines (black, red and blue) show the effect of the thickness.

The recorded spectra from visible pulses from ten different days were fitted with equation 2.8 to compare with the parameters from the etalon manufacturer (SLS Optics Ltd.). Our etalon characteristics are: R=95.5%, d=10.77 $\mu$m and $\tau_{RT}$=464.32 cm$^{-1}$. The mean from the ten spectra analysed gives R=97 ± 1% and d=9.2 ± 0.4 $\mu$m (see in bottom left figure 2.7). The source of error might come from the spectrograph calibration, where the dispersion used was 0.352 cm$^{-1}$/pixel at a center wavelength of 804 nm (see figure 2.10). The linewidth of the visible pulse and therefore our spectral resolution is 7.2

cm$^{-1}$.

The time-domain electric field of the outgoing pulse is given by the following equation [106]:

$$E_{vis,etalon} = E_0 \left(1 - R\right) \sum_{n=0}^{\infty} R^n \exp\left\{-\frac{\left(t - n\tau_{RT}\right)^2}{\sigma_{vis}^2}\right\} \times \exp\left\{-i\omega_{VIS}\left(t - n\tau_{RT}\right)\right\} \ , \tag{2.9}$$

where $\omega_{VIS}$ and $\tau_{VIS}$ are the central frequency and the pulse width of the incoming Gaussian pulse, in our case $\omega_{VIS}$= 800 nm and $\sigma_{VIS}$= 140 fs. The cross correlation was measured with an IR Gaussian pulse width of $\sigma_{IR} \sim$ 190 fs and the etalon function (eq. 2.9) was calculated with parameters R = 94%, d = 10.77 $\mu$m. The cross correlation is described by:

$$I_{SFG}\left(\tau\right) = \int_{\infty}^{\infty} E_{IR} E_{VIS}\left(t - \tau\right) \ . \tag{2.10}$$

There is good agreement between measured and calculated transients as overlap between data points and the solid line in the bottom right figure 2.7 shows.

### Fitting the SF spectra

The SF signal is proportional to the square of the nonlinear susceptibility $\chi^{(2)} = \chi^{(2)}_{NR} + \chi^{(2)}_{R}$ (see eq. (2.6)). The resonant contribution is normally assumed to have a Lorentzian shape (homogeneously broadened line) while the nonresonant contribution either has a Gaussian shape (pulse-shaper) or an almost Lorentzian shape (etalon). A Lorentzian convoluted (upconverted) by a Gaussian is called a Voigt function [110]; a Lorentzian convoluted by another Lorentzian yields a Lorentzian lineshape again.

For fitting the spectra shown in this thesis, the following conditions were used:

- CO spectra were acquired with the pulse-shaper, so a Voigt function with fixed Gaussian linewidth (measured from the visible pulse) was used, which fitted the measured lineshapes well.
- the majority of pyridine spectra were acquired with the etalon and again fit very well to a Voigt function, this time fixing the Lorentzian part to account for the visible pulse. This means that the lineshape of the C-H resonance more closely resembles a Gaussian, i.e. inhomogeneous broadening plays a role.

A much better determination of the resonant lineshape could be made in the time-domain but was not carried out here.

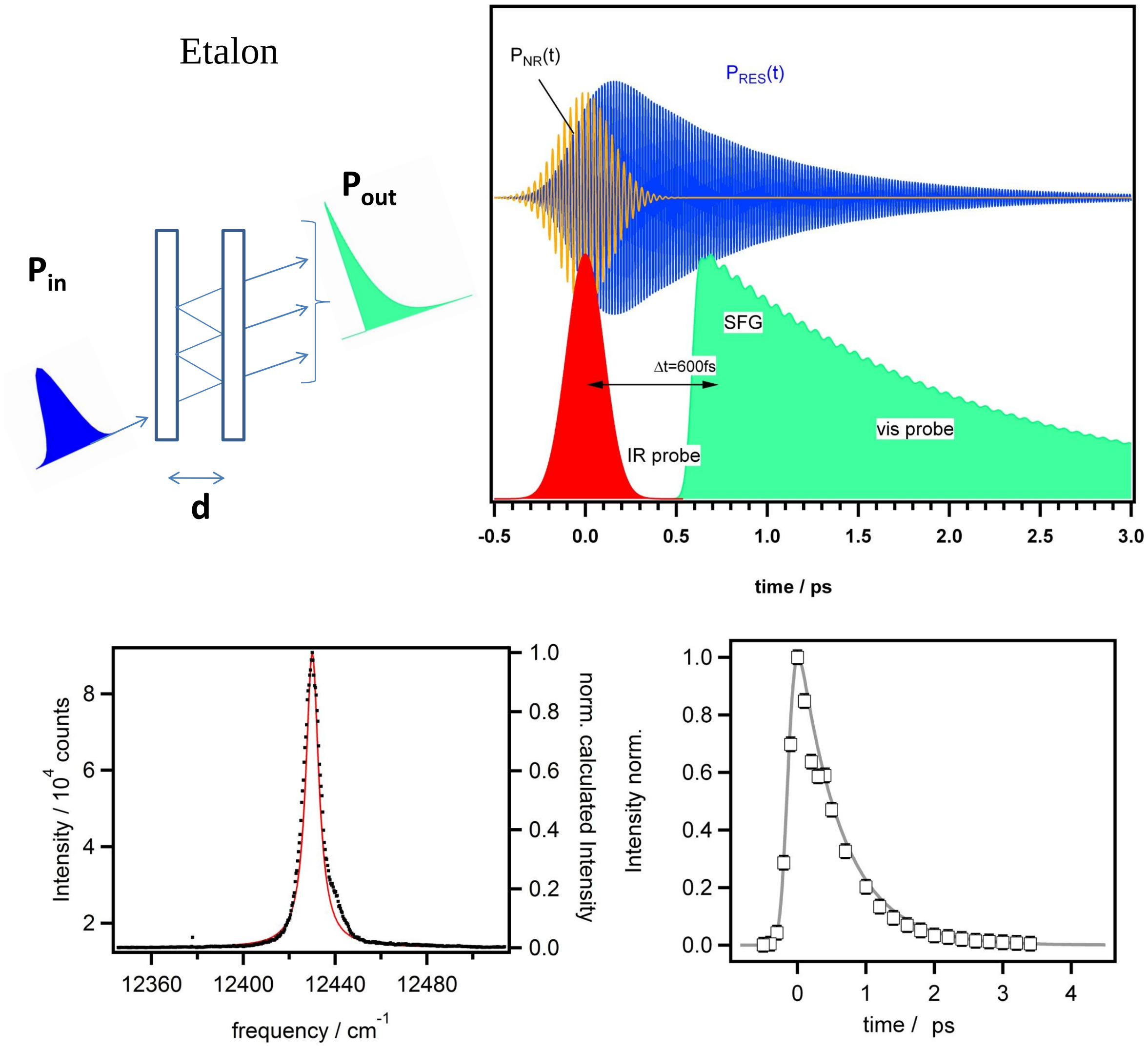

*Figure 2.7:* Top left: Etalon principle to generate a time asymmetric pulse. Top right: a time asymmetric pulse can separate resonant and nonresonant polarisations. Bottom left: frequency spectrum of the etalon pulse. Bottom right: temporal shape of the etalon pulse measured by cross-correlation.

### 2.2.3 Pump probe set-up

As a general overview, the femtosecond laser set-up can be divided into three parts (figure 2.8):

- the first one consists of the generation of high intensity ultrafast pulses. Initially, a *Millennia Pro* diode-pumped laser (532 nm, 5.75 Watts) pumps the *Tsunami* Ti:sapphire (Ti:S) oscillator , which generates 90 fs pulses centered at 800 nm at a repetition rate of 82 MHz. Secondly, these pulses are amplified in a Ti:S amplifier (TSA-10) which is pumped by a frequency-doubled Nd:YAG at 10 Hz repetition rate. The TSA delivers 120 fs pulses of 6.5 mJ energy. All of these lasers are from *Spectra Physics*.

- In the second part, the TSA output is split into three beam paths of 2 mJ each: the 800 nm upconversion pulse and two pump pulses of optical parametric amplifiers (TOPAS from Light Conversion) which produce tunable UV-VIS and IR light. The mid-IR may be tuned from 2.9 - 11 $\mu$m (30 - 1 $\mu$J) and the VIS wavelength from 200 -1200 nm (2-200 $\mu$J).
- The last part consists of beam delivery to the UHV chamber, where the pulses are overlapped in space and time on the sample. There, the SFG is generated and spectrally resolved by a spectrograph and detected by an intensified charge coupled device (ICCD) .

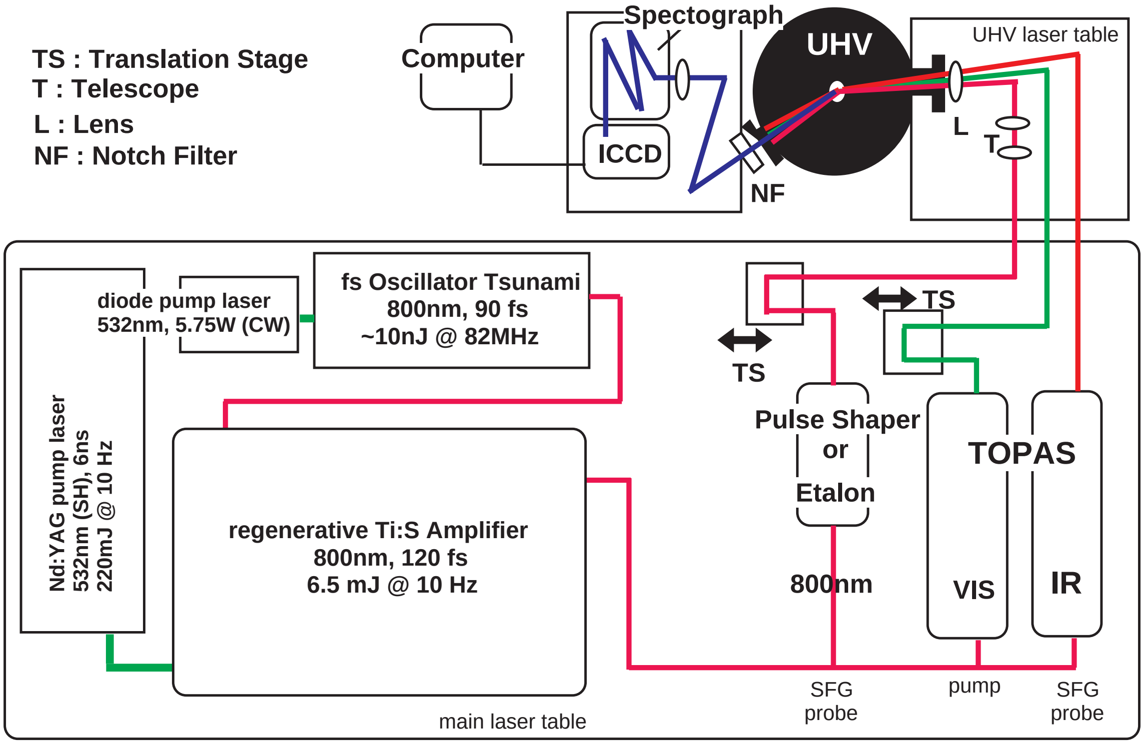

*Figure 2.8:* Setup

In the following sections, the fundamental processes for generation of ultrafast pulses and IR pulses are presented.

### Ti:Sapphire oscillator

In a laser cavity, transverse and longitudinal modes are produced. The first type of mode determines the spatial profile of the laser beam (in our case a simple Gaussian profile), while longitudinal modes are a **time-frequency property**. In the context of a laser cavity, a longitudinal mode arises when the electromagnetic field traveling in one direction interferes constructively with the wave propagating in the opposite direction. If the distance between the cavity mirrors is $L$, then the round-trip time is $T = 2L/c$ and the wavelength $\lambda$ of the longitudinal modes is given by

$$L = \frac{m\lambda}{2}, \qquad m \in N. \tag{2.11}$$

The allowed oscillating wavelengths are determined by the cavity length and the gain bandwidth of the laser medium. When the medium has a broad gain bandwidth, such as Ti:S, all the frequencies can be "locked" to lase together, superposing themselves into the form of a wave packet. This is called **mode-locking**, which is usually achieved by introducing some controllable energy loss process into the laser cavity such that all modes are in phase at one point in space and time (in our case an acousto-optic modulator). The duration of a pulse is determined of how many modes ($N$) are in phase, the overall bandwidth $\Delta\nu$ of the laser medium and the relation of amplitude and phase of the beam. For a Gaussian pulse[3]:

$$\Delta t = \frac{0.441}{N \cdot \Delta\nu} \tag{2.12}$$

This creates an intracavity pulse, which leaks out of the partially reflective cavity mirror, thus determining the repetition rate of the laser. The mode-locked laser in our lab produces nJ pulses at a repetition rate of 82 MHz with a centre frequency of 800 nm and a bandwidth of about $\sim$9 nm and a pulse width of $\sim$90 fs.

### Chirped pulse amplification

The Tsunami pulses need to be amplified because their energy is too weak for IR pulse generation, and therefore for SFG purposes. This is achieved by *chirped pulse amplification* (figure 2.9). The femtosecond pulse is first **stretched** in time by diffracting it off a grating, making the spectral components of the pulse travel in different directions along paths of different lengths, which delays them with respect to each other and creates a pulse of about 200 ps length. The chirped pulse[4] is then *amplified* in two stages. In the first stage it acts as a *seed pulse* to stimulate emission in the first Ti:S crystal in the cavity, pumped by 25% of the output of a Nd:YAG at 10 Hz. After a finite number of passes, the pulse is ejected and then passes twice through a separate Ti:S crystal pumped by the remainder of the Nd:YAG

---

[3] Time-bandwidth product for a gaussian shaped-pulse is 0.441

[4] This is called a chirped pulse because the frequency changes during the pulse.

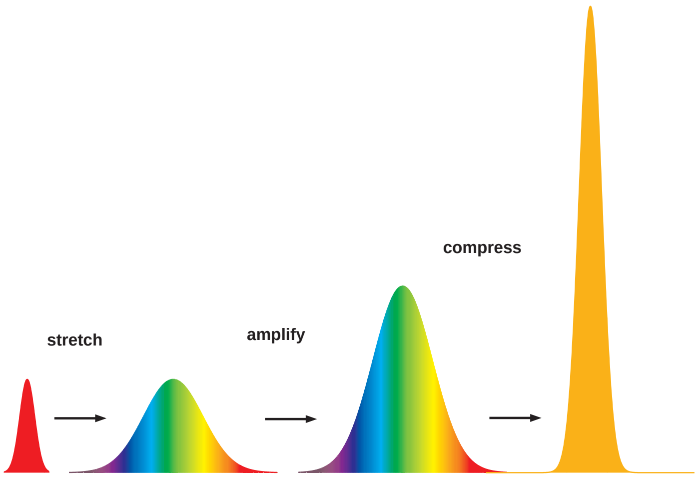

*Figure 2.9:* Principle of chirped pulse amplification

output, the double-pass. The time the pulse stays in the cavity is controlled by Pockel's cells, which are crucial for the stability, energy and performance of the next optical component stage, the TOPAS . Finally, the amplified pulse is *compressed* by diffraction and reflection to 120 fs. The beam shape, pulse width and pulse front tilt are measured by frequency resolved optical gating (FROG) [111] and an autocorrelator, for further information about the set up and pulse characterization see Symonds thesis [70]. The outgoing 800 nm pulse has a pulse front tilt of no more than 5°, a pulse width of $\sim$120 fs and a time-bandwidth product of typically 0.4.

### Optical parametric amplifier

In the second part of the setup, two TOPAS (traveling-wave optical parametric amplifier of superfluorescence) provide sources of either IR light tunable from 3-11 $\mu$m, or near-infrared, VIS and UV light from 200-1200 nm. The frequency tuneability is based on two main nonlinear processes: optical parametric amplification (OPA) and a second order of process such as sum frequency, difference frequency or second harmonic generation.

Optical Parametric Generation occurs when in a suitable nonlinear crystal, a high frequency intensity beam (*pump* $\omega_p$) amplifies a lower frequency beam (*signal* $\omega_s$) and, in addition generates a third beam (the *idler* $\omega_i$) [112], where $\omega_{idler} < \omega_{signal} < \omega_{pump}$ and $\omega_{signal} + \omega_{idler} = \omega_{pump}$. If the phase matching condition is fulfilled and the pump beam really focused, *superfluorescence* is generated [113].

In our laboratory, the pumping beam is 33% of the TSA energy (∼ 2.1 mJ) for each TOPAS. In the first stage, the TOPAS generates superfluorescence from a tightly focussed fraction of the pump beam. This broadband light is generated by three passes of the pump through the BBO crystal. A grating then selects the generated signal beam as a seed pulse for further two-stage amplification. The final stage of the amplification uses ∼90% of the pump beam which leads to saturation of the OPA process and therefore increased stability.

To generate IR pulses, idler and signal pulses pass into a separate section where the beams split, then recombine in a different nonlinear crystal ($AgGaS_2$) to produce the difference frequency, that is, the IR pulse. For example, to finally produce 3250 nm light, a known BBO phase matching angle generates a signal wave at 1287.81 nm and an idler wave at 2133.02 nm:

$$\frac{1}{800nm} = \frac{1}{1287.81nm} + \frac{1}{2133.02nm} \; .$$

Afterwards, the second crystal is set to yield the difference frequency

$$\frac{1}{1287.81nm} - \frac{1}{2133.02nm} = \frac{1}{3250nm}$$

.

In the VIS TOPAS, the first stage is identical to the one previously described. In the second stage, differently cut BBO crystals mix signal and idler with the residual pump or simply produce the second harmonic. For example, to generate 532 nm pulses (used for dynamics experiments chapter 6), the first stage produces the signal at 1580.43 nm and idler at 1624.16 nm. In the following step, the BBO crystal generates the sum frequency of the signal and the 800 nm pump:

$$\frac{1}{800nm} - \frac{1}{1580.43nm} = \frac{1}{532nm} \; .$$

**Frequency calibration of SF spectra**

In order to calibrate the SF spectra, the grating and the ICCD camera are calibrated with the spectral lines of a Ne lamp, yielding the dispersion in **nm/pixel** for different centre wavelengths (CW) of both 600 or 1800 groves/mm gratings. The dispersion for a certain CW is transformed by the relationship between the IR, VIS (802 ± 2 nm) and SFG, where the unknown is the IR:

$$\frac{1}{\lambda_{SFG}} = \frac{1}{\lambda_{IR}} + \frac{1}{\lambda_{VIS}}$$

derived from equation (2.7c). In figure 2.10, the calibration of the dispersion and the offset of the data are shown. For example, for the C-H stretch spectra of the pyridine on Cu(110) at CW of 650 nm, the

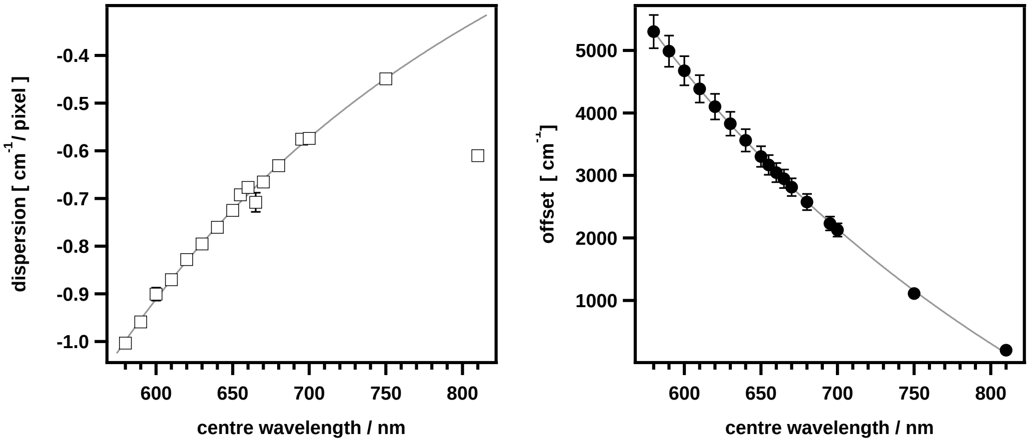

*Figure 2.10:* Measured dispersion for the 1800 groves/mm grating and the ICCD camera.

dispersion of -0.698 cm$^{-1}$/pixel and the offset of 3255 cm$^{-1}$ are used to transform the x axis, measured in pixels, into IR wavelength (cm$^{-1}$). Normally, the offset is tweaked to overlap with a value of a vibrational mode from the literature. The low resolution grating (600 g/mm) has also been calibrated (see appendix A) .

### Three beams overlapped on a crystal in UHV

Aligning the three pulses on the same space-time spot is part of the daily basics. While the first alignment into the chamber can be lengthy, the method developed by Arnolds *et al.* [105] allows a fast daily alignment. The setup on the UHV laser table is depicted in figure 2.11. The three beams are focused at an average incidence angle of 67° on the crystal surface, with an angle of 5° between the 800 nm, pump and IR beams. Initially, the flippable mirror is up, blocking the beams into the chamber; reflecting and focusing the beams into a pinhole of 150 $\mu$m at ~25 cm from the lens. The pinhole mimics the crystal position in the chamber, the same type of lens and vacuum window are placed perpendicular to the light path; tracing the same optical length. Both lenses should be equidistantly placed from the flippable mirror. Once the three beams go through the pinhole, they are overlapped in space. If the flippable mirror is lowered, a camera (connected to a computer) monitors the two visible beams impinging on the sample overlapping in space. Notice the IR is not seen!

The time overlap is obtained when the pinhole is replaced by a nonlinear crystal ($LiIO_3$) . The three beam paths may have approximately the same length, matching in time the 800 nm (VIS) beams with the IR beam, with the translation stages moved forwards or backwards until the SFG, or in the case of the VIS with the IR the difference frequency generation (DFG) , directional beam appears. The nonlinear crystal produces a strong SFG (DFG) visible by eye. Afterwards, at a long distance,

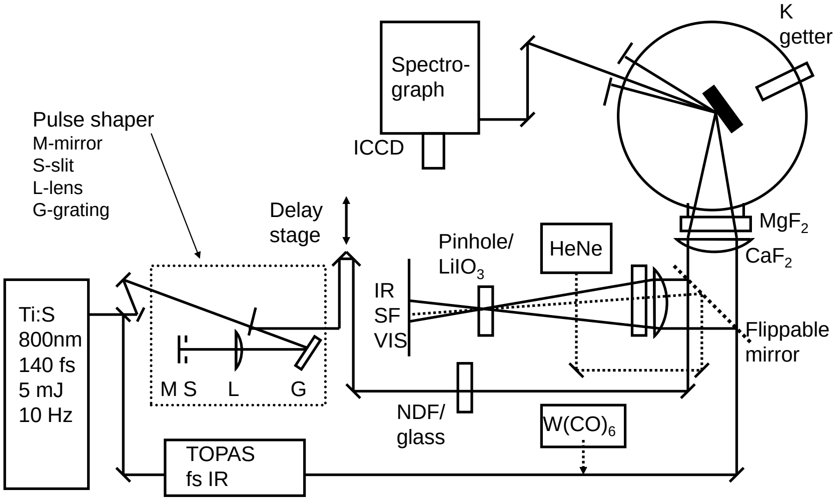

*Figure 2.11:* Schematic diagram of the optical setup. From Arnolds *et al.* [105].

equivalent to the optical path length from the sample to the spectrograph, we mark on a screen where the SFG (DFG) beam arrives. In the next step, a HeNe laser is made to retrace the SFG beam path. Once this is done, the flippable mirror is put down and the HeNe light goes into the chamber, reflects off the sample and comes out again, making it possible to align the light into the spectrograph.

Finally, blocking the HeNe and letting the fs beams into the chamber, SFG is obtained from the surface, which is not visible by *naked eye*; it passes through a notch filter and is then focused by a 100 mm lens into a 0.3 m imaging spectrograph (Acton) with a 600 or 1800 g/mm grating and is finally detected by an ICCD detector (ICCD Istar from Andor). After the SFG alignment, the angle of the crystal is changed, in order to detect the DFG between the pump and the IR, and optimized. Once this is finished, the angle is set back to the SFG position, the HeNe marks this position. The visible pump is very close in frequency to the generated SF, therefore I started to use a narrow band notch filter, instead of the previous edge-pass filters, allowing only the SFG (DFG) to pass. Even with the notch filter in the setup, the ICCD can detect scattered light from both VIS beams. Take into account one outgoing SF photon over $10^6$ photons from the reflected pump beams per shot! Two reasons let us record the spectra: both 800 nm and 532 nm pumps are spectrally far enough from the sum frequency, and the green pump must be directed at different angle and height from the 800 nm beam, and must not come out of the chamber (physical blocking), when the SF is detected.The SF signal can be usually detected after pinhole alignment. This position must be improved to get the signal from the surface without suffering too much after the alignment on the UHV table. In order to improve the position, the pump pulse is tweaked first, as a near IR fluorescent card makes it easier to return to the pinhole position. The time delay, the IR beam, the sample position and the mirrors in front of the spectrograph must be tweaked every day to improve the signal. The position of the lenses before the chamber and the spectrograph must be improved when the IR is changed to another wavelength, as well as the pinhole position (slight movement backwards or forwards).

## Take home message: tips for a SFG setup

- Check if the pulse front is tilted, misalignment of the compressor can produce that. Removing a few degrees of pulse front tilt enhances the SFG performance by 50%.
- When aligning the beams into the UHV, always check on the camera that the 800 nm pulse overlaps on the same crystal spot as the HeNe beam.
- The telescope in the VIS beam should focus the beam after the pinhole position. This will also improve the SF signal.
- The VIS pump travels at a different height than the pump pulse. However, the height might be compromised by everyday alignment, coming out roughly from the chamber in order to obtain the DF signal into the spectrograph, without need of tweaking the mirrors before the spectrograph, once the SFG is first aligned. This will be possible, if the DF signal is huge.
- The bandpass interference filter at 650 nm CW and 80 nm bandwidth from Edmund Optics covers both SFG and DFG signals without need of filter change. A narrow band one can be used if the pump wavelength is closer to the SFG signal. A wrong filter wastes a lot of time. Do not forget to use the right filter!
- The closer the spectrograph to the outgoing viewport, the better the SFG detection.

Chapter 3

# Photodissociation of NO dimers on Cu(110)

In this chapter, photo-induced desorption (PID) (sec. 2.1.4) in the visible wavelength region and reflection-absorption infrared spectroscopy (RAIRS) (sec. 2.2.1) have been used to determine the photoactive species of nitrogen monoxide (NO) on a Cu(110) surface at 86 K. For low coverages the NO adsorbs on a bridge site, which shows **no photoaction**. Meanwhile, at high coverages different species are formed and adsorbed on Cu(110): NO dimer, $N_2O$ and $O_2$, with the dimer as the only photoactive species. At 546 nm the cross section for NO dimer dissociation is $\mathbf{Q} = (2.8 \pm 0.4) \cdot 10^{-19}\ \mathrm{cm}^2$ . We propose a photoinduced dissociation mechanism, where the weak N-N bond of the dimer is broken by a substrate-mediated hot hole attachment mechanism, photodesorbing one NO(g) to the gas phase and leaving one NO(ads) adsorbed on the surface in a metastable atop position. The dimer photodissociation is reversible by either redosing NO or by thermal activation of the substrate.

## 3.1 Introduction

Photochemistry of molecules adsorbed on metal surfaces frequently offers different reaction paths and lower excitation thresholds to those found in the gas phase [114]. The reason is the commonly found substrate-mediated mechanism, where incident photons generate hot electrons (holes) in the metal, which in turn attach to an unoccupied (occupied) electronic state of the adsorbate. Compared to the adsorbate-mediated mechanism, where the excitation occurs from an occupied to an empty state of the metal-adsorbate complex, the threshold is lowered approximately by the energy difference between the occupied adsorbate state and the Fermi level. This is of great interest in the development of better photocatalysts, which ideally would make efficient use of the abundant green component of the solar spectrum. The photoexcitation of substrate-adsorbate systems is mostly through generation of hot electrons in the metal and their attachment to the adsorbate. Although, less often, it can also be driven by the direct electronic excitation of the adsorbate or by adsorbate-substrate complex excitation.

Recent interest in the photochemistry of the NO dimer on silver stems from a desire to enhance the efficiency by plasmon excitation and/or confinement effects in nanoparticles [24, 58–61]. Copper does not provide such strong plasmon effects in the blue-green region of the spectrum due to interband transitions, but it possesses a far richer NO thermal chemistry than silver and supports stable NO monomers at low coverage [62], which allows us to investigate the photochemical behavior for both NO monomers and dimers on Cu(110).

The driving mechanism for NO dimer formation on Ag(111) is the retention of the spin of the unpaired electron in the monomer [115], but dimer formation has also been observed on copper and several transition metal surfaces. In fact, the lack of paramagnetism found in an early study by metastable He deexcitation spectroscopy of NO adsorbed on Cu(110) is probably due to spin pairing in the dimer [116]. NO dimer formation is the reason why the noble metal surfaces show high reactivity to NO dissociation and $N_2O$ formation even at liquid nitrogen temperatures, as seen on Ag(111) [117, 118], Au field emitter tips [119], and low-index Cu surfaces [62, 120, 121] as well as Cu nanoclusters [96, 122]. Even on the more reactive transition metal surfaces, like Rh(111) [123], NO can dimerise and on clean and oxidized Mo(110) [124, 125] and Pd(111) [100] both NO dimers and dinitrosyl species are found to play a role in the reduction of NO. The NO dimer exhibits highly complex photochemistry in the gas phase [126], though on metal surfaces its reactivity has only been thoroughly studied on single crystalline and nanoparticulate silver, where hot electron attachment to the dimer LUMO is the prevalent mechanism, resulting in a range of reaction products [24, 58–61, 127]. On transition metal surfaces, where NO adsorbs as monomer, site, coverage and surface electronic structure have been found to play an important role in determining whether NO dissociates, desorbs or reacts upon light irradiation [128, 129]. On copper, only one early high resolution electron energy loss spectroscopy (HREELS) study on the (111) surface is available [130]. The relationship between the dimer photochemistry and the electronic structure of the substrate is currently an open question, which we address here by reporting the first detailed study of the photoactivity of NO on Cu(110). In particular, we find that the dominant mechanism at visible wavelengths is likely to be hot hole attachment to the dimer HOMO , with NO(ads) and NO(g) as the only reaction products.

## 3.2 Experimental: PID-RAIR spectrometer

All the experiments were carried out in a UHV chamber at a base pressure of $10^{-11}$ mbar, equipped with the standard cleaning and characterization techniques, including an ion gun for cleaning, RAIRS, quadrupole mass spectrometer and low electron energy diffraction (LEED). The Cu(110) single crystal has a dimension of $10\times15\times1.5$ mm and was cleaned by repeated cycles of $Ar^+$ sputtering at 300 K and annealing up to 773 K. The photon source is a 500W Hg(Xe) Arc lamp in combination with different bandpass filters (FWHM 10 nm) and a water filter, which absorbs the infrared radiation. A beam splitter creates a reference to monitor long-term stability of the arc lamp, monitored by a photodiode. The beam is focussed at $\sim35^0$ incidence angle with a spot size matching the crystal area. A $MgF_2$ UHV window transmits visible and ultra violet light into the chamber.

The experiments are performed as follows: once the sample is clean and cold at 87 K, the coverage of NO is monitored by RAIRS, in agreement with the results obtained by Brown *et al.* [62]. NO was used in the experiments from a cylinder without further purification, dosed to the sample at normal incidence by a directional doser at 10 cm from the sample, in order to avoid the NO contamination of the chamber. When the background pressure has recovered to $10^{-10}$ mbar, the crystal with the adsorbed species is irradiated by a fixed wavelength and desorption is monitored by a VG Micromass quadrupole mass spectrometer in multiple ion detection mode, acquiring: mass 28 ($N_2$), mass 30 (NO) and mass 44 ($N_2O$) at 45° off the surface normal. Simultaneously, RAIR spectra (4 $cm^{-1}$ resolution) are being recorded using a Mattson Galaxy 6020 FTIR spectrometer and a narrow band MCT detector. The time scale of the measurements is based on the mass spectrometer time channel and RAIRS timing is obtained from the data file time. In this chapter we present only the data for 546 nm irradiation, and the data recorded for different wavelengths between 365 to 695 nm show the same photochemical behavior of the various adsorbate species as described in the following sections.

## 3.3 Results

### 3.3.1 Photoactivity of species adsorbed on Cu(110)

A comparison of RAIR spectra before and after irradiation of the sample by 546 nm light at 87 K at different surface preparation is shown in figure 3.1. Solid lines correspond to the NO layer prior to irradiation, and dashed lines after 4 minutes of irradiation. At low coverages (figure 3.1(a)), only bands at $\sim$1592 and $\sim$2260 $cm^{-1}$ are observed. Brown *et al.* [62] assigned these to a bridge-bonded N-O

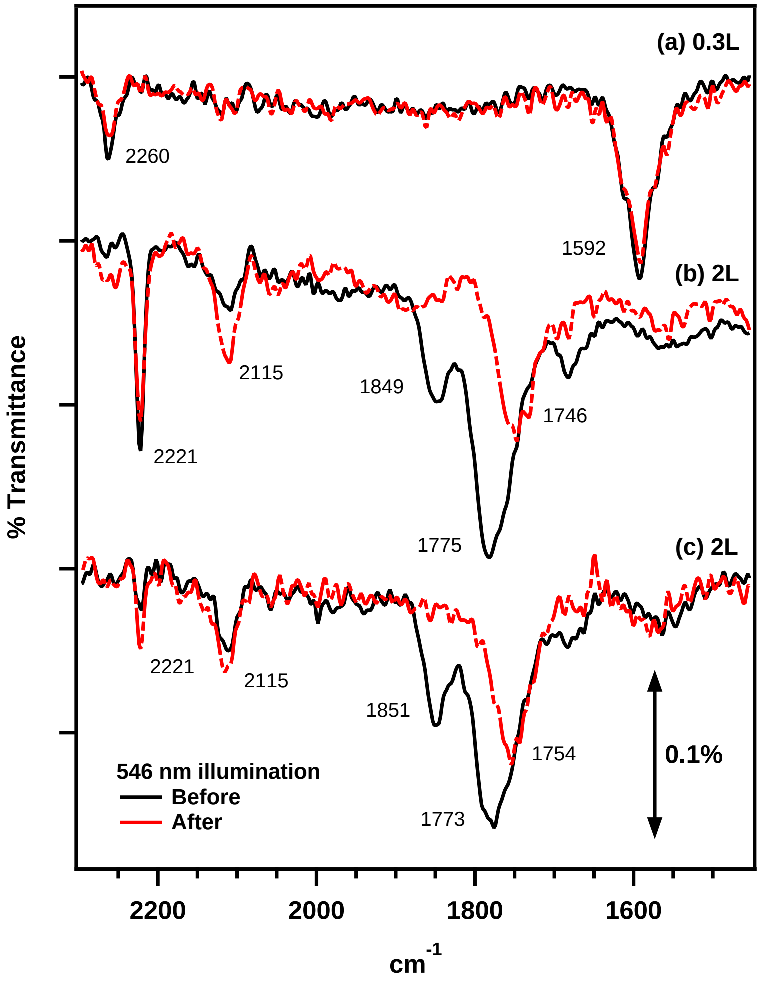

*Figure 3.1:* RAIR spectra of NO on Cu(110) before (solid line) and after (dashed line) irradiation by 546 nm light for 4 minutes. (a) Low coverage with NO on bridge site. (b,c) Saturation coverage, $(NO)_2$ symmetric and asymmetric stretches at 1849 $cm^{-1}$ and 1775 $cm^{-1}$ with (b) and without (c) coadsorbed $N_2O$ (2221 $cm^{-1}$). Exposures are given in Langmuir (L).

and the N-N stretch of $N_2O$ formed on the surface, respectively. Irradiation with 546 nm light causes no change in the infrared spectra and no increase in the mass 30 desorption, indicating that the bridge-bonded NO is photoinert.

At saturation coverage (figure 3.1(b)), peaks with maxima at ~1849 and ~1775 $cm^{-1}$ have been assigned as $(NO)_2$ symmetric and asymmetric stretching modes, respectively. The band at ~2221 $cm^{-1}$ is attributed to the N-N stretch of $N_2O$ [62]. The ~2115 $cm^{-1}$ band is CO adsorbed on the Cu surface from background contamination of the chamber, corresponding to a coverage of less than 0.05 ML. At this high NO dosage, photoinduced desorption of mass 30 is observed alongside a change of the dimer vibrational signature to a single peak at $\sim$1746 cm$^{-1}$ after irradiation for $\sim$2 minutes. This band is stable upon further irradiation. We observe no significant change in the $N_2O$ vibrational band at $\sim$2221 cm$^{-1}$, which is unexpected given published results by So *et al.* [130]. They investigated the photodesorption of NO from Cu(111) using HREELS and surmised that $N_2O$ is a photoproduct from the appearance of a peak at $\sim$1258 cm$^{-1}$, which can be assigned as the N-O stretch of $N_2O$. They also observed an irradiation-related increase of mass 44, whereas all of our mass 44 signal during irradiation is accounted for by reactions on chamber and the 2-3 K temperature increase during irradiation. The photodesorption path is not influenced by the presence of $N_2O$. This can be desorbed from the surface by heating to 110 K [62] with the same effect on the NO dimer band. As previous studies have shown [62], oxygen is also adsorbed on the surface, as a product of the formation of $N_2O$(ads) by the dimer on the surface. This reaction terminates as the O(ads) adlayer formed in the initial decomposition blocks the sites required for later decomposition. After annealing up to 300 K, O(ads) remains on the surface, as a product of the formation of $N_2O$(ads) by the dimer on the surface. The adsorbed oxygen does not seem to be involved in the photoreaction as there is no difference in LEED patterns of irradiated and as dosed layers after heating to 300 K

### 3.3.2 Reaction path and cross section

The photoinduced desorption of NO from a saturated NO layer on Cu(110) follows a single exponential time decay, as shown in figure 3.2, therefore in all likelihood only a single photoreaction path exists. The measured time constant of $\tau = 52.0 \pm 0.9$ s yields a cross section of Q $= (2.8 \pm 0.4) \cdot 10^{-19}$ cm$^{-2}$, which is a third of the value reported for NO on Cu(111) at 458 nm [130] and similar to Ag(111) at 458 nm [56, 130]. The frequency shift observed in RAIRS from the asymmetric dimer peak to the new peak at around 1759 cm$^{-1}$ follows the same exponential time decay as the PID trace with $\tau = 55 \pm 7$ s (figure 3.2) . As an explanation for the irradiation induced frequency shift we suggest asymmetric dimer dissociation with the creation of a thermally inaccessible NO monomer on an atop site, as sketched in figure 3.2 (see discussion).

### 3.3.3 Re-formation of the $(NO)_2$ and reversibility of the photoreaction

The new NO species created on the surface after irradiation can be reconverted to NO dimers either by dosing more NO, or by annealing the surface up to 111 K. Figure 3.3 shows how NO dosing creates dimer peaks comparable in IR absorption to the ones before irradiation, while thermal activation leads to smaller dimer absorption peaks with slightly reduced frequency for the asymmetric peak. The latter

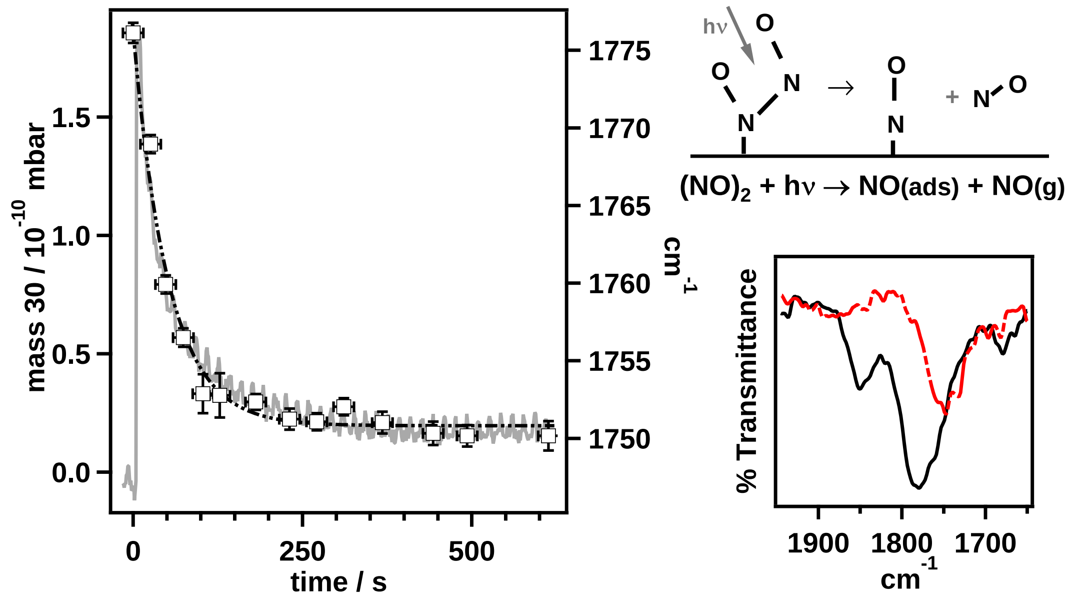

*Figure 3.2:* Photodesorption at 546 nm of $(NO)_2$ saturation coverage from Cu(110) at 87 K. The left graph shows the mass 30 desorption signal (solid line) overlaid with the RAIRS frequency (open squares) versus irradiation time. On the right, we show a sketch of the NO photodesorption mechanism and pre- and post-irradiation RAIR spectra showing the frequency shift.

observations can be explained by a reduced dimer density on the copper surface, as the asymmetric mode has been found to be more sensitive to changes in the environment than the symmetric mode in matrix isolation studies [131]. PID of both recovered dimer preparations results in the same decay curves as shown in figure 3.3 with an initial height proportional to the integrated absorption of the dimer. This reconversion can be repeated several times, in the case of thermal activation until the NO coverage on the surface is too low to form dimers and the peaks cannot be differentiated from the background any longer. There are no other changes in the RAIR spectra after repeated dimer reconversion, confirming that breaking the N-N is the only photoreaction.

## 3.4 Discussion

### 3.4.1 Nature and orientation of NO monomers and dimers

NO dimer formation has been reported on all three close-packed copper surfaces [62, 120, 121], as well as copper nanoclusters on alumina [96]. At low coverages on all three surfaces, an NO absorption peak is observed in the 1500 to 1600 cm$^{-1}$ region and assigned to NO on a bridge site. Brown *et al.* [62] assigned an absorption peak around 880 cm$^{-1}$ as the NO bending mode. An earlier electron energy loss spectroscopy (EELS) study pointed out that the high mode frequency in itself is indicative of a

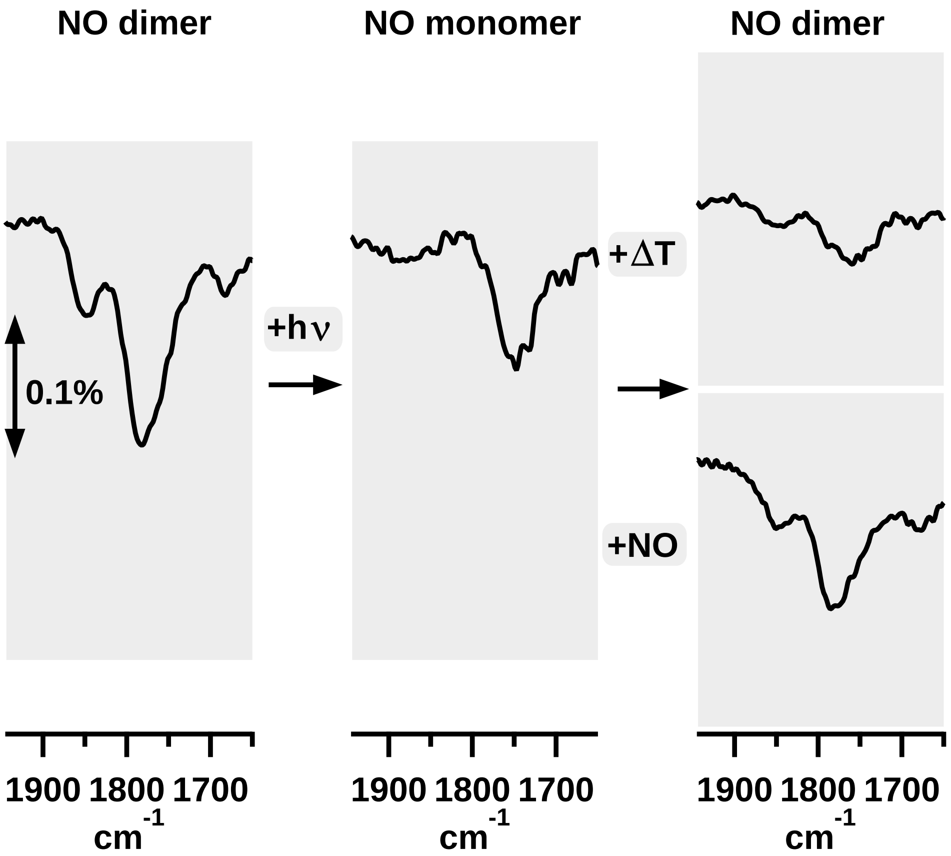

*Figure 3.3:* RAIRS of the dimer absorption band showing the reconversion of the dimer by either annealing (+ΔT) and dosing more NO (+NO).

strongly bent species [130]. An alternative interpretation is that of an N-O stretch, with the NO adsorbed horizontally in a 4-fold hollow site above the second layer copper atom in the trough of the (110) surface [132]. NO dimers form at near monolayer coverage, along with a strong attenuation of the bridge species absorption band, similar to Cu(111) and Cu(100), while NO adsorption on Cu nanoclusters shows a coexistence of dimers and bridge-bonded species. The presence of an NO dimer, on noble and transition metal surfaces this is generally the cis-ONNO isomer with a planar configuration, is usually inferred from adsorption of mixed NO isotopes [118, 121], though in the case of Cu(110) the identification has been based on frequency alone. The orientation of the NO dimer is then inferred from RAIR spectra using the metal surface selection rule, which states that only totally symmetric vibrations are allowed. On Ag(111) for example, the dimer is found to adsorb with the N-N axis parallel to the surface. On Cu(110), a C-shaped, end-on configuration was deduced [62], but in such a configuration, the symmetric stretch possesses a transition dipole moment parallel to the surface and while symmetry allowed, its effective intensity is zero due to the metal surface selection rule. The

$C_{2\nu}$ gas-phase symmetry on $(NO)_2$ actually correlates with the $C_s$ symmetry of an adsorbed, rotated dimer in such a way that both symmetric and asymmetric stretches are part of the totally symmetric representation and are therefore both IR active. The rotation angle $\beta$ of the dimer symmetry axis from the surface normal can be estimated as [133]:

$$\tan^2 \beta = \left(\frac{M_s}{M_{as}}\right)^2 \frac{\nu_s A_{as}}{\nu_{as} A_s}$$

where $A_s$, $A_{as}$, $\nu_s$, $\nu_{as}$ are the relative absorbances and frequencies of the asymmetric and symmetric dimer peaks and $M_s$, $M_{as}$ are the relative intensities of the symmetric and asymmetric stretches of a cis-NO dimer in an argon matrix [131]. From our spectra we obtain a rotation angle of **53°** with respect to the surface normal.

A similarly rotated configuration can be expected on Cu(111) with an asymmetric:symmetric peak ratio of $\geq 1$, while the asymmetric peak makes only a small contribution to the monolayer (ML) spectrum on Cu(100), inferring a nearly U-shaped configuration [120, 121]. Similarly on Ag(111), only a tilted, U-shaped configuration is known with the N-N bond parallel to the surface and a slight tilt on the N-O axis. The differences in dimer configuration on the different surfaces most likely originate in the coadsorbed species formed during adsorption. The IR absorption data on Cu(100) were gained during adsorption at 25 K, well below the reaction threshold to $N_2O$ at around 60 K. The IR data for Cu(111) and for Cu(110) were recorded at around 90-100 K, when both $N_2O$(ads) and O(ads) are formed. NO dimers in a U-shaped conformation were created on Cu(110) with the help of an STM at 12 K [134]. NO monomers were found to adsorb on the short bridge site and by pushing two monomers to within the close-packed spacing, a dimer with both NOs adsorbed on adjacent bridge sites was formed. Since the presence of $N_2O$(ads) makes no difference to the dimer vibrational signature in our data (figure 3.1 b,c), we suggest that a rotated configuration could be caused by coadsorbed oxygen.

In the absence of a mixed isotope study on Cu(110), an alternative assignment of the two peaks at ca. 1850 and 1775 $cm^{-1}$ is conceivable, following a study of NO dimers on oxidized Mo(110) by Queeney *et al.* [135]. Using post-adsorption of $^{15}NO$ after annealing a saturated surface, they proved the existence of an asymmetric dimer, where a surface-bound NO with a stretching frequency of 1728 $cm^{-1}$ is perturbed by NO in the second layer with a stretching frequency of 1871 $cm^{-1}$, close to the gas-phase value. In principle, an NO dimer and a perturbed surface-bound NO can also be distinguished by their reactivity, as weak N-N coupling should not lead to $N_2O$ formation upon heating. On Cu(110) though, $N_2O$(ads) production terminates on the surface when the oxygen coverage exceeds a certain value, so we cannot determine from our data how strong the N-N bond is with respect to, say, Ag(111). We can only state that our observed band at 1775 $cm^{-1}$ falls within the narrow range of asymmetric dimer stretches observed (1771-1788 $cm^{-1}$ [132]).

### 3.4.2 Identification of the photoproduct

Since we observe mass 30 desorption and concomitant changes in the dimer RAIR spectra upon irradiation, we suggest that these changes are due to dimer dissociation. The absorption peak at 1750 $cm^{-1}$ after irradiation has a frequency about 20 $cm^{-1}$ lower than the lowest reported frequency of the asymmetric dimer stretch [132]. We suggest that only the NO directly bonding to the surface in the dimer configuration remains there after irradiation. A likely site for this remaining NO is atop due to the rather high frequency of 1746 $cm^{-1}$. While the N-O stretching frequency is not always a good indicator of adsorption site [83], both theory and experimental data from other metal surfaces and a recent survey of vibrational spectra [132] make this a likely assignment. For example, Gajdoš *et al.* [136] report atop N-O stretching frequencies of 1792 $cm^{-1}$ from an *ab-initio* density-functional study of NO on closed-packed surfaces. A similar frequency was recently reported for atop NO on Pd(111) [100]. This atop site cannot be reached via a thermal route.

### 3.4.3 Which electronic states are involved in the photochemistry?

So *et al.* [130] were one of the first groups to study NO photochemistry on Ag(111) and Cu(111) using HREELS. They reported what is now known to be the NO dimer [118] to be photoactive on Ag(111) and Cu(111), while bridge NO on copper was found to be photoinert. Kidd *et al.* [56, 127] later investigated NO/Ag(111) in more detail and assigned a substrate mediated mechanism for NO dimer photodissociation. In a recent communication, Kim and coworkers [58] discovered a variety of photoinduced reaction paths, including breaking the N-O bond and formation of $N_2$ from $(NO)_2$. In a more detailed follow-on study, Mulugeta *et al.* studied the state-resolved photodesorption dynamics and concluded that for photon energies below the d-band transition a transient negative ion was formed, while at 4.7 eV and for small particles, a transient positive ion was the cause of photodesorption [59, 60]. This positive ion was formed by electron transfer from the dimer HOMO to the silver d-band and the confinement of hot electrons in small silver nanoparticles was found to enhance both the hot hole and the hot electron attachment mechanisms [59, 137].

Reports of the formation of transient positive ions are relatively rare in metal surface photochemistry, though a recent study of photoinduced switching of azobenzene derivatives on Au(111) also concluded that hot holes are responsible for the observed effect [138].

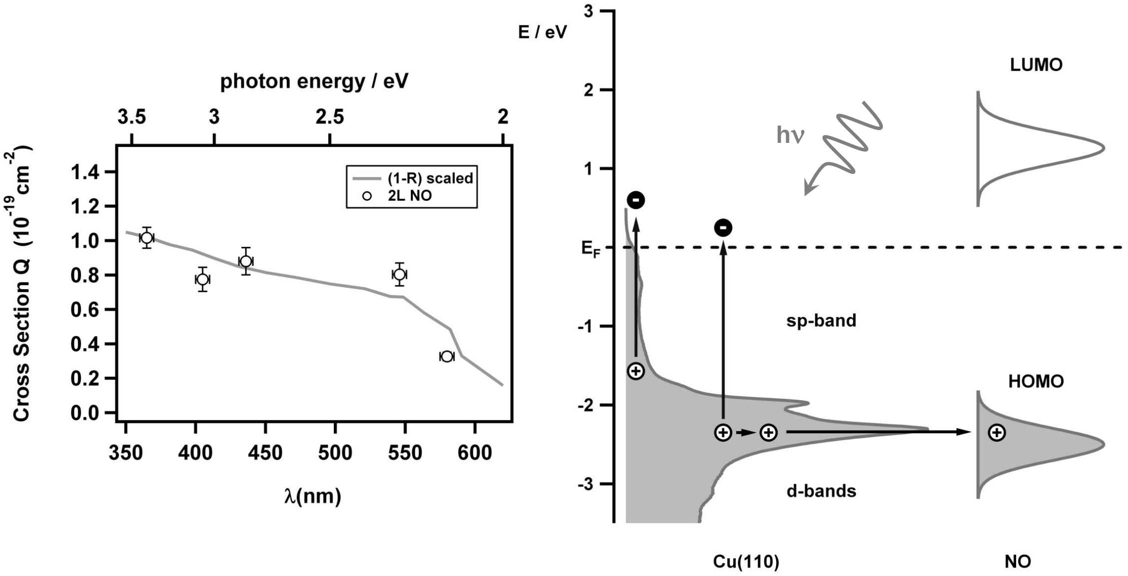

*Figure 3.4:* Left: wavelength-dependent cross section Q for saturation NO coverage. The solid line is the scaled absorbed photon power (1-R), calculated from the Cu reflectivity R. Right: sketch of the hole-induced process on NO/Cu(110). The occupied band structure of Cu(110) was measured by UPS, the NO HOMO and LUMO are approximate values from a study of NO on Cu(111) [139].

We will now make the argument that hot holes are the dominant mechanism for the observed dimer photochemistry on copper.

We have measured the dimer dissociation cross section as a function of wavelength as shown in figure 3.4. The cross section scales with the absorbed photon power (1-R), where R is the reflectivity of the surface, similar to available data on Cu(111) by So *et al.* [130]. Therefore, transitions from the filled **d-band** to empty **sp-states** clearly dominate the photochemistry. Information on occupied and unoccupied NO-related states is sparse and only available on Cu(111). A negative ion state was reported to be an 1.26 eV above $E_F$, though from the dosage given (0.7 L) it is unclear whether this is yet in the dimer regime [139]. In the same paper, the NO HOMO was been reported at 2.52 eV below $E_F$. This is within the range of NO occupied and unoccupied states reported on transition metal surfaces (see [140] and references therein). For comparison, the LUMO of the NO dimer on silver was derived to be at

1.2 eV by Kidd *et al.* [127] although a later theory re-evaluation named the LUMO+1 at 2 eV as the responsible unoccupied level [141].

The copper **d-band** edge is about 2 eV closer to the Fermi level than the silver d-band, consequently most of the photon energy for $> 2$ eV excitation is deposited in the d-band rather than the sp-band [51]. The hot electron distributions created by 578 nm (2.14 eV) and 289 nm (4.29 eV) on Cu(100) have been calculated by Germer *et al.* from the copper band structure [142]. According to their results, 2.14 eV (4.29 eV) photons only generate significant numbers of hot electrons up to 0.55 eV (2.7 eV) above $E_F$ from a filled d to empty **sp-band** transition. Therefore photon energies in the vicinity of 3 eV are needed to create a significant number of nascent electrons at energies in the vicinity of the LUMO. Especially 365 nm (3.4 eV) photons should generate a hot electron distribution that is significantly better matched to the unoccupied adsorbate state than 546 nm (2.3 eV) photons. This is clearly not reflected in the cross section, therefore we exclude a hot electron attachment mechanism.

The relative independence of the cross section on wavelength in the visible region can however be explained by the dynamics of excited electrons and holes on copper if we assume a hole-driven process for the dimer dissociation. When a photon excites an electron from within the copper **d-band**, then the remaining hole diffuses to the top of the d-band through an Auger process [50, 51, 143, 144]. These holes have a relatively long lifetime compared to excitations from the **sp-band** and have been implied to be responsible for restructuring of the Cu surface after nanosecond 532 nm excitation [145] or photoisomerisation of azobenzene on Au(111) [138].

A hot hole attachment would also explain why there is only one reaction path. If an electron is removed from the NO dimer, then the stabilization of the dimer structure by electron spin pairing is removed, which would indeed encourage N-N bond breaking rather than formation of $N_2O$ or $N_2$ as photoproducts.

In the future, it will be interesting to see whether there is a link between NO dimer reactivity and dimer orientation. If the orientation of the dimer is indeed intricately linked to the presence of coadsorbed oxygen, then photoreaction studies could be carried out at very low temperatures where the dimers cannot react thermally to $N_2O$ (like on Cu(100) [121]), or in combination with NO dimers created by STM [134].

## 3.5 Conclusions

In summary, we study the photodissociation of the NO dimer on Cu(110) by PID and RAIR spectra at 86 K. Bridge bonded NO shows no photoactivity, while NO dimers photodissociate by breaking of the N-N bond, desorbing one NO to the gas phase and the other NO remaining adsorbed on the surface in a metastable atop site. The photoreaction mechanism is most likely via hot hole attachment, that is removal of an electron from the N-N bond, resulting exclusively in dimer dissociation. We also observed the reversibility of NO dimer, by redosing more NO and by annealing.

New insights can be found in the published paper [146] about the comparison of hot-hole and hot-electron attachment mechanism.

Chapter 4

# Cu(110) electronic structure characterized by SFG

In this chapter, the analysis of vibrationally non-resonant SFG is presented for bare Cu(110) and adsorbed oxygen and pyridine. This variety of SFG probes electronic resonances at surfaces by scanning the wavelengths involved and delivers information on their spatial symmetries by changing the polarisation of the three beams. Unlike *vibrational* SFG, *electronic* SFG has not been developed into a fully fledged spectroscopy yet and this chapter explores what is and is not possible.

One of the earliest examples of scanning SFG, and second harmonic generation (SHG), is the study of a $CaF_2$/Si(111) interface by Heinz *et al.* [147], which determined the bandgap of the interface states. One of the latest examples is the work by Tahara's group, who carry out broadband electronic SFG by mixing the fundamental of Ti:S with a white-light continuum [148] to study, for example, the electronic state of the protein Cytochrome c at an air/liquid interface [149].

Doubly resonant SFG has been used in a number of cases to identify electronic resonances associated with a particular adsorbate [150–152]. The majority of nonlinear optical studies of the electronic structure of (metal) surfaces has employed SHG using a single incident beam. For example, SHG has been used on noble metal surface to reveal the onset on interband transitions [153, 154] or the transition between the d-band and an image potential state [155]. The surface sensitivity of SHG has been employed to identify surface states on Ag(110) [156, 157] and Cu(110) [158, 159]. These studies also identified the symmetry of the surface state by changing crystal azimuth or beam polarisation [158, 159]. There are numerous examples of using the azimuth dependence of SHG to identify the symmetry of the relevant electronic states [160]. This has recently been extended to SFG, where Shaw *et al.* [161] observed a phase change between the C-N resonance and the non-resonant background on

Ag(111) and Ag(110) with crystal azimuth (see equation 2.6).

Dependence of the nonlinear optical response on the polarisation of the beams involved has been used in the last few years by Kauranen's group to solve a long-standing problem in surface nonlinear optics, namely the separation of surface and bulk contributions [162]. An isotropic bulk medium can contribute to the second-order response via higher order multipole interactions, such as electric quadrupole or magnetic dipole interactions. Bloembergen *et al.* showed that these interactions generate a second order response of the following general form [163]:

$$P^{bulk}\left(2\omega\right)=\left(\delta-\beta-2\gamma\right)\left(\mathbf{E}\cdot\nabla\right)\mathbf{E}+\beta\mathbf{E}\left(\nabla\cdot\mathbf{E}\right)+\gamma\nabla\left(\mathbf{E}\cdot\mathbf{E}\right)\ , \tag{4.1}$$

which shows that electronic field gradients generate the response.

For example, on Cu(001), Vollmer *et al.* [164] detected the bulk contribution as an isotropic response when the incoming beam polarisation was varied. Wang *et al.* [162] then showed that SHG with two incoming beams can separate the surface (electric dipole) response from the bulk response (electric quadrupole and magnetic dipole) of a polycrystalline Au thin film.

SFG is naturally carried out with two incoming beams, i.e. it can distinguish surface from bulk contributions, but in addition it is possible to select whether one of the incoming photons or the outgoing SF photon is resonant with a particular electronic resonance.

Unlike UV photoelectron spectroscopy (UPS) or inverse photoemission spectroscopy (IPS), nonlinear optical spectroscopy does not involve irradiation by or detection of electrons and can therefore be carried out at any interface that is optically accessible for the wavelengths involved. The disadvantage of using an optical spectroscopy is that the response involves the joint density of states (JDOS) . Moreover, the response is an integral over the whole Brillouin zone, but polarization or azimuth variation allows deduction of the symmetry of the states involved.

The particular purpose of the work presented in this chapter was to provide a deeper understanding of the pump-probe studies of pyridine on Cu(110), which will be discussed in chapter 6.

## 4.1 Sum frequency generation: polarisation scans

In the previous chapters, I have not explained the SFG theory in detail and for the purpose of this section a deeper analysis is needed. The second order response to incoming VIS and IR fields is given by:

$$\mathbf{P}_i^{(2)} = \epsilon_0 \beta_{ijk} K_j \mathbf{E}_j^{VIS} K_k \mathbf{E}_k^{IR} \, , \tag{4.2}$$

where i, j, k can be X, Y and Z, $\beta_{ijk}$ is a $2^{nd}$-rank tensor with 27 elements [1], K$_j$ and K$_k$ are the Fresnel factors which transform incident to surface **E** fields [165]. Our Cu(110) surface has C$_{2v}$ symmetry and the only allowed tensor components (following the same reasoning as in section 2.2.2) are, apart from $\beta_{ZZZ}$, those that are quadratic in either x or y, consequently seven components survive: $\beta_{ZZZ}$, $\beta_{XXZ}$, $\beta_{YYZ}$, $\beta_{YZY}$, $\beta_{XZX}$, $\beta_{ZXX}$, $\beta_{ZYY}$. As shown in figure 2.1, our crystal main in-plane symmetry axes are rotated with respect to the lab horizontal while the surface normal coincides with the lab horizontal. The relative orientation of crystal XYZ and lab xyz is shown in figure 4.1.

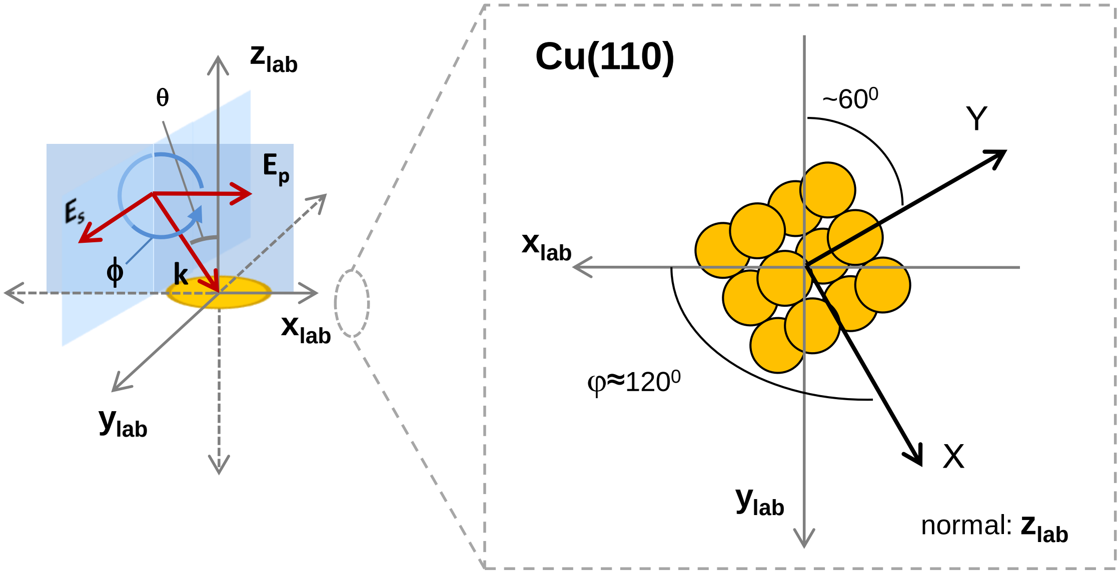

*Figure 4.1:* Cu(110) orientation with respect to lab coordinates.

A transformation of coordinates is needed in order to transform the crystal susceptibility $\beta$ into a lab susceptibility $\chi_{ijk}^{(2)}$:

$$\chi_{ijk}^{(2)} = \sum_{i'j'k'} R_{ii'} R_{jj'} R_{kk'} \beta_{ijk} \, , \tag{4.3}$$

---

[1] We use $\beta$ here instead of $\chi_{ijk}^{(2)}$ to refer to the crystal based axes: $[1\bar{1}0]$, $[001]$ and the normal to the surface coordinate system.

where $\chi^{(2)}_{ijk}$ is the polarisability with respect to the lab coordinates x, y, z and $\beta_{i'j'k'}$ is defined along the crystal axes, where i', j', k' are X, Y or Z. The rotation matrix is given by:

$$R = \begin{pmatrix} R_{xX} & R_{xY} & R_{xZ} \\ R_{yX} & R_{yY} & R_{yZ} \\ R_{zX} & R_{zY} & R_{zZ} \end{pmatrix} = \begin{pmatrix} \cos(\varphi) & -\sin(\varphi) & 0 \\ \sin(\varphi) & \cos(\varphi) & 0 \\ 0 & 0 & 1 \end{pmatrix} ,$$

where $\varphi$ = 120 ° in our case.

The rotation induces a mixing of X and Y components, and $\chi^{(2)}$ has 13 components overall: (for simplicity, the superscript (2) is omitted):

$$\chi_{zzz} = \beta_{ZZZ} \tag{4.4a}$$

$$\chi_{xxz} = \cos^2(\varphi)\beta_{XXZ} + \sin^2(\varphi)\beta_{YYZ} \tag{4.4b}$$

$$\chi_{yyz} = \sin^2(\varphi)\beta_{XXZ} + \cos^2(\varphi)\beta_{YYZ} \tag{4.4c}$$

$$\chi_{xyz} = \frac{1}{2}\sin(2\varphi)\{\beta_{XXZ} - \beta_{YYZ}\} \tag{4.4d}$$

$$\chi_{yxz} = \frac{1}{2}\sin(2\varphi)\{\beta_{XXZ} - \beta_{YYZ}\} \tag{4.4e}$$

$$\chi_{xzx} = \cos^2(\varphi)\beta_{XZX} + \sin^2(\varphi)\beta_{YZY} \tag{4.4f}$$

$$\chi_{yzx} = \frac{1}{2}\sin(2\varphi)\{\beta_{XZX} - \beta_{YZY}\} \tag{4.4g}$$

$$\chi_{zyx} = \frac{1}{2}\sin(2\varphi)\{\beta_{ZXX} - \beta_{ZYY}\} \tag{4.4h}$$

$$\chi_{zxx} = \cos^2(\varphi)\beta_{ZXX} + \sin^2(\varphi)\beta_{ZYY} \tag{4.4i}$$

From equation 4.2, the induced surface polarisation is given by:

$$P_x \cong \chi_{xxz} K_x E_x^{VIS} K_z E_z^{IR} + \chi_{xyz} K_y E_y^{VIS} K_z E_z^{IR} + \chi_{xzx} K_z E_z^{VIS} K_x E_x^{IR} \tag{4.5a}$$

$$P_y \cong \chi_{yxz} K_x E_x^{VIS} K_z E_z^{IR} + \chi_{yyz} K_y E_y^{VIS} K_y E_z^{IR} + \chi_{yzx} K_z E_z^{VIS} K_x E_x^{IR} \tag{4.5b}$$

$$P_z \cong \chi_{zzz} K_z E_z^{VIS} K_z E_z^{IR} + \chi_{zxx} K_x E_x^{VIS} K_x E_x^{IR} + \chi_{zyx} K_y E_y^{VIS} K_x E_x^{IR} \tag{4.5c}$$

The surface polarisations are multiplied by the nonlinear SF Fresnel or L-factors L$_i$, yielding the sum frequency field, see 4.6. The L-factors account for phase matching (2.7b) restrictions on the angle of SF emission [165, 166]:

$$E_i^{SF} = L_i P_i^{SF} . \tag{4.6}$$

In lab coordinates, p- and s- polarised fields are given by $\mathbf{E}_p = (E_x,\ 0,\ E_z)$ and $\mathbf{E}_s = (0,\ E_y,\ 0)$.

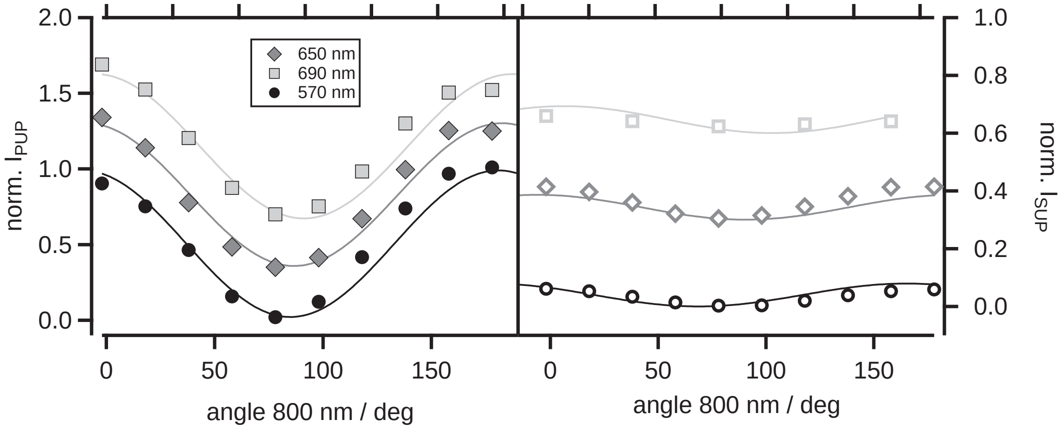

*Figure 4.2:* SF signal for outgoing p (left) and s (right) polarisation as a function of the 800 nm polarisation (0°-p-polarisation, 90°-s-polarisation). Data have been offset for clarity.

Finally, the intensity of the emitted p- or s-polarised SF light is given by:

$$I_p \approx |L_x P_x|^2 + |L_z P_z|^2 \tag{4.7a}$$

$$\approx \left| L_x \sum_j^{x,y,z} \sum_j^{x,y,z} \chi^{(2)}_{xjk} K_j E_j^{VIS} K_k E_k^{IR} \right|^2 + \left| L_z \sum_j^{x,y,z} \sum_k^{x,y,z} \chi^{(2)}_{zjk} K_j E_j^{VIS} K_k E_k^{IR} \right|^2$$

$$I_s \approx |L_y P_y|^2 \tag{4.7b}$$

$$\approx \left| L_y \sum_j^{x,y,z} \sum_k^{x,y,z} \chi^{(2)}_{yjk} K_j E_j^{VIS} K_k E_k^{IR} \right|^2 ,$$

these relatively large expressions simplify in practice because the incoming IR field is always p-polarised (no y component) and Fresnel coefficients for the x components of E$^{VIS}$ and E$^{IR}$ are relatively small.

The measured polarisation dependence is shown in figure 4.2 for three SF wavelengths. The presence of a detectable s-polarised SF signal shows immediately that the in-plane components of $\beta$ are quite strong. Equations 4.7a and 4.7b were used to fit the various tensor components of $\beta$ simultaneously to p-out and s-out SF data. The inclusion of an isotropic bulk response was tried but did not yield improved fit results. Including tensor components beyond those strongly favoured by the Fresnel coefficients (ie. $\beta_{XXZ}$, $\beta_{YYZ}$) led to an instability in the fit results (underdetermination of parameters).

The tensor components are complex-valued in principle. In practice, to keep the number of fit parameters to a minimum, we fixed $\beta_{ZZZ}$ and restricted the relative phase of $\beta_{XXZ}$ and $\beta_{YYZ}$ to $\pm\pi$.

This is possibly too severe a restriction and any ideal scanning SFG study should include a phase measurement, as demonstrated by Buck *et al.* for a hexadecane thiol-covered Au film [167].

For the three SF wavelengths shown in figure 4.2 we obtain the fit results summarised in table 4.1 These data show that as the region of interband transitions is approached by the outgoing SF photon, contributions from the $[1\bar{1}0]$ direction ($\beta_{XXZ}$) decrease in importance while those from the $[001]$ direction ($\beta_{YYZ}$) increase in importance.

| $\lambda$ / nm | eV | $\beta_{XXZ}$ | $\beta_{YYZ}$ |
|---|---|---|---|
| 690 | 1.8 | -11.7 ± 2.3 | 10.0 ± 1.5 |
| 650 | 1.91 | -8.0 ± 1.4 | 14.8 ± 1.5 |
| 570 | 2.18 | -0.3 ± 1.9 | 20.0 ± 4.3 |

*Table 4.1:* $\beta$ from the fittings of figure 4.2.

Before further interpretation of these results we will take a closer look at the copper band structure.

## 4.2 Cu(110) band structure

One of the most interesting features of the Cu(110) band structure is the existence of two intrinsic surface bands, lying either side of the band gap of the sp-band on the $\bar{Y}$ point of the Surface Brillouin Zone (SBZ). The occupied $\sigma_p$ and unoccupied $\sigma_s$ surface states (SS) are derived from p-type and s-type bands respectively. $\sigma_s$ was first reported by Heimann *et al.* [169], first observation of $\sigma_p$ was in 1985 [170–172] and theoretically predicted for surfaces by Echenique and Pendry [173]. In contrast, the close packed direction $[1\bar{1}0]$ has an sp-band gap above the Fermi level ($E_F$), and therefore two unoccupied surface bands [174, 175]. On the right of figure 4.3, the band structure of Cu(110) from Cortona *et al.* [168] is shown, where the results are from a slab calculation of 97 planes. This patterned region represents the projection of the bulk density of states onto the (110) face, and the full and bold lines depict theoretical results for the surface or resonance states. The individual symbols are experimental data [168].

The band structure of the **(2x1)O-Cu(110)** surface is also well-researched. Oxygen is an interesting case study, as copper surfaces are oxidised under ambient conditions. Bartynski *et al.* [170] observed the $\bar{Y}$ unoccupied surface state Cu(110) with inverse photoemission and noticed a strong reduction

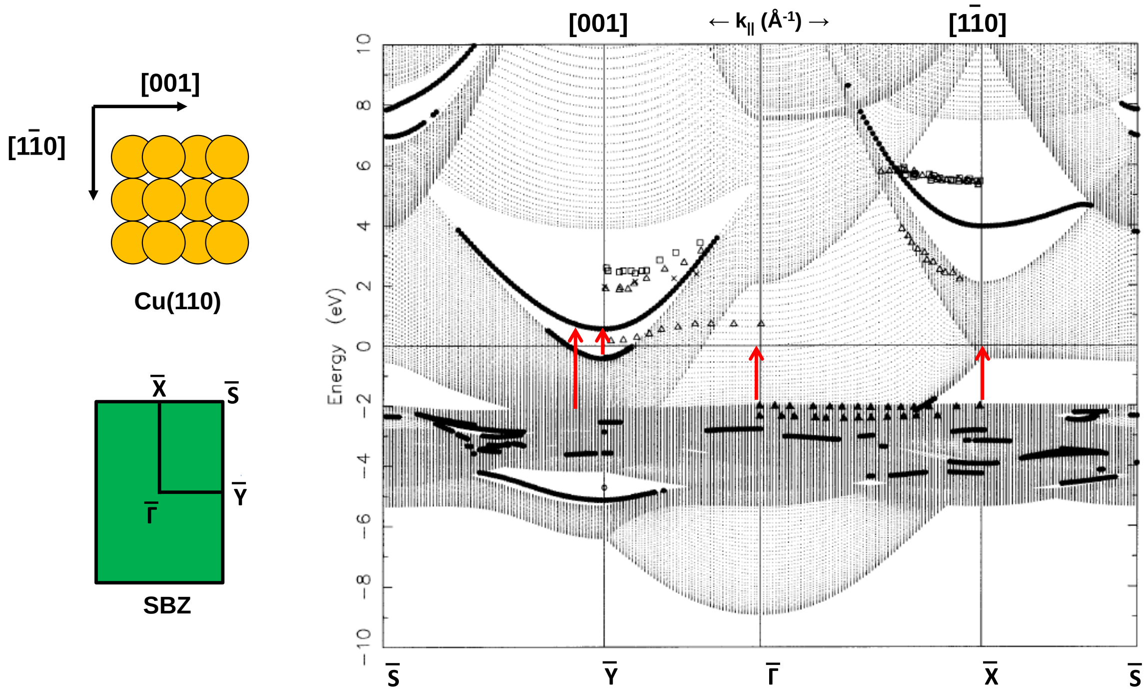

*Figure 4.3:* On the left hand side the real and reciprocal space unit cells of the fcc (110) crystal. On the right, a calculated Cu(110) band structure [168]. Red arrows represents the possible optical transitions (Compare also with table 4.2).

after $O_2$ exposure. A combined study of SHG and photoemission [158] reported later how the occupied surface state (SS) at $\bar{Y}$ shifts up to 0.7 ± 0.1 eV above the $E_F$ and reported the unoccupied states to be unaltered. They further reported that with increasing oxygen exposured the d-like surface bands split off the bulk copper bands, with energies of -1.2 eV and -1.4eV [176, 177].

### 4.2.1 Cu(110) band structure analysed by linear spectroscopies

The optical anisotropy of the Cu(110) surface has been thoroughly reported by reflection anisotropy spectroscopy (RAS) [178–184]. RA spectra shows the ratio of the difference in reflectivity for the incident p- and s- polarization along the main crystallographic axes as a function of photon energy, normalized by the mean of these reflectivities [185]. According to Jiang *et al.* [186], who studied the role of surface electronic transitions in *linear* and *nonlinear* optics on noble metal surfaces, the interband transition from $\sigma_p$ to $\sigma_s$ is only allowed, when the incident light is polarized along the [001] direction. On Cu(110) RA spectra, the peak around 2.1 eV is mainly caused by this selection rule, although Hansen *et al.* [179] and Sun *et al.* [187] show that the optical anisotropy also arises in part from surface-modified interband transitions.

Hoffmann *et al.* [178] noticed that oxygen adsorption quenches, though not completely removes, the $\sim$2.1 eV feature in RAS. The remaining RAS peak after exposure to oxygen or air was used by Hansen *et al.* [179] to assert that RAS senses anisotropic contributions from surface and bulk states and that oxygen only quenches the surface contribution.

There is only one RAS study of the adsorption of pyridine on Au(110) in an electrochemical cell [188]. Au(110) has similar occupied and unoccupied surface states to Cu(110) and Smith and coworkers report a double peak around 2.3 eV which is broadened compared to the clean surface.

### 4.2.2 Cu(110) band structure analysed by nonlinear spectroscopies

As mentioned in the introduction, the surface resonances on Cu(110) and (2x1)-O/Cu(110) have been detected in scanning SHG, in the region from 1.9 to 2.3 eV, when the incident photon makes the transition from the occupied to the unoccupied state in the $[001]$ direction of the SBZ and the polarisation is parallel to the $[001]$ direction [158, 159]. The equivalent surface resonance was also observed by SHG on Ag(110) [156] and is particularly sensitive to adsorption [189, 190].

On (2x1)-O/Cu(110), SHG detects a modified surface resonance between a split-off copper d-band and the upshifted $p_y$-like surface state [191]. RAS detects a quenching of the 2.1 eV surface state transition, as the $p_y$-state is now unoccupied, while SHG at 2.06 eV detects the change in symmetry of the bands involved through a modified polarisation anisotropy.

## 4.3 Results

In these experiments, the SF outgoing photon is scanned from ~1.8 eV to ~2.5 eV by tuning of the IR input wavelength. The data point below 2 eV was acquired with IR light at 3400 nm, for the remaining points, the wavelength of the idler was scanned. Data were normalised by IR/idler pulse energy, the visible light was spectrally narrowed by the etalon. The IR pulsewidth and shape changes slightly during the scan and was accounted for in the normalisation. The polarisation combination is either PPP (all photons p-polarised) or PSP (SF and IR p-polarised, VIS s-polarised). These polarisation combinations correspond roughly to the maxima and minima of the SF p-out curves in figure 4.2. While PPP contains in-plane and out-of-plane components, PSP senses only in-plane ones [2].

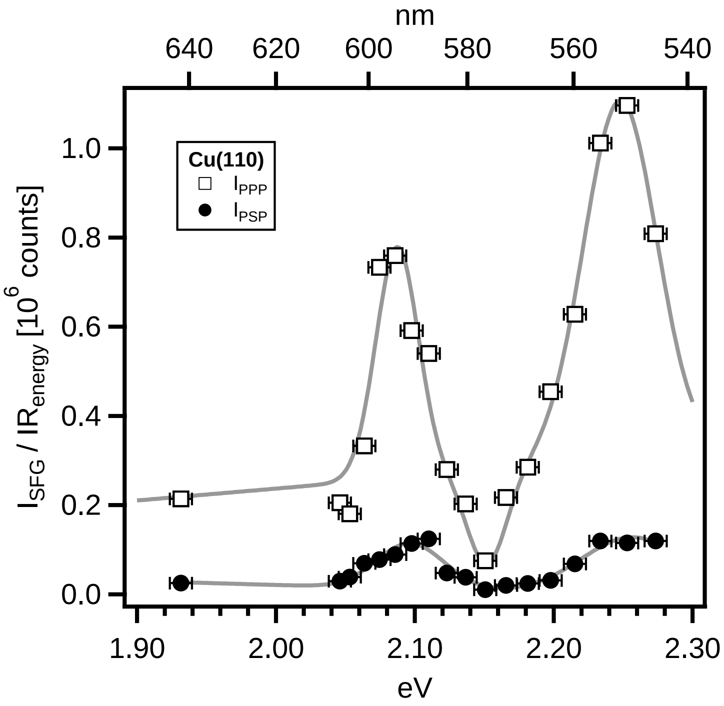

*Figure 4.4:* SF scanning for Cu(110).

### 4.3.1 SF scanning on Cu(110)

Figure 4.4 shows the results for bare Cu(110) at 100 K. Both polarisation combinations show two peaks on a smooth background. A sharp peak is seen at **2.088 ± 0.006 eV** with a width of **25 ± 6 mV**. There is a second peak near 2.2 eV, though we have too few points to precisely determine centre and width. Looking at the band structure of Cu(110) and the previous section on the surface state transition, one

---

[2] $\chi_{xyz} \approx (\beta_{XXZ} - \beta_{YYZ})$ and $\chi_{zyx} \approx (\beta_{ZXX} - \beta_{ZYY})$.

might assign at *first sight* the low peak energy to the surface state transition, however this is not possible for several reasons. The most obvious ones are that the width and the energy peak do not correspond to the expected surface state transition [159], which should be centered around 2 eV and have a FWHM of approximately 0.3 eV.

### 4.3.2 SF scanning on oxygen covered Cu(110)

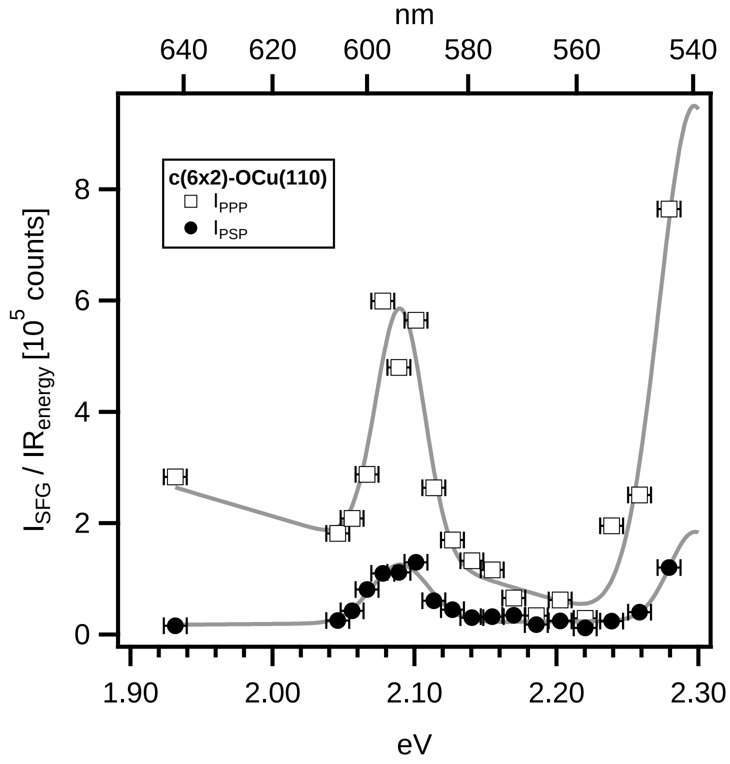

*Figure 4.5:* Scanning SFG from a c(6x2)-O/Cu(110) coverage.

The results from a SF scan on an oxygen-covered Cu(110) surface are shown in figure 4.5. We did not manage to prepare a (2x1)- O structure for this scan, instead LEED carried out after SFG showed a c(6x2) structure [192] with a 2/3 of a monolayer coverage [193].

The SF data from the oxygen-covered surface look qualitatively similar to the bare copper surface. There is a relatively sharp peak at **2.090** ± **0.002** eV (width $\sim$ **24**±**4** mV) and a rise towards 2.3 eV. In comparison to the clean surface this rise occurs $\sim$ 0.05 eV higher in energy. Similar to the clean surface, the sharp peak is much narrower than what has been reported from a scanning SH study [158]. Figure 4.6 shows the SHG data from Goldmann's group [158, 159] for O-covered and bare Cu(110) alongside our PPP results.

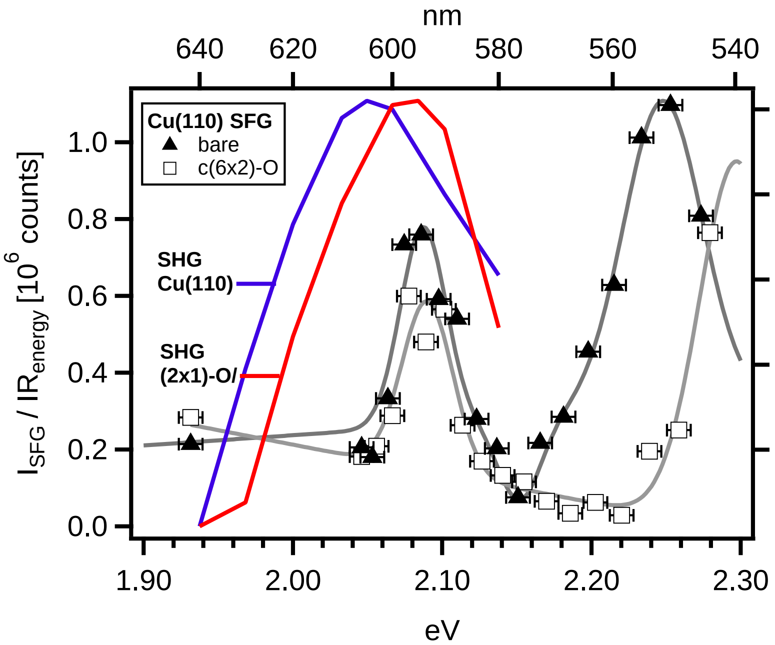

*Figure 4.6:* Comparison of SHG of (2x1)-O/Cu(110) and bare Cu(110) from Goldmann's group [158, 159] and c(6x1)-O/Cu(110) and bare Cu(110) SFG scanning.

### 4.3.3 SF scanning on pyridine-covered Cu(110)

We repeated this experiment for a 1 ML coverage of pyridine/Cu(110), see figure 4.7. While the PSP scan looks very similar to the bare Cu(110) surface, the PPP scan now possesses a very pronounced slope towards lower energies.

Little is known about the optical properties of pyridine on noble metal surfaces. From the RAS study on Au(110) [188] one might expect a peak centered around the 2.0-2.1 eV region but with a much broader linewidth of around 0.3 eV, which could roughly match the low energy PPP data. A $\pi^*$ orbital of pyridine/Cu(110) has been reported by STS to be a ∼2.3 eV above $E_F$, the with a width of ∼ 0.6 V, which is much broader than the rise seen at 2.3 eV.

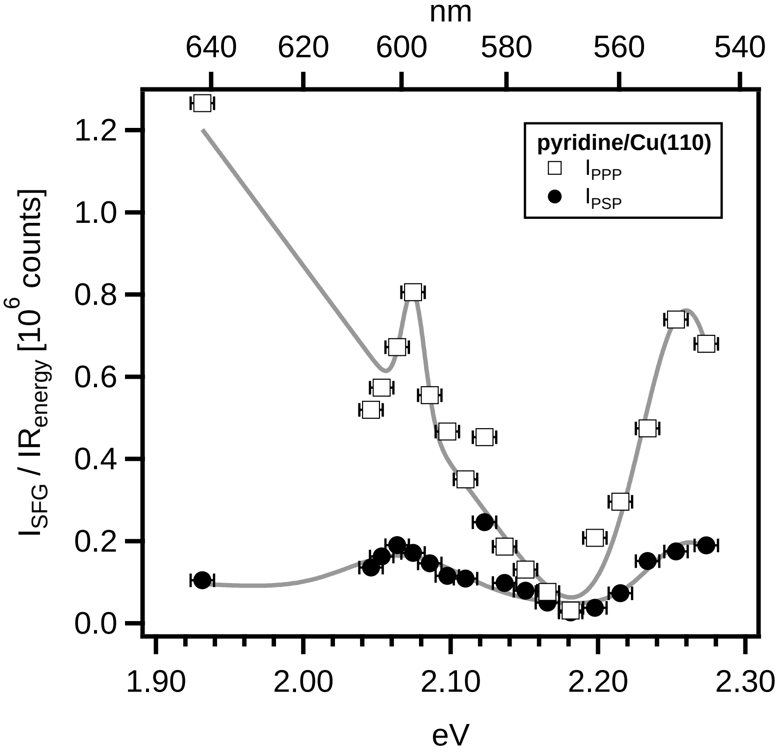

*Figure 4.7:* SF scanning of 1 ML pyridine on Cu(110)

## 4.4 Discussion

The polarisation scans analysed in figure 4.2 showed that as the SF energy increased from 1.8 eV to 2.2 eV, the $\beta_{YYZ}$ susceptibility element doubled relative to $\beta_{ZZZ}$, while the $\beta_{XXZ}$ element decreased to zero. This is in qualitative agreement with a surface state transition at the $\bar{Y}$ point in this energy range. Without absolute calibration of the sum frequency signal (e.g. from a quartz surface as used in SHG [194, 195]) and a proper phase measurement it is difficult to extract much information from these data though.

It is also very clear from the theory presented in section 4.1 that it is highly desirable to have a plane of incidence aligned with the crystal's axes as that considerably reduces the number of fitting parameters. Ideally, one would measure polarisation scans with the beams incident along $[001]$ and $[1\bar{1}0]$ as done for SHG [159]. The main difference between our work and the related SHG work on Cu(110) is that in all published SH scans the incident photon is resonant with the surface state transition at $\bar{Y}$, whereas in our case the outgoing photon experiences resonant enhancement.

The selection rule for exciting the surface state transition with one photon requires a $\bar{Y}$-polarised photon. If the same transition is carried out in a two-photon process, then a combination of a $\bar{Y}$ polarised and two polarised photon fulfills the selection rule (in the electric dipole approximation). These selection rules can be derived from the symmetries of the orbitals involved and the product table of the C$_{2v}$ group. For example, the occupied surface state at $\bar{Y}$ has p$_y$ symmetry i.e. irreducible representation B$_2$, and the unoccupied state has s-like character, corresponding to the A$_1$ irreducible representation. According to the group multiplication table:

$$B_2\ (occupied\ state)\ \otimes B_2\ (photon) = A_1\ (unoccupied\ state) \tag{4.8}$$

If this transition is carried out by two photons, then the only possibility is:

$$B_2\ (occupied\ state)\ \otimes\ [B_2 \otimes A_1]\ (photon)\ = A_1\ (unoccupied\ state). \tag{4.9}$$

A summary of various possible 2-photon transitions at $\bar{X}$, $\bar{Y}$ and $\bar{\Gamma}$ is given in table 4.2. Unfortunately, due to the mixing of [001] and [1$\bar{1}$0] directions in our setup, it is impossible to exclude any transitions as a source of our signal. Again this emphasises the need to align the incidence plane to the crystal axes. We did not do this, as the hole where the thermocouple is inserted, lies in the [001] axis.

The conclusion from the symmetry analysis is that the surface state transition should be allowed if one incoming beam is s- and the other p-polarised. The outgoing photon then has its polarisation along [001], i.e. it is s-polarised. In none of our experiments have we seen any strong s-polarised SFG, which is the reason why the SF scans were recorded with PPP and PSP polarisations.

| Brillouin Point | Initial | Final | 2 photon | Final Symmetry | $\beta$ |
|---|---|---|---|---|---|
| $\bar{X}$ | d$_{xz}$ | s | A$_1 \otimes B_1$<br>B$_1 \otimes A_1$ | A$_1$ | $XZX$<br>$XXZ$ |
| $\bar{\Gamma}$ | d$_{z^2}$ | s | A$_1\otimes$ A$_1$<br>B$_1\otimes$ B$_1$<br>B$_2\otimes$ B$_2$ | A$_1$ | $ZZZ$<br>$ZXX$<br>$ZYY$ |
| $\bar{Y}$ | p$_y$, d$_{yz}$ | s | B$_2\otimes$ A$_1$<br>A$_1\otimes$ B$_2$ | A$_1$ | $YYZ$<br>$YZY$ |

*Table 4.2:* Summarizes which $\beta$ sees which transition on the BZ.

We have calculated the expected lineshape for the surface state transition using the latest values for the energies and dispersion of the occupied and unoccupied surface states [175], assuming a parabolic shape around the $\bar{Y}$ point, a temperature dependent line broadening [187] and a constant density of states (DOS) for both states (see appendix B.1).

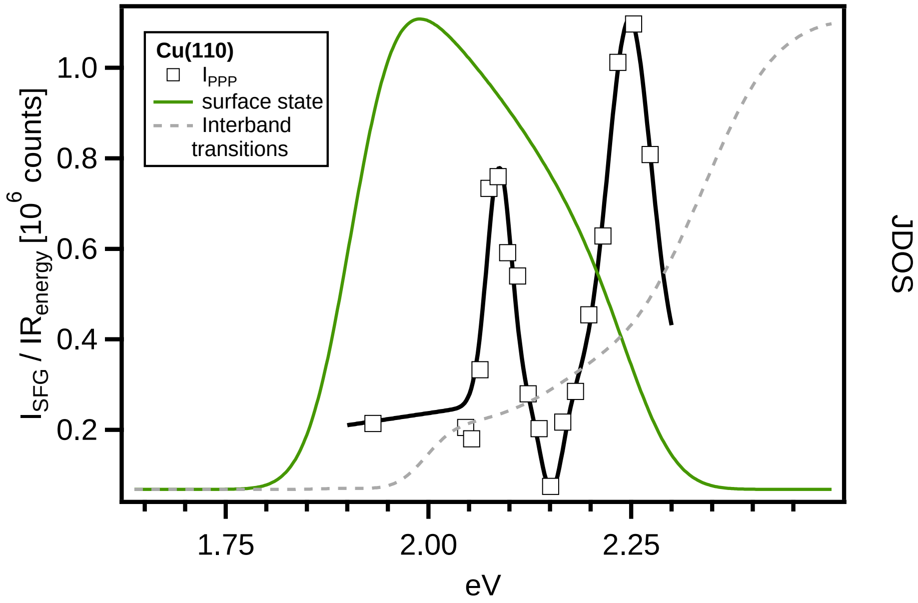

*Figure 4.8:* JDOS from surface state(green line) and interband transitions (dashed gray line), calculated for comparison with our SFG scanning (white squares) on bare Cu(110).

Figure 4.8 shows our bare Cu(110) data (PPP polarisation), the calculated surface transition lineshape and an approximate lineshape for d to sp-interband transitions using UPS data from Gerlach *et al.* [196] (see appendix B.2). It is very clear from the mismatch between the data and the calculated lineshapes that we do not see a surface state transition even though the polarisation scans produce increasing values $\beta_{YYZ}$ with increasing outgoing photon energy.

The only explanation we have for the mismatch is that although the transition is allowed in a one-photon process, its two-photon transition dipole moment is very small.

Such a dipole moment could be measured in principle by 3PPE [155] which shares the initial excitation step with SFG, but no information specific to our surface and the range of energies used could be found. A surface-state-like transition could be however the source of the large values for SFG in PPP polarisation for adsorbed pyridine. We only realised in the late stages of the analysis that points at ∼1.8

eV (mixing with 5 $\mu$m IR) would have been useful to determine the exact shape of this transition.

We have only recorded a few data points in the relevant region for 4-methylpyridine, which shows a comparable enhancement of the non-resonant background to pyridine. These data show a rapid decrease of the surface SF signal as the IR is scanned towards 4 $\mu$m (1.85 eV SF photon). If we assume that 1 ML pyridine layer causes no enhancement of the non-resonant background over bare Cu(110) at 1.8 eV, then the pyridine PPP curve is consistent with a transition between two parabolic states with $\Delta E_{min}$ = 2.1 eV and upper state electron mass of 0.7 and a lower state electron mass of 0.37. Figure 4.9 shows the calculated JDOS. This could correspond to an unchanged occupied surface state at -0.46 eV and a down shifted unoccupied at 1.64 eV with much reduced electron mass.

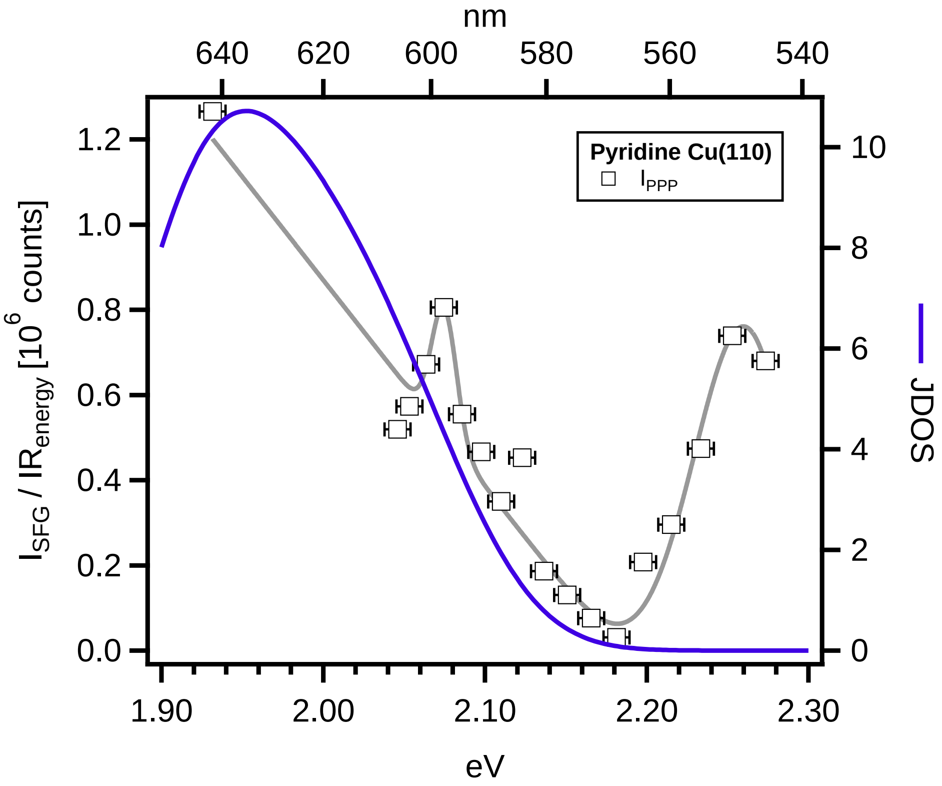

*Figure 4.9:* JDOS calculated from [187] assuming a decrease of the energy gap of the SS interband transition (blue solid line), in agreement with our SFG scanning on 1 ML of pyridine on Cu(110).

Alternatively, if we assume the unoccupied state remains at +1.81 eV with an electron mass of 1.77, then the data can be qualitatively described by an up-shifted occupied state centered at -0.29 eV and an increased electron mass of 0.55 (see figure 4.9).

Of course, the SF data can only provide the energy difference and difference in electron masses and with the rotation of the crystal it is not possible to state that only transitions at $\bar{Y}$ contribute to the signal. The symmetry could be conclusively established with a different orientation of the Cu(110) though, and the RAS spectrum of pyridine/Au(110) [188] makes it conceivable that the surface states survives.

Returning to the bare copper data, we explored whether any other transitions within the copper band structure could be responsible for the narrow peaks seen for all three adsorbates. Such a narrow peak could only be produced by a transition between two non-dispersing bands. While the d-bands are relatively far, there is no narrow state just above $E_F$ known, which could produce the shape of our spectrum (see figure 4.3). Since transitions between states cannot explain the narrow features in the SF scans, we have to think about the dynamics of the sum frequency process.

Timm and Bennemann [197] showed that the dephasing time of the polarisation created in the SF process determines the magnitude of the response. For temporally overlapped Gaussian IR and VIS pulses, the polarisation is given by:

$$P(t) \approx \int dt_1 \exp\left[i\frac{\Delta E}{\hbar}\left(t-t_1\right)\right]\exp\left[-\Gamma\left(t-t_1\right)\right]\exp\left(\frac{-2t_1^2}{\sigma^2}\right) , \tag{4.10}$$

where $\Delta E$ is the photon energy, $\sigma$ is the width of the incoming pulses and $T_2$ is the dephasing time $T_2 = 1/\Gamma$ between initial and final states and $\Gamma$ the linewidth.

To understand the meaning of the dephasing time, we use a state picture. The first photon in the SF process creates a coherent superposition bewteen ground and intermediate states i.e. an oscillating polarisation, which decays with a certain dephasing time $T_2$. The second photon that arrives a short time later changes this superposition into one between ground and excited states with a different dephasing rate. This polarisation oscillates at the sum frequency and has the dephasing time described in equation (4.10). Solving this integral, and taking into account that SF intensity is the quantity measured and is proportional to the magnitude squared of the induced polarisation the consequence of 4.10 is that, **the SF signal is proportional to $T_2$** (see the work of Tim and Bennemann for further detail [197]). Loss of the coherent electronic polarisation created by incident light can occur through two processes: population decay and pure dephasing due to elastic electron-electron scattering processes [198].

An estimate of the pure dephasing times can be made from the Drude model, which predicts charge carrier momentum scattering times of a few femtoseconds at most. Such dephasing rates have been mostly investigated in the context of plasmon excitation in nanoparticles. For example Liau *et al.* [199] used interferometric SHG to determine the dephasing rate in silver colloids to be 10 fs. Karatzas and George [200] used interferometric SHG and third harmonic generation (THG) to determine $T_2$ for a polycrystalline gold substrate to be 7.9 fs at 1.56 eV above $E_F$. Parlett used the same method to derive dephasing times of less than 15 fs for sodium and potassium clusters [201].

Dephasing times can also be measured by two-photon photoemission (2PPE) as described in the review by Petek and Ogawa [198]. Using 2PPE on a Cu(110) surface, they also report dephasing times (or hole decoherence times) as a function of initial state energy [143]. They observe an enhancement of $T_2$ at energies corresponding to critical points in the copper band structure ($K_2$ at -2.1 eV and $L_3$ at -2.24 eV).

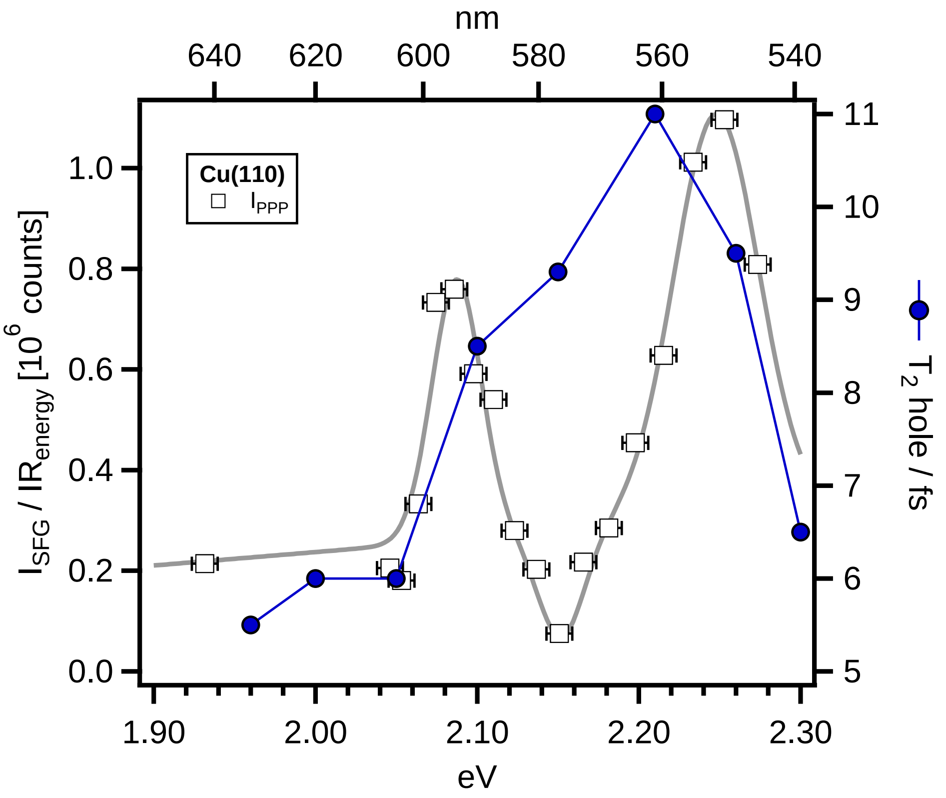

*Figure 4.10:* Closed dots, hole dephasing times ($T_2$) on Cu(110) from Petek *et al.* [143] (right axis) in comparison with our SFG scanning on bare Cu(110) (left axis).

If we plot the reported $T_2$ times alongside our SF scan, figure 4.10 shows a good agreement in the peak energies. The agreement in enhancement factor is less good at 2.09 eV we observe an enhancement of a factor 4, whereas $T_2$ increases by only a factor 2. Our SFG data should represent an integral over the whole SBZ, whereas 2PPE measurement by Petek *et al.* only senses a certain fraction of the BZ. The occurrence of the same 2.09 eV peak in all three SF scans (Cu, O-Cu, pyridine-Cu) means that this is a part of the d-band which is not strongly influenced by adsorption. Only the second peak that occurs in all three spectra is distinctly shifted upwards by oxygen adsorption (+0.05 eV).

A precise assignment of these peaks to certain points within the SBZ would be possible by a more detailed study of the symmetries of the states involved, alongside interferometric SFG measurements with very short femtosecond pulses to obtain an independent measurement of the dephasing time as a function of energy.

A good test of our model would be to repeat the measurements on Cu(001) surface which shows extremely long dephasing times of up to 30 fs around 2.0 eV [143, 198].

## 4.5 Conclusions

In this chapter, we have measured SF scans on oxygen and pyridine covered Cu(110) and bare Cu(110). For the region of 1.9 to 2.3 eV, two peaks appeared in the spectra, which we have identified with increased decoherence times for Cu(110) in this region, as reported by 2PPE. In fact, this study provides new insights into the interpretation of the SF nonresonant signal, gaining a better understanding of the optical nonlinear response with respect to the band structure. Moreover, we have explained the possible transitions induced by SFG (in the electric dipole approximation), as well as the effect upon different adsorbates ($O_2$ and pyridine). $O_2$ shows quite similar response to bare Cu(110), upshifting the spectra around the 2.3 eV region. Adsorbed pyridine, on the contrary, shows a huge enhancement around 1.9 eV, which tentatively identified a shifted surface state.

In conclusion, as far as we are aware, this is the first report of a dynamic enhancement of a sum frequency process caused by long dephasing times of the electronic polarisation.

## To do

- Rotation of the crystal in order to have the crystallographic axis perpendicular to the polarisation planes of the incident beam and repetition of the scanning IR-frequency dependence.
- For different frequencies of the SF outgoing signal measured previously, repeat the polarisation dependence experiments, to elucidate which component contribute to the signal in each case. From this study, the possible transitions can be identifyed, according with the selection rules described in the discussion. Compare with the work described by Moad and Simpson [202].
- Modeling the SFG scanning as a function of frequency, comparing with previous work [203]

# Vibrational Dynamics at Surfaces

Chapter 5

# Pyridine adsorption on Cu(110)

## 5.1 Background

Pyridine has been used as model system to understand the interaction of organic molecules with metal surfaces [39, 204–211]. Two types of interaction are known: through the delocalized $\pi$ system or via the N lone pair. On a variety of metal surfaces, low coverage pyridine interacts through its $\pi$ electrons [212–221], while high coverage pyridine forms an upright layer bonding through the nitrogen [212, 222–228]. In electrochemistry, the electrode potential can switch the molecule between upright and flat [229–236]. On Au(100) there is a pyridine-induced structural transition from a (5x2) to a (1x1) surface which goes hand-in-hand with a reorientation of pyridine from flat to upright [237]. More recently, there has been an interest in using substituted pyridines to tune work functions of self-assembled monolayers on electrodes in order to optimise charge carrier transfer across the interfaces [210, and references therein]. Pyridine adsorbed on silver surfaces has been also thoroughly studied, since it was the probe molecule when surface enhanced Raman scattering (SERS) was discovered [238]. The enhancement of the Raman signal is said to arise two main contributions [239, 240]: electric field enhancement due to the excitation of localized surface plasmons [241] or chemical enhancement [37, 39, 242–245]. In fact, these two aspects are closely related to the aims of this thesis. Chemical enhancement is caused by charge transfer between the metal and molecular states and the ultrafast dynamics of this transfer between copper and pyridine are discussed in chapter 6. Electric field enhancement and its relationship to plasmon-enhanced photochemistry is discussed in chapter 7. In this chapter, we lay the foundation for the following ones by presenting the results obtained on the adsorption of pyridine on Cu(110), studied by SFG and work function measurements.

An X-ray photoelectron spectroscopy (XPS) study has established the saturation coverage of pyridine on Cu(110) as 0.4 ML ($4{\cdot}10^{14}$ molecules$\cdot$cm$^{-2}$) [228]. Near edge X-ray absorption fine structure (NEXAFS) [222] and electron stimulated desorption ion angular distributions (ESDIAD) [227] concluded that, saturation coverage pyridine is bonding upright through the lone electron pair. The molecular plane is perpendicular to the surface, and the aromatic ring plane of pyridine is azimuthally rotated by 25° (±5) away from the [001] direction. Lee *et al.* reported an ordered (4x3) structure and the pyridine rings arranged in a chevron pattern, though the corresponding coverage ($1/12^{th}$ ML) is incompatible with the XPS result. Pyridine shows also relatively high packing densities on other surfaces. A UPS and HREELS study of pyridine/Ag(111) by Demuth *et al.* [212] found a compressional phase transition from $\pi$- to N-bonded species with a coverage of $5{\cdot}10^{14}$ molecules$\cdot$cm$^{-2}$. The N-bonded species is inclined and they speculate that this high packing density occurs because of an attractive $\pi_3$-nitrogen-lone-pair interaction. On (2x1)-O/Cu(110), XPS found a 1:1 stoichiometry between adsorbed oxygen and pyridine (i.e. 0.5 ML with respect to the Cu(110) unit cell) and a local symmetry of (3x1) [246]. XPS of intact pyridine adsorbed on W(110) at 90 K gave a coverage of $4.5{\cdot}10^{14}$ molecules$\cdot$cm$^{-2}$ [224].

The occupied electronic states of pyridine on Cu(110) have only been investigated in a single room-temperature angular-resolved photoemission study [247] with the main conclusion that pyridine adsorbs upright on this surface. A theoretical study by Atodiresei *et al.* [248] analysed the local density of states (from density functional theory (DFT) with inclusion of Van-der-Waals interactions). They concluded that the bonding mechanism consisted of a strong hybridisation of the $\sigma$-like HOMO and the $\pi$-like HOMO-2 with the copper $d_{y^2}$ and $d_{yz}$-type orbitals. The HOMO-1 does not interact strongly as it has no density on the nitrogen atom. As it is shown in figure 5.1, they found no contribution of the anti-bonding $\pi$-like LUMOs and concluded that the bond was purely covalent.

A much earlier molecular orbital study by Rodriguez [249] of pyridine on Cu(110) cluster found occupied molecular orbitals close to the Fermi level with very weak (<5%) $\pi^*$ character, i.e. there is a small degree of $\pi$-backdonation. Two-photon photoemission (2PPE) results of unoccupied states are only available on Cu(111): the $\pi^*$ states[1] are found 0.60 ± 0.05 eV and 1.20 ± 0.06 eV above the vacuum level, ie. 3.4 and 4.0 eV above $E_F$. These states are only seen for coverages > 2 ML. The earlier inverse photoemission spectroscopy (IPS) study placed the two states at much lower energies

---

[1] According to the gas phase notation $3b_1$ and $2a_2$ respectively.

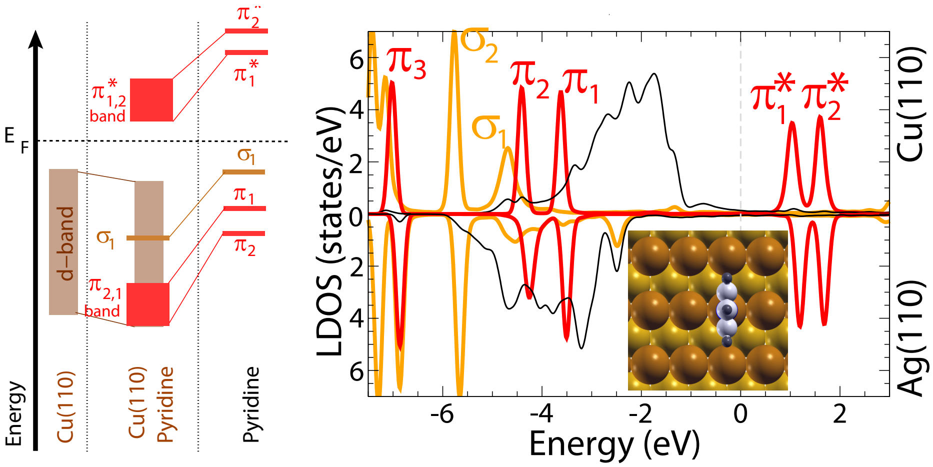

*Figure 5.1:* Left, schematic view of the hybridization of pyridine molecular orbitals with Cu(110) and d-bands in the case of the perpendicular adsorption geometry. Right, local density of states (LDOS) calculated for the perpendicular pyridine adsorption configuration, the red and orange traces corresponds to the $\pi$-type electrons and $\sigma$-type electrons, respectively. Dark line corresponds with the DOS of the Cu(110) and Ag(110) surfaces, from reference [248]. Copyright (2008) by the American Physical Society.

(2.1 and 3.1 eV above $E_F$). In this case, the coverage was estimated by dosage as 2 ± 1 ML.

## 5.2 Work function of pyridine on Cu(110)

Figure 5.2 shows the work function change as a function of pyridine adsorption. Pyridine was dosed from a background pressure in the $5{\cdot}10^{-9}$ mbar range, while the contact potential difference (CPD) measured by a Kelvin probe and the mass 79 partial pressure were recorded simultaneously. To convert from dosed pressure into surface coverage, the mass 79 was integrated over time. We defined the relative coverage as 1 ML at the minimum of the work function measured. This saturated layer of pyridine contains $4{\cdot}10^{14}$ molecules$\cdot$cm$^{-2}$ or 0.4 ML[2] [228]. The work function of Cu(110) is reduced by a substantial amount on pyridine adsorption. The clean Cu(110) work function has been determined as 4.46 eV [250] in the literature and as 4.47 ± 0.05 eV from our own UPS experiments [3]. At the minimum of the $\Delta\phi$ curve, the absolute work function of the surface is therefore 1.47 eV, ie. lower than the work function of a pure Cs surface (1.8 eV) [251]. The general shape of the curve is reminiscent of alkali adsorption [252, 253]. On metal surfaces, independent alkali adsorbates initially lower $\phi$ by a constant amount per adsorbate. At higher coverages, mutual depolarization leads to a minimum in $\phi$ [252]. A very similar shape has been observed for pyridine adsorption on Cu(111), though the work function is

---

[2] In the remainder of the thesis we will only refer to the relative coverage scale.

[3] We could not control the pyridine dosing in the UPS chamber to a sufficient degree to determine the work function.

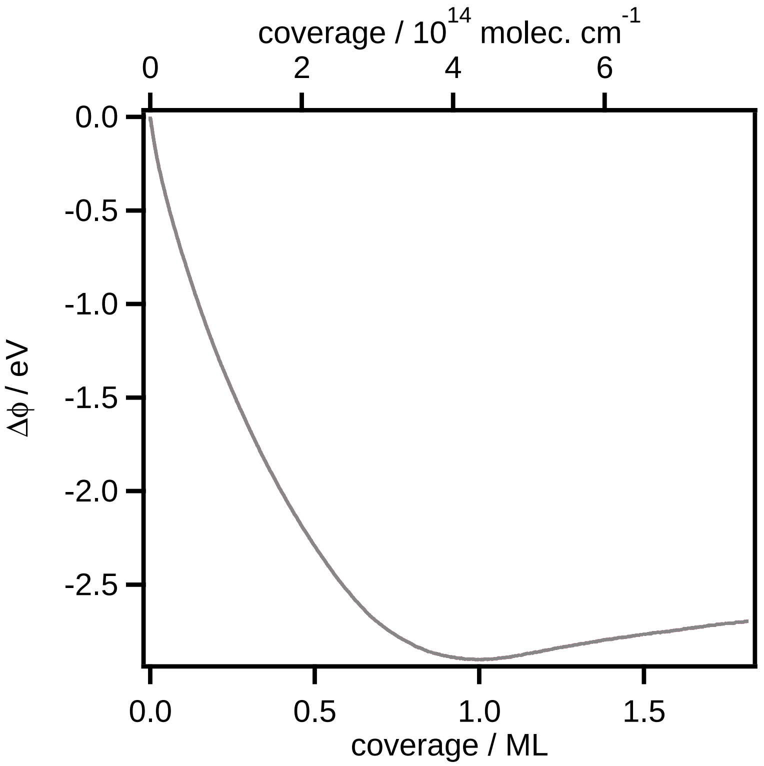

*Figure 5.2:* Cu(110) work function change $\Delta\phi$ as a function of pyridine coverage.

only reduced by 2.3 eV [254], whereas we find a reduction of 2.9 eV.

Previous studies of $\Delta\phi$ upon pyridine adsorption are summarised in table 5.1 and our value is at the top end of the reported range.

In order to check our experimental method, we have recorded the work function change caused by CO adsorption and reproduced the literature values (see appendix C.1). A possible explanation for our low work function can be found from the studies of Gland and Somorjai [255] on Pt(111) and Pt(110). They observed that a lower dosing pressure ($10^{-8}$ torr vs $2{\cdot}10^{-7}$ torr) lowered the work function by between 0.2 and 0.4 eV, presumably due to a better ordered overlayer. Our dosing pressure is typically in the $10^{-10}$ torr range, i.e. pyridine has ample time to form a highly ordered structured, which is confirmed by the very narrow vibrational linewidth of the C-H stretch (see sec. 5.3).

The dipole moment[4] in the limit of zero coverage $\mu_0$ can be extracted from the slope of the work function [257]. In our case, the initial change in $\phi$ is not a straight line, so I used linear fits to two

---

[4] 1 D = $3.336 \cdot 10^{-30} Cm$

| Substrate | $\Delta\phi$ / eV | ref. |
|---|---|---|
| Cu(110) | -3 | this work. |
| Cu(111) | -2.32 | exp. [254] |
| Pt(111) | -2.7 | exp. [255] |
| Pt(110) | -2.5 | exp. [255] |
| Au(111) | -2.33 | theory [256] |
| Au(111) | -3.05 | theory [206] |
| W(110) | -1.9 | exp. [224] |
| Ag(110) | -1.7 | exp. [223] |
| Polycrystalline Ag | -1.5 | exp. [226] |

*Table 5.1:* Work function decrease at saturation coverage for various metal substrates upon pyridine adsorption. Exp. stands for experimental.

different domains, to investigate the different values of $\mu_0$ you can obtain. The $\mu_0$ is calculated from the intercept and the gradient of the graph as (see figure C.2):

$$\mu_0 = \frac{\epsilon_0 \Delta V}{n}$$

where $\epsilon_0$= 8.85·10$^{-12}$ CV$^{-1}$m$^{-1}$, $\Delta V$ is the change in volts and $n$ is the adsorbate density. For the first and second linear fits, we obtain 6.5 ± 1.3 D and 4.29 ± 0.1 D, respectively. These values are 3x (2x) as high as the pyridine gas-phase dipole moment of 2.19 D [258]. Such enhancement is typically found for carbon monoxide (gas phase - 0.112 D [259]; on Cu(111)- 0.21 D [257]) and stems from the creation of an image dipole in the metal surface.

The initial decrease of $\phi$ is not monotonic with coverage, for which there are a number of possible explanations. Firstly, Lee *et al.* [227] studied the TPD behavior simulated by a first-order desorption spectra; at zero coverage the desorption activation energy of 0.97 eV and the repulsive adsorbate-adsorbate interaction energy is 0.16 eV/ML. Therefore, our assumption that the sticking coefficient of pyridine is constant might be wrong (there are no measurements available). Secondly, part of the curvature could be caused by a transition from flat-lying to upright pyridine, as noted by Zhong *et al.* for Cu(111) [254], which causes a different $\Delta\phi$ per adsorbate. Thirdly, pyridine might form islands on the surface, such that depolarization sets in at relatively low coverages. However, several studies of pyridine adsorpion on Cu(110) [227, 254] conclude that dipole-dipole repulsion of flat pyridine keeps the molecules apart and that island patches of the denser upright layer only form at higher coverages in agreement with earlier work on Ag(111) [212]. Molecular beam measurements and scanning tunneling microscopy (STM) over the full coverage range would be needed to fully decide these questions. Using the alkali adsorption model [252, 253] we can extract approximate values in the limit of zero coverage for the dipole moment $\mu_0$ of 4.45 ± 0.01 D and for the polarizability $\alpha$ = 19.02 ± 0.01 Å$^3$. The gas-phase electronic polarisability of pyridine is 9.3 Å$^3$ [205] and the polarisability deduced from plasmon excitation measurements on silver is 14.5 Å$^3$ [204]. To sum up, the initial dipole moment of pyridine of Cu(110) is at least twice as large as in the gas phase and its electronic polarisability is 30% higher than when adsorbed on Ag(111) [212].

## 5.3 Sum frequency measurements of pyridine on Cu(110)

In agreement with the previous RAIRS study of pyridine adsorbed on Cu(110) only one sharp C-H stretch at 3058 cm$^{-1}$ is observed [216]. There are however three modes seen in the gas phase spectra around this range which are totally symmetric ($A_1$): 3030, 3072, and 3036 cm$^{-1}$ [260], summarised in table 5.2 and figure 2.3. Only (a) will be seen, as the hydrogens in the 2, 4 and 6 positions move in phase. (b) and (c) are much weaker in the gas phase and not seen on the surface in the monolayer regime as the hydrogens move out of phase with each other.

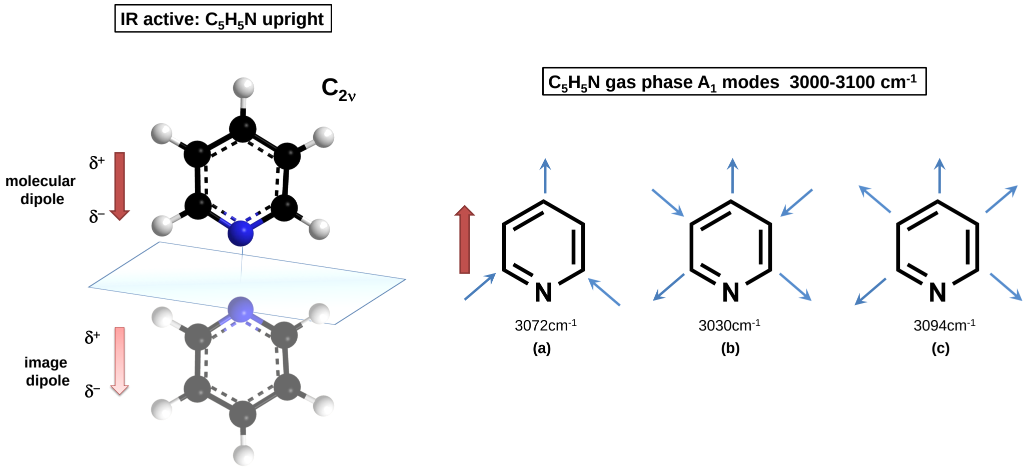

*Figure 5.3:* Left: IR active modes of upright Pyridine on Cu(110) need a molecular dipole moment perpendicular to the surface, that is the mode has to be totally symmetric ($A_1$). Right: $A_1$ modes of the pyridine, only (a) is seen by IR spectroscopy on copper.

In the calibration of our spectra, we use **3050 cm$^{-1}$** for the **1 ML** coverage. Typical SF spectra are shown in figure 5.4a as a function of coverage. We will use these to illustrate the information obtainable from SF. Firstly, there is the typical insight available from a vibrational spectrum: center frequency, linewidth and intensity. Secondly, there is the magnitude of the $SF_{NR}$ background, which is strongly enhanced upon pyridine adsorption. Thirdly, there is the coherent interaction between the two

| mode description | experimental / cm$^{-1}$ | RAIRS[216] | Label in figure 2.3 |
|---|---|---|---|
| sym C-H stretch | 3030 | | (b) |
| sym C-H stretch | 3072 | 3058 | (a) |
| sym C-H stretch | 3094 | | (c) |

*Table 5.2:* Experimental vibrational modes at 3000 cm$^{-1}$ for the pyridine gas phase [260]. Value measured by RAIRS for pyridine/Cu(110)[216]. Letters in brackets identified with the figure 2.3.

sources of SFG, which gives a relative phase value. We will discuss these in turn.

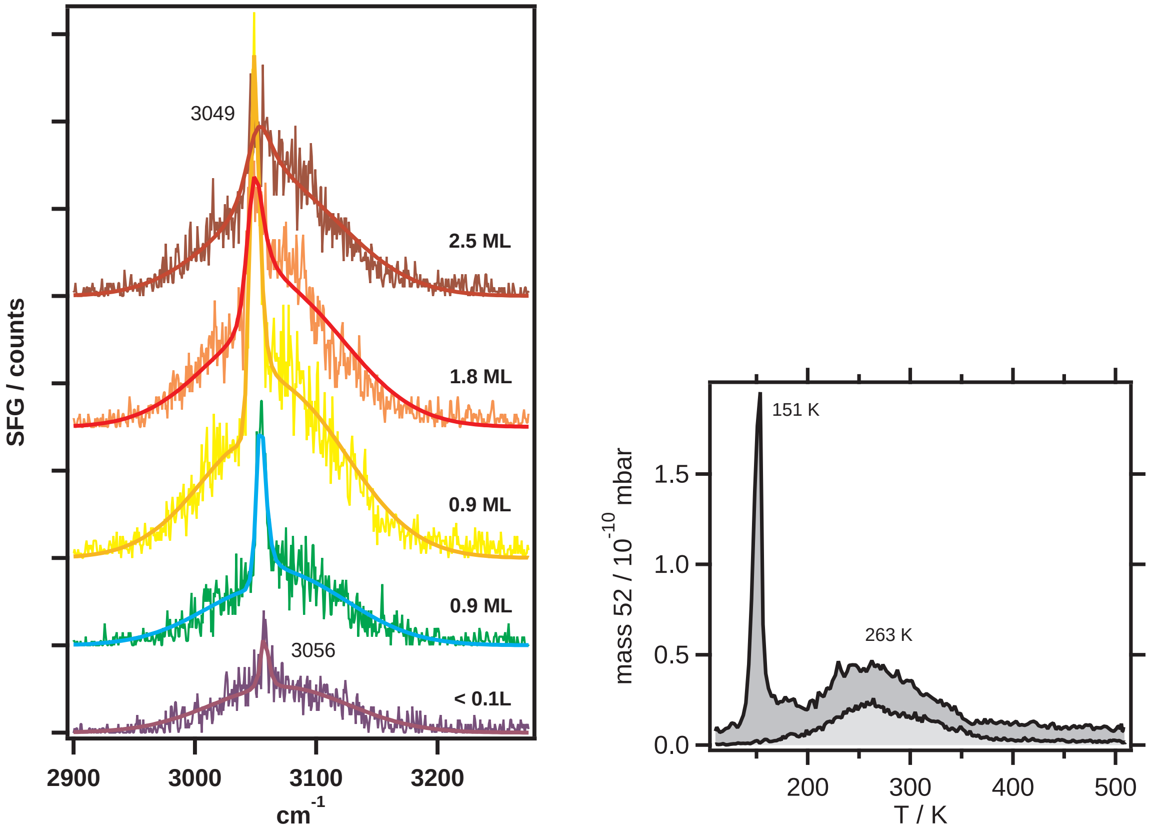

*Figure 5.4:* Left, SF spectra as a function of pyridine coverage on Cu(110). Right, TPDs for multilayer and 1 monolayer coverage.

Frequency shift and FWHM and C-H stretch intensity obtained from the spectra, in figure 5.4 are shown in figure 5.5. The SF intensity from the C-H stretch increases with coverage up to 1ML coverage. The increase can be fit with the square of the coverage as expected for the SF signal [261]:

$$SF\ intensity \approx N^2 \left(\frac{\partial \mu}{\partial Q}\right)^2 \left(\frac{\partial \alpha}{\partial Q}\right)^2 . \tag{5.1}$$

Above 1 ML, the C-H intensity decreases linearly with coverage. This could be due to random adsorption in the multilayer which might also have an effect on the order of the monolayer. Above 1 ML, a second C-H stretch is visible, though weak, at a lower frequency of 3014 cm$^{-1}$(see figure 6.11 ). This could conceivably be peak (b) from figure 5.4. Given the relative motion of the hydrogens, the C-H response of peak (b) could be out of phase with peak (a) and therefore lead to intensity reduction by interference [216].

Figure 5.5 also shows that the C-H stretch frequency red-shifts. This could be caused by different adsorption sites and/or a change of bonding. The TPDs recorded by Lee *et al.* [227] show a lot of fine structure between the multilayer desorption peak (at 151 K in our TPD on the right figure 5.4) and the main monolayer desorption peak at 263 K. Known changes in bonding are highly tilted to upright at $\sim$ 0.04 ML [221], ring plane twist around 0.04 ML ML [227], formation of an ordered densely packed layer at 1 ML. Above the 1 ML regime, there is a clear change in the width, confirming the reduction of order when the multilayer starts to grow. The second peak at coverages above 1 ML is not included in these fits, as the presence of the nonresonant background makes the fitting difficult. However, in the next chapter 6 the multilayer peak is seen clearly by suppression of the non-resonant background with the etalon. RAIR spectra shows no comparable peak in the region of 3000 cm$^{-1}$, although extra modes are seen at lower frequencies in the multilayer [216].

## 5.4 Pyridine surface interaction

We now look at changes in the surface electronic structure caused by pyridine. The left hand side of figure 5.6 shows that the nonresonant background increases monotonically with coverage while the work function continuously drops. This behavior has been reported in SHG numerous times, for example in alkali adsorption [252] or molecular adsorption [262, 263]. In the case of the SFG, this has been describe where the nonresonant background was observed to change according to [93, 264]:

$$I_{NR} \approx (1 + const \cdot .\phi(\omega))^2 \; . \tag{5.2}$$

It should be noted that the resonant and nonresonant signal have a very similar coverage dependence.

Figure 5.7 shows the relative phase change as a function of coverage between resonant and nonresonant SFG. These phase transients are characteristic for electronic structure and correlated to the orientation of the molecule on the surface [261, 265–267]. While a change in phase is known to signify changes in the electronic structure of the surface, no quantitative information has been extracted from such measurements in the SFG literature to date.

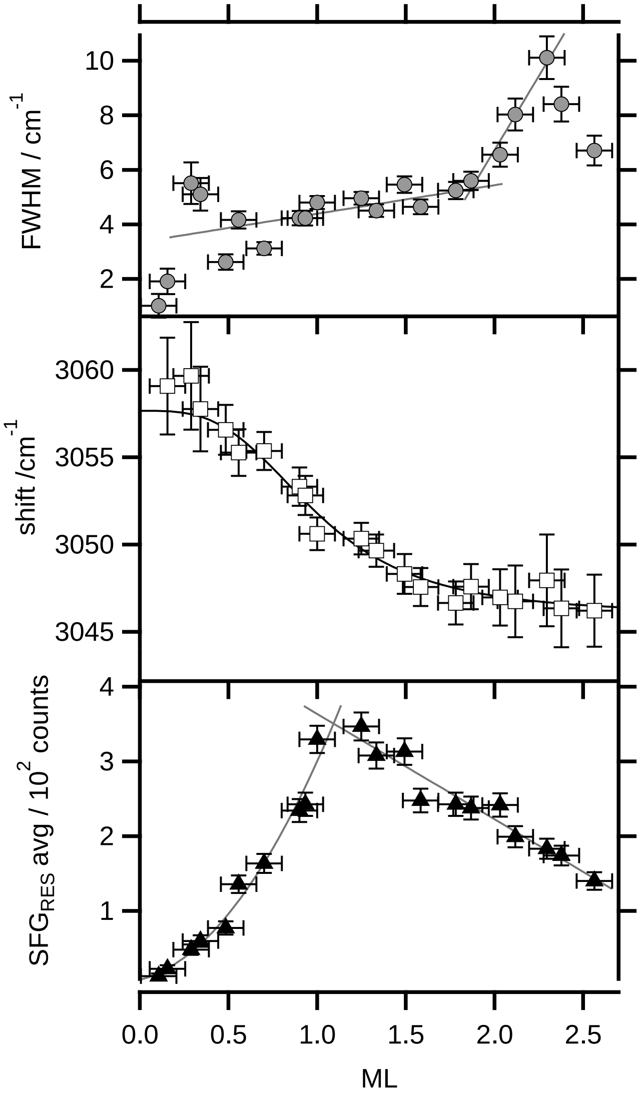

*Figure 5.5:* From top to bottom: FWHM, frequency and intensity of C-H stretch of pyridine adsorbed on Cu(110) as a function of coverage.

Finally, we show SF spectra of substituted pyridines in figure 5.8. 2-picoline, 4-methoxypyridine and 3-cyanopyridine were dosed and annealed similar to pyridine. The spectra shows that they enhance the nonresonant background by varying amounts and that the relative phase is different for all three adsorbates.

According to Morton and Jensen's calculations [39] for substituted pyridines on silver clusters, the degree of charge transfer is governed by the energy difference between the LUMO and the highest occupied energy level of the metal. Pyridine transfers 0.151 e$^-$ to Ag, while 3-cyanopyridine transfers 0.093

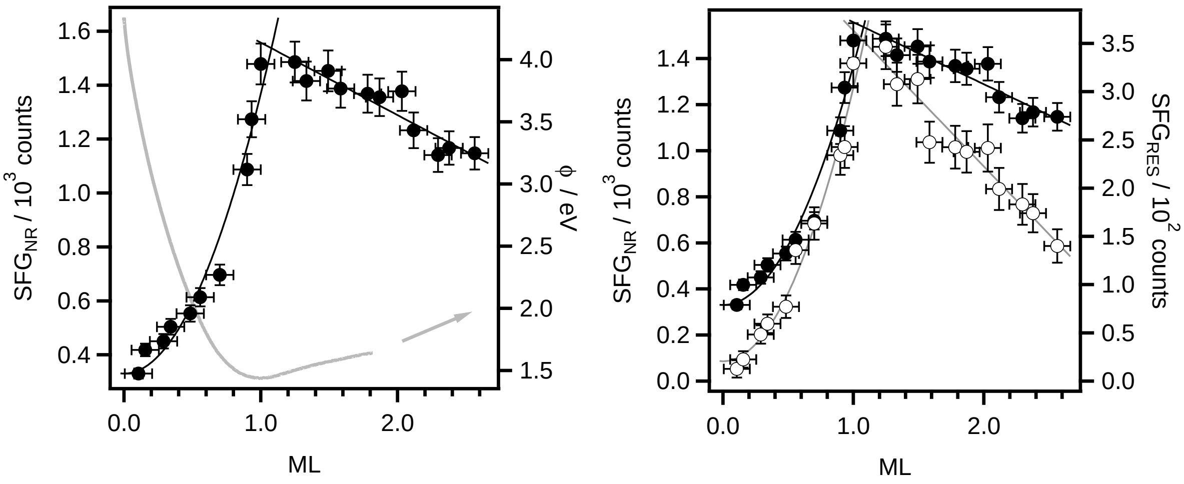

*Figure 5.6:* Left, work function change and nonresonant background as a function of coverage. Right: Resonant and nonresonant SF signals as a function of coverage.

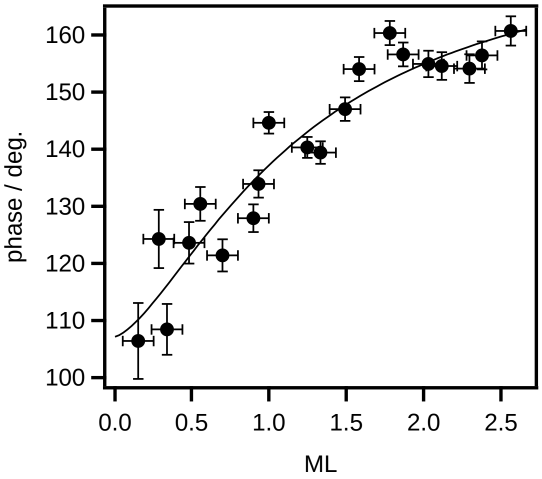

*Figure 5.7:* Phase change as a function of coverage.

e$^-$. Therefore there is less charge transfer for the -CN group and our corresponding SF$_{NR}$ is hardly enhanced with respect to the bare Cu(110) spectrum (see figure 5.8). Ma *et al.* in another theoretical study of pyridine-based self-assembly monolayers (SAM) on Au(111) also show how substitutents can shift lowest unoccupied $\pi$-states (LUPS) closer to or further away from E$_F$ [256]. Wu *et al.* [268] compute chemical enhancement of pyridine vibrational modes for noble metals concluding that chemical enhancement occurs by charge transfer between metal s-states and the LUPS. It would be interesting to correlate nonresonant enhancement and work function measurements with calculated charge transfer and SERS response for a wide range of substituted pyridines. This relatively simple surface science techniques could help with a more quantitative understanding of SERS.

Returning to pyridine on copper, this charge-transfer state lies in the blue green region of the spectrum. In the next section we will look at the difference frequency generation between green light (532 nm) and IR and the following chapter 6 is devoted to understanding charge transfer in the time domain.

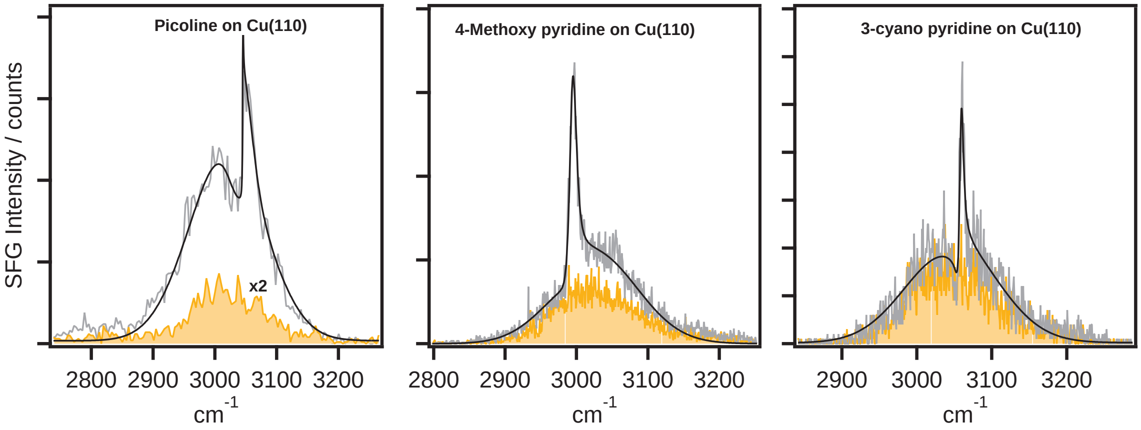

*Figure 5.8:* SF spectra from various substituted pyridines (grey line) adsorbed on Cu(110), versus bare Cu(110) (orange line).

### 5.4.1 DFG, SFG and work function

We originally use difference frequency generation between our typical 532 nm pump and the mid- IR probe pulse as a convenient means to overlap all three pulses in a pump-probe experiment in space and time. Due to the near-coincidence of the DF photon wavelength ($\sim$ 634 nm) with the SF photon ($\sim$650 nm) this method is fast and easy. A more detailed investigation of the DFG signal as a function of coverage however provides additional insights into the interaction of green light with adsorbed pyridine.

The nonlinear DFG and SFG nonresonant intensity of pyridine as a function of coverage has been recorded by stepwise annealing, after dosing pyridine to saturation coverage on the Cu(110) surface. Figure 5.9 compares the $\phi$ (left axis), recorded in a similar way and SF$_{NR}$, as well as the difference frequency (DF) (right axis). Notice, the data are in agreement with those just presented, but were obtained by stepwise annealing rather than dosing. The DFG signal consists of a resonant and a nonresonant contribution, but since the green pulse is short ($\sim$ 150 fs) the two contributions cannot be spectrally separated. Since the spectra have a near-Gaussian shape, we believe however that the resonant contribution is small.

The 3000 cm$^{-1}$ IR pulse is used for both processes, whereas the pump is at 800 nm and 532 nm for SFG and DFG, respectively. The DFG almost vanishes upon pyridine absorption, unlike the SFG which is strongly enhanced.

Hochstrasser *et al.* measured the excited state dipole moment of pyridine in a benzene host single crystal and their interaction with an external d.c. electric field, finding a change of dipole moment of $|\Delta\mu|$= 3.2 ± 0.1 D [258]. The gas phase ground state dipole moment of pyridine is 2.15 ± 0.05 D [269], therefore the excited state dipole moment is -1.05 ± 0.05 D. This huge change in dipole moment is caused by a charge migration from N to the ring, as expected far an excitation into $\pi^*$ [270]. A possible explanation for the decrease of DFG intensity with pyridine coverage is the following. On a clean copper surface the DFG signal is very large as the 532 nm (2.33 eV) photons are resonant with a d- to s transition. When pyridine is adsorbed, the green photons can in addition excite an electron from the Fermi level into the pyridine $\pi^*$ (as observed in scanning tunneling spectroscopy (STS) [221]). This excited pyridine possesses an opposite dipole moment to the ground state molecule, therefore the enhancement seen in SFG turns into a suppression in DFG. We can possibly think about this charge transfer as a transient increase in work function (discussed in more detail in the next chapter). This phenomenon is strongly coupled to the adsorbate value of the work function. For coverages around 1 ML, the pyridine $\pi^*$ state lies above the vacuum level and it appears that the electron excited by the green photon has a long lifetime within the pyridine layer. As soon as $\phi$ increases beyond 2.33 eV the DFG signal rapidly increases with decreasing coverage.

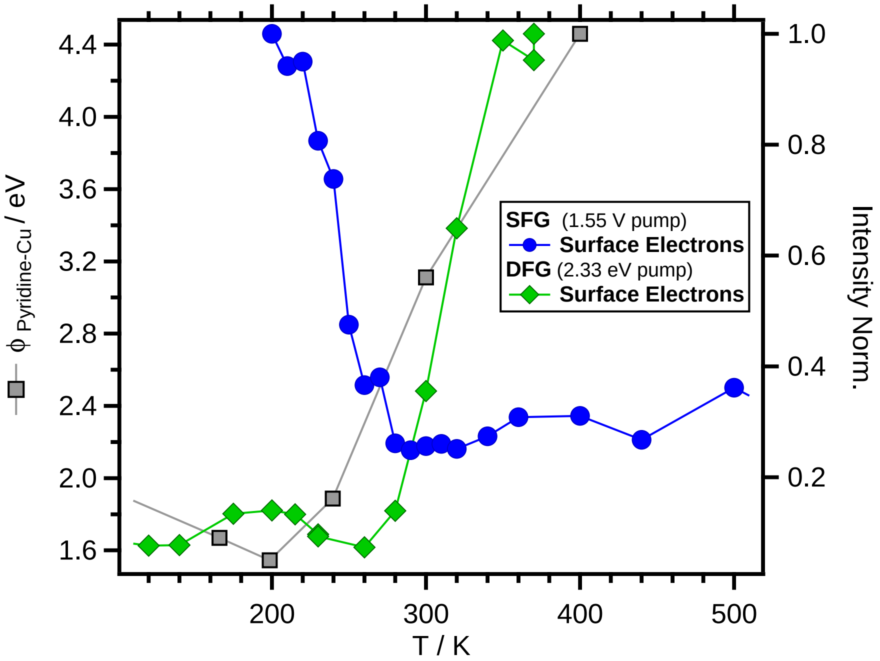

*Figure 5.9:* Left axis, $\phi$ measured as $SF_R$, $SF_{NR}$ and DFG (Right axis) were recorded after dosing a saturated pyridine layer on Cu(110) and stepwise annealing.

## 5.5 Conclusions

SFG and DFG of pyridine on Cu(110) have been reported in a combined study with work function measurements. The SFG signal is proportional to the increased polarisability upon adsorption, caused by charge donation from the nitrogen lone pair to the surface. DFG between 2.33 eV and IR photons on the contrary almost vanishes upon pyridine adsorption, which is probably caused by a reversal of the pyridine dipole moment on excitation into the $\pi^*$ orbital and the fact that this level is above $E_{vac}$.

The huge decrease of the workfunction of Cu(110) by pyridine provides an exceptional system to tune the effective $\phi$ of metallic electrodes [210, and references therein] to optimise charge transfer. Fine control can be achieved by substituting functional groups on the pyridine ring, as shown by preliminary measurements of the SFG enhancement of substituted pyridines.

Chapter 6

# Vibrational dynamics: Pyridine on Cu(110)

## 6.1 Prelude

The last chapter showed that pyridine is an intriguing molecule-enormous Cu(110) work function decrease, drastic suppression of the green-IR difference frequency signal set against the enhancement of the red-IR sum frequency signal leads us unavoidably (inevitably) to study this system by time-resolved spectroscopy. In order to understand the energy dissipation channels after laser excitation we normally think about two energy reservoirs in the metal substrate: hot electrons and phonons [271]. The hot electron temperature and relaxation timescales are high and fast ($\sim$ 100 fs) in comparison with the lower temperature and "slow" (picosecond) phonons, which are highly dependent on the material [272]. The difference between hot electron and phonon heat capacity allows us to distinguish the two dissipation channels on a metal surface by their timescale. Adsorbate vibrational energy exchange with other modes is an important factor to control and understand elementary processes on surfaces, such as diffusion, reaction or desorption [53]. Coupling between internal vibrational modes and the electron bath was one of the first evidences of non-adiabatic process on surfaces [273], which can lead to desorption [274], diffusion [68] or dissociation [66], reviewed by Frischkorn and Wolf [55]. In order to explain the ultrashort-pulse induced effects in surface femtochemistry, three heat baths need to be considered: hot electrons, phonons and adsorbate.

Figure 6.1 (left) shows the temperatures of the three heat baths as a function of time, calculated by the three temperature model for a copper surface [63, 67]:

$$\begin{aligned}\gamma T_e\frac{\partial T_e}{\partial t} &= \kappa\nabla^2 + g(T_l - T_e) + S(z,t)\\ c_l\frac{\partial T_l}{\partial t} &= -\,g(T_l - T_e)\\ \frac{\partial T_{ads}}{\partial t} &= -\,\frac{1}{\tau_e}(T_{ads} - T_e) - \frac{1}{\tau_{ph}}(T_{ads} - T_l)\end{aligned}$$

where $T_e$, $T_l$, $T_{ads}$ are the electronic, lattice and adsorbate temperatures respectively, $g=1\cdot10^{-10}$ W nm$^{-3}$ K$^{-1}$ is the electron-lattice coupling constant [272], the electron thermal conductivity is $\kappa$ = $4.28\cdot10^{-7}$ W nm$^{-1}$ K$^{-1}$, electron specific heat constant is $\gamma$ = $0.966\cdot10^{-10}$ W nm$^{-3}$ fs K$^{-2}$ and $c_l$ = $3.5\cdot10^{-6}$ W nm$^{-3}$ fs K$^{-1}$ is the lattice heat capacity [142]. $\tau_e$ and $\tau_l$ are the coupling constants between the adsorbate and electrons and phonons, respectively. This model has certain shortcomings, as the phonons are only heated by coupling to electrons. A more recent version by Carpene [275] includes the effects of a non-thermal electron distribution created immediately after the laser pulse, which provides a heat source for both hot electrons and phonons. The main effect compared to this model is a reduced maximum electron temperature that occurs later, as shown experimentally [276]. The hot electron temperature reaches thousands of K in a few hundred fs while the phonon temperature

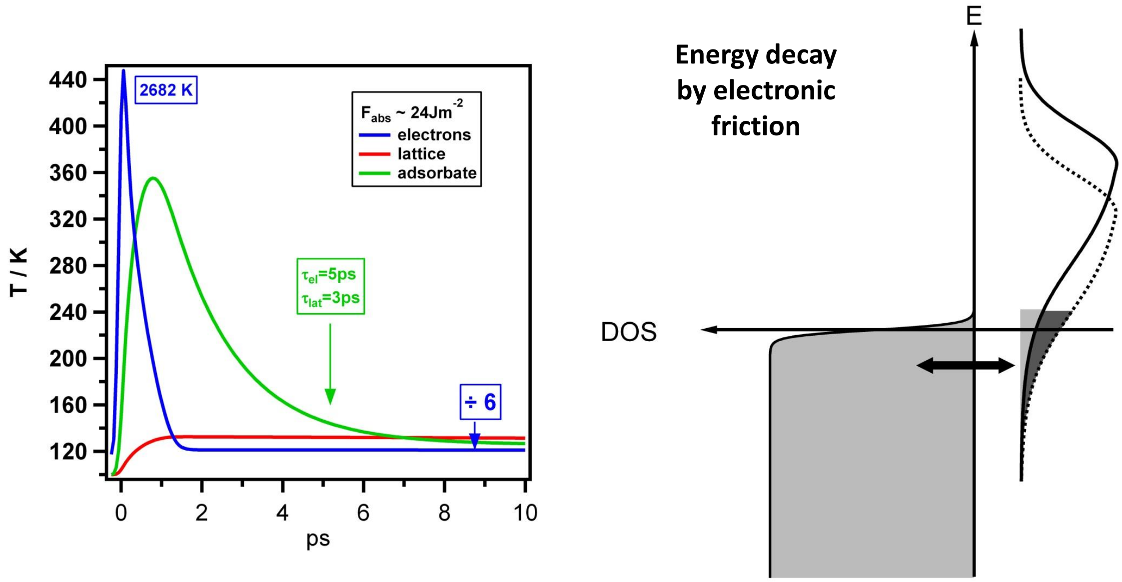

*Figure 6.1:* Left graph, temperature distribution of the hot electrons, phonons and adsorbate created by a 2.3 eV and ± 40 J m$^{-2}$ (60% absorbed) ultrashort pulse on Cu(110) at 100 K. Right graph from reference [53], the extended tail of the adsorbate LUMO shifts up and down against the Fermi sea, resulting to in effective damping mechanism called electronic friction.

merely increases by 20 K relaxing over a long time scale. The adsorbate temperature depends on both hot electron and phonon timescales. On the right of figure 6.1, a schematic representation of electronic friction, an energy transfer mechanism between adsorbate vibrations and hot electrons [277–280]. Coupling/damping by friction occurs because the long tail of the adsorbate LUMO shifts up and down in energy during the vibration, changing the overlap with the Fermi sea of the metal.

Broadband SFG allows to record a transient of a vibrational mode in a non-equilibrium situation, produced by an ultrafast pump, as described before, to determine the mechanism and rates of energy flow, reviewed by Arnolds and Bonn [54]. The majority of real time surface dynamics (near-IR pump and BB-SFG probe) have been done on adsorbed CO on metal surfaces, due to the easy handling in UHV, non-dissociative chemisorption and the large SFG resonances (easy to see and follow!). These experiments measure the coupling time of the adsorbate vibrational to the electron-phonon bath. CO on copper is easy to interpret as the large difference between electron and phonon temperatures allows an unambiguous determination of the $\tau_e$ and $\tau_l$ [142, 281]. On metals like Pt, Ru and Ir the fast equilibration between electrons and the lattice makes distinction between $\tau_e$ and $\tau_l$ difficult, although fast coupling to electrons can be observed by modulations to spectra at negative time delays [63–69]. The most recent work uses SFG with phase sensitive detection to reveal further details of the non-adiabatic coupling between the C-O stretch and hot electrons [282]. In the following, we report on the non adiabatic response of CO on Cu(110) as a way to better understand our pyridine pump-probe results, as well as testing our method and estimating the degree of heating by the pump pulse.

### 6.1.1 Nonadiabatic coupling of CO on Cu(110).

The general effect of an ultrafast pump pulse on the CO stretch frequency is a red shift. A similar red shift is observed in low temperature dependent measurements of CO. The basic mechanism in both cases is an anharmonic coupling to a low frequency mode, normally the frustrated translation. This mode physically moves the adsorbate away from its adsorption site, so for atop CO the move is to a bridge or hollow site, which has a lower C-O frequency due to increased charge donation into the $2\pi^*$ orbital. Notice that all pump-probe studies have been carried out on atop CO!CO transients are then typically fit using static temperature-dependent measurements as an input. In our case we use data by Germer *et al.* [142] for (2x2)-CO/Cu(110) as we could not measure the gradient over a wide enough temperature range.

Figure 6.2 shows the CO transients for 0.5 ML CO/Cu(110). The three-temperature model deliv-

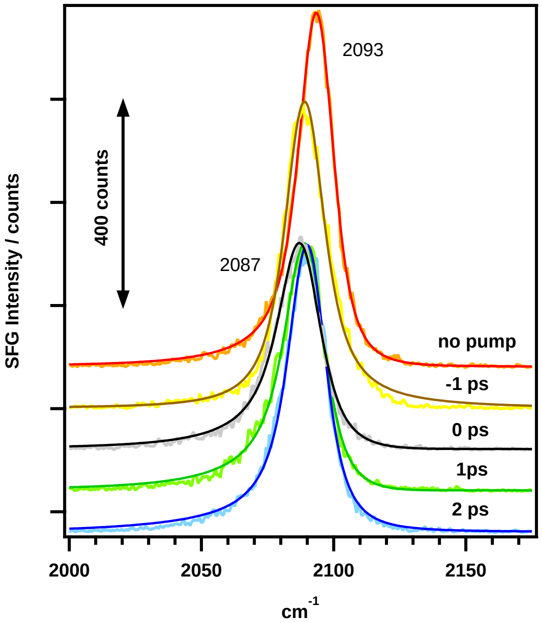

*Figure 6.2:* CO SF spectra on Cu(110) for various delay times for a 532 nm (24 Jm$^{-2}$ absorbed fluence) .

ers an adsorbate temperature as a function of time, which is turned into instantaneous time-dependent frequency and linewidth values using the static input values. These values are then fed into the Bloch equations [283] to model the effect of changes occurring during the C-O polarisation decay. Previous work done by this group used this method to investigate anharmonical coupling to a low-frequency mode, for example for CO on Ru(10$\bar{1}$0) [63], NO on Ir(111) [66], on NO and CO on Ir(111) [65, 284]. Bonn *et al.* applied this to CO on Ru(001) [285]. Nagao *et al.* also used this approach to model the energy transfer between $D_2O$ and CO on Pt(111) [286]. Further examples can be found in the following reviews [53–55].

As figure 6.3 shows, we can model transients very well if we assume coupling times of $\tau_e$ = 5 ps and $\tau_l$ = 2 ps of the adsorbate to hot electrons and phonons, respectively. (The temperature results from our calculation are shown in figure 6.1 shows the calculations of the three temperature model). Finally, figure 6.4 shows fast change in the relative phase between resonant and nonresonant SFG components. These changes look very similar to the derivative of the frequency transients and the initial positive excursion is a narrow in time as the hot electron distribution. Watanabe *et al.* [282] observed similar changes in the nonresonant response of Pt(111) and concluded that they provided a good indicator for the electron temperature.

Having established the ultrafast behaviour of CO on Cu(110), we will use it as a thermometer when we discuss the pyridine transients in the next section.

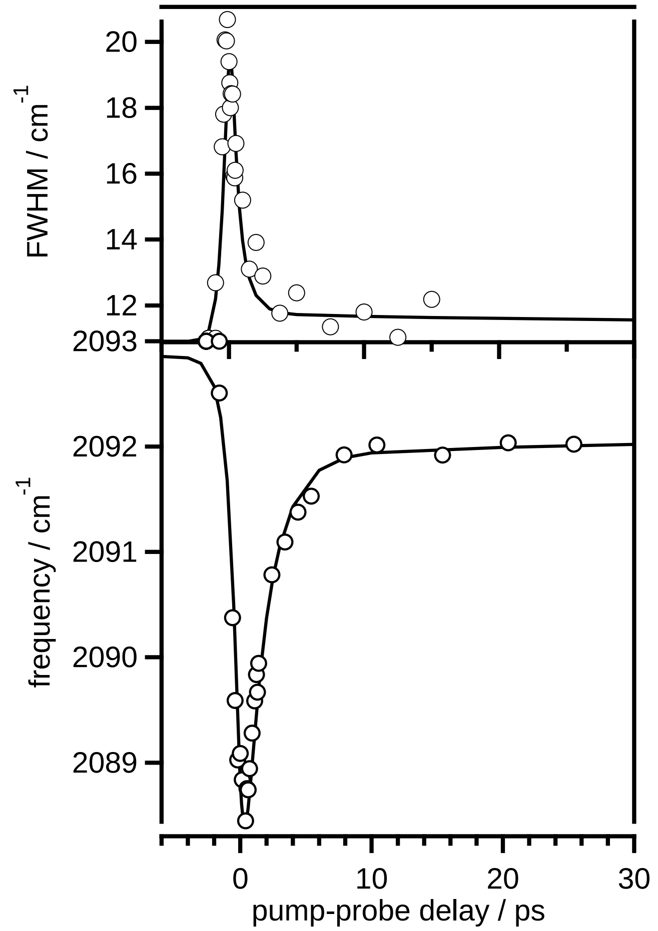

*Figure 6.3:* Frequency shift and FWHM of the C-O vibrational mode as a function of time delay after a 2.3 eV pump. Solid lines are the result of modeling (see text).

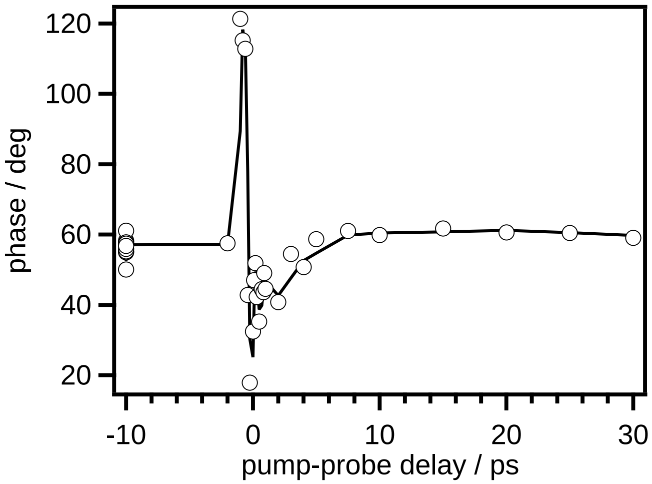

*Figure 6.4:* Phase change as a function of time delay after a 2.3 eV pump. Solid lines are to guide the eye.

## 6.2 Pump-probe spectroscopy of a complex molecule

As mentioned in the previous section, most time resolved investigations of the coupling between electrons and adsorbate vibrations have been carried out on CO or NO which only have a small number of vibrational modes available for coupling to excited electrons. What happens when we put a much larger molecule like pyridine on the surface? A lot of interest in pyridine as an adsorbate comes either from the SERS community (where pyridine is the equivalent to CO in IR spectroscopy) or from those interested in metal-organic interfaces. The common point of interest in both cases is charge transfer between the metal surface and pyridine.

As mentioned in the previous chapter, the charge transfer state of pyridine lies somewhere in the blue-green region of the spectrum for silver and copper and involves an excitation from the metal's sp-band to the pyridine $\pi^*$ (see figure 5.1). A sketch of the various resonances in a pyridine-Ag nanoparticle system can be seen in the short review by Lombardi and Birke [241], where it is centred around 600 nm. Demuth *et al.* [212] observed a corresponding peak in electron-energy-loss spectroscopy starting at 1.4 eV above $E_F$ with a maximum near 2.5 eV (500 nm) on Ag(111). Dougherty *et al.* [221] observed a resonance with STS on low coverage pyridine on Cu(110) at 2.3 eV above $E_F$ and Zhong *et al.* [254] detected a broad feature in 2PPE of submonolayer pyridine/Cu(111) approximately 1.6 eV above $E_F$. To investigate the charge transfer between our Cu(110) surface and pyridine we will use 800 nm (1.55 eV) and 532 nm (2.33 eV) pump pulses.

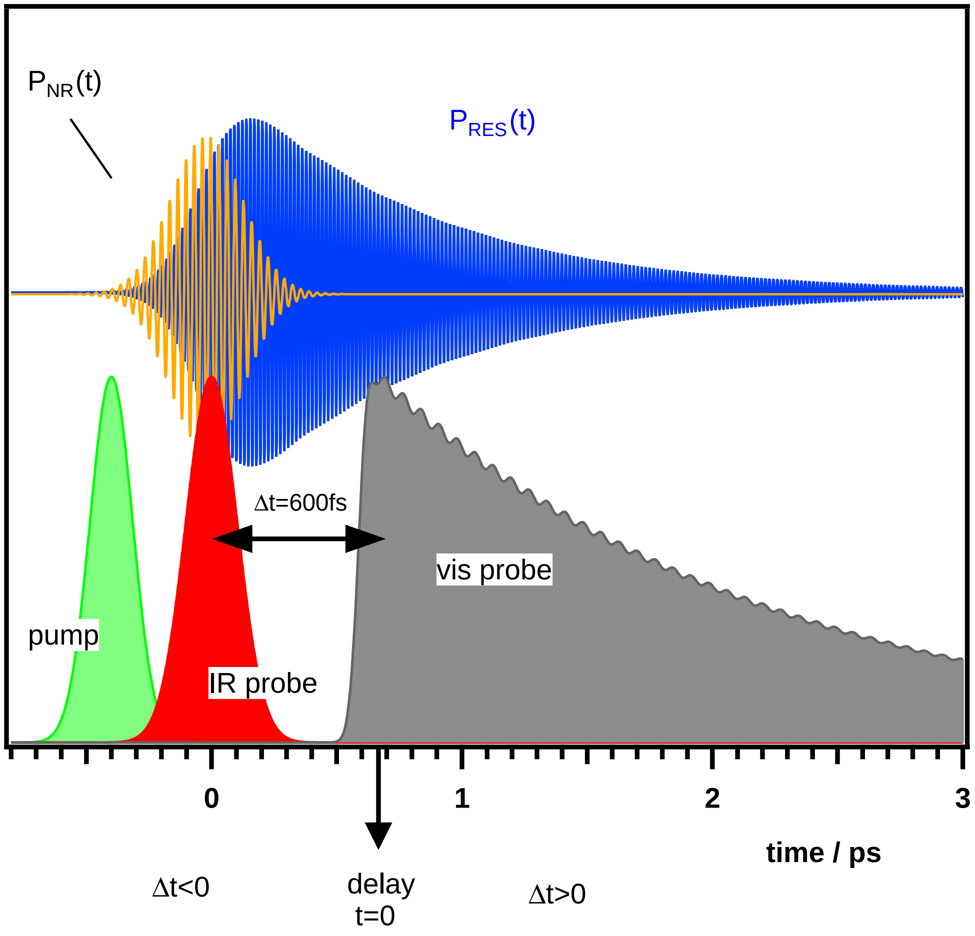

*Figure 6.5:* Sketch of a pump-probe experiment.

A general sketch of the time-sequence of pulses and the development of the electronic polarisation $P^{(2)}$ on the surface is shown in figure 6.5. Let's discuss positive delays times: the $\sim$ 150 fs short IR pulse creates a coherent vibrational ($P_{RES}$(t)) and electronic polarisation ($P_{NR}$(t)) in the mid-IR. If the visible probe pulse maximum coincides with the IR probe we upconvert both the electronic and the vibrational polarisation and obtain a spectrum like shown earlier (figure 5.4). In this configuration (pump followed by coincident IR + visible probe at varying time delays) we can detect changes in the surface electrons and the pyridine simultaneously.

This method worked very well for CO as the nonresonant contribution is very small compared to the resonant one, making data analysis easy. However, this time-sequence does not work for pyridine, because the very large nonresonant contribution obscures details of the resonance.

Therefore, we delay the visible probe pulse by 600 fs from the IR probe pulse which gives us a pure resonant spectrum. Note, in this case the time delay is

$$\Delta t = \Delta t(pump - IR) - \Delta t(IR - visible\, probe)$$

because we do not see what happens to the resonance directly after it is excited by the IR pulse. At Δt=0ps corresponds when the pump pulse arrives 600 fs after the vibrational mode of the molecule is generated. $\Delta t(IR - visible\, probe)$ =600 fs. This definition can cause controversy, as the delay time 0 can be understand when the pump and the IR pulse arrived together. However, the sfg detected is generated 600 fs after, when the probe arrives, and this is the reason for us to choose the time delay 600 fs after.

## 6.3 Results

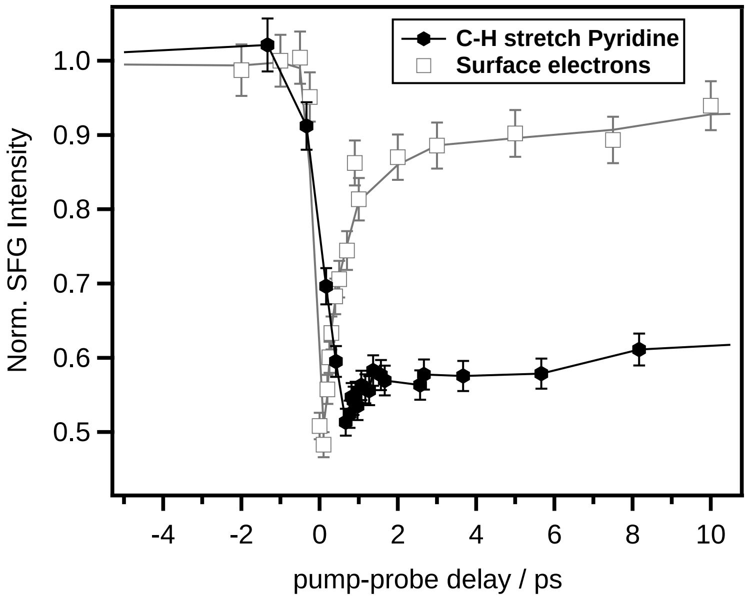

*Figure 6.6:* $SF_R$ and $SF_{NR}$ for a monolayer of pyridine on Cu(110) at 100K. Pump 532 nm ($\sim$40 $Jm^-2$)

Figure 6.6 shows the typical response of a monolayer of pyridine on Cu(110) to a 532 nm pump pulse. The SF spectra from both contributions have been integrated and normalised to no pump spectra. The main changes occur in the amplitudes of the nonresonant background $SF_{NR}$ and C-H stretch ($SF_R$). The frequency and linewidth of the C-H peak changes only slightly in the first picosecond by $\sim$ 1.5 $cm^{-1}$ and $\sim$ 1 $cm^{-1}$, respectively. Note how different this is from CO where the main changes caused by the pump occur in the frequency and linewidth of the resonance! Two timescales are visible in the response, a strong reduction of the nonresonant background and of the C-H vibration is observed almost instantaneously. The C-H signal then remains low for tens of picoseconds. The layer is stable to prolonged irradiation and we have found no evidence of photoinduced dissociation. SERS studies also report that pyridine is stable to laser irradiation [18].

### 6.3.1 Pump effects on the surface electrons

Figure 6.7 shows the nonresonant background from the previous figure overlaid with the electron temperature calculated for a total fluence of 40 $J{\cdot}m^{-2}$. The traces are very similar. If electron temperature was the cause of the changes seen in the nonresonant background, then we would expect to see a transient shape that corresponds to $T_e(t)$ convoluted by the width of the IR pulse ($SF_{NR}$ is only generated when both IR and visible probe light are present). Such a behavior has been seen before by the group

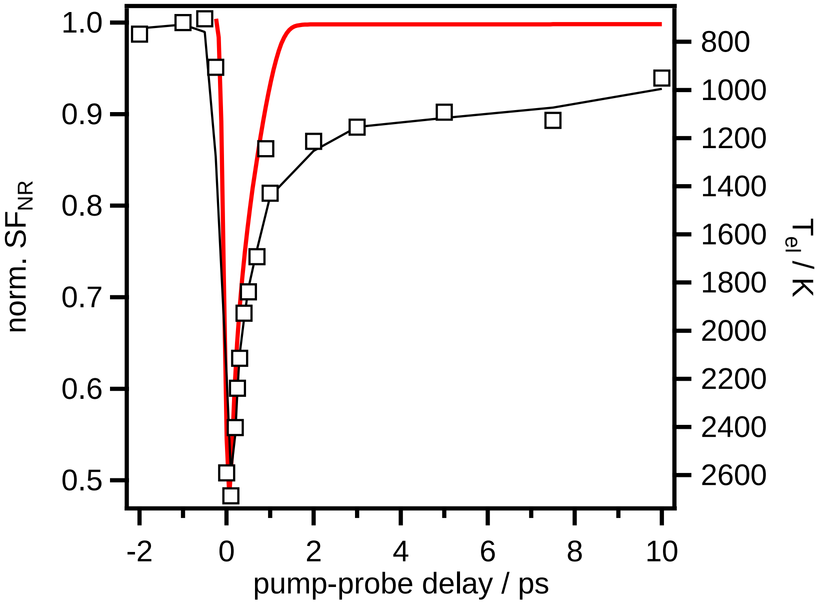

*Figure 6.7:* Comparison of $SF_{NR}$ reduction signal and the copper electron temperature for 2.3 eV pump of fluence 40 J·m$^{-2}$.

for a Cs layer on Ir(111) [65] and could be attributable to a temperature-dependent susceptibility or alternatively temperature dependent Fresnel factors.

This has been discussed in detail for copper, silver and gold surfaces by Hohlfeld *et al.* [287, 288].

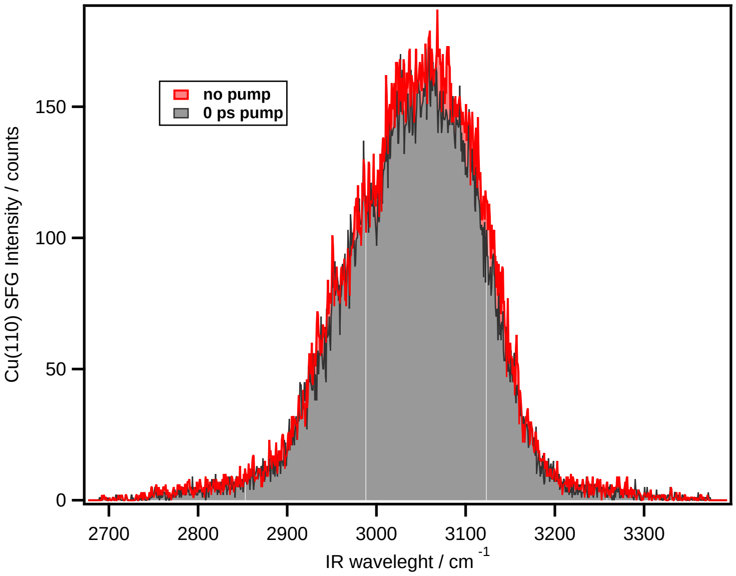

*Figure 6.8:* Effect of 2.3 eV pump (~ 40 J·m$^{-2}$) on Cu(110) SF spectra, red trace no pump and grey trace pump at 0 ps.

They carried out time resolved pump, SHG probe measurements at 625 nm and concluded that the SHG transients seen on copper were caused by temperature-dependent Fresnel coefficients, while those on silver and gold were caused by temperature dependent $\chi^{(2)}$. Their pump intensities were much higher than those used in our experiments - they report lattice temperature rises by ~500 K, whereas our lattice temperature increases by less than 50 K (see left figure 6.1). It is therefore highly unlikely that electron temperature is the cause of our transients.

In addition, we carried out the same experiment on a clean Cu(110) surface. Figure 6.8 shows the nonresonant background for no pump and for pump at time zero. We observe a reproducible distortion of the nonresonant background to higher frequencies which is only detectable when the pulses are overlapped in time.

The cause of the distortion is not quite clear, but could be related to the pump pulse changing the occupied DOS near the d-band edge which could impact on the efficiency of the SFG process. The pump pulse cannot influence the surface state as its energy is above (2.33 eV) the transition energy at the $\bar{Y}$ point ($\Delta$E = 2.27 eV according to Sonoda [175]).

### Energy dependence

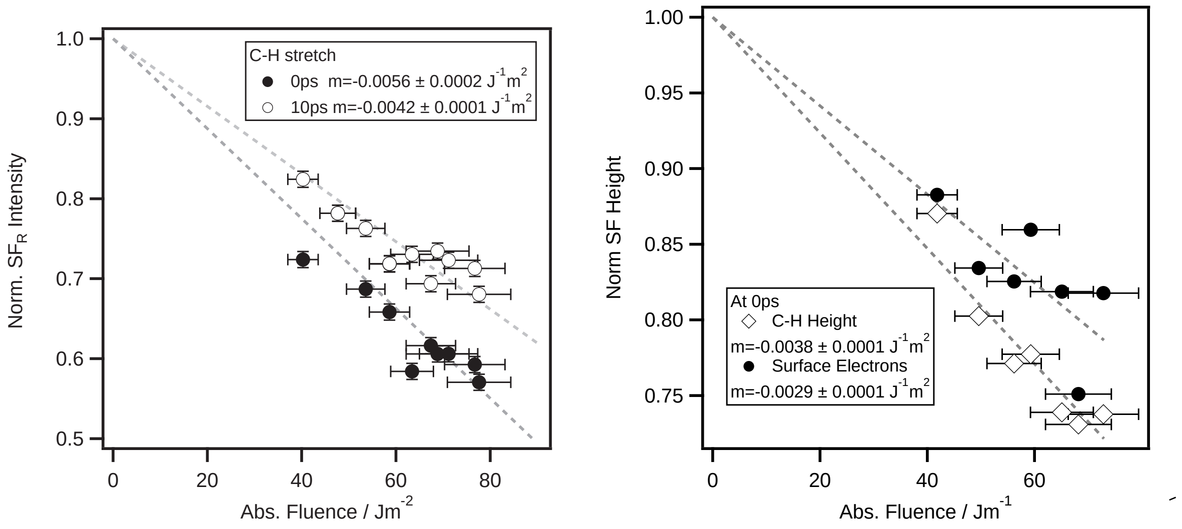

*(a)* SF$_R$ C-H stretch

*(b)* SF$_{NR}$ and SF$_R$

*Figure 6.9:* 2.3 eV pump effect as a function of energy on pyridine 1 ML on Cu(110) at 100 K. Left: Fluence dependence of the C-H intensity at 0 ps and 10 ps (resonance-only spectra with time-shifted visible probe). Right: Fluence dependence of nonresonant and resonant intensities recorded at 0 ps time delay (IR and visible probe overlapped in time). In the inset, *m* is the gradient of the linear fit.

In order to discover the mechanism behind the transients shown in figure 6.6, we have varied the fluence of a 532 nm pump pulse and recorded changes to the resonant intensity at 0 ps and 10 ps delays and changes to the nonresonant intensity at 0 ps delay, graphs shown in figure 6.9. The two data sets were acquired on different days. The overlap between pump and probe pulses was achieved in different ways: for the figure 6.9a data set we achieved overlap by optimising the DFG on the clean Cu(110) surface, for the figure 6.9b data, overlap was initially achieved by observing pump and probe pulses with a camera and then tweaked by observing the reduction in the pyridine signal. The first method achieves much better and more reproducible overlap, which is the reason for the lower gradient of the C-H signal with fluence in the right hand graph. It should also be noted that the actual beam size could have been slightly different on the two days.

Returning to the data we see that the fluence dependence of all transients (fast nonresonant, fast and slow resonant ones) is linear with fluence. If the transients were somehow coupled to the electron temperature, we would expect a nonlinear behavior reflecting the range of $T_{e,max}$ with fluence.

This question cannot be fully decided from the data as the fluence range was relatively limited both by OPA output power and by the surface damage threshold which prevented a tighter focus.

### 6.3.2 Pump effects on pyridine C-H vibrational mode

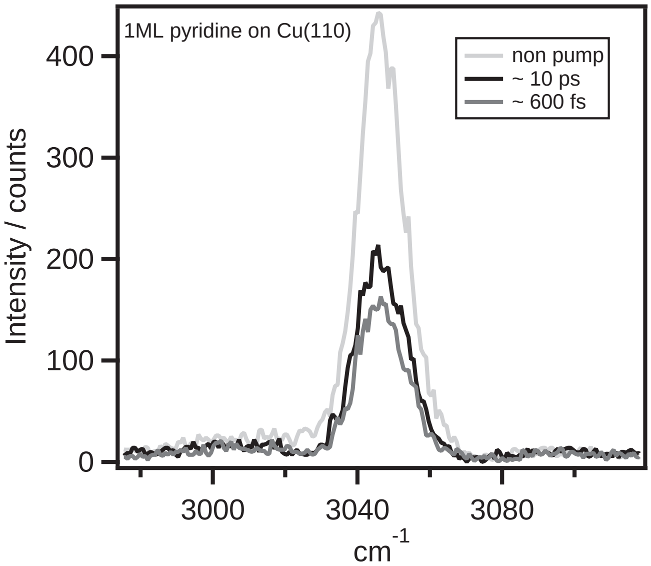

*Figure 6.10:* $SF_R$ typical spectra (light grey line), 2.3 eV reduction effect at ∼600 fs (dark grey line) and ≈ 10 ps (black line) on the C-H resonance of 1 ML of pyridine on Cu(110) at 100 K.

In this section, the effect of a visible pump ($\sim$ 45 J$\cdot$m$^{-2}$ absorbed fluence) on the C-H stretch is analysed as a function of different parameters: pyridine coverage, different pump wavelengths and pump polarisation. In these experiments, the 800 nm probe arrives $\sim$600 fs later than the IR to only study the effect on the C-H resonance. All the spectra shown are taken at 100 K and at a base pressure of $\sim 3{\cdot}10^{-10}$ mbar.

Figure 6.10 gives a general impression of the SF$_R$ signal at different time delays. The reduction is maximal at $\sim$600 fs(black line), while the light grey spectrum corresponds to no pump.

### Dependence on coverage

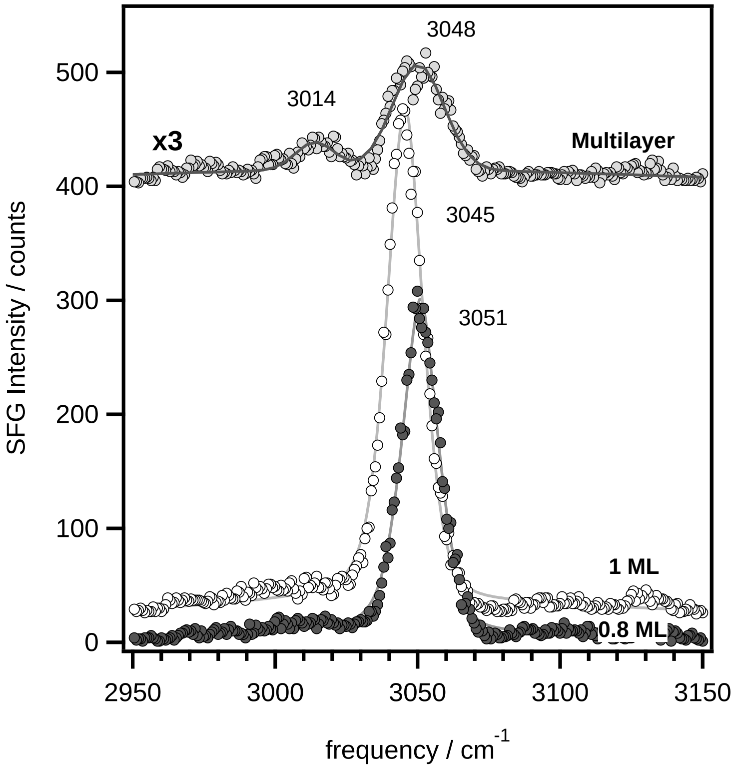

*Figure 6.11:* C-H SF spectra for different coverages of pyridine on Cu(110) at 100 K.

Figure 6.11 shows SF$_R$ spectra taken for those coverages, where the pump effect is studied. In the multilayer, two peaks are observed and the spectrum shown has been acquired for 3 times longer than the other spectra. The 1 ML spectrum has the most intense peak, indicating a well-ordered layer [227] even though the peak shape is clearly Gaussian and not Lorentzian. For a 20% lower coverage, the C-H peak is less intense and shifted to higher frequency, in accordance with the results presented in the previous section (see sec. 5.3). The pump-probe results for these layers are shown in figure 6.12.

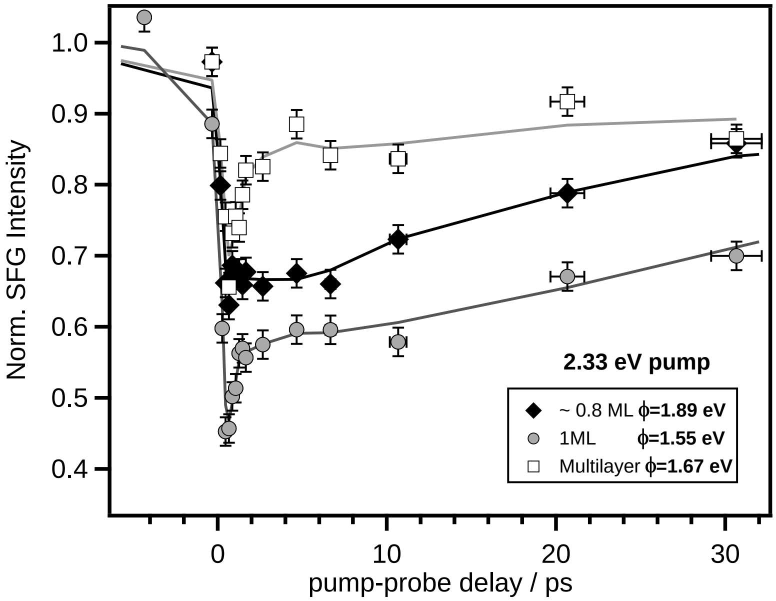

*Figure 6.12:* 532 nm-pump- C-H SF-probe as a function of Pyridine coverage on Cu(110) at 100 K.

The multilayer transient corresponds to the 3048 cm$^{-1}$ peak from figure 6.11. The 3014 cm$^{-1}$ peak is analysed separately. A fast transient is observed for all the coverages; the maximum effect is observed for the 1 ML transient, where the C-H stretch SF signal is reduced by half (see figure 6.10). At 0.8 ML, a reduced effect is observed. The slow transients are observed for all coverages and last for more than 10 ps. The largest effect at long delays is observed for 1 ML followed by 0.8 ML and the multilayer.

The work function for these layers is different, and in general is lower than the pump photon energy. Multilayer and 0.8 ML transients have similar work function but show different effects, especially at long time delays.

As mentioned earlier, in none of these experiments do we find any significant changes in peak frequency or linewidth. An exception to this observation is the second C-H peak at 3014 cm$^{-1}$ in the multilayer which is presumably due to mode (b) shown in figure 5.3. In this mode the 4-hydrogen moves out of phase with the other hydrogens. Alternatively, this peak stems purely from pyridine in the multilayer, but since the main C-H mode of the adsorbate is shifted down in frequency from the gas phase, we would expect pyridine in the second layer to have a higher frequency than in the first layer. This peak shows an upward frequency shift of $\sim$ 3.5 cm$^{-1}$ and clear peak broadening. The observed transient has a similar shape to the CO frequency transients discussed in the previous section (overlaid

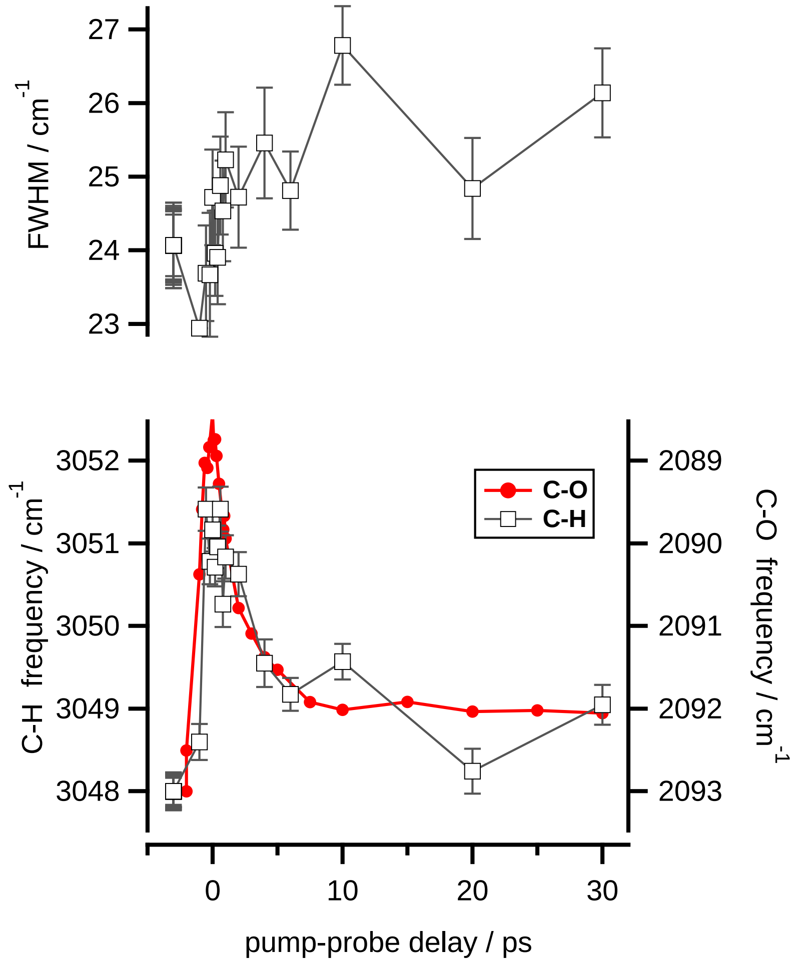

*Figure 6.13:* Frequency blue-shift observed for 3048 cm$^{-1}$ C-H peak of the pyridine multilayer coverage (left bottom axis) in comparison to the CO red-shift (right bottom axis) for similar 2.33 eV fluence pump on Cu(110) at 100 K. Top left: FWHM of the C-H transient.

in figure 6.13).

We are not able to determine determine $\tau_e$ and $\tau_l$ for this peak though, since we could not change our base temperature over a wide enough range to obtain the necessary static input data. Comparison to the CO transients however permits to make the qualitative statement that this peak couples more weakly to the lattice than CO, which could be related to its origin in the multilayer rather than the monolayer. *The most unusual fact is that the frequency shifts to the blue, unlike all reported transients of CO or NO.* This could be related to a weakening of the pyridine (multilayer) to pyridine (monolayer) band and indicate the molecules frustrated attempt to desorb.

This briefly sum up this section: *we see a fast response for various coverages though its magnitude is strongly coverage dependent. A slow response is also seen for all coverages with a magnitude that depends differently on coverage than the fast response. The main C-H vibrational mode shows no significant changes in frequency or linewidth. A second mode becomes visible in the multilayer, which possesses clear frequency and linewidth transients.*

### Dependence on pump wavelength

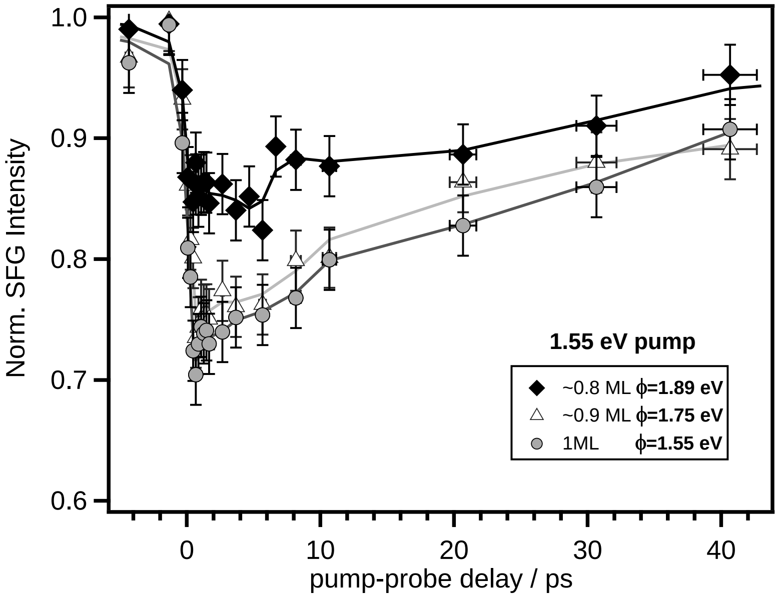

*Figure 6.14:* 800 nm pump- C-H -SF-probe as a function of pyridine coverage on Cu(110) at 100 K.

Studying the pump wavelength dependence can decide whether the observed effects are due to hot electrons or electronic transitions. If hot electrons are involved, then for similar pump fluence, ie. similar temperatures reached, one expects to see similar effects. On the other hand, if an electronic transition is involved, then the effect depends strongly on the photon energy.

Figure 6.14 shows the C-H vibrational intensity for different coverages recorded with a near-IR pump energy of 1.55 eV (800 nm). The absorbed fluence was similar to figure 6.12. In this case the multilayer was not studied. As in the previous section, lower coverage in the monolayer means less effect, however, for this pump wavelength the fast transients are nearly invisible. This photon energy is lower than or at most equal to the work function of the three coverages.

### Dependence on pump polarisation

We varied the polarisation of the green pump pulse for a 1 ML pyridine layer on Cu(110) at 100 K, as shown in figure 6.15 we chose p-polarisation, s-polarisation and polarisation aligned with the $[1\bar{1}0]$ direction. The polarisation was rotated before the final turning mirror into the vacuum chamber. At the given incidence angle of $\sim 60°$ off the surface normal and using the bulk refractive index values for copper [289] $\sim$23% for s-polarised light is absorbed versus $\sim$52% of p-polarised light. If the polarisation plane is along the $[1\bar{1}0]$ direction, then given the orientation of our crystal (figure 4.1) we have a mixture of $\sim$25% p-polarisation and $\sim$75% s-polarisation and $\sim$30% of the incoming beam should be absorbed.

Figure 6.15 very clearly shows that the depth of our transients does not scale with absorbance fluence even though the fluence dependence (previous section) is linear!

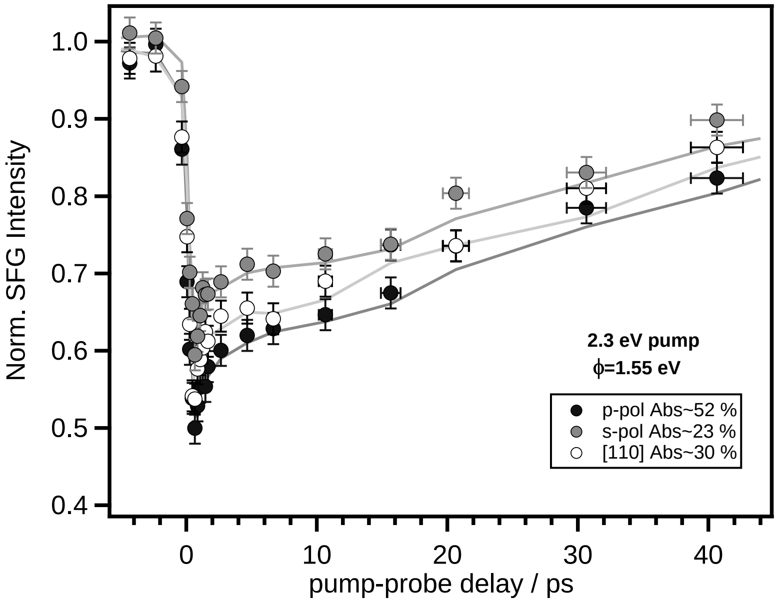

*Figure 6.15:* Dependence of transients on pump polarisation. Incoming pulse energy is fixed, polarisation is varied, leading to the absorbances indicated in the figure. 2.33 eV pump on 1 ML/Cu(110).

### Adsorbate orientation

One of our initial theories for the cause of the C-H intensity reduction was a tilting of the molecular plane against the surface normal. This would reduce the IR transition dipole as well as the Raman component of the SF process and lead to a reduced signal. A tilt should become visible if the ssp polarisation component is chosen [290].

An unpumped pyridine SFG spectrum shows no signal for ssp, neither do spectra recorded at 0 ps and 10 ps delay, therefore the signal reduction cannot be explained by dynamic tilting of the molecule

## 6.4 Discussion

At first glance the resonant and nonresonant transients had a similar character to those reported for adsorbed CO or NO, where the two timescales stem from coupling to a hot electron bath, followed by coupling to a hot lattice. A closer inspection however reveals that the standard model does not explain these transients.

Before entering into the detailed discussion we will summarise briefly our final explanation to act as a guide: *A green pump photon creates a negatively charged pyridine with a relatively long but coverage-dependent lifetime. A particular polarisation is required for excitation. In the excited state, we no longer have (electronic) resonant enhancement of the SFG process thereby reducing both resonant and nonresonant signals. Upon deexcitation, the pyridine layer disorders and due to the low base temperature the disorder can survive for tens of picoseconds. Disordering is suppressed in the first layer if a multilayer covers it due to steric hindrance. A near-IR pump pulse can just about excite some electrons into the negative ion resonance, leading to much reduced disorder.*

### 6.4.1 Coupling to hot electrons and hot lattice?

The CO transients presented in section 6.1 were recorded for a similar fluence as that used in figure 6.6. At long delay times we could cross-check the TTM calculation by converting the measured frequency shift into a lattice temperature. The result is a $\Delta T_{lat}$ of about 30 K at 10 ps delay and no more than 100 K at the highest fluence. There is no change in static pyridine SFG spectra between 100 K and 200 K base temperature, making a transient temperature increase an unlikely source for the transients. Moreover, as shown in figure 6.12, we recorded similar spectra for slightly lower pyridine coverages and with some pyridine in the $2^{nd}$ layer and found that the transient shapes were strongly coverage dependent, which again points against temperature. In addition, the nonresonant background is only reduced when pyridine is present on the surface. For a bare copper surface, pumping by 2.33 eV photons merely distorts the shape of the nonresonant spectrum but does not reduce it, excluding temperature-dependent susceptibility or Fresnel coefficients as a source.

We have recorded the fluence dependence of the C-H stretching feature and the nonresonant background at fixed delay times of 0 ps and 10 ps and find them to increase linearly with fluence. The slope of the C-H intensity with fluence 10 ps is 60% of the slope at 0 ps. The lattice temperature rise at 10 ps is only of the order of 1-2% of the electron temperature increase at 0 ps, making coupling to hot electrons and lattice in a similar fashion to CO unlikely. Strong coupling to hot electrons, as the timescale of the transients might suggest, would be seen in such a plot as a nonlinear dependence of the 0 ps data on fluence [65]. The limited fluence range investigated however would not necessarily result in a pronounced nonlinear dependence, therefore we cannot completely exclude hot electrons as source for the transient.

### 6.4.2 Spectrum of excited electrons

In order to explain the recorded transients, we consider over which energy range a green pump pulse produces excited electrons (similar to chapter 3). A calculation by Germer *et al.* [142], integrating over the whole SBZ for Cu(001), shows that a 579 nm pump pulse only efficiently generates hot electrons up to 0.5 eV above the Fermi level. These electrons originate in the Cu d-band. Much smaller numbers of hot electrons from excitation from the sp-band are generated up to 2.33 eV above $E_F$. The ratio of occupied states at the Fermi level to those at 2.33 eV below $E_F$ is 0.01 ( an approximate value from UPS figure 6.16).

The work function of the pyridine covered Cu(110) surface is extremely low with 1.46 eV, therefore, a green pump pulse also produces a significant number of photoelectrons with kinetic energies up to 0.78 eV. For the lower coverage investigated, the kinetic energy is 0.44 eV, for the multilayer coverage 0.66 eV. These photoelectrons are generated at a range of energies where the unoccupied pyridine $\pi^*$ states have been found. Yates' group saw a broad excited electronic state by STS for lower coverage pyridine/Cu(110) centred around 2.3 eV [221]. Zhong *et al.* [254] detected $\pi^*$ states for 2 ML pyridine/Cu(111) at at 0.6 and 1.2 eV above the vacuum level (2.1 and 3.1 eV relative to $E_F$) and abroad, $\pi^*$-related state for submonolayer pyridine at 1.5 eV above $E_F$.

In the following we will discuss a number of possible scenarios to explain the observed transients.

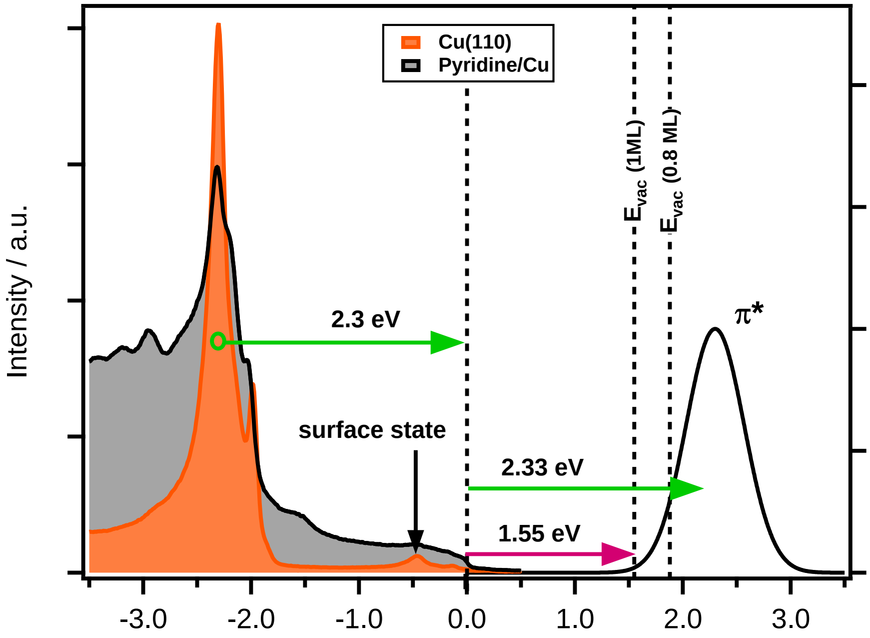

*Figure 6.16:* UPS spectra for pyridine (submonolayer coverage) and bare Cu(110) at 135 K. The STS-detected excited state is indicated.

### 6.4.3 Effect of photoelectrons

One possible cause of the transients are the photoelectrons we excite. We propose here that a fraction of these photoelectrons do not leave the surface but are captured within the pyridine layer with a lifetime of around 400 fs. This strongly reduces the nonresonant background because these electrons transiently increase the work function of the surface. For a mechanism, we can either think of the photoelectron and its image charge forming a dipole that opposes the one induced by pyridine. Alternatively, if the electron resides in the pyridine $\pi^*$ orbital, the work function would be reduced because the excited state dipole of pyridine opposes the ground state one. In either case, there is a strong connection between the pump reducing the nonresonant SFG signal and the reduction of pump-IR DFG by pyridine adsorption.

The fluence dependence of the 0 ps nonresonant data is linear, that is we see a one-photon process (with the caveat of limited fluence range mentioned above). A one-photon process is consistent with both mechanisms - each extra captured photoelectron reduces the work function by a constant amount.

For the nonresonant data, we assume that photoelectrons are created during the interaction with the 150 fs long pump pulse. Each photoelectron generated remains in the layer with a certain lifetime, then relaxes back. Fitting the transient will yield the lifetime of the photoelectron in the pyridine adlayer. For a quantitative evaluation, we need to establish the relationship between the number of electrons excited and the nonresonant background. Unfortunately there is no simple relationship. The coverage-dependent work function has a shape similar to that of alkali adsorption, while the nonresonant background increases with the square of the number of adsorbates, similar to the resonant signal. The results of chapter 4 showed that the nonresonant background is likely enhanced through an electronic resonance, even though we could not clearly identify the origin. This means we have to expect a more complex relationship between $\chi^{(2)}_{NR}$ and $\phi$ than usually assumed in the literature [291]. We will use the indirect relationship between SFG and $\phi$ shown in figure 5.9 to estimate how many photoelectrons have been captured in the layer. For example, at 1 ML coverage, the nonresonant background in figure 6.6 is reduced by the pump by 50%, then looking at the figure 5.9, this corresponds, a $\Delta\phi$ of -2.3 eV to a coverage of 0.5 ML, i.e. we have inserted 0.5 ML of photoelectrons into the layer.

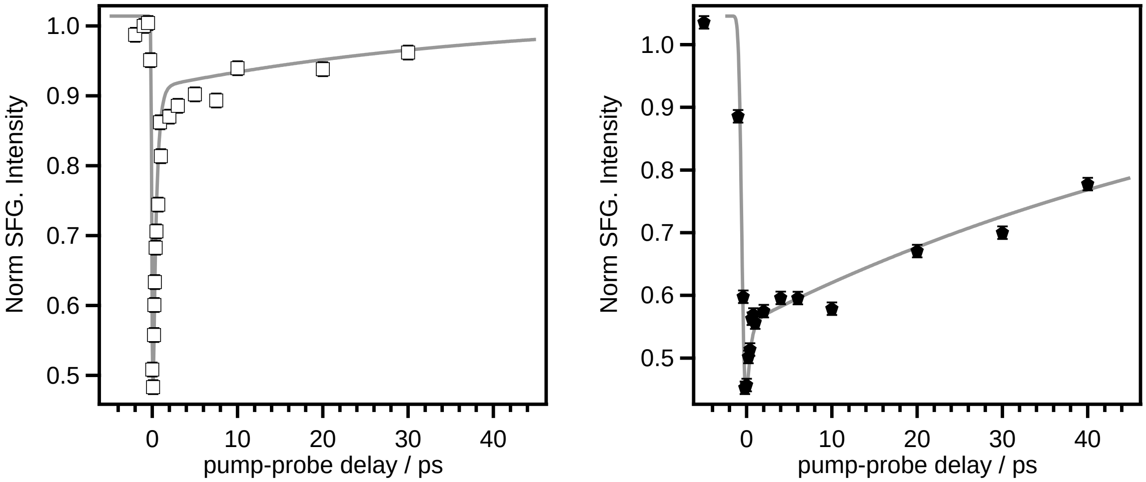

*Figure 6.17:* Phenomenological description of nonresonant (left) and resonant (right) transients by double exponential (solid lines). Data set from figure 6.6.

With an absorbed fluence of 45 J·m$^{-2}$ and 2.33 eV photons, we absorb 1.2 x 10$^{16}$ photons·cm$^{-2}$, that is 30 photons per pyridine molecule (at 1 ML = 4·10$^{14}$ cm$^{-2}$ coverage). We captured 0.5 ML photoelectrons, i.e. if each absorbed photon generates a photoelectron (maximum), then 1 in every sixty photoelectrons gets captured. This corresponds to a minimum cross section of 0.017/4 ·10$^{14}$ cm$^{-2}$=0.43 Å$^2$.

If this model is correct for the nonresonant background, then the fast transient arises from an instantaneous onset (transfer of charge) with an exponential decay (lifetime of excited state) broadened in time by the laser pulse.

Such a model results in a lifetime of 400 fs for the excited state, as shown in figure 6.17. A more typical value for the lifetime of an electronically excited state at a metal surface would be a few femtoseconds at most, though it can reach tens of femtoseconds if the surface has an appropriate surface band gap (see [143, 292]). While 400 fs would indeed be a long lifetime for a pyridine anion, a state that is related in character to an anion is a dipole-bound electron, an electron held by the dipolar field of the molecule. These states require a dipole moment of $\sim$2.5 D to exist. Gas phase pyridine is 2.15 D dipole moment cannot bind an electron in this way, but the surface enhances the dipole moment to more than 4 D and the close packing on the surface might mean that similar the gas phase, a cluster of molecules is needed to bind one electron [293, 294]. The excited state must require a certain polarisation of the exciting photon, otherwise the transients should scale with macroscopic absorbance.

We tried to compare the relative sequence of measured transients in figure 6.15 with the amount of polarisation projected along certain symmetry directions. The closest match is a projection along the $[1\bar{1}0]$ direction where 17%, 30% and 26% of incoming s-polarised, $[1\bar{1}0]$-polarised and p-polarised light is absorbed, respectively. This does not reflect the data entirely, but it should be noted that each polarisation requires optimisation of spatial overlap, which will also have an impact on the amount of reduction we see. At the moment we are not able to speculate any further on the nature of the excited state.

So far we have not addressed why this excitation would reduce the C-H stretch intensity as well. We have seen in chapter 4 that the nonresonant SFG is enhanced when our near-IR probe at 800 nm is mixed with IR light at 3200 nm, which also vibrationally excites the C-H stretch. If the SFG at this wavelength combination is resonant due to a transition involving an orbital of mixed metal-molecule character, then one would expect both resonant and nonresonant contributions to respond in the same way. This would explain why we observe such similar coverage dependencies for both resonant and nonresonant SF signals (see figure 5.6).

So, if the pump pulse shifts the resonance energy e.g. through excitation of a pyridine anion, which bonds differently to the copper surface [248] then both nonresonant and resonant transients should show the same response time.

This is indeed the case, only the resonant transient of figure 6.6 appears broader in time because it is measured with a time resolution corresponding to the $T_2$ time of the C-H stretch ($\sim$ 1 ps) whereas the nonresonant transient is measured with the time resolution of the IR probe pulse ($\sim$ 150 fs). We only detect changes in the intensity of the C-H stretch because removal of the SF resonance merely reduces $\chi^{(2)}$ but does not influence the resonance otherwise. According to Wu *et al.* [207] who studied enhancement of particular vibrational modes in SERS, the C-H stretch is not sensitive to the metal-adsorbate interaction. This interaction impacts more on the ring breathing mode and the ring asymmetric deformation.

The C-H transient is reduced at lower coverages than 1 ML (figure 6.12) either because the excited state energy or the lifetime are coverage dependent. If we use 800 nm light as the pump source, figure 6.16 shows we can only excite electrons into the tail of the resonance. Their lifetime could be much reduced because they are being generated below the vacuum level.

Let's finally come to an explanation of the slow part of the transients: we suggest that this is due to electron-induced disordering as seen for benzoate on Cu(110) [295–298]. The dynamics of the benzoate disordering has been shown to be due to capture of electrons into relatively high-lying orbitals (7-8 eV above $E_F$). A suggested mechanism for disorder was the trapping of an electron into the phenyl ring, a sudden transition to a negative ion potential energy surface and escape of the electron into vacuum or the surface, leaving the ring vibrationally excited. The vibrational excitation relaxes in part by transferring energy into a frustrated translational mode, which leads to disorder. The disordered state is not thermodynamically stable, since the phenyl ring-ring interaction strongly favors an ordered structure, so it gradually reverts back to the ordered state. If a similar process occurs in our case, then the reason we do not see the characteristic timescales of vibrational energy transfer in our transients (> 1 ps) lies in the detected mode. The C-H stretch frequency could simply be quite insensitive to vibrational excitation of the ring, since ring substitution in the 2 or 3 positions hardly shifts the frequency.

The disorder (C-H intensity) recovers with a timescale of 40 ps. This relatively fast recovery[1] indicates that the changes in the layer are not extensive. A possible disordering mechanism could be

---

[1] compared to the case of benzoate which requires minutes to re-order

twisting of the ring rather than actual translation, as seen by ESDIAD with increasing coverage.

## 6.5 Conclusions

This chapter has shown what happens when you study a more complex molecule with pump-probe spectroscopy- you obtain highly complex results which need careful analysis in order to obtain a coherent picture of the dynamics. We repeat here our earlier summary: A green pump photon creates a negatively charged pyridine with a relatively long but coverage-dependent lifetime. A particular polarisation is required for excitation. In the excited state, we no longer have (electronic) resonant enhancement of the SFG process thereby reducing both resonant and nonresonant signals. Upon deexcitation, the pyridine layer disorders and due to the low base temperature the disorder can survive for tens of picoseconds. Disordering is suppressed in the first layer if a multilayer covers it due to steric hindrance. A near-IR pump pulse can just about excite some electrons into the negative non resonance, leading to much reduced disorder.

Our explanation does not currently answer all questions. We do not know the precise nature of the excited state- is it an anion or is it is a dipole-bond electron? The long lifetime indicates it is an adsorbate-localised state that only weakly couples to the copper electrons but our particular copper surface does not have a band gap that extends across the whole SBZ, so this is unexpected.

We are collaborating with theorists in order to learn more about the system, but at the time of writing DFT cannot reproduce the measured work function change or simulate a negatively charged adsorbed pyridine. These results therefore present a challenge to theorists! Further studies, especially of lower frequency modes, like the pyridine ring breathing one, would be highly desirable.

# Surface Enhanced Photochemistry

Chapter 7

# Plasmons and photochemistry

One of the challenges of photochemistry in the last few years, is its use for cleaning air and water, as well as energy production. For the scope of this thesis, photochemistry on metal surfaces offers new pathways, as it is mainly dependent on the substrate optical properties rather than the adsorbate ones, which tends to shift photoreactivity to lower energies due to the adsorbate-metal bonding. In thinking about how to enhance the photochemistry, the plasmon comes onto the scene as a possibility to enhance the photochemistry yield by the absorption of light and consequently, creation of more electron hole pairs, which play a central role in a photochemical reaction.

For now let's simply think about a plasmon as a collective excitation of the metal free (conduction) electrons. Surface plasmons will be introduced properly in the next section.

The conditions for a plasmon resonance depend on the optical properties of a metal. These are often described with the help of the frequency-dependent dielectric constant

$$\epsilon(\omega) = \epsilon_1 + i\epsilon_2 \ ,$$

If $\epsilon_1$ is positive and real, then electromagnetic waves propagate within the metal without damping, if $\epsilon_1$ is negative, waves are totally reflected. The imaginary part ($\epsilon_2$) of $\epsilon$ describes damping effects.

For a free electron gas in the UV to near-IR region, the variation of $\epsilon$ with frequency was first explained by Drude. The real part has low values for high energies, becoming more negative towards the IR which explains the high reflectivity of the metal in this region.

The imaginary part of $\epsilon(\omega)$ reflects the presence of intra- and interband transitions. Figure 7.1 shows

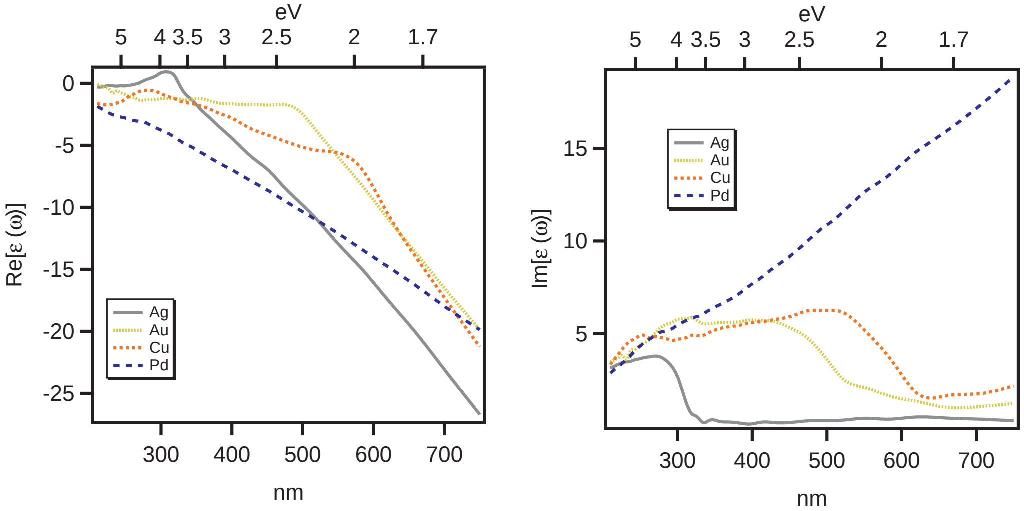

*Figure 7.1:* Dielectric constants of various metal

the real and imaginary part of $\epsilon$ for various metals. The onset of interband transitions can be seen by the step-like behavior of Im[$\epsilon(\omega)$] for the noble metals.

The real part of $\epsilon(\omega)$ determines the resonance condition for a plasmon, for example for metallic spheres in air the resonant condition is:

$$Re[\epsilon(\omega_p)] = -2 \; , \tag{7.1}$$

For noble metals this condition is fulfilled in the visible region. The plasmon resonance will be particularly strong if at $\omega_p$ the imaginary part is quite small. Looking at figure 7.1, this is the reason why silver can support strong plasmons resonances: Re[$\epsilon(\omega)$]=-2 and Im[$\epsilon(\omega)$]≈0.

For Au and Cu, the resonant condition is fulfilled at 490 nm and 366 nm, when the imaginary parts are 4.10 and 5.3, respectively. As Im[$\epsilon(\omega)$] has larger values, the nanoparticle resonance shifts away from the Re[$\epsilon(\omega)$]=-2 and now occurs around 520 nm (Au) and 580 nm (Cu). The plasmon resonance condition is strongly affected by the size and shape of the object it is excited in and has been shown to be tunable right across the visible to near-IR range in silver nanoparticles arrays.

We originally chose copper as a substrate to study plasmon-enhanced photochemistry on for several reasons. Firstly, it permits plasmon excitation in the visible (yellow-orange) region of the spectrum. Secondly, it is chemically more active than Ag and Au and thirdly, the relative abundance of copper on earth is 100 (1000) times higher than Ag(Au) making it comparatively cheap.

In this chapter, we explore the field enhancement obtainable from sub-wavelength surface structures of Ag and Cu with the help of finite-element modeling. Since field enhancement of the electric field shows the plasmon resonance condition, the average field on the surface is calculated for our Cu crystal for a range of possible nanostructures created by ion-sputtering, as an example of a UHV compatible patterning technique [46–49].

Finally, this study provides insights into the plasmon enhanced photochemistry of adsorbates, discussing a possible tuneability either by shifting the plasmon resonance via modifying the shape and size of the nanostructure, or by substituting different functional groups on the molecule, which shifts the LUMO and HOMO levels with respect to the metal [28], opening new reaction pathways.

## 7.1 Surface versus localised plasmon polaritons

In this section, a brief description of the theory of surface plasmons is presented in order to understand how plasmon excitation is related to the field of enhanced photochemistry.

The dielectric response of a metal is mainly governed by its free electron plasma, first modeled by Drude in 1900 [299]. According to this theory, the frequency dependent dielectric constant $\epsilon(\omega)$ can be written as

$$\epsilon(\omega) = 1 - \frac{\omega_p^2}{\omega(\omega + i\gamma)}, \tag{7.2}$$

where $\omega_p$ is the plasma frequency (typically $\sim$ 10 eV), $\gamma$ is the absorption, and $\omega$ the frequency of the incident wave. The most important application of this relation is to describe the propagation of electromagnetic radiation in a metal. For frequencies smaller than the plasma frequency, the real part of $\epsilon$ is negative and this condition allows a propagation of surface electromagnetic modes called surface plasmon polaritons (SPP) [300]. These EM modes propagate along the interface, and can be described as a surface charge oscillation, where the energy is trapped on the interface. The SPPs owe their existence to the interface and consequently, this excitation can be detected by a minimum in the reflectivity. SPPs are a transverse magnetic (TM) solution of Maxwell's equations for a dielectric $\epsilon_1$-metal $\epsilon_2\,(\omega)$-interface, as well as assuming that the electric charge density appearing in Maxwell's equations vanishes both inside and outside the metal [300]. The electromagnetic fields of these modes are given by:

$$\begin{aligned} E_x &= E_{x2} e^{i(k_{x2} x)} e^{-k_{z2} z} \\ E_z &= E_{z2} e^{i(k_{x2} x)} e^{-k_{z2} z} \\ H_y &= H_{y2} e^{i(k_{x2} x)} e^{-k_{z2} z} \end{aligned} \tag{7.3}$$

The dispersion of these modes can be obtained from the appropriate boundary conditions (see appendix D for a detailed description), yielding:

$$k_x = \frac{\omega}{c} \sqrt{\frac{\epsilon_1 \epsilon_2(\omega)}{\epsilon_2(\omega) + \epsilon_1}} \; . \tag{7.4}$$

One wants to examine in detail the dispersion relation in figure 7.2, which links the frequency $\omega$ to the tangential wavevector k$_x$, to realise that surface modes exist for all frequencies at a dielectric-metal interface, and that these modes are associated with the surface charge wave density, created by the discontinuity of the normal vector of the electric field. However, only the evanescent and propagating modes will correspond to actual SPPs.

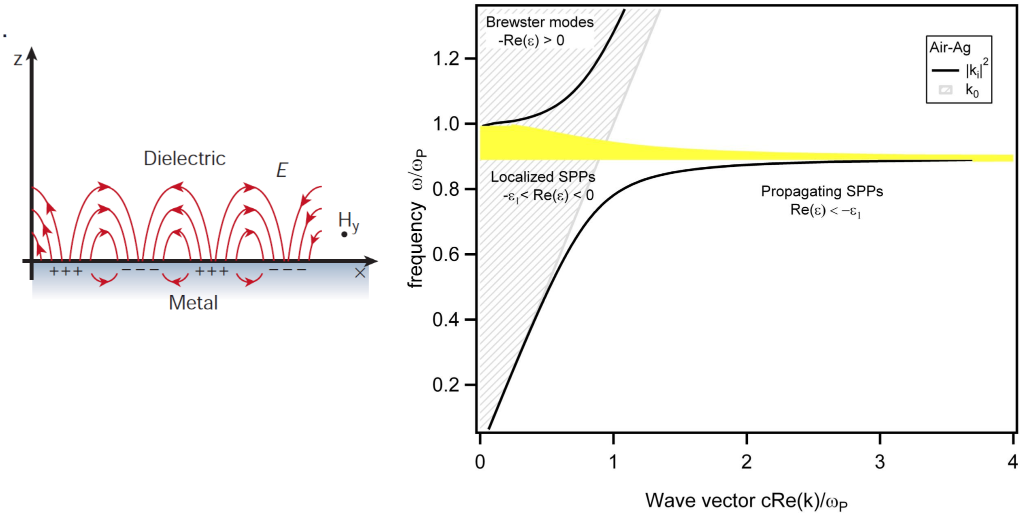

*Figure 7.2:* On the left, SPPs as a surface charge wave propagating along the interface, from reference [301]. On the right, SPP dispersion relation for the surface modes of an Air/Ag interface. The plot is shown in terms of dimensionless quantities $\frac{\omega}{\omega_p}$ and $\frac{Re(k_x)}{\omega_p/c}$. The area covered by the dispersion relations of the incident photons is shown as a patterned area. It corresponds to k$_x$ < k$_0$.

The difficulty in the interpretation of this graph comes from the ambiguity of the change of sign of the complex dielectric constant of the metal for the different frequencies. Let me explain figure 7.2 for the different frequency regions:

- for higher frequencies, $\epsilon_2(\omega) > 0$ and the metal behaves as a dielectric, in other words, metals are transparent in the UV region. SPPs in this region are called Brewster's modes.

- if $-\epsilon_1 <$ Re[$\epsilon_2(\omega)$] $< 0$, allowed frequencies are just below $\omega_p$, and $\mathbf{k}_{plasmon}$ is purely imaginary. This region is represented by the yellow shadow in figure 7.2. That means there is no propagation along x, and the energy from this *evanescent* surface wave is dissipated into a *radiative mode*. To excite this mode one needs $\mathbf{k}_x \approx 0$, however, the resonance condition is broadened, as is shown by the height of the yellow shadow. These are localised SPPs.

- finally, if Re[$\epsilon_2(\omega)$] $< -\epsilon_1$ the wave propagates along the interface (x) and is evanescent along the normal to the surface (z). These are *non-radiative* modes, so-called propagating SPPs. The energy is trapped within the interface, as depicted on the left of the figure 7.2.

Now, how do we excite the plasmons by a incident wave? Looking at the hatched area of the figure 7.2, which corresponds to the light cone $k_\circ = \omega/c$, we see that the SPPs momentum is always higher than the light momentum. Consequently, the light needs extra momentum to excite the SPP. This can be obtained by different configurations. One of the most common light-plasmon couplers is *total internal reflection* (TIR). This optical device has been studied since 1968 [302, 303], indeed, plasmon-enhanced photodesorption by UV-light was studied in TIR configuration [304, 305]. Another method to couple light into a SPP is to pattern the metal surface with a shallow grating of grooves or holes as diffraction off the grating imparts additional momentum to the light wavevector. This plasmon resonance has been studied to optimize grating parameters in order to control this propagating mode [26, 306, 307]. SPPs can propagate on corrugated metal surfaces as well [308], where enhanced photochemistry has also been reported [56, 127, 309, 310]. SPP modes are frequently just called surface plasmons in the literature and there is much confusion on the precise nature of the mode described. So let me now introduce another member of the plasmon family properly: the localised surface plasmon polariton (LSPP). When the size of the metallic feature is comparable to the wavelength of the light, the planar approach described before (see appendix D) fails. Like a particle-in-a-box the solutions are photon modes highly localised inside the cavity. Mie in 1908 already solved the problem of light interaction with metallic nanospheres [311], considering the quasistatic approximation and solving Laplace's equation, whose solutions are spherical harmonics. The radial solutions are of the form $r^l$ and $r^{l+1}$, and, for example, for l=1 the field in x direction outside the sphere is:

$$\mathbf{E_{out}} = E_\circ \mathbf{u_x} - \alpha E_\circ \left\{ \frac{\mathbf{u_x}}{r} + \frac{3x}{r^5} \left( x\mathbf{u_x} + y\mathbf{u_y} + z\mathbf{u_z} \right) \right\} , \tag{7.5}$$

where $\alpha$ is the polarizability and $\mathbf{u_i}$ are the unit vectors (i=x,y,z). Notice the first term is the applied electric field, and the second is the induced dipole field resulting from the polarisation of the conduction electrons. This mode is radiative, and therefore one can obtain the dipolar polarizability induced in the metal nanosphere. In general, the polarisability of a nanoellipsoid can be described as follows [37, 312–314]:

$$\alpha(\omega) = \frac{V_p}{4\pi} \frac{\epsilon_2(\omega) - \epsilon_1}{\epsilon_1 + L(\epsilon_2(\omega) - \epsilon_1)} \ , \tag{7.6}$$

where V$_p$ is the volume of the ellipsoid, and L is the geometric factor [37, 315]. From equation 7.6, there is a resonant condition when the denominator tends to 0, which corresponds to the LSPP mode and, therefore, depends on the metal properties $\epsilon_2\,(\omega)$, the surrounding medium $\epsilon_1$ and the size of the ellipsoid. The size and the shape will play an important role in the resonance frequency and the field enhancement (which is proportional to polarisability). For nanospheres with a radius smaller than 10 nm, the resonance condition is Re[$\epsilon_2\,(\omega)$]=-2$\epsilon_1$; these come back to the discussion presented in the introduction about the relation of the plasmon excitation with the negativity of Re[$\epsilon_2\,(\omega)$] (see figure 7.1 to see the different resonant frequencies for the noble metals). For larger particles, the quasistatic approximation must be corrected due to the retardation effects of the field inside the nanoparticle, which is called the modified long wavelength approximation (MLWA) , where the polarisation is described as [312, 316, 317]:

$$\alpha'(\omega) = \alpha(\omega)\left[1 - i\frac{k^3}{6\pi d}\alpha(\omega) - \frac{k^2}{2\pi}\alpha(\omega)\right]^{-1} \ . \tag{7.7}$$

As the distribution of charge is not homogeneous anymore, secondary radiation effects from the higher order multipoles become more important. The k$^2$ term accounts for the depolarization of the radiation across the particle surface due to the finite ratio of the particle wavelength to the size d (major axis). This term redshifts the frequency as the particle size increases. The k$^3$ term describes the radiative damping, which broadens the LSPP resonance. For the scope of this thesis, we are interested in how many more electron-hole (e-h) pairs will be generated when more light is absorbed by LSPPs [318]. For this purpose, we need to calculate the absorption cross section $\sigma_{abs}$, which is given as the difference between extinction and scattering cross sections ($\sigma_{ext}$, $\sigma_{sca}$). The relationship between the cross sections and the polarisability is as follows:

$$\begin{aligned} \sigma_{abs}(\omega) &= \sigma_{ext}(\omega) - \sigma_{sca}(\omega) \\ \sigma_{ext}(\omega) &= k\, Im\left[\alpha'(\omega)\right] \\ \sigma_{sca}(\omega) &= \tfrac{k^4}{6\pi}\left|\alpha'(\omega)\right|^2 \end{aligned} \tag{7.8}$$

These equations have been used to describe the field enhancement for different nanoparticle or rough surfaces as well as the huge cross section obtained in surface-enhanced Raman spectroscopy (SERS) [13, 314, 316]. We will use these equations later to discuss enhancement of photochemical cross sections.

## 7.2 Motivation: surface plasmon enhanced photochemistry on nanostructured surfaces

Surfaces can be described as the playground of the molecules, offering the molecules a lower energetic pathway to react. The presence of a metal surface opens up a rich range of electronic excitation and relaxation mechanism for the adsorbate when interacting with light. This process induced by the attachment of a photoexcited substrate carrier to the adsorbate is called **substrate induced photochemistry** [319]. Different responses arise from the interaction of light with the metal-adsorbate system such as photodesorption, diffusion or photodissociation. A wide range of examples are found in the literature; especially NO photochemistry is extensively studied either on metal or semiconductor surfaces [29, 57, 130, 319–321]. Figure 7.3 describes a schematic representation of the energy levels of the metal adsorbate system and the plasmon enhanced photochemistry. When the metal absorbs a photon, e-h pairs are generated, and the electron (or hole) tunnels through the barrier to the unoccupied state (or to the occupied state), producing the photochemistry. The photochemical yield depends on $\hbar\omega$, the position and width of the adsorbate resonances and the density of states of the metal. The lowest unoccupied molecular orbital (LUMO) and the highest occupied molecular orbitals (HOMO) of the adsorbate are also influenced by the bonding to the metal [28], and the energy difference between $E_F$ and HOMO or LUMO often allows visible photochemical processes to occur. Plasmon excitation is believed to enhance the creation of e-h pairs, enhancing the photochemistry [35, 127, 310]. This coupling between light, plasmons, and (e-h)-pairs has been investigated in detail for adsorbates [30, 56, 309, 310, 322]. On a flat surface, the photodesorption yield follows the trend of the absorption of light on Ag (grey squares in figure 7.4). Meanwhile, this rate changes if the molecule is adsorbed on a rough surface (blue circles), where at $\sim$350 nm an enhancement is observed. This wavelength matches with a nanoparticle LSPP excitation, in particles < 50 nm. Despite great experimental and theoretical development in the last 10 years in the area of nanofabrication of *plasmonic* surfaces [34], or SERS [37, 241], plasmon-enhanced photochemistry has not been fully developed. Part of the problem is that nanostructuring the surface to allow for light-plasmon coupling creates new adsorption sites on the metal substrate, which can also induce photodesorption [30, 323].

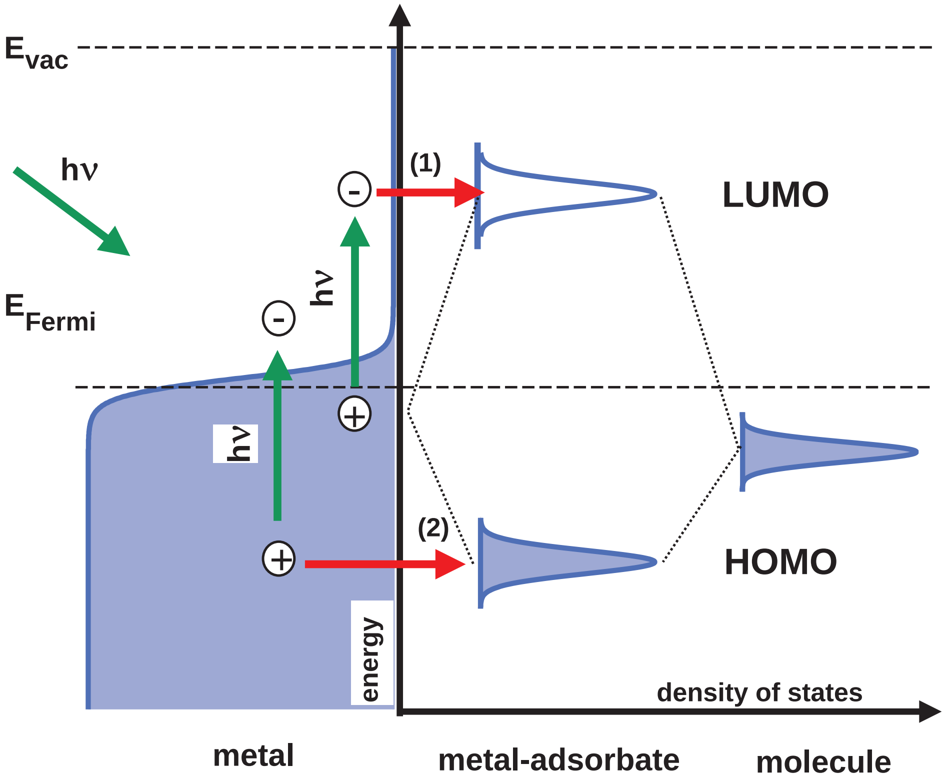

*Figure 7.3:* Energy levels of the metal-adsorbate system and two possible channels to enhance the photochemistry by **plasmon excitation**: the excited plasmon decays into an electron-hole pair (1), where the electron can tunnel into the LUMO, or the hole (2) tunnels into the HOMO.

In order to gauge whether higher field enhancements translate into more e-h pairs, on the right hand side of figure 7.4 we compare the extinction and scattering cross sections for a metal nanodisk of diameter 200 nm and 100 nm height, according to the calculations described in the previous section 7.8. The extinction cross section $\sigma_{ext}$ describes all decay processes when the light couples into the LSPP; the scattering cross section $\sigma_{scatt}$ is the part of total cross section which is not active for photochemistry, as it shows radiative LSPP decay. Finally, the absorbance cross section $\sigma_{abs}$ shows the spectral region active for photochemistry. One observes that Ag plasmons decay mostly through scattering, whereas in the Cu nanodisk, more light is absorbed and e-h pairs are created over a wider wavelength range.

**Whether this plasmon decays into electron hole pairs or by radiation will depend on the material and the size** [35, 324, 325]. We will conclude by discussing tuneability of plasmon enhanced photochemistry and the interplay between material and adsorbate properties.

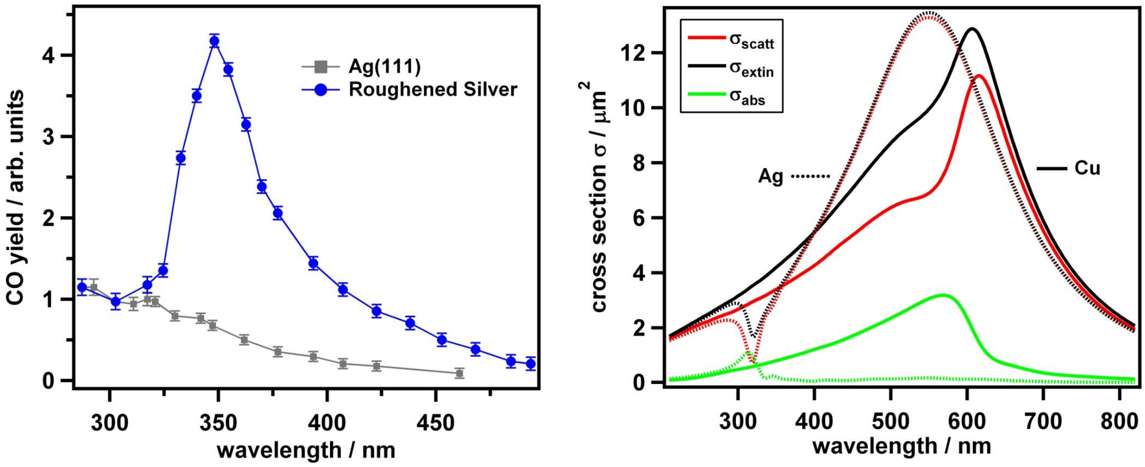

*Figure 7.4:* On the left, from Kidd *et al.* [30], comparison of the OCS photodesorption yield on flat (grey squares) and roughened (blue circles) Ag(111). On the right, the comparison of the cross sections of Cu and Ag nanodisks (d=200nm, h=100nm). Solid lines are for Cu, dotted lines are for Ag.

This has been discussed in detail by Langhammer *et al.* [35, 318, 326, 327] who conclude that transition metals like Pd might be more suitable substrates for plasmon-enhanced photochemistry, because their LSPPs decay into e-h pairs more efficiently and over a wider energy range than for Ag. In the following we will discuss Ar$^+$ sputtering as a method for surface nanostructuring and calculate the achievable electric field enhancement on Ag and Cu, since a high field enhancement is an indicator of plasmon excitation.

## 7.3 Plasmon substrates created by sputtering

Roughened surfaces induced by ion sputtering allow plasmon excitation [308]. This technique has been studied in detail [40–44] as an "easy" tool to design nanopatterns on metal and semiconductor surfaces. Advantages of the method are the capability to design periodic structures, such a pits or pyramidal-like features, on metal surfaces over larger areas. Furthermore, every UHV chamber is provided with an ion gun as part of the cleaning procedure of the crystal. Valbusa and coworkers [46–49] characterized structures formed on Cu(110) by ion sputtering as a function of incident angle, time and substrate temperature. At lower temperatures, periodic ripple structures can be formed. Moreover, the ripple orientation and periodicity can be varied depending on the crystal axis orientation and the sputtering time, respectively. At higher temperatures, random sized structures are observed (see figure 7.5). These investigations show how Cu(110) is a potential candidate to study the role of plasmon excitation in photochemistry by tuning the surface structure. In figure 7.5 STM images of the surface patterned by ion sputtering are presented. From b) to f), different substrate temperatures at normal incidence of the ion beam produce a wide range of features. On the right, ripple structure after ion sputtering at 180 K for $\theta = 45^0$ and azimuthal angle $\delta = 45°$ (see the inset 7.5 *a* for axis and angle definition). On the bottom right, a misleading STM picture of Ag(110) after sputtering at 400 K and normal incidence, where the lateral scale is 400 nm x 400 nm and the normal direction is only tens of Å.

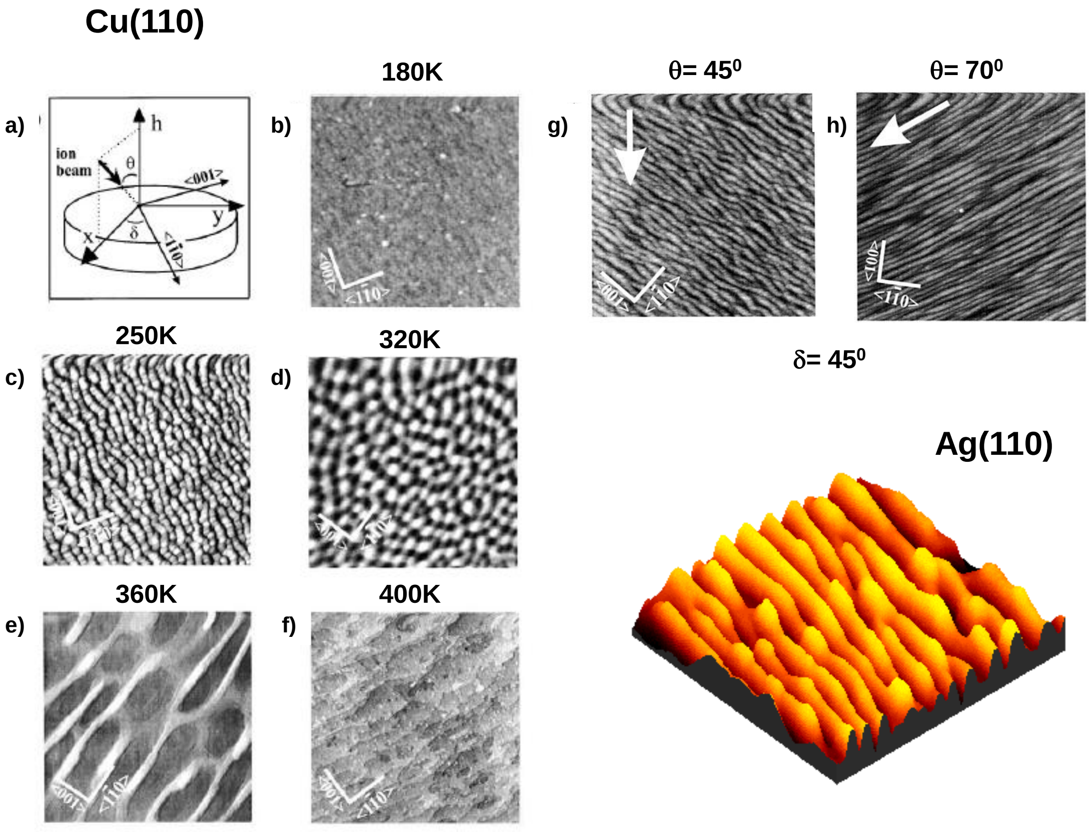

*Figure 7.5:* Image size 400 x 400 nm$^2$ for (b), (c), (d), (e), (h), (g), while for (f) the size is 800 x 800 nm$^2$. STM images of sputter-patterened Cu(110) surfaces at normal incidence for different temperatures. The inset (a) shows the experimental geometry, (x, y, h) represents the laboratory frame, h is the normal to the flat surface, while ion trajectories are assumed to lie in the x-h plane. Rippled surfaces (g),(h) after ion sputtering at T =180 K for $\theta = 45^0$ and azimuthal angle $\delta = 45^0$. The white arrow indicates the ion beam direction [48]. At the bottom right, 3D Ag(110) image, 400 x 400 nm$^2$, after sputtering at normal incidence at 320 K [328].

Having been misled such, we tried recipes available in the literature to sputter pattern our Cu(110) surface and see the effect on NO and pyridine photochemistry. Failing to obtain enhanced photochemistry, we collaborated with Dr. N. Kalashnyk and Dr. G. Costantini to record STM pictures under our conditions (45° and 300 K). Figure 7.6 shows the results: not many ripples are observed and the height

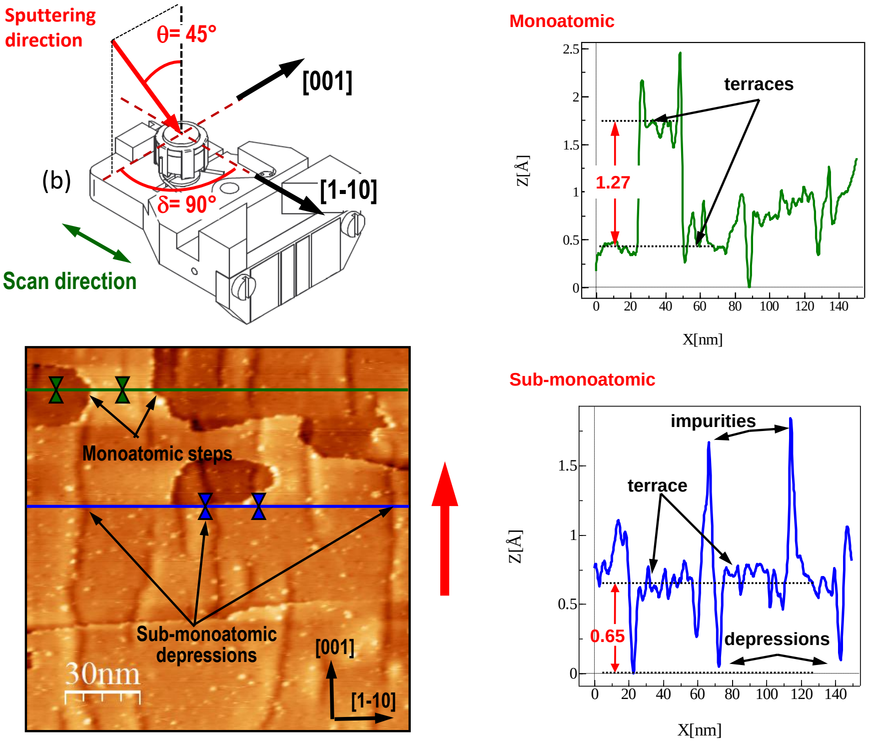

*Figure 7.6:* Sputtered surface at 45° of incidence. The red arrow shows the in-plane projection of sputtering direction. Figure courtesy of Kalashnyk and Costantini.

profile is less than 2 Å. The height of the feature created and its aspect ratio is an important parameter for plasmon excitation. If the feature is too smooth, e.g. fifty times wider than tall; the EM field will be constant over the surface, and no an extra momentum will be transfered, therefore not allowing excitation. Sizable field enhancement is possible for larger aspect ratios and the calculations and results are presented in the following sections.

## 7.4 Modeling sputtered surfaces by finite element methods

Copper shows less strong LSPP excitation due to interband transitions lying above 2 eV. On Ag these occur in the near UV, allowing a tremendous plasmon excitation just at the edge between the UV and visible spectra. This explains one of the reasons why Ag and Au are thoroughly modeled and studied for SERS [238, 329, 330] and heterogeneous photochemistry [127, 331–333]. However, Cu has not been exploited yet, although it is chemically more active than the rest of the noble metals. In this section therefore we model LSPPs on Cu nanopatterned surfaces.

### 7.4.1 Finite element method

To calculate the electric field enhancement factor (EF) of the interface, we use the commercial software COMSOL© Multiphysics 3.5a to numerically solve the Maxwell's equations. The finite element method (FEM) relies on a discretization (meshing) of the volume of study, finding approximate solutions to the partial differential equations (PDE) in such a subdomain with specific boundary conditions [334]. The size and shape of the mesh play an important role in obtaining a satisfactory solution to the geometry of study. In our case, a predefined *extremely fine* mesh with triangular shape and a maximum size element of 5 nm was used. One of most important aspects of the model is to add special boundary conditions at the bounding box edges, i.e. perfectly matched layers (PML). This truncation allows the solutions to converge, making the volume finite as well as avoiding field reflection on the outer boundaries.

We have tried two different approaches: the first one is a 2D simulation of the roughness created by $Ar^+$ sputtering on Cu(110) [46–49], see figure 7.7. The second approach consists also of a 2D model, but with axial symmetry to effectively make it 3D. In this latter case, the model represents the unit cell of a periodic structure or a nanobump on a metal substrate, but will not take into account the coupling between nanostructure features. The model can be applied to metal droplets created by nanosecond laser pulse heating [335]. As far as most of the literature is concerned, the UV-vis absorbance spectrum of nanoparticles of different shapes or sizes on a glass substrate are calculated either by the MLWA, described earlier, or by the discrete dipole approximation (DDA) [312, 336, 336, 337] which I will discuss in section 7.5.6. In contrast to these studies, our purpose is to create a more realistic model, where we take into account the effect of the substrate or precise shape of the nanofeature.

### 7.4.2 Basic equations and the modeling box

In this section, the basic equations applied to our 3D model, meaning 2D with axial symmetry, are presented. Firstly, Maxwell's equations describe the interaction of the interface with the light, and the high electron density of a metal justifies the classical approach. Secondly, for shapes and sizes of the order of the incident wavelength, there is no analytical solution, therefore numerical approaches are needed such as the Finite Element Method (FEM). In our model, a Transverse Magnetic (TM) wave oscillating harmonically in time is considered, which assumes no changes in the field normal to the

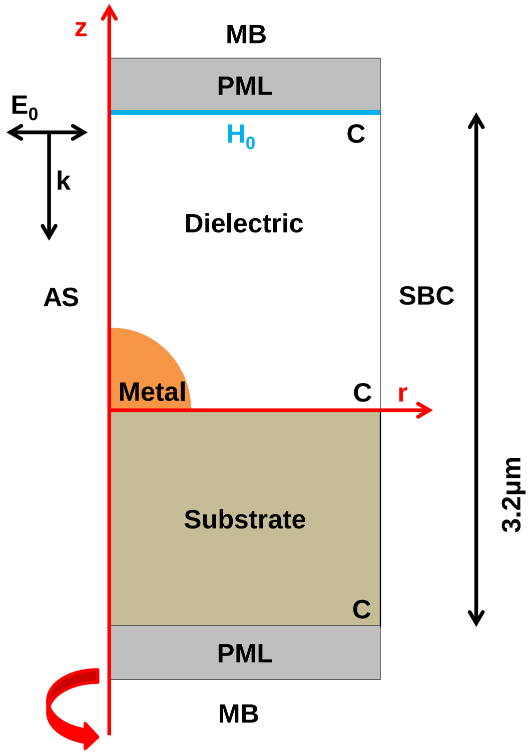

*Figure 7.7:* Model box for the 3D approach (2D model with axial symmetry). Labels: MB=Matched boundary, PML=Perfectly Matched Layers, SBC=Scattering Boundary condition, AS=Axial Symmetry, $H_0$=incident field.

plane. In other words, the magnetic field $H$ perpendicular to the plane of incidence is constant. In axial symmetry, cylindrical harmonic waves describe the problem, with the azimuthal magnetic field $H_\varphi(r, z, t)$ and the electric field $E_{r,z}(r, z, t)$. The propagation of the electromagnetic (EM) field is described by the wave equation[1], where $E_{r,z}(r, z, t)$ propagates within the plane of incidence (rz):

$$\mathbf{H(r, z, t)} = H_\varphi(r, z, t)\mathbf{u}_\varphi = H_\varphi(r, z)\mathbf{u}_\varphi e^{i\omega t} \ , \tag{7.9a}$$

$$\mathbf{E(r, z, t)} = E_r(r, z, t)\mathbf{u}_r + E_z(r, z, t)\mathbf{u}_z = \left(E_r(r, z)\mathbf{u}_r + E_z(r, z)\mathbf{u}_z\right) e^{i\omega t} \ . \tag{7.9b}$$

For the TM asymmetric mode, $H_\varphi$ is computed by solving the vector wave equation for each element of the mesh:

$$\nabla \times \left(\frac{1}{\mu}\nabla \times \mathbf{H}\right) - k_0^2\epsilon\mathbf{H} \ = \ 0 \ , \tag{7.10}$$

$$\nabla \times (H_\varphi \mathbf{u}_\varphi) \ = \ \frac{\partial H_\varphi}{\partial z}\mathbf{u}_\varphi + \frac{1}{r}\frac{\partial}{\partial r}(rH_\varphi)\,\mathbf{u}_\varphi \ . \tag{7.11}$$

---

[1] obtained from the Maxwell equations

In order to study the material properties across the visible range, the `parametric solver` repeats the simulation for each pair of desired frequency $\omega$ and index of refraction $n$. In section 7.2, the SPP and LSPP theory was explained using the dielectric constant $\epsilon(\omega)$. For our calculations, the index of refraction $n_c(\omega)$ is the material properties input [2] and $n = \sqrt{\epsilon(\omega)\mu}$. The input values are an extrapolation from Johnson and Christy's measurements of noble metal thin films [338]. The $n_c(\omega)$ data can be downloaded from nanohub.org [339].

The **boundary conditions** (BC), labeled in figure 7.7, constrain the linear system of equations. There are two types of BC listed below; internal BC, affecting both sides of the subdomain, and external ones:

**Continuity (C):** This boundary condition (7.12) means surface currents are not present. Solving for axial symmetry, as $\mathbf{H}_\varphi$ is continuous, this second condition is automatically fulfilled. **n** represents the unit vector perpendicular to the interface pointing from medium 2 into medium 1. The continuity is assigned on the boundary between the dielectric and the metal, as well as the top and bottom limits of these media:

$$\mathbf{n} \times (\mathbf{E}_1 - \mathbf{E}_2) = 0 \,, \tag{7.12a}$$

$$\mathbf{n} \times (\mathbf{H}_1 - \mathbf{H}_2) = 0 \,. \tag{7.12b}$$

**Magnetic Field ($\mathbf{H}_0$):** An internal BC (eq. 7.13) specifying a magnetic field $H_0$ at the border with user-defined initial value of the field. Consequently, the waves propagate from the top of the box down towards the interface, impinging at **normal incidence**:

$$\mathbf{n} \times \mathbf{H} = \mathbf{n} \times \mathbf{H}_0 \,. \tag{7.13}$$

**Matched Boundary (MB):** The aim of this external boundary is to absorb the field.

$$\mathbf{u}_\varphi \cdot \mathbf{n} \times (\nabla \times H_\varphi \mathbf{u}_\varphi) - i\beta H_\varphi = -2i\beta H_{0\varphi} \,,$$

$$\beta = \omega\sqrt{\mu\epsilon} \,, \tag{7.14a}$$

where $\beta$ is the wave propagation constant. In our model, we compared MB and SBC (next item), electing the former as a more stable solution for propagating the field along z.

---

[2] The software uses $n_c$=n-ik instead of the more usual $n_c$=n+ik definition.

**Scattering Boundary condition (SBC):** An open boundary (7.15), used to make the boundary transparent to the in-plane incident cylindrical wave $E_0$ traveling in **k** direction, as well as the scattered field $E_{SC}$. This condition absorbs $H_\varphi$. You need to define along which cylinder axis the waves are cylindrical, by specifying one point on the cylinder axis and the axis direction. For our case, looking at figure 7.7, the point defined is the origin of the axial axis z and the direction is r:

$$E = E_{sc}\frac{e^{-ik(\mathbf{u}_r\cdot\mathbf{r})}}{\sqrt{r}} + E_0 e^{-ik(\mathbf{k}\cdot\mathbf{r})} \ . \tag{7.15}$$

**Axial Symmetry(AS):** requires axial symmetry along the $z$ axis.

$$H_\varphi = 0 \ . \tag{7.16}$$

The different domains of the box in figure 7.7 are described in the next part.

**Perfectly Matched Layers (PML):** Additional domains, at the bottom and top of the box which absorbs the incident radiation without producing reflections. PML simulates an infinite domain where any wave can propagate and disappear, without being reflected back.

**Dielectric.** In this region, the index of refraction of air or water is used n=1 and n$_{water}$ =1.33). Notice n $\in$ $\mathbb{R}$.

**Metal.** The metal complex index of refraction $n_c\left(\omega\right)$ is loaded into the program, to repeat the simulation with $n_c\left(\omega\right) = n - ik$ for each $\omega$ value. In order to analyse and normalise the results, this region is first set to the same index of refraction as in the dielectric region. This allows to calculate the incident field $E_0$ on the exterior of the nanobump. The calculation is then repeated now with $n_c\left(\omega\right)$.

**Substrate.** This domain is split from the metallic nanobump, offering the possibility of investigating different types of underlying surface. In this thesis, a metallic substrate, with complex n$_c$, and a dielectric one corresponding to fused silica ((FS) n$_{FS}$ =1.46) are investigated.

The **data analysis** consists of the calculation of the enhancement factor (EF), otherwise called field enhancement. EF is the ratio of the intensity of the electric field $E$ across the surface over the intensity of the incident field $E_0$ (7.9b). This is the near-field region experienced by the adsorbate. Notice that the analysed value is the magnitude of E. The incident field is obtained by integration over the surface of the bump, with the index of refraction of the isolated bump set to the dielectric medium. This is followed by a post-calculation with *n* set to the metal constant, to finally obtain E$_{norm}$ including the effect of the nanobump. In COMSOL©, the `Postprocessing Data` tool allows to integrate $E_{norm}$ over every subdomain, in this case a quarter of the circumference. In the 2D axial geometry, it is noteworthy that the surface integral is computed over such a boundary. The field enhancement factor is therefore:

$$EF = \frac{\int_{SURF} |\mathbf{E}|^2}{\int_{SURF} |\mathbf{E}_0|^2} \, . \tag{7.17}$$

A radiative LSPP will show up as a resonance in the spectra.

In order to test the validity of the proposed model, the 3D model is converted into a metallic nanoparticle for comparison with Mie's theory. In addition, the pure 2D model is used for comparison with other already modeled geometries [340]. The 2D and 3D validation is presented in the next section. We have so far only introduced the near field calculation (eq. (7.17)), nevertheless, to study the scattering cross section of a metallic nanoparticle, the far-field $\mathrm{E}_{far}$ is the quantity needed since the intensity of the far-field is the quantity measured by UV-vis absorption. In the case of axisymmetric modeling, `far-field postprocessing` is set *a priori* on the `boundary settings` dialog box. The RF module computes the Stratton-Chu formula, where the near field is used to calculate the $\mathrm{E}_{far}$ [341–343]:

$$\mathbf{E}_{far}(p) = \frac{-ike^{-ikr}}{4\pi r}\mathbf{u}_r \times \int\limits_S \left[(\mathbf{n} \times \mathbf{E}_s) - \eta\left(\mathbf{u}_r \times (\mathbf{n} \times \mathbf{H}_s)\right)\right] e^{ik\mathbf{u}_r \times r'} dS' \, . \tag{7.18}$$

In equation (7.18), the far field $\mathbf{E}_{far}$ is evaluated in the direction of $\mathbf{u}_r$ at the position $p$, as well as being defined as an spherical wave, where p is defined in infinity with a well-defined angular position $(\theta, \varphi)$. On the surface $S$, the integral of the fields $\mathbf{E}_s$ and $\mathbf{H}_s$ is estimated, where **n** is the outward normal vector to $S$, $k$ the wave number and $\eta$ the vacuum impedance

$$\eta = \sqrt{\frac{\mu}{\epsilon}} \, .$$

.

## 7.5 FEM results

The commercial COMSOL© Multiphysics software, with the package `RF` Module 3.5a [341] is used to obtain the EF from the geometry studied. The field and analysis type is `TM harmonic propagation` and the solution type `asymmetric waves`.

### 7.5.1 2D vs 3D modeling

In this section, the comparison between 2D and 3D models is presented. There are several issues which one must take into account to choose a suitable model to retrieve the field enhancement solution. Hereupon, drawbacks, considerations and insight are listed from these two approaches:

- Creating a suitable 2D model can be useful to understand an effect qualitatively. For example, comparing two periodicity values of a grating or the influence of the shape can be done with the advantage of a *low computational time cost*. The reduction of a 2D approach can only be justified if *translational symmetry* exists, i.e. an infinite cylinder. Moreover, an emitting dipole, which is 3D in nature, cannot be modeled as 2D [37]. As an example, we look at an arrangement of cylinders of radius R and distance d as shown in figure 7.8. This has been modelled by Garcia-Vidal and Martin-Moreno [306] accounting for the infinite extent of the cylinders perpendicular to the plane shown. The cylinders and substrate are silver [340]. They calculate the SERS EF as:

  $$SERS_{EF} \sim \frac{\int_{SURF} |\mathbf{E}|^4}{\int_{SURF} |\mathbf{E}_0|^4} \,. \tag{7.19}$$

  Their results are shown in the middle panel on figure 7.8 and the equivalent result of our 2D calculation is seen on the right. We fail to reproduce their results. Firstly, there is no red shift observed as the distance between hemicylinders is decreased. This fact can be related to the coupling of two emitting dipoles, which is not taken into account in our model due to the reduced dimensionality. Secondly, García-Vidal and Pendry also include retardation effects, due to the EM field traveling through the metal, therefore the reflected electric field will have different phases at different points of the feature and interference can occur.

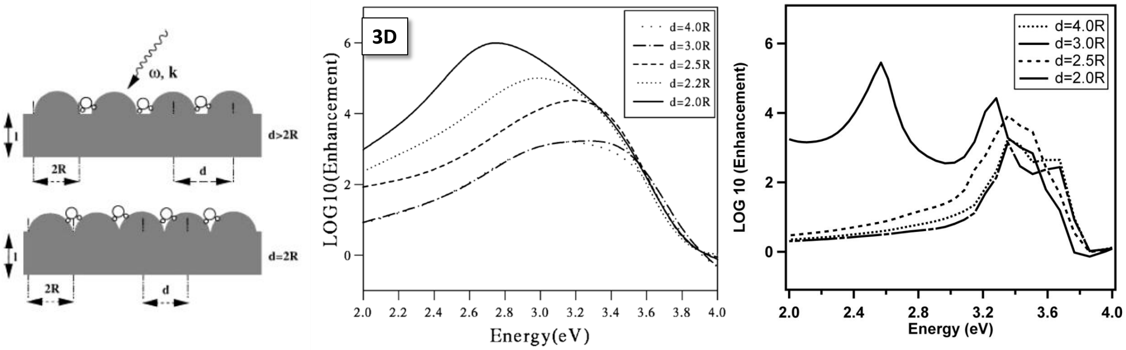

*Figure 7.8:* Left hand side, the geometry studied from García-Vidal and Pendry [340]. The graphs from their 3D calculation and our 2D calculation on centre and right panels, respectively. See text for further explanation.

- The 3D axial symmetry provides several advantages. Firstly, it is fast on a normal PC. Secondly, the model is a convenient way to study the effect of the shape of a nanobump on a metal substrate. As a consequence, we realised that sputter features, according to the STM images (see 7.6) are flat for any detectable field enhancement.

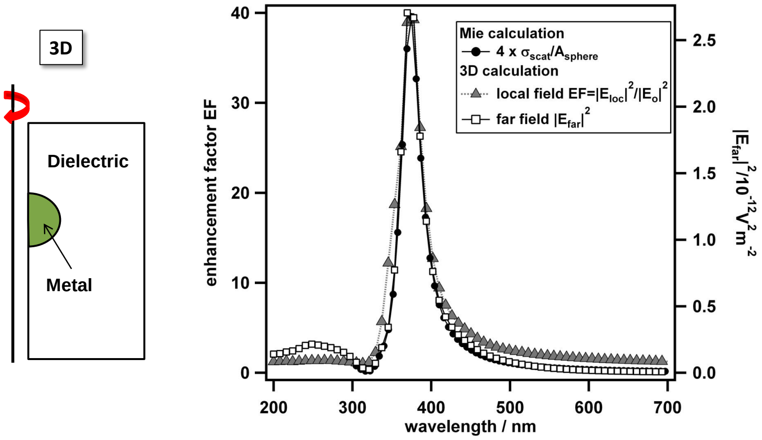

*Figure 7.9:* Testing our 3D calculation with Mie's theory for a Ag nanosphere, d=70nm.

- Figure 7.9 shows the results of testing our model with Mie's theory. These results where obtained using a free web tool to calculate the scattering cross section of the nanosphere [344]. Our far field calculation completely matches with Mie's scattering cross section. The calculated near field is also depicted, which is the relevant one for an adsorbed molecule on the surface.

- To finally discard the 2D model, we have compared 2D and 3D calculations on a well-investigated system: a silver ellipsoid. Changing the shape from spherical to oblate, the frequency should blue-shift. Changing to prolate, the frequency should red-shift (the so-called lighting-rod effect). The results for both models are presented in figure 7.10, showing inmediately that 2D does not work. The interaction between a metallic ellipsoid and a flat dielectric substrate at distance $d$ has been investigated in detail by Noguez group [313, 314, 345]. Including interaction with the image dipole induced in the substrate, the EF was investigated as function of the shape and size, as well as distance above the surface. For TM polarization and a sphere, the resonance frequency does not depend strongly on distance; only when the aspect ratio of the ellipsoid is tuned. Similar to our results, more pointy features broaden and red-shift the resonance. Noguez [313] explained that for particles bigger than 40 nm, the distribution of charge induced becomes uneven, inducing higher multipolar modes, with lower resonance wavelength than the dipolar one (see equation

(7.7)). Furthermore, another polarization field is induced by the accelerated electrons, acting against these higher modes, thus red-shifting and broadening the resonance, as shown on the left in figure 7.10.

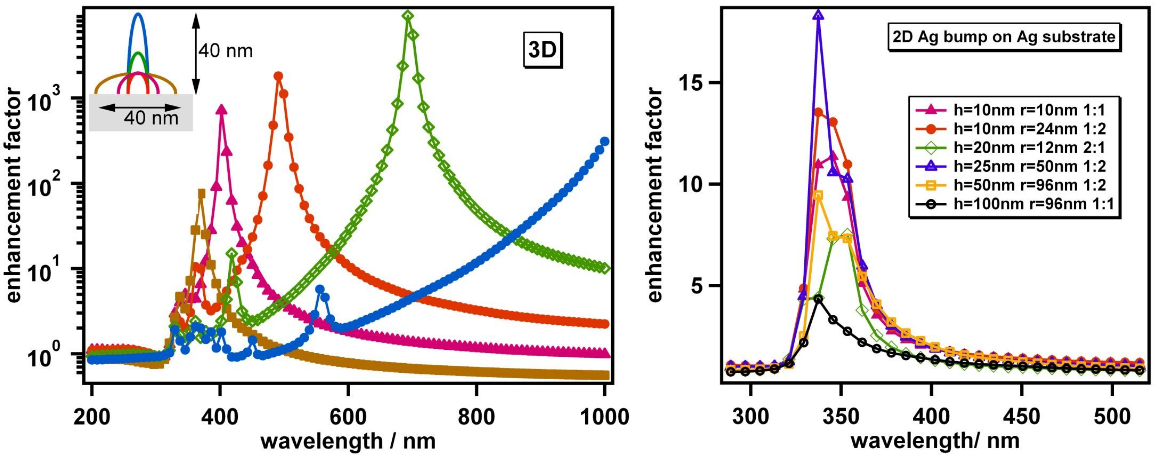

*Figure 7.10:* 3D versus 2D calculations for different aspect ratios of a Ag nanobump on a Ag substrate. For the 3D model, a shift in frequency as the aspect ratio changes is observed, as expected, whereas in the 2D model on the right, the frequency remains the same.

### 7.5.2 Sharp edges

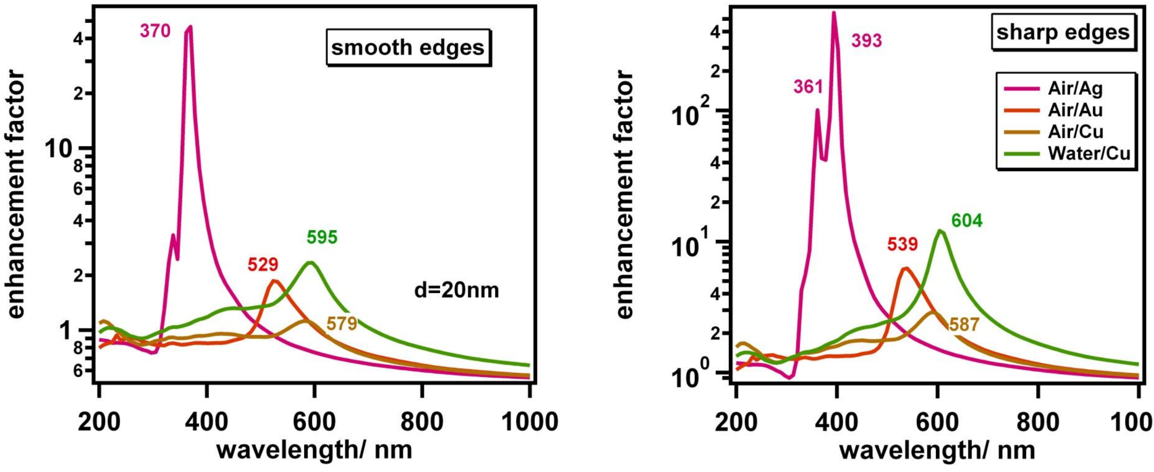

*Figure 7.11:* EF calculated for a noble metal hemisphere on the same substrate. On the right, a smoother edge geometry has been drawn.

Sharp edges can cause singularities in the solution, leading to overestimation of field enhancement.

We have investigated the effect of these sharp edges by smoothing the corner between the hemisphere and the substrate.

Smoother edges result in a 10 times smaller field enhancement (see figure 7.11). For the range of noble metals tested (Ag, Au, Cu), the 20 nm diameter nanobump is embedded in air. In addition, a Cu bump under water was also studied, where the increased dielectric constant leads to a red-shift of the frequency.

Smooth and sharp bumps are not completely equivalent, since smoothing leads to an increase in size. This alone changes the EF to a degree and shift the resonance to the blue, towards the SPP of a flat dielectric-metal interface.

### 7.5.3 Copper hemispheres on copper substrate

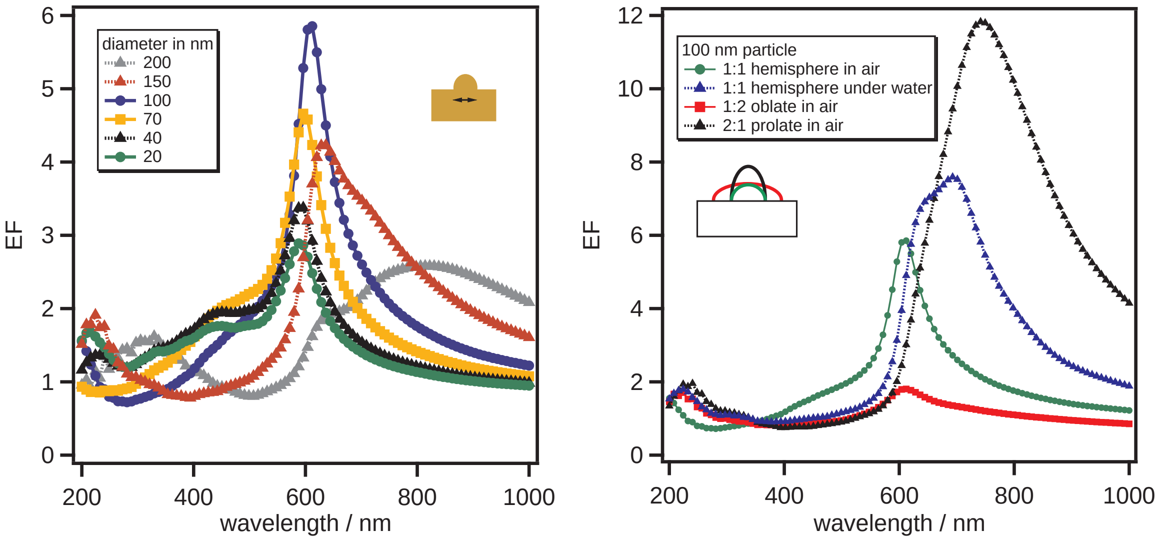

*Figure 7.12:* Cu sphere on Cu substrate calculation for various sizes (left), where the maximum EF is found for 100 nm diameter. On the right, calculations for different shapes. The inset shows the geometry used.

Figure 7.12 shows the calculation for different Cu nano-hemispheres on a copper substrate. The maximum EF is found for a 100 nm diameter particle, in agreement with Noguez [313]. Different shapes are also explored, from a Cu flatter to a more pointy feature on a copper substrate (right figure 7.12). The same effect as for the silver nano-hemispheres is seen, the frequency red-shifts as the feature becomes pointier, and blue-shifts as it gets flatter. The effect of the change in dielectric medium is also explored, which moves the resonance away from the interband transitions, consequently EF is higher than for the same nano-hemisphere size.

### 7.5.4 Dielectric versus metallic substrate

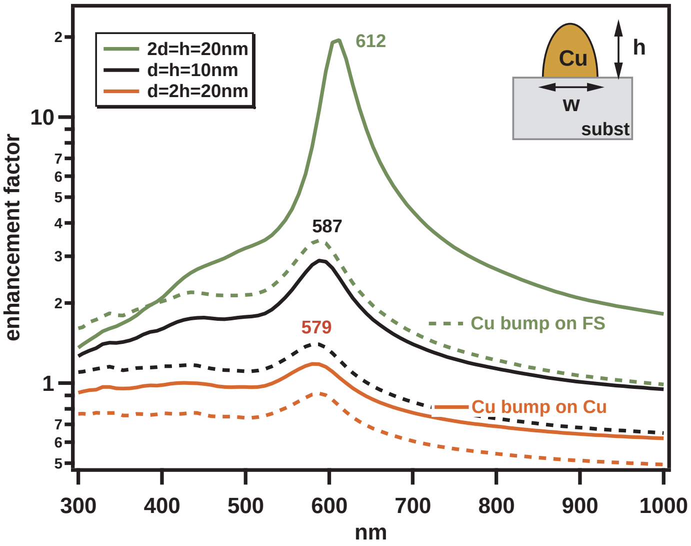

*Figure 7.13:* Solid lines represent a Cu hemisphere on a Cu substrate; dashed lines a fused silica one. The insets shows the geometry used. See text for further explanation.

This section compares field enhancement of a metallic nanobump on either fused silica or the same metallic substrate. Figure 7.13 shows how the field is enhanced more by the presence of the metal surface, this can be explained by the image dipole induced on the metal substrate, by the nano hemisphere. Moreover, the presence of corners leads to a field enhancement, too. As was previously reported, there is a red-shift for the more prolate features and a blue-shift for the oblate ones. When we compare the same aspect ratio hemispheres (the aspect ratio is height h over width w), then the metal substrate leads to a red-shift due to the coupling between the higher order modes. Only the oblate shape shows no shift.

### 7.5.5 Cu aspect ratio dependence and the tunability in photochemistry

In this section, copper EFs are presented and discussed in terms of tuning photochemical effects. Figure 7.14 shows the EF for different sizes and aspect ratio of a Cu nanobump on a Cu substrate. As the nanobump becomes larger and more pointy, the EF maximum red-shifts, broadens and becomes stronger. On the contrary, flatter shapes have weaker resonances and lower resonance wavelengths. This is in agreement with the MLWA, which explains the red-shift due to the increasing contribution from higher order modes. In particular, as the resonance shifts away from the interband transitions, it becomes much stronger. A similar effect is produced, if the medium surrounding the metal has a higher

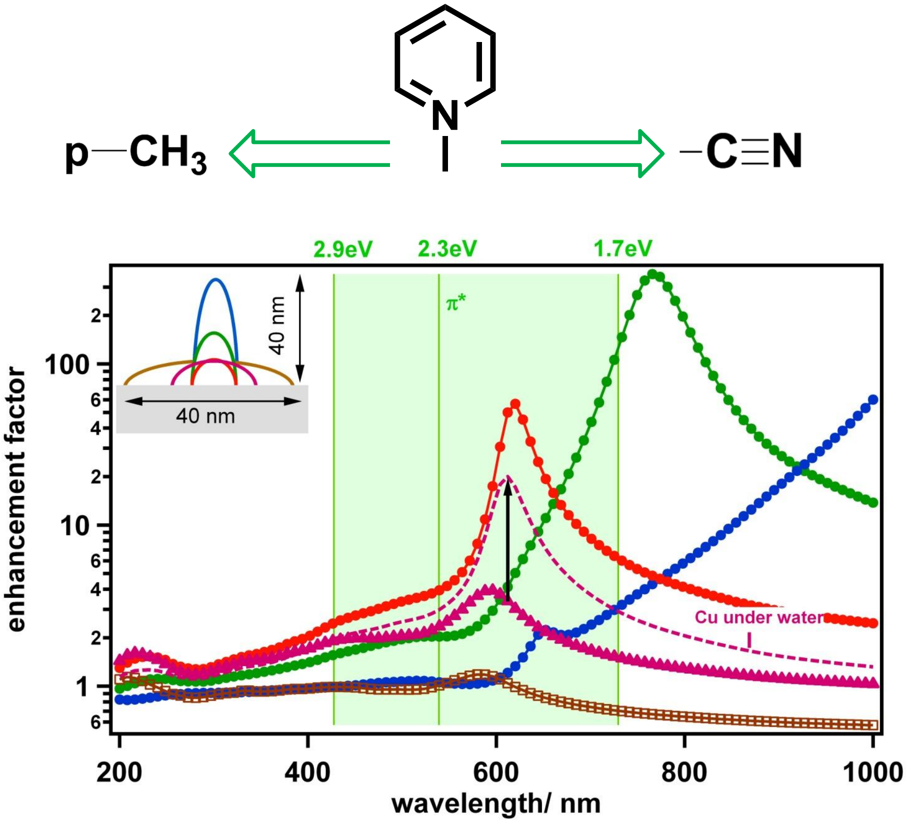

*Figure 7.14:* EF for nanosized Cu bump for a range of aspect ratios, size and shape as shown in the inset. Plasmon enhancement of photochemistry can occur efficiently if a molecular HOMO or LUMO matches with the plasmon resonance. In the case of pyridine, the LUMO can be shifted by substituting a hydrogen with a different group [39].

refraction index than air, such as water (see dashed pink line in figure 7.14). The resulting red-shift moves away from the interband transitions.

In conclusion, copper possesses a relatively strong, tuneable LSPP resonance (LSPPRs) above the interband transitions (> 580 nm). These could enhance the photochemistry if the LSPPR matches the energy gap between the Fermi level and the LUMO of the molecule. Otherwise, the main pathway for photochemistry is related to interband transitions, as discussed in the previous chapters. In the case of pyridine, there is no good match between the $E_F$-LUMO gap and the LSPPR, but a better match can be achieved by changing a functional group on the molecule. Morton *et al.* studied the chemical enhancement of meta- and para- substituted pyridines interacting with a small silver cluster ($Ag_{20}$), which changes the LUMO-HOMO energy gap. The inset in figure 7.14 shows the $\pi^*$ pyridine unoccupied level on Cu(110) at +2.3 eV (to $E_F$) measured by STS [221]. The arrows show how far the functional group could shift the energy gap, matching it with the LSPPR.

### 7.5.6 Plasmons and absorption cross section

For a few pages now we have concentrated on calculating enhancement factors. We have ignored the fact that a high EF is only an indication of where a resonance occurs and how strong it is, but does not answer the question of how efficiently the photochemistry is enhanced.

EF basically reflects the extinction cross section $\sigma_{ext}$ in that a peak in both curves is a fingerprint of the plasmon excitation. It does not tell us whether the plasmon decays by radiation ($\sigma_{scat}$) or e-h pair generation ($\sigma_{abs}$). To this end we return to equation 7.7 which connects with the polarisability $\alpha(\omega)$ generated and the various cross sections. We then take one step further and look at how the polarisability and cross sections are modified if we take coupling between nanoscale features into account.

It is known from Ag nanoparticle arrays that varying the distance between nanoparticles can tune $\sigma_{ext}$ right across the whole visible spectrum [346]. *This is of great use for optimising substrates for SERS, but is it useful for photochemistry?*

To calculate dipole coupling between nanoparticles we use the DDA as described by Schatz' group [312, 336, 337]. The single-particle nanoparticle polarisabilities are still described in the MLWA and are then modified by dipole coupling. The results for a square array of Ag and Cu ellipsoids (height 20 nm, width 40 nm) at different distances are shown in figure 7.15. Ag shows the characteristic frequency plasmon peak at 350 nm, which is responsible for the enhanced photochemistry reported for NO, OCS and $SO_2$ [30]. As the Ag particles begin to couple, we see that this resonance shifts $\sigma_{abs}$ to the visible range. The copper traces show mainly the effect of interband transitions. Coupling has again the effect of broadening $\sigma_{abs}$ and shifting it towards longer wavelengths. These curves show that we gain a certain degree of tuneability of $\sigma_{abs}$ if we couple nanoparticles. At the same time however, we lose selectivity, i.e. in the case of silver, different (unwanted) chemical pathways might open up. For copper, the effect is very similar to a simple decrease of reflectivity by roughening. Consequently, there seems little point in creating copper nanoparticles to promote plasmon excitation.

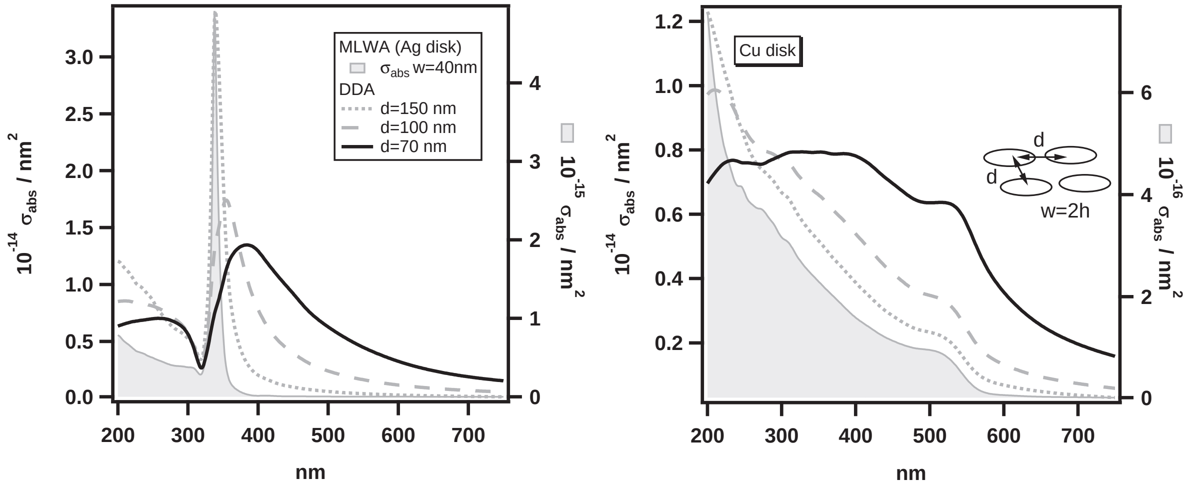

*Figure 7.15:* MLWA calculations for Ag and Cu, left and right graphs respectively. Left axis, $\sigma_{abs}$ from a rectangular arrangement (i=20) of metal ellipsoids of width w=40 nm, height h=20nm by DDA calculation. Right axis for shadowed curves calculated for a single disk.

## 7.6 Conclusions and perspectives

In this chapter a range of different calculations has been carried out to provide more insights into the photochemistry of copper. We emphasized that photochemistry in general starts by creation of electron-hole pairs, and that plasmon excited enhanced photochemistry can be explained by the plasmon decaying into e-h pairs. In order to improve the performance of Cu(110) as a photocatalyst, we have studied the plasmon induced field enhancement on copper nanostructures. Two different models have been tested: a 2D one, with translational symmetry, which is not a good approximation as it does not take into account intrinsic aspects of 3D nature (i.e. emitting dipole). Therefore a 3D model is needed, for which we used axial symmetry as an efficient way of calculating the EF and the resonant frequencies. Even though our modeling refers to a single bump on a Cu substrate, this is a good approach to estimate EF of sputtered surfaces on Cu(110). In conclusion, sputter patterning will not generate the aspect ratio needed to excite LSPPs.

We also explored tuneability of absorption cross section by looking at nanoparticle arrays. Tuneability at the expense of selectivity is possible for Ag but not for Cu. While this is a somewhat disappointing result at first sight, we have learned a lot about the mechanisms behind plasmon-enhanced photochemistry. So to cut through the multicoloured glamour of plasmonics, we have summarized here our recipe for successful plasmon-enhanced tuneable photochemistry.

## Take home message: tips for plasmon-enhanced photochemistry

- You need to understand the photochemistry you want to do before plasmons come into play. Which molecular levels are responsible? Do you have electron-induced or hole-induced photochemistry? What is the optimum energy range? How sensitive is the photochemistry to e.g. adsorption and environment? Does the reaction only work on one metal or on a range of metals? Do you get unwanted reactions at different wavelengths?
- Having identified suitable photochemical pathways at certain energies, use quick calculations for a single nanoparticle to establish whether the desired metal can support a plasmon at that wavelength. If the necessary energies are in the visible range you will want to work with silver, beyond 600 nm copper becomes a candidate while in the near-IR transition metals like Pd take over. The latter have high $\sigma_{abs}$ since the Fermi energy cuts through the d-band.

  Going from a nanoparticle to a more device-like nanoparticle array (as e.g. created by Kasemo's group [347]) means you can extend enhancement of the absorption cross section further towards longer wavelengths. At this point you need to ask yourself whether this broadening will allow unwanted photochemical reactions to occur.
- Finally, if you cannot tune the metal structure to your adsorbate photochemistry, consider tuning the adsorbate to the metal structure available by e.g. substituting functional groups. Any such change however requires a return to point 1!

# Is This the End of the Story?

## Chapter 8

# Future work and conclusions

In this thesis copper photochemistry has been studied in the visible spectral region, revealing it as a potential candidate to support a photochemical reaction. My work is relevant to a number of different communities:

- The discovery that pyridine adsorption on Cu(110) leads to a tremendous decrease on the work function makes it interesting in its own right as a good interface for a device that can use near-IR light to excite photoelectrons which can carry out useful work (in electrochemistry or photovoltaics maybe). It opens up a new perspective as different functional groups on the pyridine can shift the molecular levels and this shift can be easily detected in the form of non-resonant sum frequency enhancement at real interfaces and not just in UHV.
- This work is important for the photochemistry community since the NO/Cu(110) investigation invokes the almost forgotten hole-induced mechanism and given the position of the copper d-band hole-mediated photochemistry should be a dominant theme of copper photochemistry.
- There has been plenty of overlap between the plasmonic and SERS communities and this thesis. We have provided our own recipe of how to best employ plasmons in photochemistry and we have seen how charge transfer (so important for understanding SERS) can be detected by SFG.
- This work will hopefully stimulate the surface femtochemistry community to investigate the vibrational dynamics of bigger molecules, as their behavior has many more facets than CO or NO could ever offer.
- "Simple" sum frequency scanning turned out a new phenomenon-dynamically enhanced SFG, which, like all the other parts, requires a fundamental understanding of the interaction of light

with matter down to the femtosecond scale. On a more practical note, this work is now being applied in the lab to study fractures in airplane titanium!

Overall, this thesis need input from many fields - surface science, heterogeneous photochemistry, SERS, femtochemistry, nonlinear optics, just to name the main ones - and in return it has unified all these research studies, produced fresh knowledge and left plenty of open questions for future research students!

# Appendix

# Appendix A

# Low resolution grating calibration

The low resolution grating was also calibrated by the spectral lines of the Ne lamp. The scanning SF data from chapter 5 were measured with this grating, whose nickname in the lab is *low resolution grating*, in comparison with the higher resolution one (see figure 2.10).

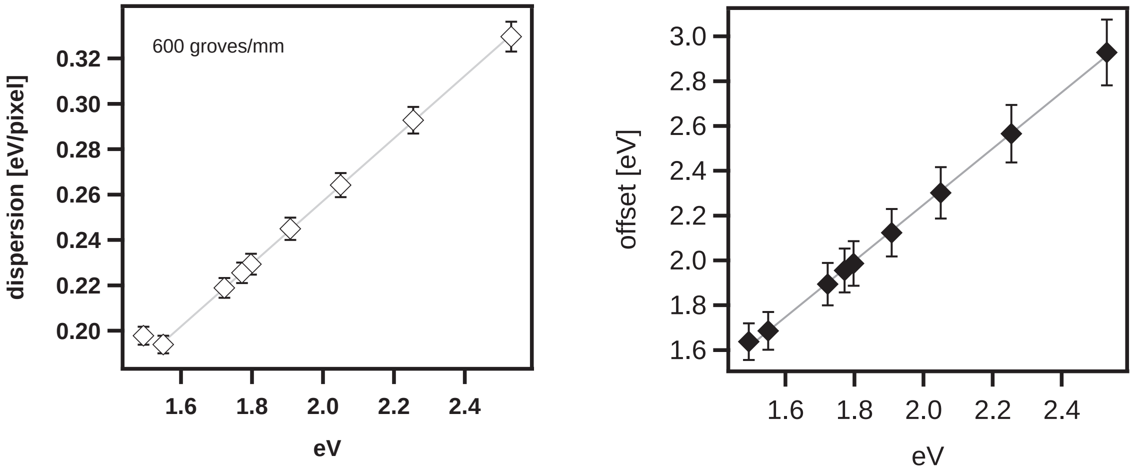

*Figure A.1:* The dispersion [eV/pixel] of the grating (600 groves/mm).

# Appendix B

# Cu(110) band structure analysed by SFG

## B.1 Joint density of states

The unoccupied and occupied surface bands are described by Sonoda [175] as:

$$E = E_0 + \frac{\hbar^2 m_0}{2m^*} \left| k_{||} - k_{||}^0 \right|^2 \quad , \tag{B.1}$$

where $k_{||}^{\circ}$ denotes the position of the $\bar{Y}$ point in reciprocal space, $E_0$ is the surface state energy at $\bar{Y}$ being $E_0$=E-$E_F$ (eV) and $m^*$ is the effective mass of the surface state electrons. The values used for both surface states are presented in the table below:

The surface bands are numerically implemented to cover the range of energies between 1.7 - 2.5 eV, and according to Sun *et al.* [187], the transition energies between bands are obtained from $\Delta E = E_f - E_i$, where *i,f* stands for initial and final, respectively. Figure B.1 shows the results calculated from equation B.1 and values in table B.1, where the black lines show the SS bands and the grey line the transition energies. Only direct optical transitions occur for all photon energies between $E_1$ and $E_2$.

The joint density of states will take account of three factors: the temperature (T) dependent width of the transition, the Fermi occupation and the isotropy of $m^*$ of the surface electrons. The lifetime broadening of the optical transition $\Delta E(k_{||})$ due to the temperature T is given by [348, 349]:

$$\sigma(T) = 50\ meV\ + (0.1\ meV/K) \cdot T$$

| Surface State | $m^*/m$ | $E_0$ / eV |
|---|---|---|
| occupied | 0.37±0.01 | -0.462 |
| unoccupied | 1.77 | 1.81 |

*Table B.1:* The values of the Energy $E_0$ at $\bar{Y}$ , effective mass* relative to the free electron mass $m_0$ from [175]

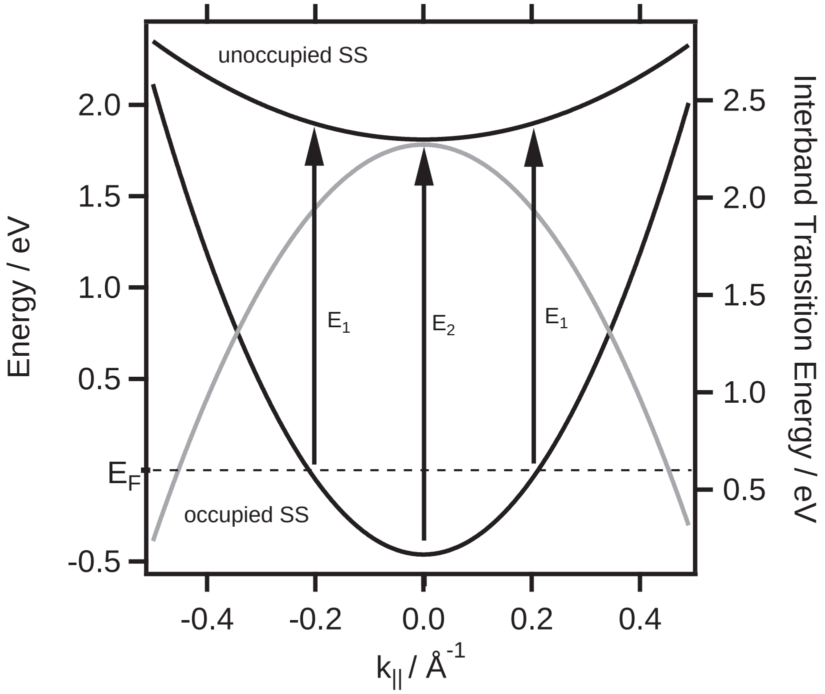

*Figure B.1:* Surface Bands at the $\bar{Y}$ on Cu(110) at 100 K. The arrows show the possible optical transitions.

for a Gaussian function: gauss $\left\{E\left(k_{||}\right) - \Delta E, \sigma(T)\right\}$. The Fermi distribution weight accounts for(see eq. B.2a) due to the occupation change as the occupied surface band (E$_i$) crosses through E$_F$. As the density of states is constant, each $k$ value contribures to to $2\pi\left|k_{||}\right|$. Finally, the absorption spectra are obtained from the integration over the given 2D Brillouin zone around the $\bar{Y}$ point:

$$f(E) = \frac{1}{1+\exp\left(\frac{E_i\left(k_{||}\right)}{KT}\right)}\ , \tag{B.2a}$$

$$JDOS = \int_{-\infty}^{\infty} gauss\left\{E\left(k_{||}\right) - \Delta E\left(k_{||}\right), \sigma(T)\right\} \cdot f(E) \cdot 2\pi\left|k_{||}\right| dk_{||} \tag{B.2b}$$

## B.2 d-band edge of Cu(110)

Looking the Cu(110) d-bands resolved by high-resolution angle resolved photoemission study compromised with the theory and 2PPE spectroscopy [196], the d-band edge data from the literature is summarized on the following table B.2:

| symmetry | $E_i$ / eV | $\Gamma_h$ / meV | Sample | Reference |
|---|---|---|---|---|
| $X_{7+}$ | -2.00 | 12±5 | Cu(110) | [196] |
| $X_{6+}$ | -2.15 | 80±20 | Cu(110) | [196] |
| $X_{7+}$ | -2.34 | 102±20 | Cu(110) | [196] |
| $d\alpha$ | -2.04 | - | Cu(110) | [175] |
| $d\beta$ | -2.18 | - | Cu(110) | [175] |
| $X_{7+}$ | -1.98 | 28±3 | Cs/Cu(110) | [198] |
| $X_{7+}$ | -1.99 | - | Cu(110) | UPS |
| $X_{7+}$ | -2.34 | - | Cu(110) | UPS |

*Table B.2:* Upper limits for the d-hole inelastic linewidth $\Gamma_h$ due to electron-hole interaction at various symmetry points of the copper bulk band structure.

Appendix C

# Pyridine adsorbed on Cu(110)

## C.1 SFG of CO on Cu(110)

The reversibility of chemisorption at room temperature, the easy CO handling in UHV and intense IR bands explain why it has been chosen for many vibrational studies.

Figure C.1 shows the evolution of the CO /Cu(110) SF spectra as a function of coverage in a good agreement with the previous RAIRS studies, the red-shift is identified with the dipole-dipole coupling between neighbouring CO molecules [92]. On the bottom right, the $\Delta\phi$ change as a function of coverage, in agreement with previous studies which show how the surface potential increases by a maximum of 290 mV [350].

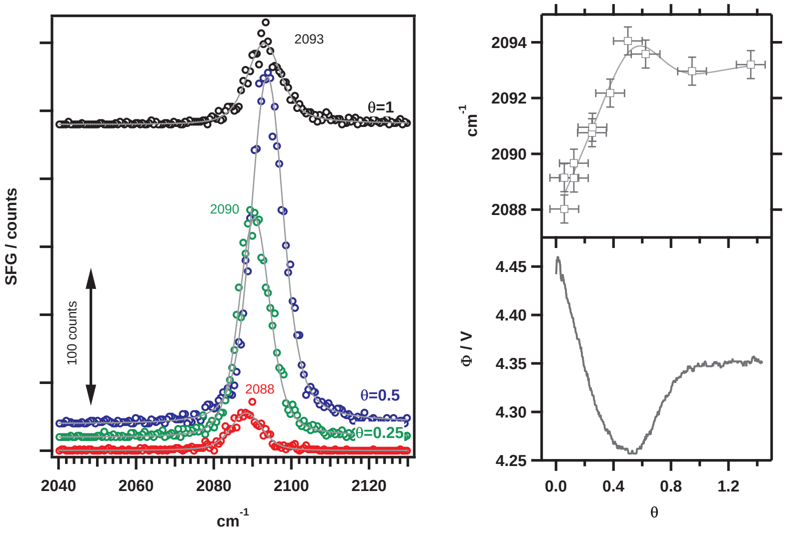

*Figure C.1:* On the left, SF spectra as a function of coverage. On top right, CO center frequency from fitting the SF spectra. On the bottom right, work function change as a function of coverage.

High frequency[1] modes of CO on metal, has been studied as a typical model to understand the interaction between molecule and metal. Frequency shifts, linewidth broadening or asymmetry changes on spectra can reveal orientation and adsorption sites [229, 351–353], interactions between the ad-layer molecules (ie. dipole coupling or stearic repulsions) [354] or the energy transfer between the bonding (ie. chemical shifts) [92, 355], as well as anharmonic coupling to low frequency modes [356].

## C.2 Polarisability of pyridine on Cu(110)

The figure shows the fitting of the measured work function and the fitting according to the alkali adsorption model [252, 253, and references therein].

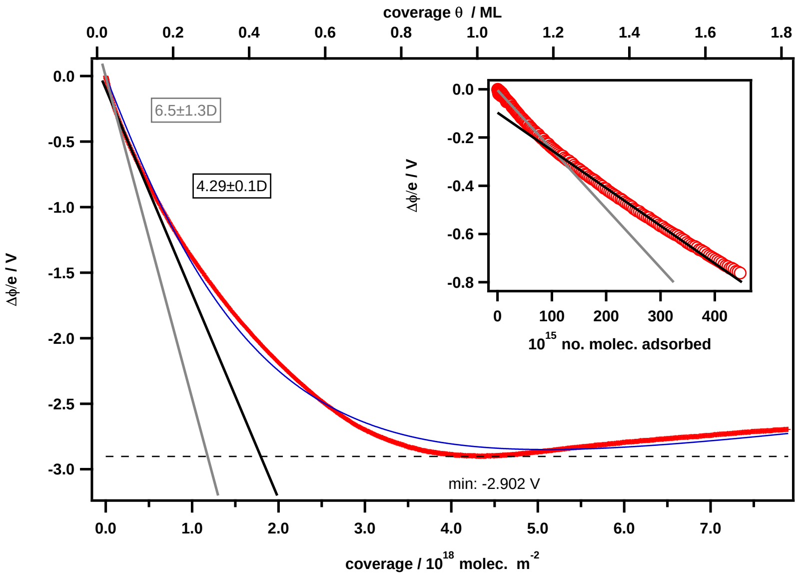

*Figure C.2:* Work function fitting.

The work function change caused by alkali-metal adsorption can be described as:

$$\Delta\phi = \frac{N \cdot \mu_0/\epsilon_0}{1 + g \cdot \alpha N^{3/2}} \, , \tag{C.1}$$

where N is the number of molecules adsorbed on the surface ($\mathrm{m}^{-2}$), g is a geometric factor, $\alpha$ is the polarizability ($m^3$) and $\epsilon_0$ is the vacuum permeability. The fitting parameters are presented in table C.2, where the value for $\mu_0$ is similar to the second linear fit calculated. The polarizability shows a value comparable with other theoretical calculations (see discussion 5.2).

| $\mu_0$(D) | $\alpha$(Å$^3$) |
|---|---|
| 4.45±0.01 | 19.02±0.01 |

---

[1] referring to the IR region.

Appendix D

# Surface plasmon polaritons at a single interface

SPs are a nonradiative electromagnetic excitation propagating along the dielectric-metal interface. Considering Maxwell's equations for both dielectric $\epsilon_1$ and metal $\epsilon_2(\omega)$, as well as assuming the electric charge density appearing in Maxwell's equations vanishes both inside and outside the metal [300], we have:

$$\begin{aligned}
\nabla \epsilon \mathbf{E} &= 0\,, \\
\nabla \mathbf{H} &= 0\,, \\
\nabla \times \mathbf{E} &= -\frac{1}{c}\frac{d\mathbf{H}}{dt}\,, \qquad \text{(D.1)} \\
\nabla \times \mathbf{H} &= \epsilon \frac{1}{c}\frac{d\mathbf{E}}{dt}\,. \qquad \text{(D.2)}
\end{aligned}$$

Let the metal be contained in the half space $z < 0$, $z > 0$ being the dielectric. The surface plasmon is a solution of Maxwell's equation, being a p-polarized wave propagating in the $x$ direction. There is no $y$ dependence, so we can write:

$$\begin{aligned}
z > 0 \quad \mathbf{E}_x &= E_{x1} e^{i(k_{x1} x)} e^{k_{z1} z} \qquad \text{(D.3)} \\
\mathbf{E}_z &= E_{z1} e^{i(k_{x1} x)} e^{k_{z1} z} \\
\mathbf{H}_z &= H_{y1} e^{i(k_{x1} x)} e^{k_{z1} z} \\
z < 0 \quad \mathbf{E}_x &= E_{x2} e^{i(k_{x2} x)} e^{-k_{z2} z} \qquad \text{(D.4)} \\
\mathbf{E}_z &= E_{z2} e^{i(k_{x2} x)} e^{-k_{z2} z} \\
\mathbf{H}_z &= H_{y2} e^{i(k_{x2} x)} e^{-k_{z2} z}
\end{aligned}$$

The boundary conditions are:

$$\begin{aligned} E_{x1} &= E_{x2}\ , \\ \epsilon_1 E_{z1} &= \epsilon_2 E_{z2}\ , \\ H_{y1} &= H_{y2}\ . \end{aligned} \tag{D.5}$$

From (D.5) follows the continuity of the x-component of the wave wector: $k_{x1} = k_{x2} = k_x$. The SP dispersion can be obtained from (D.2, D.4, D.3), yielding:

$$\begin{aligned} \frac{\epsilon_1}{k_{z1}} &= \frac{\epsilon_2}{k_{z2}} \\ k_x^2 + k_{zi}^2 &= \epsilon_i \left(\frac{\omega}{c}\right)^2 \Rightarrow \\ k_x^2 &= \left(\frac{\omega}{c}\right)^2 \left(\frac{\epsilon_1 \epsilon_2}{\epsilon_2 + \epsilon_1}\right) \end{aligned} \tag{D.6}$$

There are two possible solutions from D.6 (of opposite sign). In a metal, the imaginary part is smaller than the real part $\epsilon_2\left(\omega\right)'' < |\epsilon_2\left(\omega\right)'\ |$, while $\epsilon_1$ is real. While $k_x = k_x' + k_x''$ is a complex number, we are only interested in real $k_x'$, because $k_x''$ determines the absorption. The dispersion relation for the real part $k_x'$ is plotted in figure 7.2. See text for dispersion curve explanation in chapter 7. At larger $k_x$ or $\epsilon_1' \to -\epsilon_2$, the value of $\omega$ approaches:

$$w_{SP} = \left(\frac{\omega_p}{1+\epsilon_1}\right)^{\frac{1}{2}},$$

With increasing $\epsilon_1$, the value of $\omega_{SP}$ is reduced, and $\omega_p$ is the plasma frequency of the metal.

# List of abbreviations

| | |
|---|---|
| $\boldsymbol{\sigma}_{abs}$ | Absorption cross section |
| $\boldsymbol{\sigma}_{ext}$ | Extinction cross section |
| $\boldsymbol{\sigma}_{sca}$ | Scattering cross section |
| **AS** | Axial Symmetry |
| **C** | Continuity |
| **MB** | Matched boundary |
| **SBC** | Scattering boundary conditions |
| **$(NO)_2$** | Dinitrosyl |
| **2PPE** | Two-photon photoemission |
| **3PPE** | Three-photon photoemission |
| **$AgGaS_2$** | Silver thiogallate |
| **BBO** | $\beta$-barium borate |
| **BC** | Boundary conditions |
| **$CaF_2$** | Calcium fluoride |
| **CPD** | Contact potential difference |
| **CW** | Centre wavelength |
| **DDA** | Discrete dipole approximation |
| **DFG** | Difference frequency generation |
| **DFT** | Density functional theory |
| **DOS** | Density of states |

| | |
|---|---|
| **$E_F$** | Fermi energy |
| **EELS** | Electron energy loss spectroscopy |
| **EF** | Enhancement factor |
| **EF** | Enhancement factor |
| **EM** | Electromagnetic |
| **ESDIAD** | Electron stimulated desorption ion angular distributions |
| **FEM** | Finite element method |
| **FROG** | Frequency resolved optical gating |
| **FTIR** | Fourier transform infrared spectroscopy |
| **FWHM** | Full width half maximum |
| **HeNe** | Helium-neon |
| **HOMO** | Highest occupied molecular state |
| **HREELS** | High resolution electron energy loss spectroscopy |
| **ICCD** | Intensified charge coupled device |
| **IPS** | Inverse photoemission spectroscopy |
| **JDOS** | Joint density of states |
| **LASER** | Light amplification by stimulated emission of radiation |
| **LDOS** | Local density of states |
| **LEED** | Low-energy electron diffraction |
| **LiIO$_3$** | Lithium Iodate |
| **LSPPRs** | LSPP resonance |
| **LSPP** | Localised surface plasmon polariton |
| **LUMO** | Lowest unoccupied molecular orbital |
| **LUPS** | Lowest unoccupied $\pi$-states |
| **MCT** | Mercury cadmium telluride |
| **MgF$_2$** | Magnesium fluoride |
| **MLWA** | modified long wavelength approximation |

| | |
|---|---|
| **ML** | Monolayer |
| **N$_2$O** | Nitrous oxide |
| **Nd:YAG** | Neodymium Yttrium Aluminum Garnet |
| **NEXAFS** | Near edge X-ray absorption fine structure |
| **NO(ads)** | Nitrogen monoxide adsorbed |
| **NO(g)** | Nitrogen monoxide gas |
| **OPA** | Optical parametric amplification |
| **PDE** | Partial differential equation |
| **PID** | Photo-induced desorption |
| **PML** | Perfectly matched layers |
| **Q** | Cross section |
| **RAIRS** | Reflection-absorption infrared spectroscopy |
| **RAS** | Reflection anisotropy spectroscopy |
| **SAM** | self-assembled monolayer |
| **SBZ** | Surface Brillouin zone |
| **SERS** | Surface enhanced Raman scattering |
| **SFG** | Sum frequency generation |
| **SHG** | Second harmonic generation |
| **SPP** | Surface plasmon polaritons |
| **SS** | Surface state |
| **STM** | scanning tunneling microscopy |
| **STS** | Scanning tunneling spectroscopy |
| **T**$_a ds$ | Adsorbate temperature |
| **T**$_e$ | Electronic temperature |
| **T**$_l$ | Lattice temperature |
| **THG** | Third harmonic generation |
| **Ti:S** | Ti:sapphire |

| | |
|---|---|
| **TIR** | Total internal reflection |
| **TM** | Transverse Magnetic |
| **TOPAS** | Traveling-wave optical parametric amplifier of superfluorescence |
| **TPD** | Temperature programmed desorption |
| **TSA** | Ti:Sapphire amplifier |
| **UHV** | Ultra high vacuum |
| **UPS** | UV photoelectron spectroscopy |
| **XPS** | X-ray photoelectron spectroscopy |

# Bibliography

[1] B. O'Regan and M. Grätzel. A low-cost, high-efficiency solar cell based on dye-sensitized colloidal Tio$_2$ films. Nature, 353(6346):737–740, 1991. DOI. URL link.

[2] L. M. Peter. The grätzel cell: Where next? The Journal of Physical Chemistry Letters, 2(15): 1861–1867, 2011. DOI. URL link.

[3] K. Maeda, K. Teramura, D. Lu, T. Takata, N. Saito, Y. Inoue, and K. Domen. Photocatalyst releasing hydrogen from water. Nature, 440(7082):295–295, 2006. DOI. URL link.

[4] K. Maeda. Photocatalytic water splitting using semiconductor particles: History and recent developments. Journal of Photochemistry and Photobiology C: Photochemistry Reviews, 12(4): 237 – 268, 2011. DOI. URL link.

[5] J. Miller, M. Allendorf, R. Diver, L. Evans, N. Siegel, and J. Stuecker. Metal oxide composites and structures for ultra-high temperature solar thermochemical cycles. Journal of Materials Science, 43:4714–4728, 2008. URL link.

[6] Z. Zhang, J. Long, L. Yang, W. Chen, W. Dai, X. Fu, and X. Wang. Organic semiconductor for artificial photosynthesis: water splitting into hydrogen by a bioinspired c$_3$n$_3$s$_3$ polymer under visible light irradiation. Chemical Science, 2:1826–1830, 2011. DOI. URL link.

[7] K. Maeda and K. Domen. Surface nanostructures in photocatalysts for visible-light-driven water splitting. Topics in Catalysis, 303:95–119, 2011. URL link.

[8] S. Pillai, K. R. Catchpole, T. Trupke, and M. A. Green. Surface plasmon enhanced silicon solar cells. Journal of Applied Physics, 101(9):093105, 2007. DOI. URL link.

[9] Y. Okamoto, S. Ida, J. Hyodo, H. Hagiwara, and T. Ishihara. Synthesis and photocatalytic activity of rhodium-doped calcium niobate nanosheets for hydrogen production from a water/methanol system without cocatalyst loading. Journal of the American Chemical Society, 133(45):18034–18037, 2011. DOI. URL link.

[10] X. Lu, A. Bandara, M. Katayama, A. Yamakata, J. Kubota, and K. Domen. Infrared spectroscopic study of the potential change at cocatalyst particles on oxynitride photocatalysts for water

splitting by visible light irradiation. The Journal of Physical Chemistry C, 115(48):23902–23907, 2011. DOI. URL link.

[11] G.-W. Shu, W.-C. Liao, C.-L. Hsu, J.-Y. Lee, I-J. Hsu, J.-L. Shen, M.-D. Yang, C.-H. Wu, Y.-C. Lee, and W.-C. Chou. Enhanced conversion efficiency of GaAs solar cells using Ag nanoparticles. Advanced Scince Letters, 3(4):368–372, 2010. DOI. URL link.

[12] S. P. Sundararajan, J. M. Steele, and N. J. Halas. Propagation of surface plasmons on Ag and Cu extended one-dimensional arrays on silicon substrates. Applied physics letters, 88(6):063115, 2006. DOI. URL link.

[13] A. M. Schwartzberg and J. Z. Zhang. Novel optical properties and emerging applications of metal manostructures. The Journal of Physical Chemistry C, 112(28):10323–10337, 2008. DOI. URL link.

[14] T. W. Ebbesen, H. J. Lezec, H. F. Ghaemi, T. Thio, and P. A. Wolff. Extraordinary optical transmission through sub-wavelength hole arrays. Nature, 391(6668):667–669, 1998.

[15] G. Gbur, H. F. Schouten, and T. D. Visser. Achieving superresolution in near-field optical data readout systems using surface plasmons. Applied Physics Letters, 87(19):191109, 2005. DOI. URL link.

[16] R. F. Oulton, V. J. Sorger, D. A. Genov, D. F. P. Pile, and X. Zhang. A hybrid plasmonic waveguide for subwavelength confinement and long-range propagation. Nature Photon, 2(8): 496–500, August 2008. URL link.

[17] S. Zhang, K. Bao, N. J. Halas, H. Xu, and P. Nordlander. Substrate-induced Fano resonances of a plasmonic nanocube:a route to increased-sensitivity localized surface plasmon resonance sensors revealed. Nano Letters, 11(4):1657–1663, 2011. DOI. URL link.

[18] L. Brus. Noble metal nanocrystals: plasmon electron transfer photochemistry and single-molecule Raman spectroscopy. Accounts of Chemical Research, 41(12):1742–1749, 2008. DOI. URL link.

[19] W. Hou, Wei H. Hung, P. Pavaskar, A. Goeppert, M. Aykol, and S. B. Cronin. Photocatalytic Conversion of $CO_2$ to Hydrocarbon Fuels via Plasmon-Enhanced Absorption and Metallic Interband Transitions. ACS Catalysis, 1(8):929–936, 2011. DOI. URL link.

[20] C. Langhammer, E. M. Larsson, B. Kasemo, and Igor Zorić. Indirect nanoplasmonic sensing: ultrasensitive experimental platform for nanomaterials science and optical nanocalorimetry. Nano Letters, 10(9):3529–3538, 2010. DOI. URL link.

[21] H. Takei and T. Yamaguchi. A combinatorial approach toward fabrication of surface-adsorbed metal nanoparticles for investigation of an enzyme reaction. Physical Chemistry Chemical Physics, 12:4505–4514, 2010. DOI. URL link.

[22] V. P. Zhdanov and B. Kasemo. Efficiency of the plasmon-mediated enhancement of photoexcitation of adsorbate on nm-sized metal particles. Chemical Physics Letters, 443(1-3):132 – 135, 2007. DOI. URL link.

[23] E. M. Larsson, I. Langhammer, C.and Zorić, and B. Kasemo. Nanoplasmonic probes of catalytic reactions. Science, 326(5956):1091–1094, 2009. DOI. URL link.

[24] K. Watanabe, D. Menzel, N. Nilius, and H-J. Freund. Photochemistry on Metal Nanoparticles. Chemical Reviews, 106(10):4301–4320, 2006. DOI. URL link.

[25] R. A. Dynich. Utilization efficiency of spherical metal nanoparticles that increase light absorption in absorbing media. Journal Of The Optical Society Of America. A, Optics, Image Science, And Vision, 28(2):222 – 228, 2011. URL link.

[26] J. Le Perchec, P. Quémerais, A. Barbara, and T. López-Ríos. Why metallic surfaces with grooves a few nanometers deep and wide may strongly absorb visible light. Physical Review Letters, 100 (6):066408, 2008. DOI. URL link.

[27] M. Osawa. Surface-enhanced infrared absorption. Topics in Applied Physics, 81:163–187, 2001. URL link.

[28] B. Hammer and J. K. Norskov. Theoretical surface science and catalysis-calculations and concepts. Advances in Catalysis, 45:71 – 129, 2000. DOI. URL link.

[29] X. L. Zhou, X. Y. Zhu, and J. M. White. Photochemistry at adsorbate/metal interfaces. Surface Science Reports, 13(3-6):73 – 220, 1991. DOI. URL link.

[30] R.T. Kidd, D. Lennon, and S. R. Meech. Surface plasmon enhanced substrate mediated photochemistry on roughened silver. The Journal of Chemical Physics, 113(18):8276–8282, 2000. DOI. URL link.

[31] G. M. Goncher, C. A. Parsons, and C. B. Harris. Photochemistry on rough metal surfaces. The Journal of Physical Chemistry, 88(19):4200–4209, 1984. DOI. URL link.

[32] C. J. Chen and R. M. Osgood. Direct Observation of the local-field-enhanced surface photochemical-reactions. Physical Review Letters, 50(21):1705–1708, 1983. URL link.

[33] J. Dintinger, S. Klein, F. Bustos, W. L. Barnes, and T. W. Ebbesen. Strong coupling between surface plasmon-polaritons and organic molecules in subwavelength hole arrays. Physical Review B, 71(3):035424, 2005. URL link.

[34] G. V. Hartland and G. Schatz. Virtual issue: plasmon resonances - a physical chemistry perspective. The Journal of Physical Chemistry C, 115(31):15121–15123, 2011. DOI. URL link.

[35] I. Zorić, M. Zaich, B. Kasemo, and C. Langhammer. Gold, Platinum, and Aluminum nanodisk plasmons: material independence, subradiance, and damping mechanisms. ACS Nano, 5(4): 2535–2546, 2011. DOI. URL link.

[36] S. A. Maier. Plasmonics: fundamentals and applications. Springer, 2007. URL link.

[37] E. C. Le Ru and P. G. Etchegoin. Principles of SERS and related plasmonic effects. Elsevier, 2009.

[38] S. Mahajan, R. M. Cole, J. D. Speed, S. H. Pelfrey, A. E. Russell, P. N. Bartlett, S. M. Barnett, and J. J. Baumberg. Understanding the surface-enhanced Raman spectroscopy background. The Journal of Physical Chemistry C, 114(16):7242–7250, 2010. DOI. URL link.

[39] S. M. Morton and L. Jensen. Understanding the molecular surface chemical coupling in SERS. Journal of the American Chemical Society, 131(11):4090–4098, 2009. DOI. URL link.

[40] G. Costantini, F. Buatier de Mongeot, S. Rusponi, C. Boragno, U. Valbusa, L. Vattuone, U. Burghaus, L. Savio, and M. Rocca. Tuning surface reactivity by in situ surface nanostructuring. The Journal of Chemical Physics, 112(15):6840–6843, 2000. DOI. URL link.

[41] G. Costantini, S. Rusponi, F. Buatier de Mongeot, C. Boragno, and U. Valbusa. Periodic structures induced by normal-incidence sputtering on Ag(110) and Ag(001): flux and temperature dependence. Journal of Physics: Condensed Matter, 13(26):5875, 2001. DOI. URL link.

[42] D. Sekiba, S. Bertero, R. Buzio, F. Buatier de Mongeot, C. Boragno, and U. Valbusa. Fabrication of stable nanopatterns on metals. Applied Physics Letters, 81(14):2632–2634, 2002. DOI. URL link.

[43] A. Chandra Bose and M. Yoshitake. Pattern formation induced by $Ar^+$ sputtering on Au(111). Applied Surface Science, 241(1-2):174–178, 2005. DOI. URL link.

[44] F. Buatier de Mongeot and U. Valbusa. Applications of metal surfaces nanostructured by ion beam sputtering. Journal of Physics: Condensed Matter, 21(22):224022, 2009. DOI. URL link.

[45] G. H. Chan, J. Zhao, E. M. Hicks, G. C. Schatz, and R. P. Van Duyne. Plasmonic properties of Copper nanoparticles fabricated by nanosphere lithography. Nano Letters, 7(7):1947–1952, 2007. DOI. URL link.

[46] S. Rusponi, G. Costantini, C. Boragno, and U. Valbusa. Ripple wave vector rotation in anisotropic crystal sputtering. Physical Review Letters, 81(13):2735–2738, 1998. DOI. URL link.

[47] S. Rusponi, G. Costantini, C. Boragno, and U. Valbusa. Scaling laws of the ripple morphology on Cu(110). Physical Review Letters, 81(19):4184–4187, 1998. DOI. URL link.

[48] S. Rusponi, G. Costantini, F. Buatier de Mongeot, C. Boragno, and U. Valbusa. Patterning a surface on the nanometric scale by ion sputtering. Applied Physics Letters, 75(21):3318–3320, 1999. DOI. URL link.

[49] C. Boragno, F. Buatier, G. Costantini, A. Molle, D. de Sanctis, U. Valbusa, F. Borgatti, R. Felici, and S. Ferrer. Time evolution of the local slope during Cu(110) ion sputtering. Physical Review B, 68(9):094102, 2003. DOI. URL link.

[50] E. Knoesel, A. Hotzel, and M. Wolf. Ultrafast dynamics of hot electrons and holes in copper: Excitation, energy relaxation, and transport effects. Physical Review B, 57(20):12812–12824, 1998. DOI. URL link.

[51] H. Petek, H. Nagano, and S. Ogawa. Hot-electron dynamics in copper revisited: The d-band effect. Applied Physics B: Lasers and Optics, 68:369–375, 1999. DOI. URL link.

[52] Y. R. Shen. Surfaces probed by nonlinear optics. Surface Science, 299-300(0):551 – 562, 1994. DOI. URL link.

[53] H. Arnolds. Vibrational dynamics of adsorbates - Quo vadis? Progress in Surface Science, 86 (1-2):1 – 40, 2011. DOI. URL link.

[54] H. Arnolds and M. Bonn. Ultrafast surface vibrational dynamics. Surface Science Reports, 65 (2):45 – 66, 2010. DOI. URL link.

[55] C. Frischkorn and M. Wolf. Femtochemistry at metal surfaces: Nonadiabatic reaction dynamics. Chemical Reviews, 106(10):4207–4233, 2006. DOI. URL link.

[56] R. T. Kidd, S. R. Meech, and D. Lennon. Enhanced photodesorption of NO on roughened silver surfaces. Chemical Physics Letters, 262(1-2):142 – 150, 1996. DOI. URL link.

[57] T. Vondrak, D. J. Burke, and S. R. Meech. The dynamics and origin of NO photodesorbed from NO/Ag(111). Chemical Physics Letters, 327(3-4):137 – 142, 2000. DOI. URL link.

[58] K. H. Kim, K. Watanabe, D. Menzel, and H-J. Freund. Photoinduced abstraction reactions within NO dimers on Ag(111). Journal of the American Chemical Society, 131(5):1660–1661, 2009. DOI. URL link.

[59] D. Mulugeta, K. H. Kim, K. Watanabe, D. Menzel, and H.-J. Freund. Size effects in thermal and photochemistry of (NO)$_2$ on Ag nanoparticles. Physical Review Letters, 101(14):146103, 2008. DOI. URL link.

[60] D. Mulugeta, K. Watanabe, D. Menzel, and H-J. Freund. State-resolved investigation of the photodesorption dynamics of NO from (NO)$_2$ on Ag nanoparticles of various sizes in comparison with Ag(111). The Journal of Chemical Physics, 134(16):164702, 2011. DOI. URL link.

[61] K. Wettergren, B. Kasemo, and D. Chakarov. Photodesorption of NO from graphite(0001) surface mediated by silver clusters. Surface Science, 593(1-3):235 – 241, 2005. DOI. URL link.

[62] W. A. Brown, R. K. Sharma, D. A. King, and S. Haq. Adsorption and reactivity of NO and N$_2$O on Cu(110): Combined RAIRS and molecular beam studies. The Journal of Physical Chemistry, 100(30):12559–12568, 1996. DOI. URL link.

[63] J. P. R. Symonds, H. Arnolds, and D. A. King. Femtosecond pump/probe spectroscopy of CO on Ru(1010) from experimental and theoretical perspectives. The Journal of Physical Chemistry B, 108(38):14311–14315, 2004. DOI. URL link.

[64] M. Bonn, S. Funk, Ch. Hess, D. N. Denzler, C. Stampfl, M. Scheffler, M. Wolf, and G. Ertl. Phonon- versus electron-mediated desorption and oxidation of CO on Ru(0001). Science, 285 (5430):1042–1045, 1999. DOI. URL link.

[65] I. M. Lane, Z-P. Liu, D. A. King, and H. Arnolds. Ultrafast vibrational dynamics of NO and CO adsorbed on an Iridium surface. The Journal of Physical Chemistry C, 111(38):14198–14206, 2007. DOI. URL link.

[66] I. M. Lane. Ultrafast molecular dynamics at surfaces. PhD thesis, Department of Chemistry, University of Cambridge, 2006. URL link.

[67] T. A. Germer, J. C. Stephenson, E. J. Heilweil, and R. R. Cavanagh. Picosecond measurement of substrate to adsorbate energy transfer: The frustrated translation of CO/Pt(111). The Journal of Chemical Physics, 98(12):9986–9994, 1993. DOI. URL link.

[68] E. H. G. Backus, A. Eichler, A. W. Kleyn, and M. Bonn. Real-time observation of molecular motion on a surface. Science, 310(5755):1790–1793, 2005. DOI. URL link.

[69] F. Fournier, W. Zheng, S. Carrez, H. Dubost, and B. Bourguignon. Vibrational dynamics of adsorbed molecules under conditions of photodesorption: Pump-probe SFG spectra of CO/Pt(111). The Journal of Chemical Physics, 121(10):4839–4847, 2004. DOI. URL link.

[70] J. P. R. Symonds. Femtosecond sum-frequency spectroscopy of metal-adsorbate systems. PhD thesis, Department of Chemistry, University of Cambridge, 2003. URL link.

[71] A. Zangwill. Physics at Surfaces. Cambridge University Press, Cambridge, 1988.

[72] D. R. Penn. Electron mean free paths for free-electron-like materials. Physical Review B, 13: 5248–5254, 1976. DOI. URL link.

[73] N. D. Lang and W. Kohn. Theory of metal surfaces: work function. Physical Review B, 3: 1215–1223, Feb 1971. DOI. URL link.

[74] I. Langmuir. The effect of space charge and initial velocities on the potential distribution and thermionic current between parallel plane electrodes. Physical Review, 21:419–435, 1923. DOI. URL link.

[75] H. P. Bonzel. Alkali-metal-affected adsorption of molecules on metal surfaces. Surface Science Reports, 8(2):43 – 125, 1988. DOI. URL link.

[76] M. P. Kiskinova. Electronegative additives and poisoning in catalysis. Surface Science Reports, 8(8):359 – 402, 1988. DOI. URL link.

[77] H. Ibach. Physics of surfaces and interfaces. Springer-Verlag Berlin Heidelberg, Heidelberg, 1941. URL link.

[78] V. G. Bordo and R. Horst-Günter. Optics and spectroscopy at surfaces and interfaces. John Wiley and Sons, 2005.

[79] J. Pritchard. Reflection-absorption infrared spectroscopy. In Chemical Physics of Solids and their Surfaces, volume 7, pages 157–179. 1978. DOI. URL link.

[80] N. V. Richardson and A. M. Bradshaw. The frequencies and amplitudes of CO vibrations at a metal surface from model cluster calculations. Surface Science, 88(1):255 – 268, 1979. DOI. URL link.

[81] H. Froitzheim, H. Ibach, and S. Lehwald. Surface sites of H on W(100). Physical Review Letters, 36(26):1549–1551, 1976. DOI. URL link.

[82] R. Raval. Probing the nature of molecular chemisorption using RAIRS. Surface Science, 331: 1–10, 1995. DOI. URL link.

[83] W. A. Brown and D. A. King. NO chemisorption and reactions on metal surfaces: A new perspective. The Journal of Physical Chemistry B, 104(12):2578–2595, 2000. DOI. URL link.

[84] P. S. Cremer, B. J. McIntyre, M. Salmeron, Y. R. Shen, and G. A. Somorjai. Monitoring surfaces on the molecular level during catalytic reactions at high pressure by Sum Frequency Feneration vibrational spectroscopy and scanning tunneling microscopy. Catalysis Letters, 34:11–18, 1995. DOI. URL link.

[85] P. S. Cremer, X. Su, G. A. Somorjai, and Y. R. Shen. High pressure catalytic processes studied by infrared-visible Sum Frequency Generation. Journal of Molecular Catalysis A: Chemical, 131(1-3):225 – 241, 1998. DOI. URL link.

[86] C. Hess, S. Funk, M. Bonn, D.N. Denzler, M. Wolf, and G. Ertl. Femtosecond dynamics of chemical reactions at surfaces. Applied Physics A: Materials Science & Processing, 71:477–483, 2000. DOI. URL link.

[87] G. Rupprechter. Sum frequency laser spectroscopy during chemical reactions on surfaces. MRS Bulletin, 32:1031–1037, 2007. DOI. URL link.

[88] Y. Hu and K. Griffiths. Investigation of the role of oxygen in NO reduction by $C_2H_4$ on the surface of stepped Pt(332). Applied Surface Science, 254(16):5048 – 5054, 2008. DOI. URL link.

[89] M. M. M. Jansen, O. Caniaz, B. E. Nieuwenhuys, and J. W. Niemantsverdriet. Interaction and reaction of coadsorbed NO and CO on a Rh(100) single crystal surface. Langmuir, 26(21): 16239–16245, 2010. DOI. URL link.

[90] K. Lass, X. Han, and E. Hasselbrink. The surprisingly short vibrational lifetime of the internal stretch of CO adsorbed on Si(100). The Journal of Chemical Physics, 123(5):051102, 2005. DOI. URL link.

[91] I. M. Lane, D. A. King, and H. Arnolds. The determination of an inhomogeneous linewidth for a strongly coupled adsorbate system. The Journal of Chemical Physics, 126(2):024707, 2007. DOI. URL link.

[92] D. P. Woodruff, B. E. Hayden, K. Prince, and A. M. Bradshaw. Dipole coupling and chemical shifts in IRAS of CO adsorbed on Cu(110). Surface Science, 123(2-3):397–412, 1982. DOI. URL link.

[93] M. Cho, C. Hess, and M. Bonn. Lateral interactions between adsorbed molecules: Investigations of CO on Ru(001) using nonlinear surface vibrational spectroscopies. Physical Review B, 65 (20):205423, May 2002. DOI. URL link.

[94] E. H.G. Backus and M. Bonn. A quantitative comparison between reflection absorption infrared and sum-frequency generation spectroscopy. Chemical Physics Letters, 412(1-3):152 – 157, 2005. DOI. URL link.

[95] G. A. Somorjai and K. R. McCrea. Sum frequency generation: Surface vibrational spectroscopy studies of catalytic reactions on metal single-crystal surfaces. In Impact of Surface Science on Catalysis, volume 45 of Advances in Catalysis, pages 385–438. 2000. DOI. URL link.

[96] S. Haq, A. Carew, and R. Raval. Nitric oxide reduction by Cu nanoclusters supported on thin $Al_2O_3$ films. Journal of Catalysis, 221(1):204 – 212, 2004. DOI. URL link.

[97] G. A. Somorjai and J. Y. Park. Molecular surface chemistry by metal single crystals and nanoparticles from vacuum to high pressure. Chemical Society Reviews, 37:2155–2162, 2008. DOI. URL link.

[98] C. T. Williams and D. A. Beattie. Probing buried interfaces with non-linear optical spectroscopy. Surface Science, 500(1-3):545 – 576, 2002. DOI. URL link.

[99] H.-J. Freund, M. Bumer, J. Libuda, T. Risse, G. Rupprechter, and S. Shaikhutdinov. Preparation and characterization of model catalysts: from ultrahigh vacuum to in situ conditions at the atomic dimension. Journal of Catalysis, 216(1-2):223 – 235, 2003. DOI. URL link.

[100] C. Hess, E. Ozensoy, C-W. Yi, and D. W. Goodman. NO dimer and dinitrosyl formation on Pd(111): From ultra-high-vacuum to elevated pressure conditions. Journal of the American Chemical Society, 128(9):2988–2994, 2006. DOI. URL link.

[101] E. L. Wilson and W. A. Brown. Low pressure RAIRS studies of model catalytic systems. The Journal of Physical Chemistry C, 114(15):6879–6893, 2010. DOI. URL link.

[102] K. B. Eisenthal. Liquid interfaces probed by second-harmonic and sum-frequency spectroscopy. Chemical Reviews, 96(4):1343–1360, 1996. DOI. URL link.

[103] A. Tadjeddine, A. Le Rille, O. Pluchery, F. Vidal, W. Q. Zheng, and A. Peremans. Sum and difference frequency generation at the electrochemical interface. Physica Status Solidi (a), 175 (1):89–107, 1999. DOI. URL link.

[104] W. Gan, Z. Zhang, R. Feng, and H. Wang. Spectral interference and molecular conformation at liquid interface with sum frequency generation vibrational spectroscopy (SFG-VS). The Journal of Physical Chemistry C, 111(25):8726–8738, 2007. DOI. URL link.

[105] H. Arnolds, J. P. R. Symonds, V. L. Zhang, and D. A. King. In situ characterization of ultrafast laser pulses for sum frequency surface studies. Review of Scientific Instruments, 74(9):3943–3946, 2003. DOI. URL link.

[106] I. V. Stiopkin, H. D. Jayathilake, C. Weeraman, and A. V. Benderskii. Temporal effects on spectroscopic line shapes, resolution, and sensitivity of the broad-band sum frequency generation. The Journal of Chemical Physics, 132(23):234503, 2010. DOI. URL link.

[107] A. S. Lagutchev, J. E. Patterson, W. Huang, and D. D. Dlott. Ultrafast dynamics of self-assembled monolayers under shock compression: Effects of molecular and substrate structure. The Journal of Physical Chemistry B, 109(11):5033–5044, 2005. DOI. URL link.

[108] A. Lagutchev, A. Lozano, P. Mukherjee, S. A. Hambir, and D. D. Dlott. Compact broadband vibrational sum-frequency generation spectrometer with nonresonant suppression. Spectrochimica Acta Part A-molecular and Biomolecular Spectroscopy, 75(4):1289–1296, 2010. DOI. URL link.

[109] M. Born and E. Wolf. Principles of Optics. Cambridge University Press, 7th edition edition, 1999.

[110] A.B. McLean, C.E.J. Mitchell, and D.M. Swanston. Implementation of an efficient analytical approximation to the Voigt function for photoemission lineshape analysis. Journal of Electron Spectroscopy and Related Phenomena, 69(2):125 – 132, 1994. DOI. URL link.

[111] X. Gu, S. Akturk, A. Shreenath, Q. Cao, and R. Trebino. The measurement of ultrashort light pulses: simple devices, complex pulses. Optical Review, 11:141–152, 2004. URL link.

[112] G. Cerullo and S. De Silvestri. Ultrafast optical parametric amplifiers. Review of Scientific Instruments, 74(1):1–18, 2003. DOI. URL link.

[113] S. E. Harris, M. K. Oshman, and R. L. Byer. Observation of tunable optical parametric fluorescence. Physical Review Letters, 18(18):732–734, 1967. DOI. URL link.

[114] R. Franchy. Surface and bulk photochemistry of solids. Reports on Progress in Physics, 61(6):691, 1998. DOI. URL link.

[115] M. P. Jigato, D. A. King, and A. Yoshimori. The chemisorption of spin polarised NO on Ag(111). Chemical Physics Letters, 300(5-6):639 – 644, 1999. DOI. URL link.

[116] W. Sesselmann, B. Woratschek, J. Küppers, G. Doyen, G. Ertl, H. Haberland, and H. Morgner. Evidence for paramagnetism of NO molecules chemisorbed on transition-metal surfaces. Physical Review Letters, 60:1434–1437, 1988. DOI. URL link.

[117] W. A. Brown, P. Gardner, and D. A. King. Very low temperature surface reaction: $N_2O$ formation from NO dimers at 70 to 90 K on Ag(111). The Journal of Physical Chemistry, 99(18):7065–7074, 1995. DOI. URL link.

[118] W. A. Brown, P. Gardner, M. Perez Jigato, and D. A. King. Characterization and orientation of adsorbed NO dimers on Ag(111) at low temperatures. The Journal of Chemical Physics, 102 (18):7277–7280, 1995. DOI. URL link.

[119] T.-D. Chau, T. Visart de Bocarme, and N. Kruse. Formation of $N_2O$ and $(NO)_2$; During NO Adsorption on Au 3D Crystals. Catalysis Letters, 98:85–87, 2004. DOI. URL link.

[120] P. Dumas, M. Suhren, Y. J. Chabal, C. J. Hirschmugl, and G. P. Williams. Adsorption and reactivity of NO on Cu(111): a synchrotron infrared reflection absorption spectroscopic study. Surface Science, 371(2-3):200 – 212, 1997. DOI. URL link.

[121] C. M. Kim, C.-W. Yi, and D. W. Goodman. Adsorption and reaction of NO on Cu(100): an infrared reflection absorption spectroscopic study at 25 K. The Journal of Physical Chemistry B, 106(28):7065–7068, 2002. DOI. URL link.

[122] S. Haq and R. Raval. NO and dichloroethene reactivity on single crystal and supported Cu nanoparticles: just how big is the materials gap? Physical Chemistry Chemical Physics, 9: 3641–3647, 2007. DOI. URL link.

[123] A. Beniya, T. Koitaya, H. Kondoh, K. Mukai, S. Yoshimoto, and J. Yoshinobu. Adsorption and reaction of NO on the clean and nitrogen modified Rh(111) surfaces. The Journal of Chemical Physics, 131(8):084704, 2009. DOI. URL link.

[124] L. J. Deiner, D.-H. Kang, and C. M. Friend. Low-temperature reduction of $NO_2$ on oxidized Mo(110). The Journal of Physical Chemistry B, 109(26):12826–12831, 2005. DOI. URL link.

[125] K. Queeney and C. Friend. Site-selective surface reactions: Nitric Oxide reduction on Mo(110). ChemPhysChem, 1(3):116–125, 2000. DOI. URL link.

[126] O. Gessner, A. M. D. Lee, J. P. Shaffer, H. Reisler, S. V. Levchenko, A. I. Krylov, J. G. Underwood, H. Shi, A. L. L. East, D. M. Wardlaw, E. T. Chrysostom, C. C. Hayden, and A. Stolow. Femtosecond multidimensional imaging of a molecular dissociation. Science, 311(5758):219–222, 2006. DOI. URL link.

[127] R.T. Kidd, D. Lennon, and S. R. Meech. Comparative study of the primary photochemical mechanisms of Nitric Oxide and Carbonyl Sulfide on Ag(111). The Journal of Physical Chemistry B, 103(35):7480–7488, 1999. DOI. URL link.

[128] K. Fukutani and Y. Murata. Photoexcited processes at metal and alloy surfaces: electronic structure and adsorption site. Surface Science, 390(1-3):164 – 173, 1997. DOI. URL link.

[129] T. Itoyama, M. Wilde, M. Matsumoto, T. Okano, and K. Fukutani. Adsorption and photoexcitation of NO on Ag/Pt(1 1 1). Surface Science, 493(1-3):84 – 90, 2001. DOI. URL link.

[130] S. K. So, R. Franchy, and W. Ho. Photodesorption of NO from Ag(111) and Cu(111). The Journal of Chemical Physics, 95(2):1385–1399, 1991. DOI. URL link.

[131] L. Krim and N. Lacome. The NO dimer, $^{14}N$ and $^{15}N$ isotopomers isolated in Argon matrix: A near-, mid-, and far-infrared study. The Journal of Physical Chemistry A, 102(13):2289–2296, 1998. DOI. URL link.

[132] N. Sheppard and C. De La Cruz. A systematic review of the application of vibrational spectroscopy to the determination of the structures of NO adsorbed on single-crystal metal surfaces. Physical Chemistry Chemical Physics, 12:2275–2284, 2010. DOI. URL link.

[133] J. Fan and M. Trenary. Symmetry and the surface infrared selection rule for the determination of the structure of molecules on metal surfaces. Langmuir, 10(10):3649–3657, 1994. DOI. URL link.

[134] A. Shiotari, Y. Kitaguchi, H. Okuyama, S. Hatta, and T. Aruga. Imaging covalent bonding between two NO molecules on Cu(110). Physical Review Letters, 106(15):156104, 2011. DOI. URL link.

[135] K. T. Queeney, S. Pang, and C. M. Friend. Spectroscopic evidence for perturbed NO dimers on oxidized Mo(110). The Journal of Chemical Physics, 109(18):8058–8061, 1998. DOI. URL link.

[136] M. Gajdoš, J. Hafner, and A. Eichler. Ab initio density-functional study of NO adsorption on close-packed transition and noble metal surfaces: II. Dissociative adsorption. Journal of Physics: Condensed Matter, 18(1):41, 2006. DOI. URL link.

[137] K. H. Kim, K. Watanabe, D. Mulugeta, H.-J. Freund, and D. Menzel. Enhanced photoinduced desorption from metal nanoparticles by photoexcitation of confined hot electrons using femtosecond laser pulses. Physical Review Letters, 107:047401, 2011. DOI. URL link.

[138] S. Hagen, P. Kate, F. Leyssner, D. Nandi, M. Wolf, and P. Tegeder. Excitation mechanism in the photoisomerization of a surface-bound azobenzene derivative: Role of the metallic substrate. The Journal of Chemical Physics, 129(16):164102, 2008. DOI. URL link.

[139] I. Kinoshita, A. Misu, and T. Munakata. Electronic excited state of NO adsorbed on Cu(111): A two-photon photoemission study. The Journal of Chemical Physics, 102(7):2970–2976, 1995. DOI. URL link.

[140] P. D. Johnson and S. L. Hulbert. Inverse-photoemission studies of adsorbed diatomic molecules. Physical Review B, 35:9427–9436, 1987. DOI. URL link.

[141] H. Nakamura and K. Yamashita. Theoretical study of the photodesorption mechanism of nitric oxide on a Ag(111) surface: A nonequilibrium Green's function approach to hot-electron tunneling. The Journal of Chemical Physics, 125(8):084708, 2006. DOI. URL link.

[142] T. A. Germer, J. C. Stephenson, E. J. Heilweil, and R. R. Cavanagh. Picosecond time-resolved adsorbate response to substrate heating: Spectroscopy and dynamics of CO/Cu(100). The Journal of Chemical Physics, 101(2):1704–1716, 1994. DOI. URL link.

[143] H. Petek, H. Nagano, M. J. Weida, and S. Ogawa. The role of Auger decay in hot electron excitation in copper. Chemical Physics, 251(1-3):71 – 86, 2000. DOI. URL link.

[144] R. Knorren, G. Bouzerar, and K. H. Bennemann. Dynamics of excited electrons in copper: The role of Auger electrons. Physical Review B, 63(9):094306, 2001. DOI. URL link.

[145] H.-J. Ernst, F. Charra, and L. Douillard. Interband electronic excitation-assisted atomic-scale restructuring of metal surfaces by nanosecond pulsed laser light. Science, 279(5351):679–681, 1998. DOI. URL link.

[146] N. Garcia Rey and H. Arnolds. Hot hole-induced dissociation of no dimers on a copper surface. The Journal of Chemical Physics, 135(22):224708, 2011. DOI. URL link.

[147] T. F. Heinz, F. J. Himpsel, E. Palange, and E. Burstein. Electronic transitions at the $CaF_2$/Si(111) interface probed by resonant three-wave mixing spectroscopy. Physical Review Letters, 63:644–647, 1989. DOI. URL link.

[148] S. Yamaguchi and T. Tahara. Novel interface-selective even-order nonlinear spectroscopy. Laser & Photonics Reviews, 2(1-2):74–82, 2008. DOI. URL link.

[149] P. Sen, S. Yamaguchi, and T. Tahara. New insight into the surface denaturation of proteins: electronic sum frequency generation study of cytochrome c at water interfaces. The Journal of Physical Chemistry B, 112(43):13473–13475, 2008. DOI. URL link.

[150] K. C. Chou, S. Westerberg, Y. R. Shen, P. N. Ross, and G. A. Somorjai. Probing the charge-transfer state of CO on Pt(111) by two-dimensional infrared-visible sum frequency generation spectroscopy. Physal Review B, 69:153413, 2004. DOI. URL link.

[151] T. Maeda, T. Nagahara, M. Aida, and T. Ishibashi. Identification of chemical species of fluorescein isothiocyanate isomer-I (FITC) monolayers on platinum by doubly resonant sum-frequency generation spectroscopy. Journal of Raman Spectroscopy, 39(11):1694–1702, 2008. DOI. URL link.

[152] D. Wu, G.-H. Deng, Y. Guo, and H.-F. Wang. Observation of the Interference between the Intramolecular IR-Visible and Visible-IR Processes in the Doubly Resonant Sum Frequency Generation Vibrational Spectroscopy of Rhodamine 6G Adsorbed at the Air/Water Interface. The Journal of Physical Chemistry A, 113(21):6058–6063, 2009. DOI. URL link.

[153] G. Petrocelli, S. Martellucci, and R. Francini. Wavelength dependence of second-harmonic generation at the copper surface. Applied Physics A: Materials Science & Processing, 56:263–266, 1993. URL link.

[154] C. Matranga and P. Guyot-Sionnest. Absolute intensity measurements of the optical second-harmonic response of metals from 0.9 to 2.5 eV. Journal of Chemical Physics, 115(20):9503–9512, 2001. DOI. URL link.

[155] F. Bisio, A. Winkelmann, W.-C. Lin, C.-T. Chiang, M. Nývlt, H. Petek, and J. Kirschner. Band structure effects in surface second harmonic generation: The case of Cu(001). Physical Review B, 80:125432, 2009. DOI. URL link.

[156] L. E. Urbach, K. L. Percival, J. M. Hicks, E. W. Plummer, and H.-L. Dai. Resonant surface second-harmonic generation: Surface states on Ag(110). Physical Review B, 45:3769–3772, 1992. DOI. URL link.

[157] S. M. Dounce, M. Yang, and H.-L. Dai. Surface-state relaxation dynamics on Ag(110) probed by temperature-dependent resonantly enhanced second-harmonic generation. Physal Review B, 67:205410, 2003. DOI. URL link.

[158] J. Woll, G. Meister, U. Barjenbruch, and A. Goldmann. Oxygen-chemisorption on Cu(110) - a combined study by 2nd-harmonic spectroscopy and photoemission. Applied Physics A-materials Science & Processing, 60(2):173–178, 1995. URL link.

[159] C. Schwab, G. Meister, J. Woll, A. Gerlach, and A. Goldmann. Experimental intensity analysis of second harmonic generation at the Cu(110) surface. Surface Science, 457(1-2):273 – 284, 2000. DOI. URL link.

[160] R. M. Corn and D. A. Higgins. Optical second harmonic generation as a probe of surface chemistry. Chemical Reviews, 94(1):107–125, 1994. DOI. URL link.

[161] S. K. Shaw, A. Lagutchev, D. D. Dlott, and A. A. Gewirth. Sum-frequency spectroscopy of molecular adsorbates on low-index Ag surfaces: Effects of azimuthal rotation. Analytical Chemistry, 81(3):1154–1161, 2009. DOI. URL link.

[162] F. X. Wang, F. J. Rodriguez, W. M. Albers, R. Ahorinta, J. E. Sipe, and M. Kauranen. Surface and bulk contributions to the second-order nonlinear optical response of a gold film. Physical Review B, 80:233402, 2009. DOI. URL link.

[163] N. Bloembergen, R. K. Chang, S. S. Jha, and C. H. Lee. Optical second-harmonic generation in reflection from media with inversion symmetry. Physical Review, 174:813–822, 1968. DOI. URL link.

[164] R. Vollmer, M. Straub, and J. Kirschner. Second harmonic generation from the Cu(001) surface. Surface Science, 352-354(0):684 – 688, 1996. DOI. URL link.

[165] A. G. Lambert, P. B. Davies, and D. J. Neivandt. Implementing the theory of sum frequency generation vibrational spectroscopy: a tutorial review. Applied Spectroscopy Reviews, 40(2): 103–145, 2005. DOI.

[166] C. Hirose, N. Akamatsu, and K. Domen. Formulas for the analysis of the surface SFG spectrum and transformation coefficients of cartesian SFG tensor components. Applied Spectroscopy, 46 (6):1051–1072, 1992. URL link.

[167] M. Buck, F. Eisert, M. Grunze, and F. Trager. Second-order nonlinear susceptibilities of surfaces. A systematic study of the wavelength and coverage dependence of thiol adsorption on polycrystalline gold. Applied Physics A: Materials Science & Processing, 60:1–12, 1995. DOI. URL link.

[168] P. Cortona and C. Sapet. The (100), (110), and (111) Cu surfaces revisited by the semiempirical LCAO method. International Journal of Quantum Chemistry, 99(5):713–723, 2004. DOI. URL link.

[169] P. Heimann, J. Hermanson, H. Miosga, and H. Neddermeyer. Photoemission observation of a new surface state band on Cu(110). Surface Science, 85(2):263 – 268, 1979. DOI. URL link.

[170] R. A. Bartynski, T. Gustafsson, and P. Soven. Observation of an unoccupied surface state on Cu(110) by inverse photoemission. Physical Review B, 31(8):4745–4750, 1985. DOI. URL link.

[171] B. Reihl and K. H. Frank. Unoccupied electronic surface states on Cu(110). Physical Review B, 31(12):8282–8284, 1985. DOI. URL link.

[172] A. Goldmann, V. Dose, and G. Borstel. Empty electronic states at the (100), (110), and (111) surfaces of Nickel, Copper, and Silver. Physical Review B, 32(4):1971–1980, 1985. DOI. URL link.

[173] P. M. Echenique and J. B. Pendry. The existence and detection of Rydberg states at surfaces. Journal of Physics C: Solid State Physics, 11(10):2065, 1978. DOI. URL link.

[174] E. Dietz and F.J. Himpsel. Photoemission via Bloch states and evanescent band gap states for Cu(110). Solid State Communications, 30(4):235 – 238, 1979. DOI. URL link.

[175] Y. Sonoda. Electronic states of Cu(110) investigated with angle-resolved two-photon photoemission spectroscopy. Physical Review B, 83(24):245410, 2011. DOI. URL link.

[176] W. Jacob, V. Dose, and A. Goldmann. Atomic adsorption of oxygen on Cu(111) and Cu(110). Applied Physics A: Materials Science &amp; Processing, 41:145–150, 1986. URL link.

[177] R. Courths, S. Hüfner, P. Kemkes, and G. Wiesen. Electronic structure investigation of Cu(110), Ag(110) and Ni(110) surfaces covered with chemisorbed oxygen up to half a monolayer. Surface Science, 376(1-3):43 – 59, 1997. DOI. URL link.

[178] Ph. Hofmann, K. C. Rose, V. Fernandez, A. M. Bradshaw, and W. Richter. Study of surface states on Cu(110) using optical reflectance anisotropy. Physical Review Letters, 75(10):2039–2042, 1995. DOI. URL link.

[179] J. K. Hansen, J. Bremer, and O. Hunderi. The electronic structure of Cu(110) and Ag(110) surfaces studied by reflection anisotropy spectroscopy. Surface Science, 418(2):L58 – L61, 1998. DOI. URL link.

[180] D. S. Martin and P. Weightman. Reflection anisotropy spectroscopy of molecular assembly at metal surfaces. Thin Solid Films, 455-456:752 – 758, 2004. DOI. URL link.

[181] D. S. Martin, R. J. Cole, and P. Weightman. Effects of ion bombardment on the optical and electronic properties of Cu(110). Physical Review B, 72(3):035408, 2005. DOI. URL link.

[182] G. E. Isted and D. S. Martin. Preparation and characterisation of Au(110) and Cu(110) surfaces for applications in ambient environments. Applied Surface Science, 252(5):1883 – 1890, 2005. DOI. URL link.

[183] P. D. Lane, G. E. Isted, and R. J. Cole. Effect of surface defects and adsorbates on the optical anisotropy of Cu(110). Physical Review B, 82(7):075416, 2010. DOI. URL link.

[184] G. E. Isted, P. D. Lane, R. J. Cole, M. Caffio, and R. Schaub. Estimating the range of influence of point defects on Cu(110) surface states. Physical Review B, 83(15):155403, 2011. DOI. URL link.

[185] D. S. Martin and P. Weightman. Reflection anisotropy spectroscopy: a new probe of metal surfaces. Surface and Interface Analysis, 31(10):915–926, 2001. URL link.

[186] M.Y. Jiang, G. Pajer, and E. Burstein. Role of surface electronic transitions in linear and nonlinear electromagnetic phenomena at noble metal surfaces: beyond jellium. Surface Science, 242 (1-3):306 – 313, 1991. DOI. URL link.

[187] L. D. Sun, M. Hohage, P. Zeppenfeld, and R. E. Balderas-Navarro. Origin and temperature dependence of the surface optical anisotropy on Cu(110). Surface Science, 589(1-3):153 – 163, 2005. DOI. URL link.

[188] C. I. Smith, A. J. Maunder, C. A. Lucas, R. J. Nichols, and P. Weightman. Adsorption of Pyridine on Au(110) as measured by reflection anisotropy spectroscopy. Journal of The Electrochemical Society, 150(4):E233–E236, 2003. DOI. URL link.

[189] S. Reiff and J. H. Block. Oxygen chemisorption and surface reconstruction on Ag(110) investigated with second-harmonic generation. Surface Science, 345(3):281 – 289, 1996. DOI. URL link.

[190] S. M. Dounce, M. Yang, and H.-L. Dai. Physisorption on a metal surface probed by surface state resonant second harmonic generation. Surface Science, 565(1):27–36, 2004. DOI. URL link.

[191] R. Courths, B. Cord, H. Wern, H. Saalfeld, and S. Hüfner. Dispersion of the oxygen-induced bands on Cu (110) - an angle-resolved ups study of the system p(2x1)O/Cu(110). Solid State Communications, 63(7):619 – 623, 1987. DOI. URL link.

[192] G. R. Gruzalski, D. M. Zehner, J. F. Wendelken, and R. S. Hathcock. LEED observations of oxygen ordering on Cu(110). Surface Science, 151(2-3):430 – 446, 1985. DOI. URL link.

[193] R. Feidenhans'l, F. Grey, R. L. Johnson, and M. Nielsen. Determination of the Cu(110)-c(6x2)-O structure by x-ray diffraction. Physical Review B, 44:1875–1879, 1991. DOI. URL link.

[194] D. A. Pinnick, S. A. Lee, X. Sun, and H. J. Simon. Optical second-harmonic-generation study of quartz up to 31 GPa. Physical Review B, 55:8031–8033, 1997. DOI. URL link.

[195] M. Harada, S. Kurimura, K. Kitamura, K. Muramatsu, and M. Ueda. Polarization Dependence of SHG Efficiency in Periodically-Twinned QPM Quartz. In Conference on Lasers and Electro-Optics/Quantum Electronics and Laser Science Conference and Photonic Applications Systems Technologies, page JTuA116. Optical Society of America, 2007. URL link.

[196] A. Gerlach, K. Berge, A. Goldmann, I. Campillo, A. Rubio, J. M. Pitarke, and P. M. Echenique. Lifetime of *d* holes at Cu surfaces: Theory and experiment. Physical Review B, 64:085423, 2001. DOI. URL link.

[197] C. Timm and K. H. Bennemann. Response theory for time-resolved second-harmonic generation and two-photon photoemission. Journal of Physics: Condensed Matter, 16(4):661, 2004. DOI. URL link.

[198] H. Petek, H. Nagano, and S. Ogawa. Hole decoherence of $d$ bands in Copper. Physical Review Letters, 83:832–835, 1999. DOI. URL link.

[199] Y.-H. L. Liau, A. N. Unterreiner, Q. Chang, and N. F. Scherer. Ultrafast dephasing of single nanoparticles studied by two-pulse second-order interferometry. The Journal of Physical Chemistry B, 105(11):2135–2142, 2001. DOI. URL link.

[200] N. E. Karatzas and A. T. Georges. Model for ultrafast harmonic generation from a gold surface: extraction of dephasing times for continuum-continuum transitions. Journal of the Optical Society of America B, 26(12):2218–2227, 2009. DOI. URL link.

[201] L. C. Parlett. Laser-induced ESR shifts in the sodium atom spectrum. Chemical Physics Letters, 296(5-6):571 – 578, 1998. DOI. URL link.

[202] A. J. Moad and G. J. Simpson. A unified treatment of selection rules and symmetry relations for sum-frequency and second harmonic spectroscopies. The Journal of Physical Chemistry B, 108 (11):3548–3562, 2004. DOI. URL link.

[203] C. Humbert, L. Dreesen, S. Nihonyanagi, T. Masuda, T. Kondo, A. A. Mani, K. Uosaki, P. A. Thiry, and A. Peremans. Probing a molecular electronic transition by two-colour sum-frequency generation spectroscopy. Applied Surface Science, 212âĂŞ213(0):797 – 803, 2003. DOI. URL link.

[204] J. Giergiel, C. E. Reed, S. Ushioda, and J. C. Hemminger. Attenuated-total-reflection study of pyridine overlayers on silver films. Physical Review B, 31:3323–3329, 1985. DOI. URL link.

[205] A. K. Burnham and T. D. Gierke. A comparison of effective polarizabilities from electro-optical experiments using microscopic and macroscopic theories of the local electric field. The Journal of Chemical Physics, 73(10):4822–4831, 1980. DOI. URL link.

[206] A. Bilić, J. R. Reimers, and N. S. Hush. Adsorption of Pyridine on the Gold(111) surface: Implications for alligator clips for molecular wires. The Journal of Physical Chemistry B, 106 (26):6740–6747, 2002. DOI. URL link.

[207] D. Y. Wu, M. Hayashi, Y. J. Shiu, K. K. Liang, C. H. Chang, Y. L. Yeh, and S. H. Lin. A quantum chemical study of bonding interaction, vibrational frequencies, force constants, and vibrational coupling of pyridine-$M_n$ (M = Cu, Ag, Au; n=2-4). Journal of Physical Chemistry A, 107(45): 9658–9667, 2003. DOI. URL link.

[208] D. Y. Wu, M. Hayashi, C. H. Chang, K. K. Liang, and S. H. Lin. Bonding interaction, low-lying states and excited charge-transfer states of pyridine-metal clusters: Pyridine-$M_n$ (M=Cu, Ag, Au; n=2-4). Journal of Chemical Physics, 118(9):4073–4085, 2003. DOI. URL link.

[209] S. A. Krasnokutski and D.-S. Yang. High-resolution electron spectroscopy and $\sigma/\pi$ structures of M(pyridine) and $M^+$(pyridine) (M=Li, Ca, and Sc) complexes. Journal of Chemical Physics, 130(13):134313, 2009. DOI. URL link.

[210] Z. Ma, F. Rissner, L. Wang, G. Heimel, Q. Li, Z. Shuai, and E. Zojer. Electronic structure of pyridine-based SAMs on flat Au(111) surfaces: extended charge rearrangements and Fermi level pinning. Physical Chemistry Chemical Physics, 13:9747–9760, 2011. DOI. URL link.

[211] Y. P. Zhang, S. Wang, G. Q. Xu, and E. S. Tok. Tuning molecular binding configurations of Pyridine on Si(111)-(7x7) via surface modification. The Journal of Physical Chemistry C, 115 (5):2140–2145, 2011. DOI. URL link.

[212] J. E. Demuth, K. Christmann, and P. N. Sanda. The vibrations and structure of pyridine chemisorbed on Ag(111): the occurrence of a compressional phase transformation. Chemical Physics Letters, 76(2):201 – 206, 1980. DOI. URL link.

[213] C. M. Mate, G. A. Somorjai, H. W. K. Tom, X. D. Zhu, and Y. R. Shen. Vibrational and electronic spectroscopy of pyridine and benzene adsorbed on the Rh(111) crystal surface. The Journal of Chemical Physics, 88(1):441–450, 1988. URL link.

[214] F. P. Netzer and G. Rangelov. The orientation of Pyridine on Rh(111). Surface Science, 225(3): 260–266, 1990. DOI. URL link.

[215] F. P. Netzer and M. G. Ramsey. Structure and orientation of organic-molecules on metal-surfaces. Critical Reviews In Solid State and Materials Sciences, 17(5):397–475, 1992. DOI. URL link.

[216] S. Haq and D. A. King. Configurational transitions of Benzene and Pyridine adsorbed on Pt(111) and Cu(110) surfaces: An infrared study. The Journal of Physical Chemistry, 100(42):16957–16965, 1996. DOI. URL link.

[217] M. E. Bridge, M. Connolly, D. R. Lloyd, J. Somers, P. Jakob, and D. Menzel. Electron spectroscopic studies of pyridine on metal surfaces. Spectrochimica Acta Part A: Molecular Spectroscopy, 43(12):1473 – 1478, 1987. DOI. URL link.

[218] M. P. Andersson and P. Uvdal. Transformation of pyridine to $\alpha$-pyridyl on W(110) as probed by vibrational spectroscopy: Experiments and calculations. Journal of Physical Chemistry B, 105 (39):9458–9462, 2001. DOI. URL link.

[219] P. Jakob, D. R. Lloyd, and D. Menzel. Pyridine on Ru(001) - thermal evolution. Surface Science, 227(3):325–336, 1990. DOI. URL link.

[220] Q.-X. Li, X.-K. Xue, Q.-J. Xu, and W.-B. Cai. Application of surface-enhanced infrared absorption spectroscopy to investigate pyridine adsorption on platinum-group electrodes. Applied Spectroscopy, 61(12):1328–1333, 2007. DOI. URL link.

[221] D. B. Dougherty, J. Lee, and J. T. Yates. Role of conformation in the electronic properties of chemisorbed Pyridine on Cu(110): An STM/STS study. The Journal of Physical Chemistry B, 110(24):11991–11996, 2006. DOI. URL link.

[222] M. Bader, J. Haase, K. H. Frank, C. Ocal, and A. Puschmann. Near Edge X-Ray absorption fine-structure studies of ring molecules adsorbed on single-crystal surfaces. Journal of de Physique, 47(C-8):491–496, 1986. DOI. URL link.

[223] D. Heskett, L.E. Urbach, K.J. Song, E.W. Plummer, and H.L. Dai. Oxygen and pyridine on Ag(110) studied by second harmonic generation: Coexistence of two phases within monolayer pyridine coverage. Surface Science, 197(1-2):225 – 238, 1988. DOI. URL link.

[224] J. E. Whitten. Adsorption of thiophene and pyridine on W(110). Surface Science, 546(2-3): 107–116, 2003. DOI. URL link.

[225] M. Yang and H. L. Dai. Determination of molecular ordering at a buried interface and the effect of interfacial ordering on thin film crystallization by second harmonic generation. Langmuir, 20 (1):37–40, 2004. DOI. URL link.

[226] S. Bahr and V. Kempter. Comparative study of the interaction of pyridine with polycrystalline Ag and amorphous solid water. Journal of Chemical Physics, 127(17):174514, 2007. DOI. URL link.

[227] J. G. Lee, J. Ahner, and J.T. Yates. The adsorption conformation of chemisorbed pyridine on the Cu(110) surface. The Journal of Chemical Physics, 114(3):1414–1419, 2001. DOI. URL link.

[228] T. Gießel, O. Schaff, R. Lindsay, P. Baumgartel, M. Polcik, A. M. Bradshaw, A. Koebbel, T. McCabe, M. Bridge, D. R. Lloyd, and D. P. Woodruff. Adsorption site and orientation of pyridine on Cu110 determined by photoelectron diffraction. The Journal of Chemical Physics, 110(19): 9666–9672, 1999. DOI. URL link.

[229] O. Pluchery and A. Tadjeddine. Investigation of the adsorption of 4-cyanopyridine on Au(111) by in situ visible-infrared sum frequency generation. Journal of Electroanalytical Chemistry, 500 (1-2):379 – 387, 2001. DOI. URL link.

[230] O. Pluchery, M. Tadjeddine, J.-P. Flament, and A. Tadjeddine. Adsorption of 4-cyanopyridine on au(111): ab initio calculations and sfg measurements. Phys. Chem. Chem. Phys., 3:3343–3350, 2001. DOI. URL link.

[231] Y. Ie, T. Hirose, H. Nakamura, M. Kiguchi, N. Takagi, M. Kawai, and Y. Aso. Nature of electron transport by Pridine-based tripodal anchors: potential for robust and conductive single-molecule junctions with gold electrodes. Journal of the American Chemical Society, 133(9):3014–3022, 2011. DOI. URL link.

[232] M. Kamenetska, S. Y. Quek, A. C. Whalley, M. L. Steigerwald, H. J. Choi, S. G. Louie, C. Nuckolls, M. S. Hybertsen, J. B. Neaton, and L. Venkataraman. Conductance and geometry of Pyridine-linked single-molecule junctions. Journal of the American Chemical Society, 132(19): 6817–6821, 2010. DOI. URL link.

[233] Z. Liu, S.-Y. Ding, Z.-B. Chen, X. Wang, J.-H. Tian, J. R. Anema, X.-S. Zhou, D.-Y. Wu, B.-W. Mao, X. Xu, B. Ren, and Z.-Q. Tian. Revealing the molecular structure of single-molecule junctions in different conductance states by fishing-mode tip-enhanced Raman spectroscopy. Nature Communications, 2:305, 2011. DOI. URL link.

[234] S. Y. Quek, M. Kamenetska, M. L. Steigerwald, H. J. Choi, S. G. Louie, M. S. Hybertsen, J. B. Neaton, and L. Venkataraman. Mechanically controlled binary conductance switching of a single-molecule junction. Nature Nanotechnology, 4(4):230–234, 2009. DOI. URL link.

[235] E. S. Tam, J. J. Parks, W. W. Shum, Y.-W. Zhong, M. B. Santiago-Berrios, X. Zheng, W. Yang, G. K. . L. Chan, H. D. Abruna, and D. C. Ralph. Single-molecule conductance of Pyridine-terminated dithienylethene switch molecules. Acs Nano, 5(6):5115–5123, 2011. DOI. URL link.

[236] C. Fan, B. Gillespie, G. Wang, A. J. Heeger, and K. W. Plaxco. Spectroscopy and electrochemistry of the covalent Pyridine-Cytochrome c complex and a Pyridine-induced, alkaline-like conformation. The Journal of Physical Chemistry B, 106(43):11375–11383, 2002. DOI. URL link.

[237] F. Henglein, D. M. Kolb, L. Stolberg, and J. Lipkowski. Electroreflectance spectroscopy of Au(100) covered by adsorbed pyridine molecules. Surface Science, 291(3):325 – 336, 1993. DOI. URL link.

[238] M. Fleischmann, P. J. Hendra, and A. J. McQuilla. Raman-spectra of pyridine adsorbed at a silver electrode. Chemical Physics Letters, 26(2):163–166, 1974. DOI. URL link.

[239] Y. Fang, N.-H. Seong, and D. D. Dlott. Measurement of the distribution of site enhancements in surface-Enhanced Raman Scattering. Science, 321(5887):388–392, 2008. DOI. URL link.

[240] E. J. Blackie, E. C. Le Ru, and P. G. Etchegoin. Single-molecule surface-enhanced Raman spectroscopy of nonresonant molecules. Journal of the American Chemical Society, 131(40): 14466–14472, 2009. DOI. URL link.

[241] J. R. Lombardi and R. L. Birke. A unified view of surface-enhanced Raman scattering. Accounts of Chemical Research, 42(6):734–742, 2009. DOI. URL link.

[242] J. R. Lombardi, R. L. Birke, T. Lu, and J. Xu. Charge transfer theory of surface enhanced Raman spectroscopy: Herzberg-Teller contributions. The Journal of Chemical Physics, 84(8): 4174–4180, 1986. DOI. URL link.

[243] D.-Y. Wu, B. Ren, X. Xu, G.-K. Liu, Z.-L. Yang, and Z.-Q. Tian. Periodic trends in the bonding and vibrational coupling: Pyridine interacting with transition metals and noble metals studied by surface-enhanced Raman spectroscopy and density-functional theory. Journal of Chemical Physics, 119(3):1701–1709, 2003. URL link.

[244] D. Y. Wu, B. Ren, and Z. Q. Tian. Binding interactions and Raman spectral properties of pyridine interacting with bimetallic silver-gold clusters. ChemPhysChem, 7(3):619–628, 2006. DOI. URL link.

[245] A. Kaczor, K. Malek, and M. Baranska. Pyridine on colloidal Silver. Polarization of surface studied by surface-enhanced Raman scattering and density functional theory methods. Journal of Physical Chemistry C, 114(9):3909–3917, 2010. DOI. URL link.

[246] A. Carley, P. Davies, D. Edwards, R. Jones, and M. Parsons. Molecularly resolved studies of the reaction of Pyridine and Dimethylamine with Oxygen at a Cu(110) surface. Topics in Catalysis, 36:21–32, 2005. DOI. URL link.

[247] B. J. Bandy, D. R. Lloyd, and N. V. Richardson. Selection rules in photoemission from adsorbates: Pyridine adsorbed on copper. Surface Science, 89(1-3):344 – 353, 1979. DOI. URL link.

[248] N. Atodiresei, V. Caciuc, J.-H. Franke, and S. Blügel. Role of the van der Waals interactions on the bonding mechanism of pyridine on Cu(110) and Ag(110) surface: First-principles study. Physical Review B, 78(4):045411, 2008. DOI. URL link.

[249] J. A. Rodriguez. The bonding of acetate, methoxy, thiomethoxy and pyridine to Cu surfaces: a molecular orbital study. Surface Science, 273(3):385 – 404, 1992. DOI. URL link.

[250] B. Quiniou, V. Bulović, and R. M. Osgood. Observation of image-potential-induced resonances on Cu(110) using the two-photon photoemission technique. Physical Review B, 47(23):15890–15895, 1993. DOI. URL link.

[251] B.H. Blott, B.J. Hopkins, and T.J. Lee. The work function of caesium coated polycrystalline tungsten. Surface Science, 3(5):493 – 496, 1965. DOI. URL link.

[252] R. W. Verhoef and M. Asscher. The work function of adsorbed alkalis on metals revisited: a coverage-dependent polarizability approach. Surface Science, 391(1-3):11 – 18, 1997. DOI. URL link.

[253] L. M. Brian and J. P. Cowin. Corrected electrostatic model for dipoles adsorbed on a metal surface. The Journal of Chemical Physics, 101(9):8138–8151, 1994. DOI. URL link.

[254] Q. Zhong, C. Gahl, and M. Wolf. Two-photon photoemission spectroscopy of pyridine adsorbed on Cu(111). Surface Science, 496(1-2):21 – 32, 2002. DOI. URL link.

[255] J. L. Gland and G. A. Somorjai. Low energy electron diffraction and work function studies of benzene, naphthalene and pyridine adsorbed on Pt(111) and Pt(100) single crystal surfaces. Surface Science, 38(1):157 – 186, 1973. DOI. URL link.

[256] Z. Ma and S. Dai. Design of novel structured Gold nanocatalysts. ACS Catalysis, 1(7):805–818, 2011. DOI. URL link.

[257] G. Attard and C. Barnes. Surfaces. Oxford chemistry primers. Oxford Science Publication, Bath, 2003.

[258] R. M. Hochstra and J. W. Michaluk. Excited state dipole moment of Pyridine. Journal of Chemical Physics, 55(9):4668, 1971. DOI. URL link.

[259] A. L. McClellan, W. H. Freeman, and Co. Select values of the dipole moment of molecules in the gas phase., 1963. URL link.

[260] A. C. Testa. Animation of 27 fundamental vibrations of Pyridine. URL link.

[261] M. Morkel, H. Unterhalt, T. Kluner, G. Rupprechter, and H.-J. Freund. Interpreting intensities in vibrational sum frequency generation (SFG) spectroscopy: CO adsorption on Pd surfaces. Surface Science, 586(1-3):146 – 156, 2005. DOI. URL link.

[262] Z. Rosenzweig and M. Asscher. Optical second-harmonic generation from surfaces as a monitor for adsorbate induced work function changes. Surface Science, 204(1-2):L732 – L738, 1988. DOI. URL link.

[263] M. Asscher and Z. Rosenzweig. Adsorbate-metal interactions: An optical second harmonic generation study. Journal of Vacuum Science and Technology A, 9(3):1913–1918, 1991. DOI. URL link.

[264] A. D. Curtis, S. B. Reynolds, A. R. Calchera, and J. E. Patterson. Understanding the role of nonresonant sum-frequency generation from polystyrene thin films. The Journal of Physical Chemistry Letters, 1(16):2435–2439, 2010. DOI. URL link.

[265] S. Westerberg, C. Wang, K. Chou, and G. A. Somorjai. High-pressure ammonia adsorption and dissociation on clean Fe(111) and Oxygen-precovered Fe(111) studied by sum frequency generation vibrational spectroscopy. The Journal of Physical Chemistry B, 108(20):6374–6380, 2004. DOI. URL link.

[266] L. Dreesen, C. Volcke, Y. Sartenaer, A. Peremans, P. A. Thiry, C. Humbert, J. Grugier, and J. Marchand-Brynaert. Comparative study of decyl thiocyanate and decanethiol self-assembled monolayers on gold substrates. Surface Science, 600(18):4052–4057, 2006. DOI. URL link.

[267] F. Vidal and A. Tadjeddine. Sum-frequency generation spectroscopy of interfaces. Reports on Progress in Physics, 68(5):1095, 2005. URL link.

[268] D.-Y. Wu, X.-M. Liu, S. Duan, X. Xu, B. Ren, S.-H. Lin, and Z.-Q. Tian. Chemical enhancement effects in SERS spectra: a quantum chemical study of Pyridine interacting with Copper, Silver, Gold and Platinum metals. The Journal of Physical Chemistry C, 112(11):4195–4204, 2008. DOI. URL link.

[269] B. B. DeMore, W. S. Wilcox, and J. H. Goldstein. Microwave spectrum and dipole moment of Pyridine. The Journal of Chemical Physics, 22(5):876–877, 1954. DOI. URL link.

[270] M. Kasha. Characterization of electronic transitions in complex molecules. Discussions of the Faraday Society, 9:14–19, 1950. DOI. URL link.

[271] S. I. Anisimov and B. Rethfeld. Theory of ultrashort laser pulse interaction with a metal. Nonresonant Laser-Matter Interaction (NLMI-9), 3093(1):192–203, 1997. DOI. URL link.

[272] M. Bonn, D. N. Denzler, S. Funk, M. Wolf, S.-S. Wellershoff, and J. Hohlfeld. Ultrafast electron dynamics at metal surfaces: Competition between electron-phonon coupling and hot-electron transport. Physical Review B, 61:1101–1105, 2000. DOI. URL link.

[273] E. Hasselbrink. How non-adiabatic are surface dynamical processes? Current Opinion in Solid State and Materials Science, 10(3-4):192–204, 2006. DOI. URL link.

[274] J. W. Gadzuk. Inelastic resonance scattering, tunneling, and desorption. Physical Review B, 44: 13466–13477, 1991. DOI. URL link.

[275] E. Carpene. Ultrafast laser irradiation of metals: Beyond the two-temperature model. Physical Review B, 74:024301, 2006. DOI. URL link.

[276] J. Garduno-Mejia, M. P. Higlett, and S. R. Meech. Modelling the influence of nonthermal electron dynamics in thin and ultrathin gold films. Chemical Physics, 341(1-3):276 – 284, 2007. DOI. URL link.

[277] F. Budde, T. F. Heinz, A. Kalamarides, M. M. T. Loy, and J. A. Misewich. Vibrational distributions in desorption induced by femtosecond laser pulses: coupling of adsorbate vibration to substrate electronic excitation. Surface Science, 283(1-3):143 – 457, 1993. DOI. URL link.

[278] D. M. Newns, T. F. Heinz, and J. A. Misewich. Desorption by femtosecond laser pulses: an electron-hole effect? Progress of Theoretical Physics Supplement, 106:411–418, 1991. DOI. URL link.

[279] H. Ueba and B. N. J. Persson. Heat transfer between adsorbate and laser-heated hot electrons. Journal of Physics: Condensed Matter, 20(22):224016, 2008. DOI. URL link.

[280] M. Brandbyge, P. Hedegaard, T. F. Heinz, J. A. Misewich, and D. M. Newns. Electronically driven adsorbate excitation mechanism in femtosecond-pulse laser desorption. Physical Review B, 52(8):6042–6056, 1995. DOI. URL link.

[281] J. P. Culver, M. Li, L. G. Jahn, R. M. Hochstrasser, and A. G. Yodh. Vibrational response of surface adsorbates to femtosecond substrate heating. Chemical Physics Letters, 214(5):431 – 437, 1993. DOI. URL link.

[282] K. Watanabe, K.-I. Inoue, I. F. Nakai, and Y. Matsumoto. Nonadiabatic coupling between C-O stretching and Pt substrate electrons enhanced by frustrated mode excitations. Physical Review B, 81(24):241408, 2010. DOI. URL link.

[283] M. Bonn, H. Ueba, and M. Wolf. Theory of sum-frequency generation spectroscopy of adsorbed molecules using the density matrix method broadband vibrational sum-frequency generation and applications. Journal of Physics: Condensed Matter, 17(8):S201, 2005. DOI. URL link.

[284] H. Arnolds, D. A. King, and I. M. Lane. Inducing non-adiabatic effects through coadsorption: CO+NO on iridium. Chemical Physics, 350(1-3):94 – 103, 2008. DOI. URL link.

[285] M. Bonn, C. Hess, S. Funk, J. H. Miners, B. N. J. Persson, M. Wolf, and G. Ertl. Femtosecond surface vibrational spectroscopy of CO adsorbed on Ru(001) during desorption. Physical Review Letters, 84:4653–4656, 2000. DOI. URL link.

[286] M. Nagao, K. Watanabe, and Y. Matsumoto. Ultrafast vibrational energy transfer in the layers of $D_2O$ and CO on Pt(111) studied with time-resolved sum-frequency-generation spectroscopy. The Journal of Physical Chemistry C, 113(27):11712–11719, 2009. DOI. URL link.

[287] J. Hohlfeld, U. Conrad, and E. Matthias. Does femtosecond time-resolved second-harmonic generation probe electron temperatures at surfaces? Applied Physics B: Lasers and Optics, 63: 541–544, 1996. DOI. URL link.

[288] J. Hohlfeld, D. Grosenick, U. Conrad, and E. Matthias. Femtosecond time-resolved reflection second-harmonic generation on polycrystalline copper. Applied Physics A: Materials Science & Processing, 60:137–142, 1995. DOI. URL link.

[289] D. R. Lide. CRC Handbook of Chemistry and Physics. CRC Press, 82th edition, 2001. URL link.

[290] F. Cecchet, D. Lis, J. Guthmuller, B. Champagne, Y. Caudano, C. Silien, A. Addin Mani, P. A. Thiry, and A. Peremans. Orientational analysis of dodecanethiol and p-nitrothiophenol SAMs on metals with polarisation-dependent SFG spectroscopy. ChemPhysChem, 11(3):607–615, 2010. DOI. URL link.

[291] U. Schröder and P. Guyot-Sionnest. Optical sum frequency studies of adsorption and laser-induced desorption of CO on W(110). Surface Science, 421(1-2):53 – 58, 1999. DOI. URL link.

[292] P. Castrucci, R. Gunnella, R. Bernardini, P. Falcioni, and M. De Crescenzi. Magnetic force microscopy study of perpendicular magnetization reorientation for Fe grown on Cu/Si(111). Physical Review B, 65:235435, 2002. DOI. URL link.

[293] S. Y. Han, J. H. Kim, J. K. Song, and S. K. Kim. Simultaneous observation of dipole-bound and valence electron states in Pyridine tetramer anion. The Journal of Chemical Physics, 109(22): 9656–9659, 1998. DOI. URL link.

[294] S. Y. Han, J. K. Song, J. H. Kim, H. B. Oh, and S. K. Kim. Photoelectron spectroscopy of pyridine cluster anions, $(\mathrm{Py})_n^-$(n = 4-13). The Journal of Chemical Physics, 111(9):4041–4050, 1999. DOI. URL link.

[295] B.G. Frederick, Q. Chen, F. M. Leibsle, S. S. Dhesi, and N. V. Richardson. Electron-stimulated disordering in c(8x2) benzoate/Cu(110): a combined STM, LEED and HREELS study. Surface Science, 394(1-3):26 – 46, 1997. DOI. URL link.

[296] B. G. Frederick, A. Munz, Th. Bertrams, Q. Chen, C. C. Perry, and N. V. Richardson. Negative ion mediated molecular manipulation with STM of c(8x2) benzoate /Cu(110). Chemical Physics Letters, 272(5-6):438 – 444, 1997. DOI. URL link.

[297] E.T. Jensen, R.E. Palmer, and P.J. Roust. Transient negative ions in the Spectroscopy and dynamics of molecules on surfaces: orientational effects. Journal of Electron Spectroscopy and Related Phenomena, 54-55:519 – 527, 1990. DOI. URL link.

[298] Q. Chen, B. G. Frederick, and N. V. Richardson. An HREELS study of $\pi^*$ and $\sigma^*$ negative ion resonances of c(8x2) benzoate on Cu(110). The Journal of Chemical Physics, 108(14):5942–5947, 1998. DOI. URL link.

[299] N. W. Ashcroft and N. D. Mermin. Solid State Physics. Holt, Rinerhart and Winston, Ithaca, 1st edition, 1976.

[300] H. Raether. Surface plasmons on smooth and rough surfaces and on gratings. Nature Publishing Group, 1988.

[301] W. L. Barnes, A. Dereux, and T. W. Ebbesen. Surface plasmon subwavelength optics. Nature, 424(6950):824–830, 2003. URL link.

[302] A. Otto. Excitation of nonradiative surface plasma waves in Silver by method of frustrated total reflection. Zeitschrift Fur Physik, 216(4):398, 1968. URL link.

[303] E. Kretschm and H. Raether. Radiative decay of non radiative surface plasmons excited by light. Zeitschrift Fur Naturforschung Part A-astrophysik Physik Und Physikalische Chemie, A 23(12): 2135–&, 1968.

[304] M. Wolf, X., Y. Zhu, J. M. White, T. H. Koschmieder, and J. C. Thompson. Surface plasmon enhanced photochemistry: Mo(CO)$_6$-Al-quartz. Journal of Chemical Physics, 97(9):7015–7016, 1992. DOI. URL link.

[305] K. Watanabe, K. Sawabe, and Y. Matsumoto. Adsorbate-localized excitation in surface photochemistry: Methane on Pt(111). Physical Review Letters, 76(10):1751–1754, 1996. DOI. URL link.

[306] F. J. García-Vidal and L. Martín-Moreno. Transmission and focusing of light in one-dimensional periodically nanostructured metals. Physical Review B, 66(15):155412, 2002. URL link.

[307] E. K. Popov, N. Bonod, and S. Enoch. Comparison of plasmon surface waves on shallow and deep metallic 1D and 2D gratings. Optics Express, 15(7):4224–4237, 2007. DOI. URL link.

[308] F. Everts, H. Wormeester, and B. Poelsema. Optical anisotropy induced by ion bombardment of Ag(001). Physical Review B, 78(15):155419, 2008. DOI. URL link.

[309] D. J. Burke, T. Vondrak, and S. R. Meech. Photochemistry of Fe(CO)$_5$ adsorbed on single crystal and roughened silver. Journal of Physical Chemistry B, 106(39):10205–10214, 2002. URL link.

[310] D. J. Burke, T. Vondrak, and S. R. Meech. Photodesorption and photochemical dynamics on roughened silver: sulphur dioxide and carbonyl sulphide. Surface Science, 585(1-2):123–133, 2005. URL link.

[311] G. Mie. Articles on the optical characteristics of turbid tubes, especially colloidal metal solutions. Annalen der Physik, 330(3):377–445, 1908. DOI. URL link.

[312] K. L. Kelly, E. Coronado, L. L. Zhao, and G. C. Schatz. The optical properties of metal nanoparticles: the influence of size, shape, and dielectric environment. The Journal of Physical Chemistry B, 107(3):668–677, 2003. DOI. URL link.

[313] C. Noguez. Surface plasmons on metal nanoparticles: the influence of shape and physical environment. The Journal of Physical Chemistry C, 111(10):3806–3819, 2007. DOI. URL link.

[314] J. Zhang and C. Noguez. Plasmonic optical properties and applications of metal nanostructures. Plasmonics, 3:127–150, 2008. URL link.

[315] J. Gersten and A. Nitzan. Electromagnetic theory of enhanced Raman-scattering by molecules adsorbed on rough surfaces. Journal of Chemical Physics, 73(7):3023–3037, 1980. URL link.

[316] A. Wokaun, J. P. Gordon, and P. F. Liao. Radiation damping in surface-enhanced Raman scattering. Physical Review Letters, 48(14):957–960, 1982. DOI. URL link.

[317] W. Yang, G. C. Schatz, and R. P. Van Duyne. Discrete dipole approximation for calculating extinction and Raman intensities for small particles with arbitrary shapes. The Journal of Chemical Physics, 103(3):869–875, 1995. DOI. URL link.

[318] C. Langhammer, B. Kasemo, and I. Zorić. Absorption and scattering of light by Pt, Pd, Ag, and Au nanodisks: Absolute cross sections and branching ratios. The Journal of Chemical Physics, 126(19):194702, 2007. DOI. URL link.

[319] X. Zhu. Surface photochemistry. Annual Review of Physical Chemistry, 45(1):113–144, 1994. DOI. URL link.

[320] J. W. Gadzuk, L. J. Richter, S. A. Buntin, D. S. King, and R. R. Cavanagh. Laser-excited hot-electron induced desorption: A theoretical model applied to NO/Pt(111). Surface Science, 235 (2-3):317 – 333, 1990. DOI. URL link.

[321] W. Ho. Surface photochemistry. Surface Science, 299-300:996–1007, 1994. DOI. URL link.

[322] K. B. Myli, S. R. Coon, and V. H. Grassian. Photon-induced reactions of aromatics adsorbed on rough and smooth Silver surfaces. Journal of Physical Chemistry, 99(44):16407–16415, 1995. URL link.

[323] D. V. Heyd, R. J. Scharff, and J. T. Yates. Comparison of thermal and photochemical behavior of $O_2$ chemisorbed on Pt(335). The Journal of Chemical Physics, 110(14):6939–6946, 1999. DOI. URL link.

[324] M. Rycenga, P. H. C. Camargo, W. Li, C. H. Moran, and Y. Xia. Understanding the SERS effects of single silver nanoparticles and their dimers, one at a time. The Journal of Physical Chemistry Letters, 1(4):696–703, 2010. DOI. URL link.

[325] C. Farcau and S. Astilean. Mapping the SERS efficiency and hot-spots localization on Gold film over nanospheres substrates. The Journal of Physical Chemistry C, 114(27):11717–11722, 2010. DOI. URL link.

[326] C. Langhammer, Z. Yuan, I. Zorić, and B. Kasemo. Plasmonic properties of supported Pt and Pd nanostructures. Nano Letters, 6(4):833–838, 2006. DOI. URL link.

[327] C. Langhammer, M. Schwind, B. Kasemo, and I. Zorić. Localized surface plasmon resonances in aluminum nanodisks. Nano Letters, 8(5):1461–1471, 2008. DOI. URL link.

[328] G. Costantini. Nanostructuring of metal surfaces by homoepitaxial growth and ion etching. PhD thesis, Faculty of Mathematical, Physical and Natural Science. University of Genova, 1999.

[329] C. K. Chen, T. F. Heinz, D. Ricard, and Y. R. Shen. Surface-enhanced 2nd-harmonic generation and Raman-scattering. Physical Review B, 27(4):1965–1979, 1983. URL link.

[330] M. Lust, A. Pucci, and A. Otto. SERS and infrared reflection-absorption spectroscopy of NO on cold-deposited Cu. Journal of Raman Spectroscopy, 37(1-3):166–174, 2006. DOI. URL link.

[331] T. Y. Olson, A. M. Schwartzberg, C. A. Orme, C. E. Talley, B. O'Connell, and J. Z. Zhang. Hollow Gold-Silver double-shell nanospheres: structure, optical absorption, and surface-enhanced Raman scattering. The Journal of Physical Chemistry C, 112(16):6319–6329, 2008. DOI. URL link.

[332] L. Rodríguez-Lorenzo, R. A. Álvarez Puebla, F. J. G. de Abajo, and L. M. Liz-Marzán. Surface enhanced Raman scattering using star-shaped Gold colloidal nanoparticles. The Journal of Physical Chemistry C, 114(16):7336–7340, 2010. DOI. URL link.

[333] P.-F. Guo, S. Wu, Q.-J. Ren, J. Lu, Z. Chen, S.-J. Xiao, and Y.-Y. Zhu. Fluorescence enhancement by surface plasmon polaritons on metallic nanohole arrays. The Journal of Physical Chemistry Letters, 1(1):315–318, 2010. DOI. URL link.

[334] Comsol3.5a. COMSOL Multiphysiscs. User's guide. COMSOL AB, 2008. URL link.

[335] S. J. Henley, J. D. Carey, and S. R. P. Silva. Pulsed-laser-induced nanoscale island formation in thin metal-on-oxide films. Physical Review B, 72(19):195408, 2005. DOI. URL link.

[336] L. Zhao, K. L. Kelly, and G. C. Schatz. The extinction spectra of silver nanoparticle arrays: influence of array structure on plasmon resonance wavelength and width. The Journal of Physical Chemistry B, 107(30):7343–7350, 2003. DOI. URL link.

[337] C. L. Haynes, A. D. McFarland, L. Zhao, R. P. Van Duyne, G. C. Schatz, L. Gunnarsson, J. Prikulis, B. Kasemo, and M. Kall. Nanoparticle optics: the importance of radiative dipole coupling in two-dimensional nanoparticle arrays. The Journal of Physical Chemistry B, 107(30): 7337–7342, 2003. DOI. URL link.

[338] P. B. Johnson and R. W. Christy. Optical-constants of noble-metals. Physical Review B, 6(12): 4370–4379, 1972. URL link.

[339] X. Ni, Z. Liu, and A. V. Kildishev. PhotonicsDB: optical constants, 2008. URL link.

[340] F. J. García-Vidal and J. B. Pendry. Collective theory for surface enhanced Raman scattering. Physical Review Letters, 77(6):1163–1166, 1996. DOI. URL link.

[341] Comsol3.5a. RF module. User's Guide, 2008. URL link.

[342] J. Jin. The finite element method in electromagnetics. Wiley, 2nd edition edition, 2002.

[343] A. Pors, O. Albrektsen, S.I. Bozhevolnyi, and M. Willatzen. The optical properties of a truncated cavity embedded in gold. In Proceedings of the Comsol Conference 2009 Milan, 2009. URL link.

[344] J. Camden and G. C. Schatz. Nanosphere optics lab, 2006. URL link.

[345] C. E. Román-Velázquez, C. Noguez, and R. G. Barrera. Substrate effects on the optical properties of spheroidal nanoparticles. Physical Review B, 61(15):10427–10436, 2000. DOI. URL link.

[346] H. C. Van de Hulst. Light scattering by small particles. John Wiley & Sons, New York, 1957.

[347] C. Langhammer, I. Zorić, B. Kasemo, and B. M. Clemens. Hydrogen storage in Pd nanodisks characterized with a novel nanoplasmonic sensing scheme. Nano Letters, 7(10):3122–3127, 2007. DOI. URL link.

[348] A. Gerlach, G. Meister, R. Matzdorf, and A. Goldmann. High-resolution photoemission study of the $\bar{Y}$ surface state on Ag(110). Surface Science, 443(3):221 – 226, 1999. DOI. URL link.

[349] R. Matzdorf. Quasi-particle lifetimes on noble metal surfaces studied by ARPES and STM. Chemical Physics, 251(1-3):151 – 166, 2000. DOI. URL link.

[350] K. Horn, M. Hussain, and J. Pritchard. The adsorption of CO on Cu(110). Surface Science, 63 (C):244–253, 1977. URL link.

[351] A. M. Bradshaw and F. M. Hoffmann. The chemisorption of carbon monoxide on palladium single crystal surfaces: IR spectroscopic evidence for localised site adsorption. Surface Science, 72(3):513 – 535, 1978. DOI. URL link.

[352] W. X. Huang and J. M. White. Propene adsorption on Ag(111): a TPD and RAIRS study. Surface Science, 513(2):399 – 404, 2002. DOI. URL link.

[353] P. Galletto, H. Unterhalt, and G. Rupprechter. The molecular orientation of CO on Pd(111): a polarization-dependent SFG study. Chemical Physics Letters, 367(5-6):785 – 790, 2003. DOI. URL link.

[354] M. Scheffler. The influence of lateral interactions on the vibrational spectrum of adsorbed CO. Surface Science, 81(2):562 – 570, 1979. DOI. URL link.

[355] M. Moskovits and J. E. Hulse. Frequency shifts in the spectra of molecules adsorbed on metals, with emphasis on the infrared spectrum of adsorbed CO. Surface Science, 78(2):397 – 418, 1978. DOI. URL link.

[356] B. N. J. Persson and R. Ryberg. Brownian motion and vibrational phase relaxation at surfaces: CO on Ni(111). Physical Review B, 32(6):3586–3596, 1985. DOI. URL link.